

**Influence of Crystallisation Environment on the
Nucleation and Growth of Single Crystals of
(RS)-Ibuprofen**

by

Thai Thu Hien Nguyen

A dissertation submitted in accordance with the requirements for
the degree of

DOCTOR OF PHILOSOPHY

(Chemical Engineering)

UNIVERSITY OF LEEDS

Institute of Particle Science & Engineering

School of Process, Environmental and Materials Engineering

Dec 2013

The candidate confirms that the work submitted is her own and that appropriate credit has been given where reference has been made to the work of others.

This copy has been supplied on the understanding that it is copyright material and that no quotation from the thesis may be published without proper acknowledgement.

2013 The University of Leeds Thai Thu Hien Nguyen

Acknowledgements

I wish to express my gratitude to the following:

Professor Kevin J. Roberts at the University of Leeds for his excellent supervision, enthusiasm, encouragement and endless support, throughout which he provided a good balance between guidance and freedom during my research.

Dr Robert Hammond at the University of Leeds for his guidance, invaluable comments and advice, particularly on molecular modelling work and many different aspects of crystallisation.

Dr Ivan Marziano at Pfizer, UK, Ltd. for sharing his extensive valuable experience of the pharmaceutical industry and for facilitating and organising a research visit to Pfizer, Sandwich, UK. Dr. Kevin Girard and Dr. Paul Meenan for hosting a research visit to Pfizer, Groton, US where technology transfer and a part of this research was carried out; working in Pfizer was a truly remarkable experience. Dr Gary Nichols from Pfizer, UK for his inspiration in designing the 15mL jacketed vessel based on an inverted microscope.

Members in the Crystallisation Science and Engineering research groups at the University of Leeds for their endless support, particularly Dr. Vasuki Ramachandran, for her help in the area of morphological simulation; Mr. Steve Caddick and Mr. Simon Lloyd for their efforts in designing and building the crystallisation cells and experimental set-up which were of enormous importance to this PhD work and Mr. Thomas Turner for his support and proof-reading of my thesis.

Dr. Ardhendu Behera and Prof. David Hogg of the Artificial Intelligence Group at the Computing School, University of Leeds, for developing image analysis software.

Pfizer, UK and the Molecular Engineering Translational Research Center (METRC), UK for funding this project and Malvern Instrument Ltd., for their Morphologi G3 particle shape analysis system.

IPSE/SPEME for providing facilities and creation of such a great research environment.

My parents and my brother for their constant support and encouragement throughout my studies, without them this study would not have been achievable.

Abstract

The crystal growth of ibuprofen as a function of crystallisation environment is presented. Measurement of solubility as a function of solvent (ethanol 95%, ethyl acetate, acetonitrile and toluene) and temperature using UV/Vis spectroscopy and gravimetric analysis reveals less than ideal behaviour, consistent with strong solute-solute interactions, particularly in the case of acetonitrile. Examination of the nucleation kinetics reveals a comparatively small metastable zone width (MSZW) ($\Delta T = 10.0 - 13.9^\circ\text{C}$) with interfacial tensions in the range $2.56 - 5.52 \cdot 10^{-3} \text{ (J/m}^2\text{)}$.

The growth rates for the $\{001\}$ and $\{011\}$ faces of spontaneously nucleated single crystals are precisely measured in-situ using optical microscopy revealing that their growth rates increase with increasing supersaturation to different extents, depending on the solvent type with concomitant impact on the crystal habit. For similar supersaturations, the growth rate of $\{011\}$ is lowest in ethanol and highest in acetonitrile, whilst that of $\{001\}$ is lowest in toluene and highest in ethanol. The aspect ratios, as a function of supersaturation, are generally higher at the 15 mL than the 0.5 mL crystalliser scale size. The data is consistent with a 2-D Birth and Spread growth model for both surfaces and scale sizes. This is in good agreement with the calculated surface entropy α factor.

The measured growth rate dispersion for these faces is much less for these spontaneously nucleated crystals in stagnant, supersaturated solutions when compared to the literature data obtained for a stirred batch crystalliser. Additional higher index re-entrant faces are found at high levels of supersaturation consistent with their alignment either parallel to the $\{012\}$ or $\{112\}$ face.

The growth rate in the non-agitated jacketed vessel is found to be slightly higher than that for the agitated reactors with both being in quite in a good agreement with literature data suggesting that these results on single crystals will have utility in representative the growth rates of a population of crystals in an agitated crystallizer.

Observations are rationalised using molecular and crystallographic modelling revealing e.g. that polar protic solvents inhibit the growth rate of faces containing

available hydrogen bonding binding sites, such as carboxylic acid groups. Molecular conformational searching reveals the molecular structure in the solid-state to be close to that of molecules minimum intra-molecular energy. Conformer population analysis as a function of solvent reveals no significant solvent effect on the low energy conformer distribution indicative a low likelihood of polymorphic behaviour for this compound in good agreement with literature.

Contents

1	Introduction.....	1
1.1	Research Background	2
1.2	Research objectives	6
1.3	Project management.....	7
1.4	Thesis organisation	7
2	Crystal and Crystallisation Science	10
2.1	Introduction.....	11
2.2	Basic crystallography.....	11
2.2.1	Crystalline and amorphous solid	11
2.2.2	Lattices, unit cells and crystal systems	12
2.2.3	Crystal defects	15
2.3	Crystal chemistry and polymorphism	18
2.3.1	Crystal chemistry	18
2.3.2	Polymorphism.....	19
2.4	Crystal morphology	21
2.5	Crystallisation process	25
2.5.1	Solutions, solubility and supersaturation.....	26
2.5.2	Nucleation.....	28
2.5.3	Crystal growth	39
2.6	Design of crystal and particle properties by crystallisation.....	47
2.6.1	Background.....	47
2.6.2	The interrelationship among the structure, properties, performance and processing of crystalline material	51
2.7	Crystallisation characterisation.....	53
2.7.1	Optical microscopy.....	54
2.7.2	Differential scanning calorimetry (DSC)	54
2.7.3	Attenuated total reflection ultraviolet visible (ATR UV/Vis) spectroscopy ..	55
2.8	Closing remarks	57
3	Crystal growth rate kinetics and mechanism.....	58
3.1	Introduction.....	59
3.2	Expression of crystal growth rates.....	59
3.3	Growth rate dispersion (GRD).....	61

3.4	Techniques for studying crystal growth rate	63
3.4.1	Microscopy technique.....	64
3.4.2	On-line high speed imaging.....	65
3.4.3	Focus beam reflectance measurement (FBRM)	67
3.4.4	AFM	68
3.4.5	Interferometry.....	69
3.5	Choice of experiment system for measuring crystal growth	70
3.5.1	Crystallography structures.....	70
3.5.2	RS-ibuprofen	71
3.5.3	S-ibuprofen	73
3.5.4	Solubility	74
3.5.5	Crystal morphology	74
3.5.6	Crystal growth rates.....	76
3.6	Closing Remarks.....	77
4	Materials, instrumentation and methodology	78
4.1	Introduction.....	79
4.2	Materials	79
4.3	Computational methods	80
4.3.1	Conformational analysis	80
4.3.2	Conformational propensity as a function of solvents	81
4.3.3	Intermolecular force calculations	83
4.4	Experimental method.....	86
4.4.1	Polymorph and solvent screening.....	86
4.4.2	Solubility measurements	86
4.4.3	Polythermal and isothermal crystallisation.....	89
4.4.4	Single crystal growth rate measurements	93
4.4.5	Comparison of the growth rate in non-agitated vessel and in agitated-vessel	98
4.5	Conclusions.....	100
5	Modelling the molecular and crystallography structure and its mediation by its solution state environment	102
5.1	Introduction.....	103
5.2	Conformational analysis for a free ibuprofen molecule	103
5.3	Predicted morphology compared to experimental morphology	110

5.3.1	Attachment energy morphological simulation for a growth unit based on a monomer	111
5.3.2	Attachment energy morphological simulation for a growth unit based on a dimer	120
5.4	Detailed surface chemistry analysis of the {001}, {011}, {100} and {110} face	125
5.5	Conformer population in solutions	129
5.6	Conclusions.....	132
6	Crystallisation process characterisation and analysis.....	134
6.1	Introduction.....	135
6.2	Polymorphism screening	135
6.3	Solubility measurements.....	137
6.4	Polythermal crystallisation as a function of solvent	144
6.5	Isothermal crystallisation as a function of solvent	148
6.6	Conclusions.....	155
7	Growth kinetic and mechanism.....	157
7.1	Introduction.....	158
7.2	Mean growth rate of the {001} and {011} faces as a function of growth environment	158
7.3	Crystal morphology as a function of growth environment.....	165
7.4	Variation in growth rates crystal by crystal.....	167
7.5	Rationalisation the growth rates with intermolecular bonding and surface chemistry.....	170
7.6	Growth rate mechanism of {001} and {011} at two scales 0.5mL and 15mL...	172
7.7	Correlation between the calculated α factor and the growth mechanism	175
7.8	Analysis of the re-entrant faces	178
7.9	Analysis of the curved {001} faces of ibuprofen in toluene	182
7.10	Crystal population growth rate measurements at 7mL reactor scale	184
7.10.1	Growth rate in 7mL non-agitated vessel.....	184
7.10.2	Growth rate in 7mL agitated vessel.....	185
7.11	Discussion.....	189
7.12	Conclusions.....	192
8	Technology transfer: Growth rate measurements in an industrial R&D workstream.....	193
8.1	Introduction.....	194

8.2	Solubility.....	194
8.3	Growth rate determination for compound A	195
8.3.1	Growth rate in 2-MeTHF.....	195
8.3.2	Growth rate in a mixture of 99% 2-MeTHF and 1% water.....	199
8.4	Discussion.....	200
9	Conclusions and suggestions for future work	202
9.1	Introduction.....	203
9.2	Conclusions for this study	203
9.2.1	Molecular modelling	204
9.2.2	Solid-state and morphological simulation	204
9.2.3	Instrumentation for studying the growth kinetics.....	206
9.2.4	Nucleation as a function of solvent	206
9.2.5	Effect of crystallisation environmental conditions on the growth rate of individual crystal faces	207
9.3	Review aims and objectives.....	210
9.4	Suggestions for future work.....	210
9.4.1	The measurement of the growth rate for the {100} face.....	210
9.4.2	Development of a medium throughput screening particle characterisation system facility using the Morphologi G3	211
9.4.3	Development of software for automated image analysis.....	212
9.4.4	Measurement of the growth rate at 0.5L scale –sizes.....	213
9.4.5	Dissolution modelling using Peltier crystallisation cell	214
9.4.6	Modelling crystal growth in the {001} and {011} directions using morphological population balance.....	216
9.4.7	Integration with grid search to calculate solvent binding the surface	216

List of Tables

Table 2.1 The seven crystal systems [5]	13
Table 2.2 Summary for types of crystal defects [35]	16
Table 2.3 Predicted growth mechanism according to the value of α	45
Table 2.4. The critical values $\alpha_{hkl}R$ of the α_{hkl} factors of crystal habit faces of biphenyl and naphthalene.....	46
Table 3.1 Microscopy techniques for studying crystal growth kinetics and mechanisms	64
Table 4.1 Solvents used in studying polymorphism	79
Table 5.1 Total energy changed when rotating each torsion angle using the Conformer module in Material Studio.....	104
Table 5.2 Measured torsion angles T3, T4, T5 and T8 from the structure of an ibuprofen molecule before and after geometry optimisation, which were used to mark on the energy map	104
Table 5.3 Energy change when rotating two torsion angles (T3-T4), (T3-T5), (T3-T8), (T4-T5), (T4-T8) and (T5-T8) from -180 to 180 degree (kcal/mol).....	106
Table 5.4 Atomic charges of all atoms in the ibuprofen crystal structure	111
Table 5.5 Five strongest intermolecular interactions on the crystal lattice corresponding to the different molecular distance	114
Table 5.6 Contributions of different type of atoms in the asymmetric unit to the lattice energy (%).....	114
Table 5.7 Interplanar spacing (in Å) and attachment energies (in kcal/mol) for a growth unit based on a monomer	116
Table 5.8 Bonding analysis for the {011}, {001} and {100} faces with for a growth unit based on a monomer.....	118
Table 5.9 Atomic charges of two molecules for the dimer calculation	120
Table 5.10 Attachment energies (kcal/mol) calculated for a growth unit based on a dimer	122
Table 5.11 Full calculation mode analysis for the {011}, {001}, {100} and {110} faces with for a growth unit based on a dimer	123
Table 5.12 Percentage of ibuprofen conformer in solvents (%) calculated from COSMOtherm software package	130
Table 5.13 Torsion angles of preferred conformations in solutions	131

Table 6.1 DSC data: onset of melting point, melting point peak and enthalpy of fusion	136
Table 6.2 Calibration line of ibuprofen in ethanol 95%, ethyl acetate and acetonitrile at temperature from 15-35°C	139
Table 6.3 Solubility of ibuprofen in ethanol, ethyl acetate, acetonitrile and toluene (g/ml).....	140
Table 6.4 Calculated activity coefficients of ibuprofen in various solvents as a function of temperature	143
Table 6.5 Enthalpy of dissolution, ΔH , and entropy of dissolution, ΔS , derived from solubility data, together with calculated activity coefficient and temperature dependence fitting parameter. Logarithm of activity coefficients of as a function of saturation temperature ($\text{Ln}\gamma = aT + b$)	144
Table 6.6 MSZW of ibuprofen in ethyl acetate, acetonitrile and toluene solutions and the relationship between $\text{Log}(b)$ vs $\text{Log}(\Delta T)$	147
Table 6.7 Induction times of acetonitrile, toluene, ethanol 95% and ethyl acetate.....	149
Table 6.8 The interfacial energy calculated from the slopes of the straight lines $\text{Ln}\tau_{\text{ind}}$ versus $T^{-3}(\text{lnS})^{-2}$	153
Table 6.9 The nucleation order and calculated interfacial energy calculated from MSZW	155
Table 7.1 Mean growth rate of face {011} and {001} of ibuprofen in ethanol 95%, ethyl acetate, acetonitrile and toluene in prototype cell 0.5 mL and jacketed-vessel 15 mL.	162
Table 7.2 Comparison of the mean growth rates of face {011} and {001} of ibuprofen in ethanol with the growth rate calculated from $G = k_G \sigma^n$ (with $k_G = 15$, $n=1$) [15].	163
Table 7.3 The coefficient of variation for the growth rate of the crystal faces.....	168
Table 7.4 Growth Rate Dispersion of some other organic and inorganic materials	169
Table 7.5 Fitting parameters for the faces {011} and {001} of ibuprofen grown in ethanol 95%, ethyl acetate, acetonitrile and toluene with B&S model and BCF models together with the adjusted coefficient of determination adjusted R^2 (adj. R^2).....	173
Table 7.6 The surface anisotropy factors ξ_{hkl} calculated from E_{crys} and E_{latt} for a growth unit based on a monomer and the surface entropy factor α_{hkl}	176
Table 7.7 The surface anisotropy factors ξ_{hkl} calculated from E_{crys} and E_{latt} for a growth unit based on a dimer and the surface entropy factor α_{hkl}	176
Table 7.8 The critical supersaturation for the appearance of the re-entrant faces	179

Table 7.9 Overall growth rates obtained from microscopy method and CRYSTALLINE experiments at various supersaturation levels, σ	188
Table 8.1 The growth rate of the length and width at $\sigma = 0.65$ and 0.52 in stagnant solutions	198
Table 8.2 The growth rate of the length and width at $\sigma = 1.00$ and 0.38 in turbulent solutions	198
Table 8.3 Growth rate of length and width in 99% 2-MeTHF 1% water at $\sigma = 1.07$ and 0.87	199
Table 9.1 Comparison of the growth rate of face $\{011\}$ and $\{001\}$ in ethanol in the 0.5ml cuvette crystallisation cell using a re-circulation bath and peltier heat-pump....	215

List of Figures

Figure 1.1 Schematic of medical product development from basic research in lab to launching in the market [3].	3
Figure 1.2 A crystallisation process for non-specific pharmaceutical drug substance [4].	3
Figure 2.1 (left) Crystalline SiO ₂ (quartz), in which atomic arrangements are regular; (right) amorphous SiO ₂ (glass) refers to objects having no definite shape and is defined as non-crystal material (irregular atomic arrangements) [29].	12
Figure 2.2 Miller indices of a plane derived from the intercept of the plane on the crystallographic axes.	14
Figure 2.3 Bravais lattices classified into three main types: primitive, body center and face center [33].	15
Figure 2.4 (a) Edge dislocation, (b) screw dislocation and (c) the Burgers' vector is perpendicular to the line of distortion in the case of edge dislocation and in screw dislocation the Burger's vector is parallel to the line of distortion [36].	17
Figure 2.5 Factors impacting on the crystal structure comprise direction and strength of intermolecular forces.	18
Figure 2.6 Relationship between the Gibbs free energy G and the temperature T for two polymorphs for an enantiotropic system (left) and a monotropic system (right) [41].	20
Figure 2.7 Various crystal shapes [43].	21
Figure 2.8 Procedure to construct a Wulff plot where O is the nucleation centre. The equilibrium shape of a crystal can be constructed by drawing vectors to all possible crystallographic faces from O and marked on the vectors with the distances proportional to γ_n , and then planes normal to the vectors are built through the marks on the vectors creating a closed polyhedron [46].	22
Figure 2.9 Basic approach of calculating the intermolecular interactions using the atom-atom method: C is the central molecule, P is a molecule outside the slice and S is a molecule inside the slice [52].	24
Figure 2.10 Schematic showing the classification of the nucleation stage in a crystallisation process.	28
Figure 2.11 Solubility-supersolubility diagram showing three regions with different behaviours: (1) a stable or unsaturated zone; (2) a metastable zone and (3) an unstable zone [56].	29

Figure 2.12 Schematic plot of the nucleation rate versus the degree of supersaturation showing the nucleation rate increases considerably when approaching critical supersaturation [58].	31
Figure 2.13 Free energy associated with a molecule cluster diagram for the nucleation explaining the critical nucleus.	33
Figure 2.14 Interfacial tension at the boundaries between two solids and one liquid [26].	36
Figure 2.15 Entacapone crystal (left) Needle-like crystals of form D obtained from with absence of SALE; (right) cubic crystal of form A in the presence of SALE [63].	39
Figure 2.16 Kossel model of a crystal surface [60].	40
Figure 2.17 Concentration driving forces of two stages (diffusion and adsorption) in crystal growth from the solution [26].	41
Figure 2.18 Crystal grown by the BCF mechanism shows the surface of the crystal with a screw dislocation and development of a spiral [60].	43
Figure 2.19 Crystal grown by birth and spread mechanism in which nucleation may occur at the edges, corners, or on the faces of the crystals [26].	43
Figure 2.20 (a) Ice (snow) crystal morphology changes by roughening occurring at the corner of a crystal; (b) Dendritic ice crystals [71].	44
Figure 2.21 Schematic showing the crystal growth rate mechanism taking place at the crystal/solution interface, involving screw dislocation (a) 2D surface nucleation (b) together with the expected crystal growth mechanisms as a function of solution supersaturation (c) and the transition between stable growth on a smooth surface to unstable growth at the roughened crystal/solution interface ((d) and (e)) [72].	44
Figure 2.22 Summary of physical properties of a crystal.	47
Figure 2.23 Diagrammatic route map of the influence of crystallisation conditions on crystal properties.	48
Figure 2.24 Morphology diagram of snow crystals showing various shapes under different crystallising conditions and only shapes grow under fixed conditions [84].	49
Figure 2.25 Inter-dependent relationship among the structure, properties, performance and processing of a drug [28].	51
Figure 2.26 Molecular packing in crystal structure of acetaminophen (a) form I (monoclinic); (b) form II (orthorhombic) [28].	52
Figure 2.27 Relationship between crystal structures and the powder tableability [28].	53
Figure 2.28 Schematic diagram of a UV-Vis spectroscopy.	56

Figure 2.29 ATR probe using 3-bounce sapphire ATR crystal.	56
Figure 3.1 An example of the experiment set-up for measurement of the growth rate of L-glutamic acid using online imaging system [17].....	66
Figure 3.2 2D projected image of L-glutamic acid generated through predicted 3-D shapes [22].	67
Figure 3.3 Focused Beam Reflectance Measurement [112].	68
Figure 3.4 Diagram of atomic force microscope (redraw after [120]).....	69
Figure 3.5 Schematic diagram of interferometry system (redraw after [121]).	69
Figure 3.6 Molecular diagram showing (a) structure and (b) packing in the crystallographic unit cell of the ibuprofen molecule.....	71
Figure 3.7 Molecular packing of ibuprofen (a) in the xz plane; (b) in the yz plane and (c) in the xy plane. A slightly tilted projection close to the yz plane reveals that hydrogen bonds are formed across the unit cell and between molecules 1 and 3 in the unit cell of the first row and the unit cell in the third row.....	72
Figure 3.8 Molecule structures of R-ibuprofen and S-ibuprofen.	73
Figure 3.9 Two molecules of S-(+)-ibuprofen in the asymmetric unit form a cyclic hydrogen-bonded dimer [132].....	73
Figure 3.10 Solubility of ibuprofen in various solvents [135].	74
Figure 3.11 Morphologies of ibuprofen in various solutions [136].	76
Figure 4.1 Structure of an ibuprofen molecule highlighting the potential torsion angles involved in double bonds and bonds terminated with hydrogen (not including bonds in benzene rings).	80
Figure 4.2 Schematic diagram of conformational analysis using CONFORMER in Material Studio.....	81
Figure 4.3 Schematic diagram of the examination of the conformer distribution in solvents.....	82
Figure 4.4 Flowchart describing the calculation of lattice energy from crystallographic information.....	84
Figure 4.5 Flowchart describing crystal morphology predictions from calculated attachment energies.....	85
Figure 4.6 DSC 820 Mettler used to determine melting points of ibuprofen recrystallised from series of solvents.	86
Figure 4.7 ATR UV-Vis spectroscopy Cary 50 from Variant employed to measure solubility of ibuprofen. The inset shows the probe.	87

Figure 4.8 (a) A 7ml crystalliser with overhead and bottom magnetic stirring which can be fitted in blocks of Avantium Crystalline platforms ; (b) Multi-reactor Avantium Crystalline platforms with parallel 7ml crystallizers with overhead and bottom stirring [154]	90
Figure 4.9 A sample turbidimetric profile for polythermal studies of 0.72g/ml of ibuprofen in ethyl acetate at the heating/cooling rate 0.1C/min: the transmittance and temperature as a function of time (a); plot of the transmittance as a function of temperature (b). From these plots, temperature of dissolution and temperature of crystallisation at different heating/cooling rates were investigated.	91
Figure 4.10 An example of isothermal crystallisation for ibuprofen crystallising from acetonitrile: Induction time is the period of time between the solution being saturated at a given temperature and the appearance of first nuclei of ibuprofen (the transmittance drops indicating the onset of crystallisation).	92
Figure 4.11 Diagram of scale-up crystallisation instrumentation for measurement of crystal growth rate at single particle level (pink block); for measurement of crystal growth rate in a population of crystals (blue block).	93
Figure 4.12 Prototype cell for measurement growth rate of individual faces of ibuprofen.	94
Figure 4.13 Crystallisation system set up for measurement of crystal growth rate in a 15ml jacketed vessel.	95
Figure 4.14 Image of crystal with overlaid annotations highlighting the methodology for the measurement of growth rate of the individual faces.	97
Figure 4.15 Sketch for the calculation of an area of a crystal; from this the equivalent diameter can be calculated.	100
Figure 5.1 RS-ibuprofen molecules with measured torsion angles T3, T4, T5 and T8 (a) before geometry optimization; (b) after geometry optimization and (c) S-ibuprofen molecules.....	105
Figure 5.2 Energy minimisation using the Geometry Optimization in Material Studio.	106
Figure 5.3 Energy map of a free ibuprofen molecule together with marked torsion angles for an isolated racemate-ibuprofen molecule before and after geometry optimization and S-ibuprofen molecules.	109
Figure 5.4 Numbering of the atoms in an ibuprofen molecule structure.	111

Figure 5.5 Lattice energy which is a sum of the van der Waals and electrostatics interactions which converges at 20 Å. The van der Waals and electrostatic contributions also converge with distance.	113
Figure 5.6 Morphology of ibuprofen calculated using (a) Lifson force field; (b) Momany force field; and (c) ibuprofen crystal grown from vapour phase [136].	116
Figure 5.7 Morphology of ibuprofen recrystallised in ethanol (a), ethyl acetate (b); acetonitrile (c); toluene (d).....	117
Figure 5.8 Thin crystal morphology of ibuprofen recrystallised in ethanol solutions ..	117
Figure 5.9 Molecular interaction of the 5 strongest bonds (a) The strongest bond type a (-7.47 kcal/mol) is a hydrogen-bond between carboxylic acid -COOH groups of ibuprofen (homosynthon); (b) Second strongest bond type b (-2.58 kcal/mol); (c) Third strongest bond type c (-2.26 kcal/mol); (d) Fourth strongest bond type d (-2.25 kcal/mol); (e) Fifth strongest bond type e (-1.33 kcal/mol).	119
Figure 5.10 Lattice energy which is a sum of the van der Waals interaction and electrostatics which converges at 20 Å in the dimer calculation.	121
Figure 5.11 Predicted crystal shapes of (RS)- ibuprofen in a dimer using Momany (a); Lifson force field (b).	122
Figure 5.12 Molecular interaction of the 5 strongest bonds in (a) The strongest bond type a (-4.49 kcal/mol); (b) Second strongest bond type b (-3.71 kcal/mol); (c) Third strongest bond type c (- 2.29 kcal/mol); (d) Fourth strongest bond type d (- 1.36 kcal/mol); (e) Fifth strongest bond type e (- 0.79 kcal/mol).	124
Figure 5.13 Molecular packing diagrams based upon the crystallographic structures of the {001} face viewed along the y axis (a) and along the x axis (b) showing its hydrophobic nature with -CH ₃ groups exposed at the surface with the -COOH groups exposed in one direction and in a quite restricted position.	126
Figure 5.14 Molecular packing diagrams based upon the crystallographic structures of the {011} face viewed along the x axis (a) and along the y axis (b) showing a more polar surface with exposed -COOH groups at the surface with two different directions.	127
Figure 5.15 Molecular packing diagrams based upon the crystallographic structures of the {100} face viewed along the x axis (a); viewed along the y axis (b).....	127
Figure 5.16 Molecular packing diagrams based upon the crystallographic structures of the {110} face viewed along the x axis (a) and viewed along the y axis (b).	128

Figure 5.17 10 lowest energy and optimised conformers were chosen for the conformational distribution study.	130
Figure 5.18 Population of four conformers (2, 4, 7 and 10) in solvents.	131
Figure 6.1 DSC data of ibuprofen raw material together with ibuprofen recrystallised from solvents showing similar melting points and melting peak shapes.	136
Figure 6.2 Spectra of ibuprofen in ethanol 95%, ethyl acetate and acetonitrile showing absorbance at 264 nm increase with increasing concentration of solutions.....	138
Figure 6.3 Calibration curves were obtained from the absorbances at 264 nm of the known concentration solutions.....	139
Figure 6.4 Spectra of ibuprofen in ethyl acetate showing solubility increase with increasing temperature and λ_{max} does not shift with temperature. The λ_{max} was not found to shift even in different solvents and concentration nor even as a function of temperature.....	140
Figure 6.5 Polynomial regression lines of the solubility of ibuprofen in ethanol, ethyl acetate, acetonitrile and toluene at temperatures from 15-35°C (left); and plot of 1/T versus lnX of the ideal solubility and the real solubility (right).	142
Figure 6.6 Comparison of the solubility (a) in ethanol; (b) in ethyl acetate; (c) in toluene; (d) in acetonitrile in this study with published data.	143
Figure 6.7 Experimental polythermal data for ibuprofen in ethanol 95% solution illustrating that (a) ibuprofen (1.4g/ml) does not crystallise under polythermal crystallisation at a heating/cooling rate of 0.1 °C/min when cooling from 55°C to -15°C; (b) ibuprofen (0.98g/ml) does not crystallise under polythermal crystallisation at heating/cooling rate 0.5°C/min when cooling down from 50°C to -15°C. Crystallisation only occurs during the hold segment of the program i.e after the cooling stage is complete.	145
Figure 6.8 Plots of the dissolution and nucleation on-set temperatures for ibuprofen in ethyl acetate (0.72g/ml), acetonitrile (0.28g/ml), and toluene (0.65g/ml) as a function of solution cooling/ heating rate. The dissolution and crystallisation temperature are determined from the intercepts.....	146
Figure 6.9 An example of the measured induction time of ibuprofen in acetonitrile (0.4g/ml) at S = 6.86.	148
Figure 6.10 Induction time of acetonitrile, toluene, ethanol 95% and ethyl acetate at different supersaturation ratios.....	150

Figure 6.11 Viscosity of ibuprofen solution examined as a function of solvents and temperature.....	152
Figure 6.12 Plot of $\ln\tau_{ind}$ versus $T^{-3}(\ln S)^{-2}$ of ibuprofen in 4 solvents. Interfacial tension can be calculated from the slope of the line.	153
Figure 6.13 The size of the critical nucleus as a function of temperature and supersaturation (a) in acetonitrile; (b) in toluene; (c) in ethanol 95% and (d) in ethyl acetate.....	154
Figure 7.1 Series of optical micrographs of ibuprofen crystals grown in ethanol 95% between $\sigma = 1.17$ and $\sigma = 0.66$ (a), in ethyl acetate between $\sigma = 1.20$ and $\sigma = 0.69$ (b), in acetonitrile between $\sigma = 1.12$ and $\sigma = 0.79$ (c) and in toluene between $\sigma = 1.17$ and $\sigma = 0.70$ (d) at the 0.5ml scale size showing the growth of the crystals and their morphology as a function of solvent, elapsed time and solvent supersaturation.....	160
Figure 7.2 The distance from the centre of the crystals to the faces was plotted as a function of time. The slope of the line gives the measured growth rate of the face measurement for the estimation of the growth rate for the {011} and {001} face.	161
Figure 7.3 ATR UV/Vis spectra of ibuprofen in ethanol during crystallisation obtained every minute in 50 mins (left); Solute concentration and relative supersaturation calculated from the UV/Vis absorbance calibration model in 15mL jacketed vessel (right).....	161
Figure 7.4 Mean growth rate of the {011} and {001} face versus supersaturation of crystals grown in ethanol 95%, ethyl acetate, acetonitrile and toluene.	163
Figure 7.5 Photographs of aspect ratios (the ratios of the length and the width of crystals) of ibuprofen crystal grown from ethanol, ethyl acetate, acetonitrile and toluene versus relative supersaturation together with the vacuum morphology figure from Bunyan [136]. Note that the aspect ratios mostly tend to increase with decreasing supersaturation.	166
Figure 7.6 Aspect ratios of ibuprofen crystals grown from ethanol, ethyl acetate, acetonitrile and toluene versus relative supersaturation at two scale-sizes: 0.5ml and 15ml.	167
Figure 7.7 Distribution spread CV_v versus experimental growth time at 25°C in absolute ethanol) (reproduced with permission from Rashid et al [15])......	169
Figure 7.8 Plots of the growth rate versus supersaturation together with fitted B&S and BCF mechanism models for both {011} face (left) and {001} face (right) and for both 0.5mL (top) and 15mL (bottom).	173

Figure 7.9 Schematic diagram (a) and ibuprofen crystals grown from ethanol (b), acetonitrile (c), ethyl acetate (d), and toluene (e) with high index re-entrant faces.....	178
Figure 7.10 Ibuprofen crystal grown in ethanol at $\sigma = 0.97$ (a), $\sigma = 0.79$ (b) and $\sigma = 0.66$ (c) showing these re-entrant faces are likely appear at high supersaturation and not present at lower supersaturation.....	179
Figure 7.11 The series of polarized-light photographs of ibuprofen crystals in various optical rotation positions showing the whole crystal body became darker or brighter, in which both parts are of equal brightness. This proves that the re-entrant (concave) edges are not due to twinning.....	180
Figure 7.12 Schematic diagram showing the formation of re-entrant faces (a) The interfacial angle of the {011} and {012} face from the experimental morphology (b) and from morphological simulation (c).....	181
Figure 7.13 Molecular packing on the {012} viewed along x axis (a) and along y axis (b).....	182
Figure 7.14 Molecular packing on the {112} viewed along x axis (a) and along y axis (b).....	182
Figure 7.15 (a) Morphology of ibuprofen in toluene was found to be grown in elongated shape with a tapering of the {001} face; (b) Schematic showing the typical growth morphology for KDP crystals with pure KDP and impurity-doped KDP. Crystal grow elongated associated with impurities, being preferentially incorporated into the (100) and (010) crystal growth sectors [178-180].	183
Figure 7.16 Ibuprofen single crystals growing in stagnant solution after seeding at $\sigma = 0.157$. From these images, the area of crystals can be calculated and then the equivalent diameter.....	184
Figure 7.17 Growth rate (in equivalence diameter) in a 7mL non-agitated jacketed reactor at $\sigma = 0.157$ and 0.105.....	185
Figure 7.18 A sequence of crystals grown in ethanol after seeding at $\sigma = 0.157$ in an agitated reactor (a); the images of crystals before and after segmentation for image analysis (b).	186
Figure 7.19 Plots of equivalent diameter of ibuprofen crystals grown in ethanol versus time at $\sigma = 0.157$ and 0.105.....	187
Figure 8.1 Solubility of compound A in 2-MeTHF and in a mixture of 99% 2-MeTHF and 1% water.....	195

Figure 8.2 A sequence of in-situ crystal growth observations of 4 crystals grown from 2-MeTHF at $\sigma = 0.65$ with 10 minute intervals between images.....	196
Figure 8.3 A sequence of in-situ crystal growth observations of 2 crystals grown from 2-MeTHF at $T = 25^{\circ}\text{C}$ ($\sigma = 0.52$) with 10 minutes interval between images.	196
Figure 8.4 A sequence of in-situ crystal growth observations of 3 crystals nucleated and grown from 2-MeTHF isothermal at $T = 15^{\circ}\text{C}$ ($\sigma = 1.00$) after tilting the cuvette.....	197
Figure 8.5 A sequence of in-situ crystal growth observations of a crystal nucleated and from 2-MeTHF isothermal at $T = 28^{\circ}\text{C}$ ($\sigma = 0.38$) after tilting the cuvette with 10 minutes interval between images.	197
Figure 8.6 An example of the growth rate of the length and width of crystals grown from 2-MeTHF isothermal at $T = 22^{\circ}\text{C}$ ($\sigma = 0.65$) in stagnant conditions. Each line represents the growth rate of individual crystals over time.	198
Figure 8.7 A sequence of in-situ crystal growth observations at $\sigma = 1.07$ (above) and $\sigma = 0.87$ (below) with 10 minutes interval between images together with an example of the plot of the length and width versus time of crystals grown from the mixture of 99% 2-MeTHF 1% water.....	199
Figure 9.1 (a) Multi-micro-reactor (8-cell crystalliser) designed to be integrated with the Morphologi G3; (b) Malvern Instruments Morphologi G3; (c) Representative images of crystals captured in the in-situ cell.....	212
Figure 9.2 (a) Experiment set-up for 0.5L scale-size using a Perdix camera for the measurement of the size distribution of crystals versus time; (b) Perdix camera probe with 19mm diameter and 2.5 micron optical resolution.	214
Figure 9.3 Peltier crystallisation cell based on an inverted microscope using a Labview program for controlling the temperature of the peltier.....	215
Figure 9.4 A sequence of in situ crystals grown from ethanol 95% at $\sigma = 0.79$ in the peltier crystallisation cell with 4 minute intervals between images captured.....	215
Figure 9.5 Schematic diagram for calculating specific surface energies of crystal surface in solution.....	217

List of Symbols

Greek letters

α is the surface entropy factor

γ is interfacial energy (tension) of the solid (crystalline phase) with the solution phase

γ_i^{sat} is the activity coefficient of the solute in the saturated solution

δ is the thickness of the laminar layer

θ is the angle contact between the crystal and the foreign solid surface

Δc is maximum supersaturation

ΔH_{fus} is the enthalpy of fusion of the pure solute;

ΔH_{mix} is the enthalpy of mixing

ΔH_{dis} is the enthalpy of dissolution of solute

ΔH_{sub} is the enthalpy of sublimation

ΔS_{dis} is the entropy of dissolution of solute

ΔG is the free energy change associated with nucleus formation

ΔG_s is the surface free energy

ΔG_v is the volume excess free energy between the solid and the liquid phase

ϵ is the molar extinction coefficient (or molar absorptivity)

ϵ_p is the average power input

μ is dynamic viscosity of the solution

ν is the kinematic viscosity

ξ is the surface anisotropy factor

ρ is the density of the solid

σ is relative supersaturation

τ is crystallisation induction time

ν is the numbers of mole of ions formed from one mole of electrolyte

$\omega(i)$ is a multiplicity of the conformer (i)

Latin letters

a_i^{sat} is the activity of the solute i in the saturated solution

A_b is the absorbance of the material

A is the area of crystal surface

Adj. R^2 is the adjusted coefficient of determination

b is the path length
 C is the solution concentration at a specific temperature
 C^* is the equilibrium concentration at that temperature
 d_{hkl} is the interplanar spacing of the crystal face (hkl)
 d is the agitator diameter
 d_m is the molecular diameter
 D is the diffusion coefficient
 E_{att} is the attachment energy
 E_{latt} the crystal lattice energy or crystallisation energy
 E_{sl} is the intermolecular bonding energy within the surface growth slice
 g is gravitational acceleration
 I is the transmitted intensity
 I_0 is the incident intensity
 J is the nucleation rate
 K is the Boltzmann constant
 k is the nucleation rate constant
 k_m is the coefficient of mass transfer
 L is the characteristic size of the crystal
 m is the nucleation rate order
 n is the population density per unit volume
 N_A is the Avogadro number
 q_i and q_j are the fractional charges on atom i and j separated by distance r
 r is the solid particle radius
 R is the ideal gas constant
 R_G is the overall mass growth rate
 $R_{\{001\}}$ is the growth rate of the $\{001\}$ face
 $R_{\{011\}}$ is the growth rate of the $\{011\}$ face
 R^2 is the coefficient of determination
 S is supersaturation ratio
 T_m is the melting point
 T_g is the glass transition temperature
 v_{hkl} is the growth rate of the (hkl) face
 V_{cell} is the volume of the unit cell

V_{kij} is the interaction energy between atom i in the central molecule and the atom j in the k^{th} surrounding molecule

V is the total suspension volume of the crystalliser

X is the mole fraction of the solute

Z is the number of molecules in the unit cell

List of Abbreviations

API: Active pharmaceutical ingredients

ADP: Ammonium dihydrogen phosphate

AFM: Atomic force microscopy

ATR UV/Vis: Attenuated total reflection ultraviolet visible

BFDH: Bravais-Friedel and Donnay-Harker

BCF: Burton, Cabrera and Frank

B&S: Birth and spread

CCG: Constant crystal growth

CFD: Computational fluid dynamic

COSMO: Conductor-like screening model

CSD: Crystal size distribution

CV_v: Coefficient of variation

DFT: Density functional theory

DSC: Differential scanning calorimetry

FBRM: Focused beam reflectance measurement

FDA: Food and drug administration

FTIR: Fourier transform infrared spectroscopy

GRD: Growth rate dispersion

ISPV: In-situ particle viewer

iPRD: Institute of Process & Development

MeTHF: Methyl tetrahydrofuran

METRC: Molecular Engineering Translational Research Centre

MSZW: Metastable zone width

MEK: Methyl ethyl ketone

MIBK: Methyl isobutyl ketone

MSMPR: Mixed suspension, mixed product removal

NSAID: Non-steroid anti-inflammatory drug

PBM: Population balance model

PVM: Process vision viewer

RF: Random fluctuation model

SALE: Self-assemble molecular layer

SDG: Size dependent growth

THF: Tetrahydrofuran

XRD: X-ray diffraction

1 Introduction

Summary:

The background underpinning this research together with aims and objectives of this study are presented. Details of the research's project management and summary of the thesis plan is also provided.

1.1 Research Background

Industry estimates that 70% of all chemical products manufactured involve a unit operation requiring solid particulate processing [1]. Within this, perspective crystallisation represents an important purification, separation and pre-formulation process in the pharmaceutical and fine chemical process industries. It is the primary method applied for the final stage production of a wide range of materials from inorganic compounds to high value-added organic materials such as active pharmaceutical ingredients (API) and specialty chemicals. However, the crystallisation process associated with nucleation and the crystal growth process has often been considered more as an art rather than a science [2] reflecting the fact that it has been considered difficult to control due to its unpredictable behaviour.

The 3D nature of a crystalline material combined with the complex molecular and crystal chemistry of many specialty compounds can conspire to produce a high degree of variability in product forms. For example, this may lead to production of a dispersion of non-equant particle morphologies which can be both difficult to both separate and purify. Such materials can also be problematic downstream in terms of challenges in their powder flow, blending ability and formulation. Variation in crystallisation processes can also impact in terms of concomitant product crystal chemistry (polymorphism or solvate formation), leading, in turn, to significant changes in product quality, i.e. through factors such as the stability, bioavailability, processability, crystallinity and/or purity of a drug product. The latter can lead to quality assurance problems such as rejection in terms of product specification and performance. Such factors have been known to impact on the product economic profitability and viability leading, in turn, to the potential for loss of market share and in extreme cases product withdrawal. According to the Food and Drug Administration (FDA) (2004) [3], the number of new drug and biologic applications submitted to the FDA has declined significantly because the current drug product development path (Figure 1.1) is becoming increasingly challenging, inefficient, and costly.

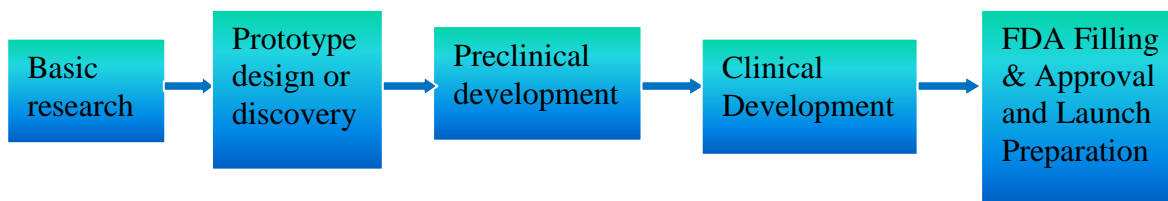


Figure 1.1 Schematic of medical product development from basic research in lab to launching in the market [3].

Most of the cost increases are within the development phase, between discovery and launch. In this critical path, a new drug needs to prove safety, efficiency and industrialisation. Reflecting basic chemical engineering principles, the ‘industrialisation’ stage must be feasible from lab concept to manufacturability as a high-quality product in mass production. The challenges involved in successful industrialization are complex including, unpredicted problems in physical design, characterization, manufacturing scale-up and quality control. The stages of the development of robust, reproducible and scalable crystallization processes are shown in Figure 1.2.



Figure 1.2 A crystallisation process for non-specific pharmaceutical drug substance [4].

A crystallisation process starts from initial screens at microgram scale right through to plant scale operations. Variation of crystallisation parameters is tested on a ml scale size to generate growth kinetics data for further optimization and production to ensure a rapid development for a product. Hence, in order to isolate the crystals exhibiting the desired physical properties, the fundamental process of crystal growth and its associated kinetics need to be understood, characterised, controlled and be scalable. In addition, crystallisation parameters and testing process robustness are required to be validated.

Previously studies have mostly presented measurements of growth rate of individual faces for seed crystals grown at comparatively low supersaturations [4-10]. Alternatively, measurements have been made of the growth rates of a population of crystals as prepared under crystallisation reactor environment conditions e.g. through the measurement of the growth characteristic dimensions (such as length, width, and equivalent diameter etc.) of the crystals [11-18]. In the former case whilst this is measuring the individual growth faces, the influence on the measurements imposed either by the hydrodynamic environment associated with the measurements or by the selection of specific seeds [19] is unknown. Similarly, in the latter case, it is hard to extract out the kinetics associated with the growth of individual habit faces. Within this overall context, there have been surprisingly limited kinetic studies on the growth of the individual faces of spontaneously-nucleated crystals prepared under diffusion limited growth in stagnant solutions. Such measurements are helpful in that they provide baseline crystal growth kinetics with respect to which the impact of agitation and mixing can be assessed. Additionally, there have also been few detailed studies of the crystal growth-rates of populations of spontaneous nucleated single-crystals in particular through research seeking to probe growth-rate dispersion [20, 21].

A significant factor in the scarcity of research resulting from investigations into the growth rate of individual single crystal growth perhaps lies in the lack of rapid and routine experimental methodologies, for studying this aspect mindful that the most common techniques available for crystallisation monitoring are intended for use at large scale and are aimed at measuring average growth rate values based on an assessment of a crystal population e.g. focused beam reflectance measurement (FBRM) [22-24], rather than face-specific growth rates for batches of individual crystals. FBRM gives a correlation between the number of counts per second, the cord-length distribution of particles and from these particle sizes can be inferred. However, such measurements do not provide the face-specific growth rate data needed for the ‘first-principle’ understanding of the process and indeed from the FBRM approach it is hard to deduce quantitative kinetics. In addition, the population balance model (PBM) [25] was also developed and employed in the crystallisation process to study the evolution of crystal-size distribution as a function of time to estimate the growth rate in the volume equivalence diameter. This does not take into account the effect of crystal shape.

However, though the particles possess the same volume equivalence diameter, they might present in completely different shapes associated with different surface areas. This significantly impact on dissolution and growth kinetic rates or downstream processing etc. Hence, a study of the fundamental growth kinetics governed by the face-specific growth rate should be carried out on individual crystal habit faces, not by the dm/dt (mass overall growth rate) or dL/dt (the growth rate of characteristic dimension), described in PBM. A fundamental evaluation of the growth kinetics must be based on the growth rates of individual faces [26] for which the crystal shape is a crucial factor in the growth rate determination.

The above scenario sets the backdrop to this PhD study which involves research related to the development of methodology and instrumentation for crystal growth characterisation at different scale-sizes. The facility developed in this work was used to understand the effect of crystallisation environment conditions (e.g. solvents and supersaturation) and scale-sizes on the crystallisation process itself and for obtaining fundamental data for process scale-up. From this the interface crystal growth kinetics are extracted and the growth mechanism was assessed. Although based on small-scale laboratory test work and optimized for enabling the design of reproducible processes, ideally such tools would also be designed for deriving some of the data needed for process scale-up to manufacturing. In addition, in this work, the above experimental strategy is complemented with molecular and crystallographic modelling studies, a revised approach is proposed whereby the shape-dependant features of both predicted and observed particle shapes were cross-correlated. In this, the solvent and supersaturation-dependant growth rate of crystal faces, which characterise the shapes of crystals, can be rationalized by molecular modelling, intermolecular interactions involved in the growth process through an analysis of the surface chemistry of crystal habit faces. Furthermore, according to Ma et al. [27], the growth rate of individual faces produced and the crystal morphology either obtained from experiments or morphological prediction can be imputed directly into a morphological population balance model to predict the evolution of crystal population in terms of surface area of individual crystal habit faces, crystal shapes and sizes. It also allows studying the effect of hydrodynamic factors and the scale-up of vessel size by integrating this with Computer Fluid Dynamics (CFD).

In this study, ibuprofen materials were selected as a model material for measuring growth rate of crystal faces and for investigating growth mechanism in terms of being non-toxic and reactively amenable to laboratory and molecular scale modelling. It also exhibits morphological changes from prisms to needles and plates depending on environment or crystallising conditions and hence is representative of the kinds of material typically processed by the pharmaceutical industry.

1.2 Research objectives

The research question underlying this PhD study is as follows:

What is the influence of the crystallisation environment on the crystal growth of Ibuprofen as measured at the single crystal level and what are the molecular-scale processes that underpinning these interactions?

This can be delivered through the following core overall objectives:

- Developing a series of novel and effective platforms for the measurement of face-specific growth rates in crystalline systems at various crystalliser scale-sizes such as a 0.5ml cuvette cell, a 0.5ml Peltier crystallisation cell, a medium throughput 8-cell crystalliser unit (sample volume ca. 100 μ l) and a 15 ml small jacketed vessel for in-situ crystallisation studies.
- Studying and characterising solution behaviour in terms of solubilities and solution idealities of ibuprofen as a function of solvent and temperature using ATR UV/Vis and gravimetric method.
- Assessment of nucleation kinetics including MSZW and induction time determinations using polythermal and isothermal methods to estimate the nucleation order and the interfacial energy.
- Studying the crystal growth kinetics and growth mechanism of individual crystal habit faces (hkl) during representative crystallisation processes as a function of solvent type, supersaturation and reactor scale-sizes.
- Correlation and rationalisation of the experimental data through morphological prediction, the analysis of crystal surface chemistry and intermolecular bonding on these measured growth faces.

- Developing a computational methodology based on image analysis to extract crystal growth rates of surrounding faces from on-line images.
- Correlating and comparing the measurements of crystal growth rates in a non-agitated vessel to the growth rate in an 7ml agitated batch vessels and to larger 0.5L scale size using a commercial Perdix ISPV insertion optical camera probe to enhance understanding, control & scale-up of crystal growth processes.

1.3 Project management

This project was jointly funded through research grants from Pfizer, UK Ltd, the UK's Northern universities N8 Molecular Engineering Translational Research Center (METRC) consortium and Malvern Instruments who support project access to their Morphologi G3 particle shape analysis system.

This research work was carried out in the Institute of Particle Science & Engineering and Institute of Process Research & Development (iPRD) at University of Leeds under the supervision of Professor Kevin J. Roberts and Dr Robert B. Hammond, and Dr. Ivan Marziano at Pfizer. The system developed is planned to be integrated into Pfizer's product development workflow, and is expected to bring about an improvement in manufacturing productivity and efficiency. Annual progress reports were submitted to Pfizer showing details of the work done and progress made on achieving the outlined objectives. There was a technology transfer from Leeds University to Pfizer, UK (Feb 2012 - Mar 2012) hosted by Dr. Ivan Marziano and to Pfizer, US (Apr 2013) hosted by Dr. Kevin Girard as routine equipment to study the effect of crystallising conditions on the solid-state material.

Collaboration with Artificial Intelligence Group of Computing School at University of Leeds (Prof. David Hogg and Dr. Ardhendu Behera) was established for developing image analysis software for estimation of growth rate of crystal faces in a population of crystals.

The 15ml jacketed vessel cell was built with the advice of Dr Gary Nichols at Pfizer, UK.

1.4 Thesis organisation

This thesis consists of eight chapters (Figure 1.1) with references and appendices.

Chapter 1 presents the introduction, background to the study highlighting the research question set with the resulting objectives outlining project management and providing a route map to the thesis structure

Chapter 2 offers a literature review on the fundamental concepts of crystallography and theories underpinning crystallisation processes, beginning with solubility, supersaturation and moving on to nucleation theory and crystal growth. In addition, the design of crystal and particle properties by crystallisation and crystallisation characterisation are also presented.

Chapter 3 reviews the crystal growth rate and growth mechanism, growth rate dispersion and the methodology for the measurement of the crystal growth rate on single crystals and on a population of crystals. A detailed review on the crystal growth process is then described, mainly focusing on the measurement of crystal growth.

Chapter 4 describes the materials, instrumentation, and computational and experimental methods used in this study.

Chapter 5 Molecular modelling study including conformational analysis, morphological simulation, characterisation of intermolecular interactions and surface chemistry analysis of the crystal habit faces are presented and discussed.

Chapter 6 presents polymorph screening, solubility determination and nucleation kinetics of ibuprofen in ethanol 95%, ethyl acetate, toluene and acetonitrile which were examined involving MSZW and induction time measurements.

Chapter 7 begins with the solubility of ibuprofen together with their ideal solution behavior, van't Hoff analysis and activity coefficient. The mean crystal growth rate of the (011) and (001) faces as a function of solvent type and supersaturations are examined and discussed at the single crystal level. In addition, the influence of reactor scale size and solution agitation is also assessed.

Chapter 8 Technology Transfer: Growth rate measurements in an industrial R&D workstream: Industrial case studies of drug compound A at Pfizer, UK.

Chapter 9 presents the key outcome of this work and makes some suggestions for the future work.

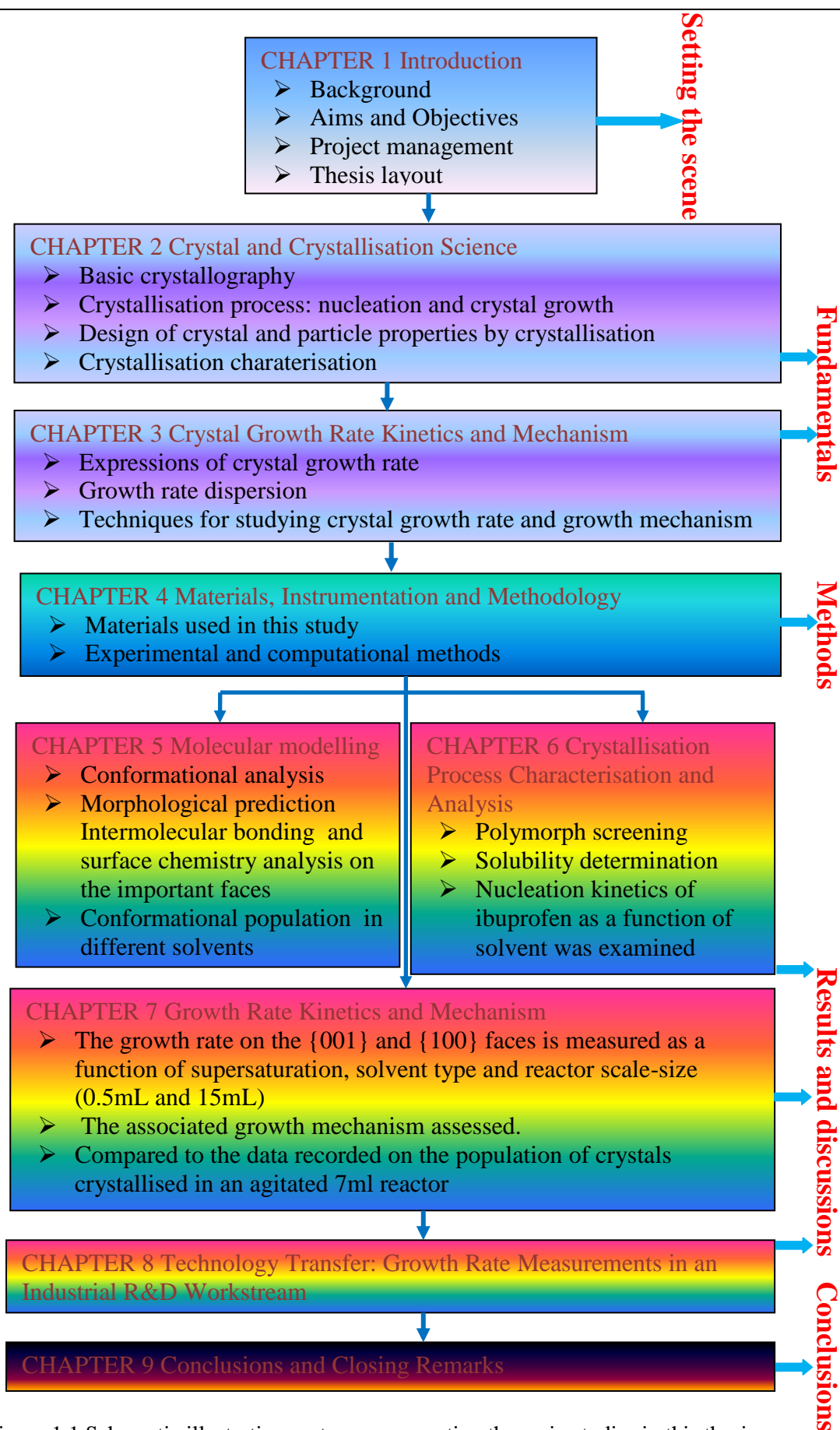


Figure 1.1 Schematic illustrative route map presenting the main studies in this thesis.

2 Crystal and Crystallisation Science

Summary:

This chapter presents the fundamentals of crystal and crystallisation science including crystal nucleation and growth, together with experimental and computational methodologies for their characterisation and the influence of crystallisation environmental conditions on crystal properties (polymorphism, size and shape).

2.1 Introduction

The fundamentals, concepts and theories of crystal science and crystallisation processes including crystal nucleation, crystal growth, polymorphism and the effects of shape and polymorphism on properties, performance of final products are described in this chapter. One of the important aspects in studying crystal science is to comprehend how crystal structures and shapes influence the chemical and physical properties of materials and how to manipulate and create crystal shapes with desired properties for optimal downstream processing. These can be investigated and explained with the aid of molecular packing, intermolecular interactions studies in the solid state and also of nucleation and crystal growth theory. Sun [28] described the interrelationship among the structure, properties, performance and processing in the design and development of a new drug and developed a concept of the material science tetrahedron (MST). Through some detailed case examples, the MST tool can be applied in pharmaceutical research and development of new drug compounds to enable the pharmaceutical product development and manufacturing to become more rapidly commercialized in order to meet market demands.

This chapter starts with a brief overview of basic crystallography notably crystal systems, crystal chemistry, Bravais lattices, Miller indices, followed by an overview of the theories of nucleation and crystal growth, which are applied in the later chapters of this thesis. The concepts are discussed and analyzed with respect to solid-state and crystal surface parameters.

2.2 Basic crystallography

2.2.1 Crystalline and amorphous solid

Crystals can be divided into crystalline and amorphous state. A solution can transform into an amorphous, semi-crystalline or crystalline solid mainly depending on supersaturation (cooling rate). For example, if the cooling rate is faster than the rate at which molecules can nucleate and rearrange themselves into a thermodynamically favorable order, it is likely that an amorphous solid will be produced. In contrast, if

molecules have sufficient time to organize into a structure with two- or three-dimensional order, it is much more likely that a crystalline or semi crystalline solid will be obtained. Hence, whilst the crystalline state possesses an ordered and regular arrangement of the molecules in a crystal, amorphous materials are converse cases. For example, silicon can be formed in both cases; amorphous and crystalline forms (see in Figure 2.1), and both states can be used for different applications.

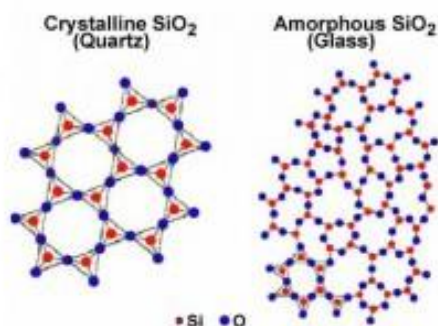


Figure 2.1 (left) Crystalline SiO₂ (quartz), in which atomic arrangements are regular; (right) amorphous SiO₂ (glass) refers to objects having no definite shape and is defined as non-crystal material (irregular atomic arrangements) [29].

In the pharmaceutical industry, amorphous forms of poorly-soluble drugs are generally considered to offer substantial improvements in drug dispersability, dissolution behaviour and bioavailability compared with the corresponding crystalline forms. Nevertheless, amorphous forms are less thermodynamically stable there is thus a risk that they may ultimately revert to the crystalline form [29].

Organic crystalline materials can adopt a number of structural architectures, e.g. polymorphs, solvates, hydrates salts etc. Solvates are solvent molecules incorporated in the crystal lattice in a stoichiometric and non- stoichiometric way. Hydrates are solvates where the solvent is water. If non-volatile molecules incorporated in the crystal lattice, the solid forms are called co-crystals [30].

2.2.2 Lattices, unit cells and crystal systems

A crystal is a polyhedral solid state bounded by plane faces and is built by the regular repetition of identical units in space. Its internal structure contains atoms or molecules arranged in a three dimensional network. A three dimensional arrangement of atoms or molecules can be represented as a ‘crystal lattice’. Each lattice point is representative of an atom or a group of atoms with the lattice representing the scheme of repetition patterns of atoms in the space. A small part of identical units defining how the pattern is repeated is referred to as a unit cell. It can be defined by three vectors a , b , c (along the crystallographic axes) and the angles α , β , γ between these vectors.

The science of crystallography is developed based on three basic rules [31]:

- Law of Constancy of the Interfacial Angles: The angles between specified surfaces of a crystal remain constant when they grow.
- Law of Rational Indices: refers to the orderly arrangement of the crystal planes in space. These planes represent the various faces of crystals and are referred to by the three-coordinate-axes systems. The intercept of planes with axes can be represented by a whole integer number.
- Symmetry: Plane symmetry can be defined by the means of imaginary planes which divide the crystal into two exact and completely the same parts. At a simple fraction of a complete rotation around an axis of symmetry, the faces, edges and corners of crystals will duplicate.

These concepts are reflected in the seven types of unit cell as shown in Table 2.1.

Table 2.1 The seven crystal systems [5]

System	Angles between axes	Length of axes	Crystal shapes
Cubic	$\alpha = \beta = \gamma = 90$	$a = b = c$	
Tetragonal	$\alpha = \beta = \gamma = 90$	$a=b \neq c$	
Orthorhombic	$\alpha = \beta = \gamma = 90$	$a \neq b \neq c$	
Monoclinic	$\alpha = \beta = 90 \neq \gamma$	$a \neq b \neq c$	

Triclinic	$\alpha \neq \beta \neq \gamma \neq 90$	$a \neq b \neq c$	
Trigonal	$\alpha = \beta = \gamma \neq 90$	$a = b = c$	
Hexagonal	$\alpha = \beta = 90, \gamma = 120$	$a = b \neq c$	

The cubic (regular system) shows the highest degree of the symmetry in the crystal system. All the faces of crystals have intercepts with their axis (Figure 2.2). Miller [32] suggested that each face of the crystal can be represented by the Miller plane (hkl) with

$$h = \frac{OX'}{OX}, k = \frac{OY'}{OY}, l = \frac{OZ'}{OZ}$$

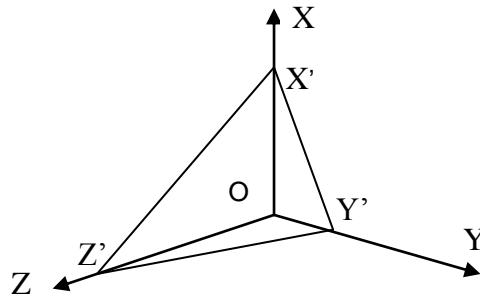


Figure 2.2 Miller indices of a plane derived from the intercept of the plane on the crystallographic axes.

For example: h k l

$$\begin{array}{ccc} \frac{1}{1} & \frac{1/2}{1} & \frac{1}{1} \\ 1 & \frac{1}{2} & 1 \\ 2 & 1 & 2 \end{array}$$

In 1850 Bravais [33] demonstrated that there are 14 possible basic types of lattice (Figure 2.3). These can be rationalized with respect to the concept of 7 crystal systems through the presence of centering e.g. through a body centre (with an additional point at the centre of the unit cell), face centre (with additional lattice points at the centre at the cell faces) etc.

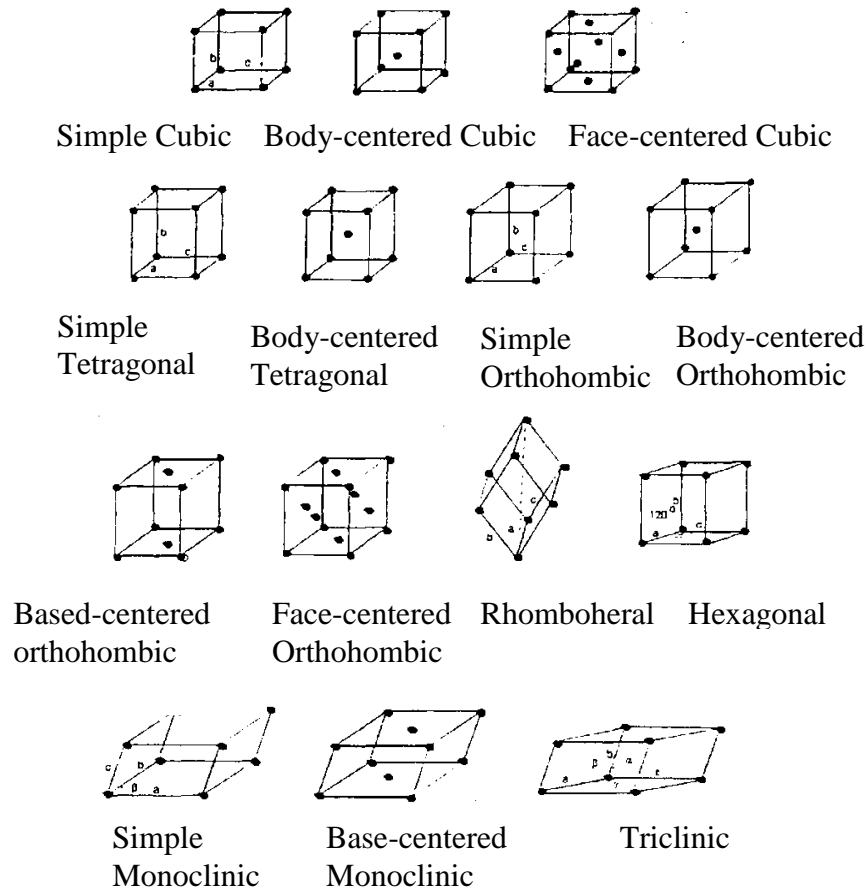


Figure 2.3 Bravais lattices classified into three main types: primitive, body center and face center [33].

2.2.3 Crystal defects

In perfect crystals nearly all atoms lie in the position that they should have in three dimensional arrangements. They have exact repetition parameters of a unit cell. e.g. single crystals of silicon are produced without any defects with a distance of more than ten million unit cells [34]. However, above 0°K in reality the atoms are not static and can be mobilized in particularly at the elevated temperatures at which crystals are produced. Raw materials are not completely pure and the materials can contact with the wall of a vessel and with the surrounding environment so defects can be formed within the periodic arrangement. There are several kinds of such defects (Table 2.2).

Table 2.2 Summary for types of crystal defects [35]

Point	Line	Two dimensional defect (Area or plane defect)	The dimensional defect (Volume)
Vacancies: Occurrence of vacant lattice sites Interstitials: Inclusions of atoms not on lattice sites Impurities: Occurrence of foreign particles in the lattice	Dislocations: Gliding motions with combination of slip plane and Burgers vector	Stacking faults: Additional of odd atoms sequence (twin) compared to original	Inclusions and precipitations

The vacancies or point defects have a great influence on the properties of solid materials; particularly electronic and mechanical properties since they have greater internal energy than crystals with close packing atoms. The presence of vacancies in the crystal structure plays an important role on the process of the solid-state diffusion. In a crystal where the atoms are packed closely together, there is a very low chance of this process happening even at high temperature. However, it is possible to happen if there are some vacancies in the crystal structure to impede the movement of atoms. Besides, there are other point defects such as interstitial atoms and impurities. In interstitials, additions of atoms of the same type as those in the crystal structure are sited in the interstices so distortion appears.

The dislocations are known as one-dimensional defects (line defects). They can be an edge or screw in character or a combination of both of them. These dislocations can be defined by both the direction of strain caused by defect (Burgers' vector) and a line around the distortion occurs. An edge dislocation is a defect where an extra half-plane of atoms is inserted into the crystal, leading to compression of inter-atomic distances. The Burger's vector is perpendicular to the line of distortion. However, in the screw dislocation, the Burger's vector is parallel to the line of distortion (Figure 2.4)

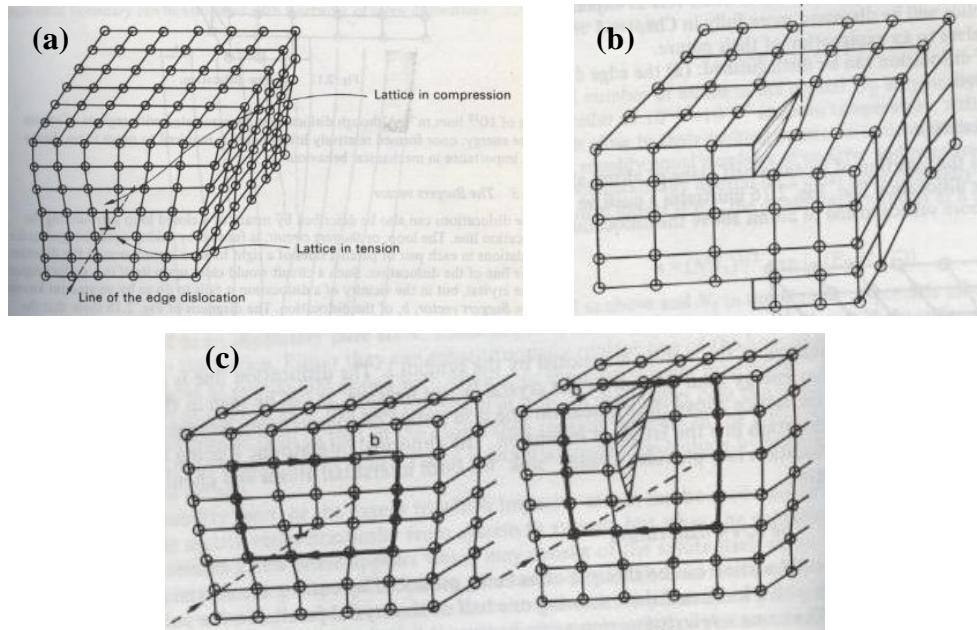


Figure 2.4 (a) Edge dislocation, (b) screw dislocation and (c) the Burgers' vector is perpendicular to the line of distortion in the case of edge dislocation and in screw dislocation the Burger's vector is parallel to the line of distortion [36].

Two dimensional defects (plane defects) will propagate much further into the crystal lattice than point or line defects. These can arise on growth sector boundaries or due to stacking faults within the crystal. The plane defect also may happen in many crystal structures during the growth process or in crystals grown by the deposition of successive close packing layers, the sequence is ABCABCABC... If the sequence has a stacking fault in the stacking sequence, e.g. ABCABCACBA, twinning may occur. The two parts of the crystal have the same structure and are mirror images of one another. They possess a common plane (C) (a twin plane) which acts as a mirror [34, 36].

Three dimensional defects (volume defects) are gross distortions to the crystal lattice. These can arise from the incorporation of materials of different chemical composition (for instance the solution solvent) or a material of different crystalline structure into the crystal lattice.

2.3 Crystal chemistry and polymorphism

2.3.1 Crystal chemistry

In a crystal there are many component molecules held together in a 3D periodic arrangement by various intermolecular interactions which can be quite weak when compared to chemical bonds. Generally interactions can be classified into 5 groups (Figure 2.5): (a) co-valance; (b) ionic; (c) non-bonded attractive and repulsive van der Waals interactions; (d) metal and (e) hydrogen bonding.

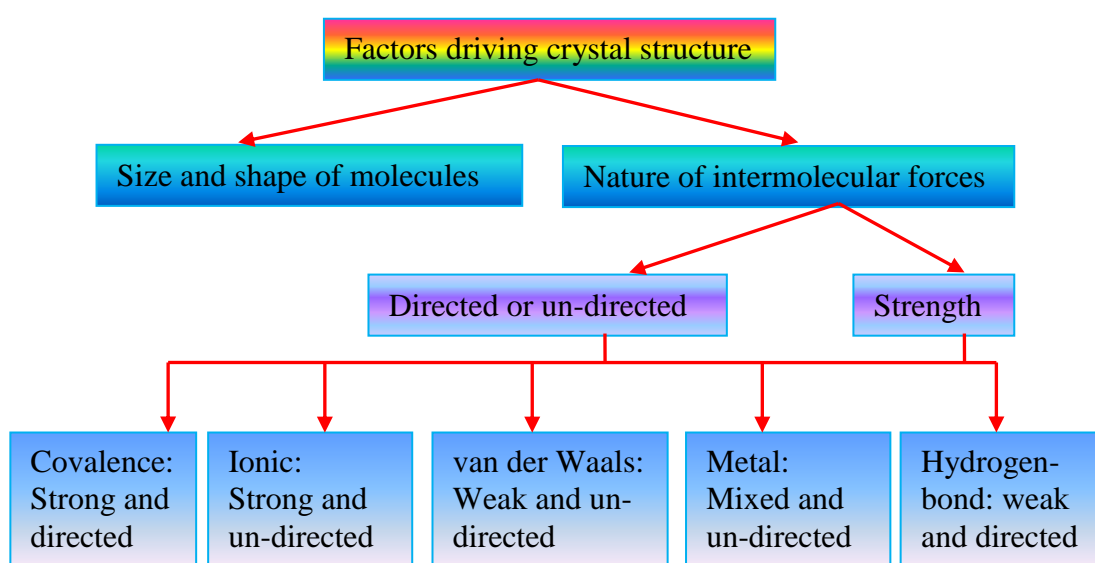


Figure 2.5 Factors impacting on the crystal structure comprise direction and strength of intermolecular forces.

Dipole-dipole interaction: In a covalent diatomic molecule, the electron density will be higher in the more electronegative atom. A permanent dipole on one molecule produces an electric field that can interact with the permanent dipole on a neighbour molecule. The molecules tend to orientate themselves in a position of minimum energy such as end to end or side by side position.

Van der Waals force refers to the attractive or repulsive forces between molecules or between parts of the same molecule in a non-bonded interaction. Van der Waals forces include momentary attractions between molecules or atoms. When the electron distribution of a molecule is changed due to the random collision, they become

temporary polarization particles. Although they are not stable, many such temporary dipoles formed at a given time will interact with neighbour dipoles to produce a net attraction between molecules. The van der Waals interaction also usually includes the dispersive and repulsive force.

Hydrogen bonding is the electrostatic force between an electronegative atom such as nitrogen, oxygen, fluorine etc. and a hydrogen atom. This causes an electric dipole: the hydrogen atom with a partial positive charge and the oxygen or nitrogen group with a partial negative charge. The hydrogen bonding performs a very strong influence on solubility of solute molecules in a solvent. The strength of a hydrogen bond (between 10 and 40 kJ/mol) is stronger than a typical van der Waals bond (about 1 kJ/mol); however both of them are much weaker than the covalent or ionic bonds (about 5000 kJ/mol) [37].

Crystal chemistry impacts on physical and chemical properties such as melting point, hardness, polymorphism, surface properties etc.

2.3.2 Polymorphism

According to McCrone, 'The polymorphism of any element or compound is its ability to crystallise as more than one distinct crystal species' [37]. Polymorphs are crystals with the same molecule but different crystal structures due to different arrangements and/or different conformations of the molecules. It is a significant and complex issue in the pharmaceutical industry because there are a few active pharmaceutical ingredients that exhibit only one single crystal structure. In addition, the transformation between the polymorphic forms during the processing and storing time can also cause significant problems to the pharmaceutical industry.

According to Ostwald rules, polymorphs can convert from less stable to more stable forms and the most stable form is expected to be the least soluble [38]. The unstable form does not always transform directly to the most stable form. The metastable form appears first and then transform to the next most stable solid state until the most stable form is achieved associated with the minimum energy. In a polymorphic system,

thermodynamics favours the formation of the stable form while kinetics can favour the formation of the metastable form [38-40].

There are two specific types of polymorphs:

- **Monotropic:** There is no reversible transition between polymorphic forms below the melting point of both solids. The free energy and solubility curves do not cross so only one polymorph is likely to be stable below the melting point (Figure 2.6).
- **Enantiotropic:** A transition point exists below the melting point and this transition is reversible. The free energy and solubility curves cross before the melting point (Figure 2.6)

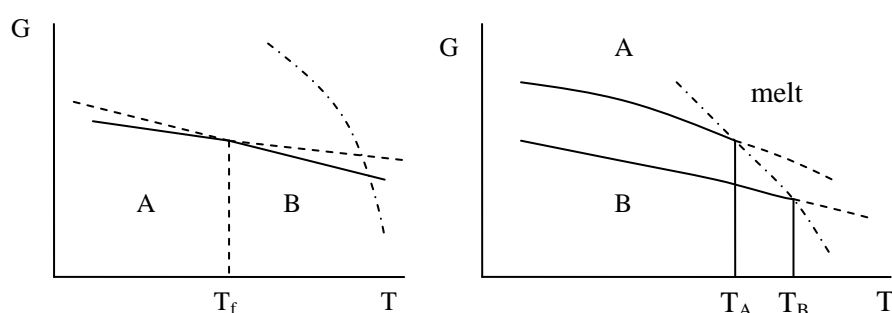


Figure 2.6 Relationship between the Gibbs free energy G and the temperature T for two polymorphs for an enantiotropic system (left) and a monotropic system (right) [41].

The various polymorphs of a substance can exhibit different physical and mechanical properties. Since polymorphs are different in the dimensions, shape, symmetry, capacity and the void volumes of their unit cells, they have differences in molecular packing, causing different physical properties such as refractive index, thermal conductivity, electrical conductivity [42]. The differences in the melting point can be explained by dissimilarities of the interactions of the molecules in the solid-state as compared with the liquid state. In addition, the differences in packing properties and the intermolecular interaction energy among polymorph can cause differences in the mechanical properties.

Hence, although polymorphs are identical in their chemical compositions, they can differ in terms of their solubility, dissolution rate, bioavailability, chemical stability, physical stability, melting point, flow behaviour and other properties. In particular, a

change of the solubility of different polymorphs can affect the efficacy, bioavailability and safety of the drug [37]. Experimental or process conditions are crucial factors to determine the production of a particular polymorph. Hence, understanding and controlling the transformation process between polymorphs is important in terms of obtaining a desired form via the crystallisation process.

2.4 Crystal morphology

Habit and morphology are terms that represent the external shape and appearance of a crystal. Even though crystals are in the same crystal system, they may be different in terms of their external form or morphology (Figure 2.7) which depends in turn on the relative growth rates of the different crystal faces. If a crystal grows in different process conditions, the growth rate of a particular face can be accelerated compared to other faces, resulting in a different shape. The growth of an individual face is effected by the crystal structure, crystallising environment conditions (the degree of supersaturation, solvent and impurities) and defects.

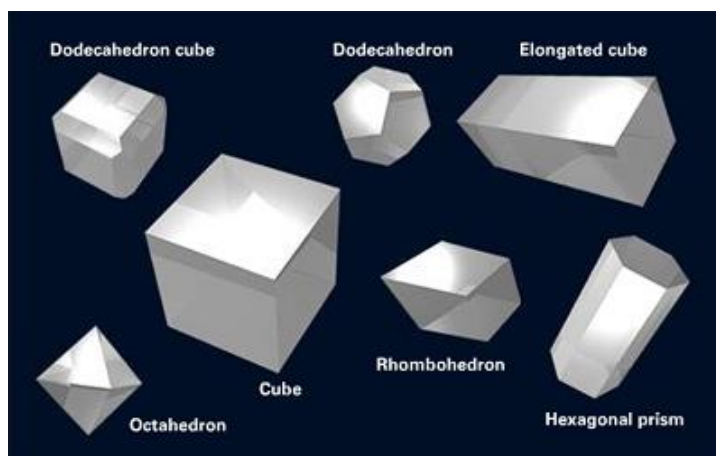


Figure 2.7 Various crystal shapes [43].

The morphology of crystals can have a significant influence on both the solid state and the downstream processing including material handling and particle processing, for example, filtration, compression, flowability.

In 1978 Gibbs [44] proposed that for the equilibrium shape of a crystal, the total surface energy should be a minimum for a constant volume of crystal

$$d \sum_n A_n \gamma_n = \sum_n \gamma_n dA_n = 0 \quad (2.1)$$

where A_n is the area of the n^{th} face and γ_n is the surface tension of the n^{th} face.

Gibbs' concept was further extended by Wulff [45] who stated that the equilibrium form of a crystal should be bounded by faces whose distances from the origin should be proportional to the specific surface energies of the faces and similar to the relative rates at which the surfaces grow out from the nucleation centre of the crystal;

$$\gamma_n/h_n = \text{constant} \quad (2.2)$$

where γ_n is the surface tension of crystal face n ; h_n is the distance from a point in the crystal known as Wulff's point.

The equilibrium shape of a crystal can be constructed by drawing vectors normal to all possible crystallographic faces from an arbitrary point and marked on the vectors with the distances proportional to γ_n , and then planes normal to the vectors are built through the marks on the vectors creating a closed polyhedron (Figure 2.8), called the equilibrium form.

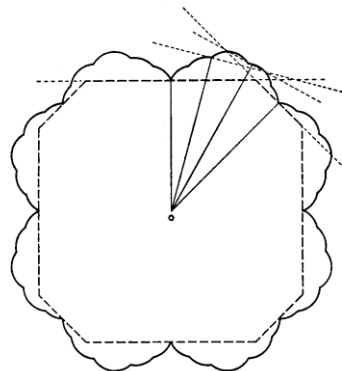


Figure 2.8 Procedure to construct a Wulff plot where O is the nucleation centre. The equilibrium shape of a crystal can be constructed by drawing vectors to all possible crystallographic faces from O and marked on the vectors with the distances proportional to γ_n , and then planes normal to the vectors are built through the marks on the vectors creating a closed polyhedron [46].

Morphological crystal shapes of materials have been becoming more and more significantly important in the particle science and engineering. Clydesdale et al. [47] has developed the HABIT simulation program which calculates attachment energy E_{att} as a function of the intermolecular interactions where the latter draws down the crystal structure for the material examined. These calculations can be carried out in a fairly

routine manner and have been used to predict the crystal morphology of a wide range of organic crystals revealing good correlation between observed and simulated crystal shapes (biphenyl, naphthalene, α -Glycine, L-alanine, benzoic acid, urea, β -succinic acid) [47]. The principle of modelling work is that the external morphology of crystalline materials can be predicted from the internal crystal structure. Bravais-Friedel and Donnay-Harker (BFDH) analysis which is one of the initial methods based on the crystallographic geometrical considerations can be used to predict the morphology of a crystal. The BFDH rule states that:

“after allowing for the reduction of the growth slice thickness from space group symmetry considerations, the most morphologically important forms (hkl), and hence those with the lowest growth rates, are those having the greatest interplanar spacings d_{hkl} ” [48].

For a given structure, the BFDH method is able to predict the habit or shape of a crystal using the corresponding unit cell parameters (a , b , c , α , β and γ) and the symmetry operator information. This method uses the crystal lattice and symmetry to generate a list of the possible growth faces and their relative growth rates. As a result, the theoretical crystal morphology can be generated from these relative growth rates.

Hartman and Perdok [49] extended and developed BFDH theory by calculating the intermolecular interactions in the crystallisation process. In this theory, the attachment energy is related to the crystal lattice energy or crystallisation energy (E_{latt}) through the slice energy (E_{sl}) which is released upon the formation of a slice of thickness d_{hkl}

$$E_{latt} = E_{att} + E_{sl} \quad (2.3)$$

where E_{sl} is the intermolecular bonding energy within the surface growth slice.

The attachment energy (E_{att}) represents for the relative (hkl) surface growth rate as the slowest growing face is the one with lowest attachment energy and hence the most morphologically important.

The total intermolecular interaction can be considered as the summation of the interactions between a central molecule and the surrounding molecules. Each of the

intermolecular interactions is calculated by the summation of pairwise atom-atom interactions, using the atom-atom approximation through summing the interatomic energies between pairs of non-bonded atoms (Figure 2.9).

If there are n atoms in the central molecule and n' atoms in each of the N surrounding molecules then the lattice energy can be expressed by:

$$E_{cr} = \frac{1}{2} \sum_{k=1}^N \sum_{i=1}^n \sum_{j=1}^{n'} V_{kij} \quad (2.4)$$

where V_{kij} is the interaction energy between atom i in the central molecule and the atom j in the k th surrounding molecule. The interaction V_{kij} between any of the non-bonded atoms i and j can be described by a number of intermolecular potential functions (Momany [50], Lifson [51]). The potential energy of interactions between two atoms includes the van der Waals forces having an attractive and repulsive as a function of atom-atom separation distance and the Coulomb potential for the calculation of the electrostatic interactions. A simple Lennard-Jones potential combined with an additional Columbic term to describe the electrostatic interactions:

$$V_{ij} = -\frac{A}{r_{ij}^6} + \frac{B}{r_{ij}^{12}} + \frac{q_i q_j}{Dr_{ij}} \quad (2.5)$$

where A and B are parameters for describing a particular atom-atom interaction, q_i and q_j are the fractional charges on atom i and j separated by distance r , and D is the dielectric constant.

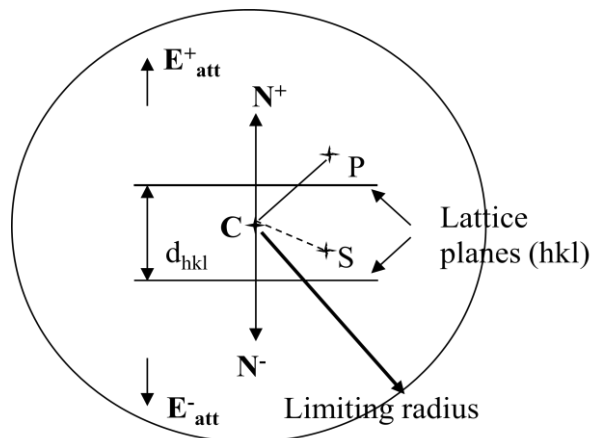


Figure 2.9 Basic approach of calculating the intermolecular interactions using the atom-atom method: C is the central molecule, P is a molecule outside the slice and S is a molecule inside the slice [52].

Since the interactions are between two atoms, the factor of $\frac{1}{2}$ appears in the equation to avoid a double count of the atom-atom interactions.

A computer program HABIT was written and developed to aid in the morphological predictions of molecular crystals by calculating such interactions between the crystallising molecules in the solid state. The program calculates the lattice, slice and attachment energies by a summation of atom-atom interactions in a certain molecule and interactions of atoms this molecule has with atoms of all surrounding molecules inside a given radius of the sphere. This program requires the fractional atomic coordinates of one asymmetric unit of the system; the atomic charges file for this asymmetric unit, symmetry operators from the relevant space group, and important growth faces.

The specific surface energy (γ_{hkl}) for the individual faces can be calculated based upon the attachment energy [53] using the equation

$$\gamma_{hkl} = \frac{ZE_{att}d_{hkl}}{2V_{cell}N_A} \quad (2.6)$$

where Z is the number of molecules in the unit cell; E_{att} is the attachment energy; d_{hkl} is the d-spacing of individual face (hkl); V_{cell} is the volume of the unit cell and N_A is the Avogadro number.

Moreover, the HABIT program also enables examination of the intermolecular interactions and through this is able to identify the strong bonds and, particularly atom-atom their constituent or atom type contributions. It can also sort the various interactions in terms of either their relative strength or distance [47].

2.5 Crystallisation process

In order to obtain the desired crystal morphology, size and properties suitable for further downstream processes, concepts of crystallisation processes including solubility, supersaturation, crystal nucleation, crystal growth, polymorphism and the effects of shape and polymorphism on properties and performance of a chemical compound need

to be understood and controlled. Solution properties, nucleation and crystal growth are important components in crystallisation processes.

2.5.1 Solutions, solubility and supersaturation

2.5.1.1 Solutions and solubility

The solubility of a solid compound in a solvent and mixtures of solvents play a key role in crystallisation processes. Why do solids dissolve in solvents e.g. sugar and salt is dissolved in water? In order to make it occur, it needs energy to break the bonds between the sugar molecules and the hydrogen bond in water to add sugar molecules into solution. Generally a solution is a homogeneous mixture of two or more substances [26]. A mixture of solvents might be found to be useful in obtaining the desired properties of crystal shapes and morphology. Solvents that have been used in industry include water, methanol, ethanol, iso-propanol, n-butanol, t-amyl alcohol, acetone, methyl ethyl ketone (MEK), methyl isobutyl ketone (MIBK), tetrahydrofuran (THF) etc. A saturated solution in a solvent represents the thermodynamic equilibrium between solution and the solid phase. Understanding the solubility of a chemical compound in solvents is one of the first requirements for the development of a crystallisation process.

Thermodynamics shows a way to calculate the ideal solubility of a solute in any solvent. In this calculation, the solubility is independent of the chemical composition of the solvent because the ideal solution is formed in this system. The ideal solubility of a crystalline material in a solvent was shown by Hilderbrand and Scott [54]:

$$\ln X = -\frac{\Delta H_{fus}(T_m - T)}{RT_m T} + \left(\frac{\Delta C_p}{R}\right)\left[\frac{T_m - T}{T} + \ln\left(\frac{T}{T_m}\right)\right] \quad (2.7)$$

where X is the mole fraction of the ideal solubility of the solute; ΔH_{fus} is the molar enthalpy of fusion of the pure solute; T_m is the melting point (K); T is the solution temperature; $\Delta C_p = C_{p_m} - C_{p_s}$ is the heat capacity difference (at constant pressure) between the melt and the solid states.

Equation (2.7) can be used to evaluate the ideal solubility of a solute in different solvents. However, all solutions are not ideal to some extent as the interaction energy

between solvent/solvent, solute/solute and solvent/solute are different particularly for complex solvents and solute molecules. If the solubility curve lies below the ideal solubility curve, the solution shows a less than ideal behaviour since the intermolecular interactions of solute-solute and solvent-solvent are much stronger than those related to the interaction between the solute-solvent molecules and the solute has a lower solubility in the solvent.

2.5.1.2 Supersaturation

Supersaturation is the driving force of the crystallisation process. The supersaturated solution contains more dissolved solid than that required for the equilibrium state. Supersaturation can be defined in the different expressions. The most common expressions of supersaturation are:

The concentration driving force

$$\Delta c = C - C^* \quad (2.8)$$

The supersaturation ratio

$$S = \frac{C}{C^*} \quad (2.9)$$

The relative supersaturation

$$\sigma = \frac{\Delta C}{C^*} = S - 1 \quad (2.10)$$

where C^* is the equilibrium saturation of the solution at the given temperature; and C is the actual solution concentration at the same temperature

The production of a solid-state through the crystallisation process might appear to be simple but despite this it is not completely and clearly understood since the crystallisation process includes many complex stages related to the nucleation and crystal growth processes.

2.5.2 Nucleation

In crystallisation process, nucleation is the first stage of the crystallisation process in which the formation and dissolution of small clusters of solute occur with some of these clusters continuing to develop to form crystals.

The nucleation concept and mechanism encompass primary nucleation (homogeneous nucleation and heterogeneous nucleation) and secondary nucleation (induced by crystal seed) (Figure 2.10). Primary nucleation does not involve the presence of any crystal matter in the system when there is no induction of foreign particles and crystals in the crystallisation solution; this process is called homogeneous nucleation. Heterogeneous nucleation is referred to as the nucleation of materials upon a foreign substrate. However, secondary nucleation occurs with the presence of seeds which can be served as a template for the solute molecule to aggregate and grow within the metastable zone.

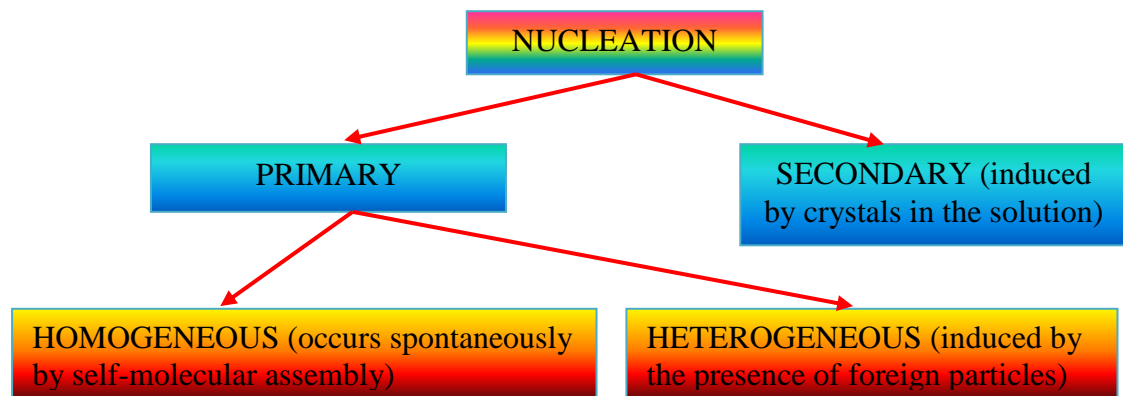


Figure 2.10 Schematic showing the classification of the nucleation stage in a crystallisation process.

2.5.2.1 MSZW

The state of supersaturation is the prerequisite for the crystallisation process. Ostwald [55] first introduced the terms ‘labile’ and ‘metastable’ supersaturation to classify a supersaturated solution in which spontaneous nucleation occurs or does not occur, respectively. Miers and Isaac constructed the solubility–supersolubility diagram based on the relationship between the supersaturation and spontaneous crystallisation [56, 57].

The solubility-supersolubility diagram showing three regions with different behaviours is shown in Figure 2.11.

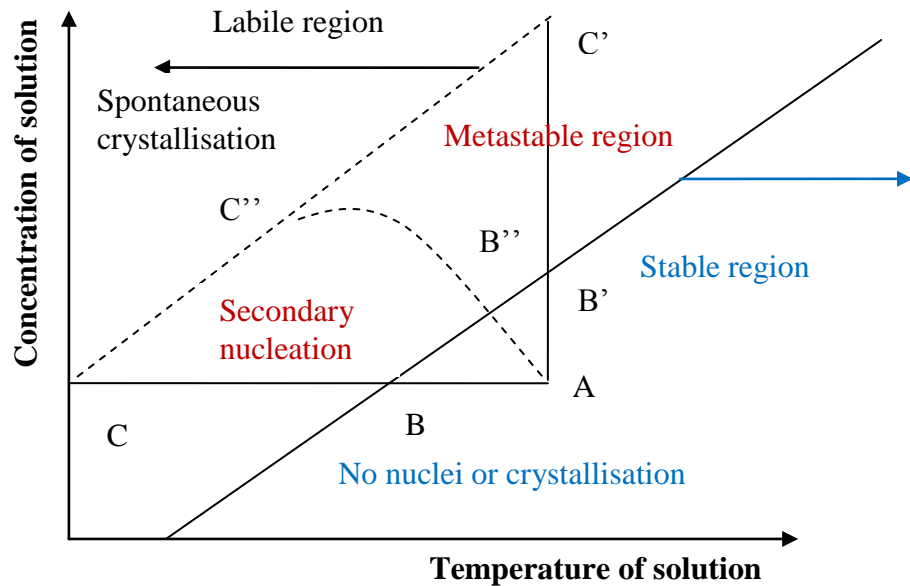


Figure 2.11 Solubility-supersolubility diagram showing three regions with different behaviours: (1) a stable or unsaturated zone; (2) a metastable zone and (3) an unstable zone [56].

This diagram includes three zones:

- The stable or unsaturated zone where the crystallisation cannot happen. If seeding crystals are added at higher temperature (in stable region), they will be dissolved.
- The metastable zone (supersaturated zone) between the solubility and supersolubility curves where the concentration of solution becomes saturated but the crystallisation only occurs after a period of time or if crystal seeds are introduced in the solution. In this zone, crystallisation is possible and when the supersolubility curve is reached, spontaneous crystallisation takes place. Seed crystals placed in solutions in this region will grow.
- The unstable or labile zone where spontaneous crystallisation occurs due to the high supersaturation of solution. If seed crystals are added in the labile zone, nucleation will occur spontaneously in an uncontrolled manner.

Related to this, two approaches for supersaturation generation can be considered:

- Evaporative crystallisation (along the vertical line AB'C'), a solution is becoming more concentrated in solute through evaporation of the solvent from the solution at constant temperature.
- Cooling crystallisation (along the line horizontal ABC), a solution is undergoing cooling crystallisation.
- Combined evaporation and cooling crystallisation (along the curved AB''C''), a combination of cooling and evaporation are employed in this process.

Whilst the solubility curve reflects the thermodynamic equilibrium of the system, the supersolubility curve reflects the kinetics and consequently is less well-defined as it is more stochastic and can be expected to change with e.g. cooling rate, solvent type and composition, agitation rate and impurity content. Therefore, the metastable zone width, a crucial parameter of crystallisation process, which gives a significant insight into the nucleation behaviour of a crystallisation system, can also be expected to change with the above processing conditions. Hence the nucleation process and its kinetics for a given system is usually characterised by changing these factors.

2.5.2.2 Polythermal crystallisation for the determination of nucleation kinetics using Nyvlt method

Nyvlt [58] proposed a method for the evaluation of nucleation kinetics. In this method, the nucleation rate J is defined as the formation of number of nuclei in the unit volume in a period of time $d\tau$:

$$J = \frac{dN}{d\tau} = k_n \Delta c_{\max}^m \quad (2.11)$$

where Δc_{\max} is the maximum possible supersaturation, m is the order of nucleation.

The nucleation rate versus the degree of supersaturation showing the nucleation rate increases significantly when solutions reach critical supersaturation (Figure 2.12).

Δc_{\max} can be written as a function of the maximum possible undercooling Δt_{\max} through the equation:

$$\Delta c_{\max} = \frac{dc}{dt} \Delta t_{\max} \quad (2.12)$$

where $\Delta t_{max} = t_{sat} - t_{dis}$; t_{sat} and t_{dis} are the saturation and dissolution temperatures, respectively.

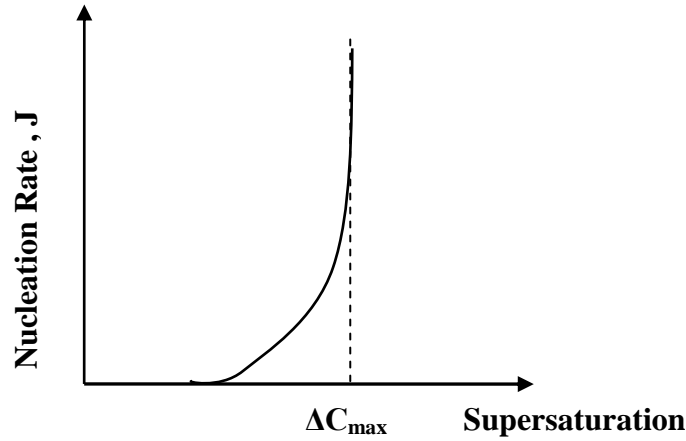


Figure 2.12 Schematic plot of the nucleation rate versus the degree of supersaturation showing the nucleation rate increases considerably when approaching critical supersaturation [58].

The nucleation rate may be expressed to be equal to the rate at which supersaturation is achieved at the time when first nuclei are detected.

$$J = k_1 b = \varepsilon \left(\frac{dc}{dt} \right) \left(- \frac{dt}{d\tau} \right) \quad (2.13)$$

where k_1 is a constant, ε is a correction factor for the change in concentration in the case where species are being hydrated, and b is cooling rate.

Combining the equation (2.11) (2.12) and (2.13), an expression for dependence of the MSZW Δt_{max} on the cooling rate b can be obtained:

$$\varepsilon \frac{dc}{dt} b = k_n \left[\left(\frac{dc}{dt} \right) \Delta t_{max} \right]^m \quad (2.14)$$

This equation can be rewritten after taking logarithms:

$$\log b = (m-1) \log \frac{dc}{dt} - \log \varepsilon + \log k_n + m \log \Delta t_{max} \quad (2.15)$$

Plotting $\log b$ against $\log \Delta t_{max}$ yields a straight line with slope equal to the order of nucleation m .

Using equation (2.15) for fitting experimental data of more than 25 chemical substances, Nyvlt [58] also reported that the nucleation m seemed to be a function of the molecular weight of the crystallising substance at certain extent. The data showed the mean value of m decreases slightly with increasing molecular weight which confirmed the nucleation order m is related to the number of particles forming a nucleus in the solution. The measured nucleation order m from the Nyvlt equation will give an indication as to the ease at which the crystallising material will nucleate. It is a helpful parameter to assess the effect of solvents and/or solvent compositions on the MSZW of a crystallising system.

2.5.2.3 Homogeneous nucleation

Nucleation is originated from a sequence of molecular additions into aggregates. Only aggregates having a size greater than a critical value will be stable and grow into a crystal. The nucleation process includes two competing processes: coagulation and redissolution. The free energy changes associated with these may be considered assuming a spherical nucleus.

$$\Delta G = \Delta G_s + \Delta G_v = 4\pi r^2 \gamma + \frac{4}{3} \pi r^3 \Delta G_v \quad (2.16)$$

where ΔG_s is the surface free energy; ΔG_v is the volume excess free energy between the solid and the liquid phase; r is radius of nucleus; and γ is the interfacial tension between the crystal surface and the solution. This is shown schematically in Figure 2.13.

Examination of equation 2.16 reveals ΔG reaches a maximum value, ΔG_{crit} , when

$\frac{d\Delta G}{dr} = 0$ and hence:

$$\frac{d\Delta G}{dr} = 8\pi r \gamma + 4\pi r^2 \Delta G_v = 0 \quad (2.17)$$

Thus the critical cluster size can be given as:

$$r_c = -\frac{2\gamma}{\Delta G_v} \quad (2.18)$$

The critical size r_c is the minimum size for a stable crystalline cluster to be able to grow to macroscopic proportions. Thus, in a supersaturated solution, nuclei can either grow into macroscopic crystals or redissolve into the solution depending on their size. When particles of a crystallising phase are small, the surface free energy term (positive term) dominates over the volume or bulk free energy term (negative term). Hence, the particles smaller than r_c will dissolve. However as the particles become larger, the volume term dominates. Hence, the free energy passes through a maximum point. This represents the critical cluster size or minimum size of clusters and the particles larger than the critical size will continue to grow. The process will occur with the decrease of the free energy (Figure 2.13). The value of r_c decreases as supersaturation increases, showing the possibility of nucleation will be higher at a higher supersaturation for a particular system. When r_c approaches molecular dimension an amorphous phase results.

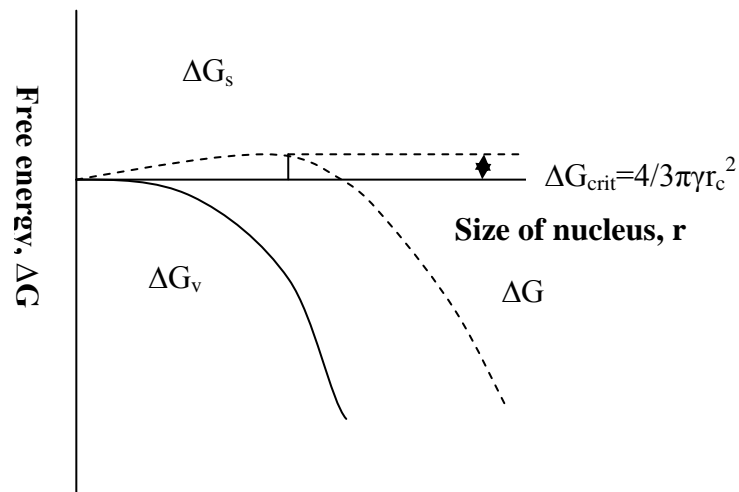


Figure 2.13 Free energy associated with a molecule cluster diagram for the nucleation explaining the critical nucleus.

Replacing the value of r_c into above equation, we get:

$$\Delta G_{crit} = \frac{16\pi\gamma^3}{3(\Delta G_v)^2} = \frac{4\pi\gamma r^2}{3} \quad (2.19)$$

2.5.2.4 Isothermal crystallisation for induction time determination

The rate of nucleation J is defined as the number of nuclei produced per time per volume using the Arrhenius relationship. Using the Arrhenius relationship:

$$J = A \exp\left(\frac{-\Delta G}{KT}\right) \quad (2.20)$$

where A is the pre-exponential factor, K is the Boltzmann constant.

Reflecting the small size expected for a critical nucleation cluster, the nucleation rate can be difficult to directly measure. In a practical situation, the induction time to the initiation of crystallisation is often employed to estimate the nucleation rate J using the approximation $J \sim 1/\tau$ for calculation of the interfacial energy. According to the classic nucleation theory, spontaneous nucleation will occur when supersaturation is achieved. However, in reality there is a period of time between the achievement of supersaturation and the appearance of crystals known as the induction time τ_{ind} . In cooling crystallisation, a supersaturated solution can be obtained by cooling rapidly the solution and then the temperature maintained until crystals appear. The induction time can be determined when the first crystals appear.

Assuming that the nucleation time is primarily for the formation of the nucleus, the induction time τ is inversely proportional to the rate of nucleation, J

$$\tau = 1/J \quad (2.21)$$

Besides, the Gibbs-Thomson relationship [40, 59] represented the relationship between particle size and solubility by the equation:

$$\ln\left[\frac{C}{C^*}\right] = \ln S = \frac{2M\gamma}{vRT\rho r} \quad (2.22)$$

where C is the solubility of particles; C^* is the equilibrium solubility of the substance, R is the gas constant, T is the absolute temperature, ρ is the density of the solid, M is the molar mass of the solid in the solution, γ is the interfacial tension of the solid with solution, v is the numbers of mole of ions formed from one mole of electrolyte.

For non-electrolyte, $v = 1$, therefore:

$$-\Delta G_v = \frac{2\gamma}{r} = \frac{kT \ln S}{v} \quad (2.23)$$

Thus from the equation (2.19)

$$\Delta G_{crit} = \frac{16\pi\gamma^3 v^2}{3(kT \ln S)^2} \quad (2.24)$$

From equation (2.20), the rate of nucleation can be expressed as:

$$J = A \exp\left[-\frac{16\pi\gamma^3 v^2}{3k^3 T^3 (\ln S)^2}\right] \quad (2.25)$$

Combining equation (2.21) and (2.15) and taking natural logarithm for both sides of the equation, we can obtain this:

$$\ln \tau = \left[\frac{16\pi\gamma^3 v^2}{3k^3 T^3 (\ln S)^2} \right] - \ln A \quad (2.26)$$

According to the equation (2.26), three variables which have significant effects to the rate of nucleation are the temperature, the degree of supersaturation, and the interfacial tension. This relationship indicates that the rate of nucleation increases with increasing degree of supersaturation. Higher levels of saturation will generate a large number of nuclei whilst lower levels of supersaturation produce a smaller amount of nuclei that will grow into bigger crystals.

2.5.2.5 Heterogeneous nucleation

According to equation (2.18) both ΔG and r_c depend profoundly on the surface free energy so any modifications are able to change these values would be most likely to have an effect on the possibility of the nucleation process. It has been verified that the presence of foreign bodies or a surface in a crystallising solution can reduce the positive free energy change (activation energy) therefore this reduces the values of ΔG and r associated with the formation of the critical nuclei at constant supersaturation, that is, making nucleation more favourable. A decrease in surface free energy would also decrease the value of the critical supersaturation, since the nucleation rate is also

dependent on the surface energy (equation 2.20). These factors can be expected to make heterogeneous nucleation more viable than homogeneous nucleation particularly at low supersaturation levels. The reduction of the surface energy will be the highest when the best match between the substrate and the crystallising substance is achieved [60].

The overall free energy change to form critical nuclei associated with heterogeneous critical nucleus formation will be less than the free energy change in homogeneous nucleation, ΔG_{crit} .

$$\Delta G'_{crit} = \Phi \Delta G_{crit} \quad (2.27)$$

where $\Delta G'_{crit}$ is the free energy change when forming a critical nucleus under heterogeneous condition; and ΔG_{crit} is the free energy change when forming a critical nucleus under homogeneous conditions where $0 < \Phi < 1$

A model for the effect of a solid crystal nucleus forming on a solid foreign body can be built by relating the reduction in the free energy of nucleus formation to the contact angle θ (Figure 2.14).

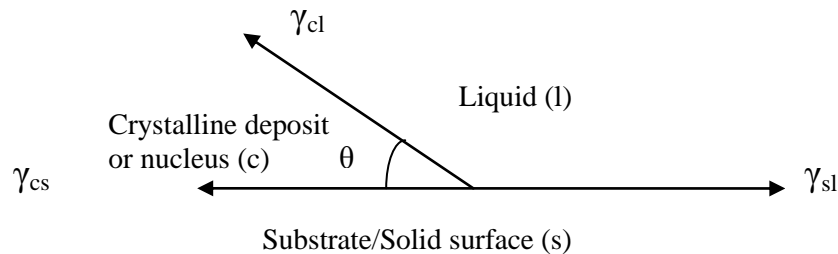


Figure 2.14 Interfacial tension at the boundaries between two solids and one liquid [26].

where θ is the angle of contact between the crystal and the foreign solid surface (angle of wetting in liquid-solid systems); γ_{cl} is the interfacial tension between the crystalline phase and the mother liquor, γ_{sl} is the interfacial tension between the solid foreign-body surface and the mother liquor, and γ_{cs} is the interfacial tension between the solid crystalline phase and the foreign body.

The relationship between the surface energies and the contact angle of the nucleus and the substrate is given by:

$$\gamma_{sl} = \gamma_{cs} + \gamma_{cl} \cos \theta \quad (2.28)$$

$$\cos \theta = \frac{\gamma_{sl} - \gamma_{cs}}{\gamma_{cl}} \quad (2.29)$$

Volmer [61] suggested that:

$$\Phi = \frac{(2 + \cos \theta)(1 - \cos \theta)^2}{4} \quad (2.30)$$

For the limiting case when $\theta = 180^\circ$ then there is no wetting, ($\cos \theta = -1$, $\Phi = 1$) so there is no reduction in the energy barrier and the free energy required for the homogeneous and heterogeneous nucleation become the same.

When $0^\circ < \theta < 180^\circ$ (partial wetting), there is a reduction in nucleation energy barrier. The total free energy required for heterogeneous nucleation is less than for homogeneous nucleation and thus the nucleation in this case is easier to achieve.

When the other limiting case where $\theta = 0^\circ$, there is complete wetting and hence no energy barrier to nucleation or the free energy of nucleation is zero.

A surface or an interface of different composition than the solute may serve as a nucleation substrate in heterogeneous nucleation. It decreases the energy barrier for the formation of nuclei which may grow into crystals. The free energy of nuclei formation can be expected to be lowered with the presence of a substrate as a result of favourable surface interactions between the aggregate and the substrate. Hence, with the presence of foreign particles or template surfaces, the nucleation can be induced at lower supersaturation or a lower degree of supercooling than homogeneous nucleation. Also, nucleation can be promoted by the increase of the surface area of the substrate.

2.5.2.6 Secondary nucleation

When both the substrate and the crystallising substance are the same, it is called secondary nucleation. This mechanism will be more favourable than both heterogeneous

and homogeneous nucleation and thus crystals can be produced at a lower supersaturation [60].

Secondary nucleation is induced by crystals that are present in the supersaturated solution. The presence of a crystal (seeding) in the supersaturated solution may cause further nucleation at a degree of supersaturation for which spontaneous nucleation can not occur due to the lower interfacial tension at the surface. This phenomenon is called 'breeding of nuclei' or 'secondary nucleation'. Breeding can be occurred by several mechanisms [62]:

- Initial (dust) breeding: This occurs when a crystal is first introduced to a solution as long as it has not been specially treated before. It is attributed to the existence of crystal dust on the surface of the seed. These crystals are washed off and grow into new crystals.
- Needle or polycrystalline breeding: At a high supersaturation, crystals often grow imperfectly. In some cases, they develop as needles or dendrites, and in others they grow as a conglomerate polycrystalline which is easily broken up into further crystals if the solution is agitated.
- Collision breeding: This occurs in the supersaturated solution when a crystal collides with or slides along another one. Collision breeding appears as a main cause of secondary nucleation in most of the agitated seeded crystallisation systems.

When crystals of solute present in the solution intentionally or unintentionally, the supersaturated solution will be easier to nucleate i.e. at a lower supersaturation compared to heterogeneous nucleation. The process in which small crystals are introduced in the solution has been known as seeding. Seeding is able to control polymorphs as well. Kwokal et al [63] used a self-assembled molecular layer of Entacapone (SALE) on an Au (100) surface for polymorph-directing seeding of Entacapone crystallisation in aqueous/acetone solution. This study reveals the possibility of directing nucleation from uncontrolled nucleation sites toward a more directed crystallisation process and thus more stable polymorphic form via a selective choice of an adsorbed polymorph on a substrate (see Figure 2.15).

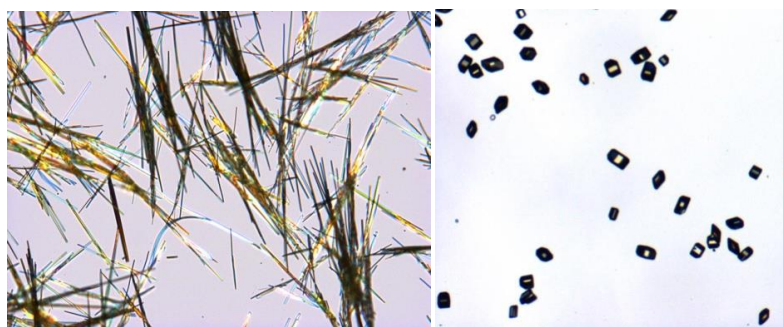


Figure 2.15 Entacapone crystal (left) Needle-like crystals of form D obtained from with absence of SALE; (right) cubic crystal of form A in the presence of SALE [63].

2.5.3 Crystal growth

Crystal growth is composed of the series of stages by which an atom or a molecule is incorporated onto the crystal surfaces. Stages involved in the crystal growth process can be summarised as follows:

- (i) Transport of solute molecules toward the boundary layer neighbouring to the crystal surface
- (ii) diffusion of solute thorough the boundary layer due to the concentration gradient
- (iii) Adsorption of solute molecule on the crystal surface
- (iv) Diffusion over the crystal surface to choose the energetically favourable binding site
- (v) Attachment onto step sites of the crystal surface
- (vi) Diffusion along the surface step
- (vii) Attachment to the kink site of the crystal surface

It is not necessarily that the processes from (i) to (vii) occur in the growth process of some materials. Solute particles may omit stage (iv) and (v) and directly incorporate onto the kink site or some stages may occur more rapidly comparing to some other stages so the slower stage can be neglected.

The model of the mechanism by which crystals grow is represented in Figure 2.16.

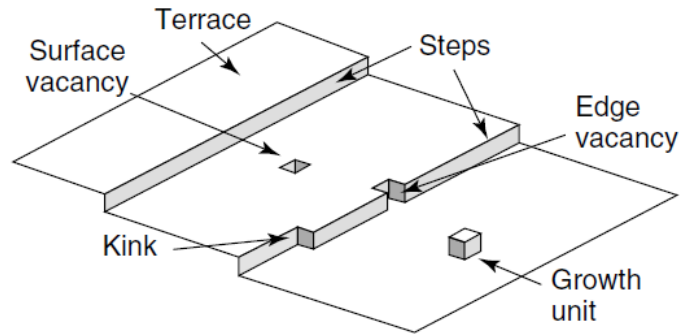


Figure 2.16 Kossel model of a crystal surface [60].

In this model, three sites considered for molecules adsorbed or desorbed from the growth layer are steps, terraces and faces. A growth unit (atom, ion, and molecule) is represented by a cube. One cube molecule can have a maximum of six bonds with surrounding units. A molecule adsorbing on the step site forms two bonds, on the kink forms three bonds and on the terrace forms only one bond. When a cube is incorporated onto the layer to form a crystal, it will find a position or a crystal face to attach. There are three different types of crystal faces: flat (F) face, stepped (S) face and kink (K) face. In this model, if a molecule incorporates onto the kink faces, it will stay there and become a part of the crystal. However, there are very few molecules adsorbing directly on the kink face. They adsorb on the step face first and then diffuse to the kink site later. They may be desorbed many times before incorporating onto the kink faces. Hence, it is obvious that the molecules will adsorb on the rough surface; S and K will have a greater probability to become a part of this surface than those adsorbing on the F face. This results in the rate of crystal growth on the flat face (smooth surface) being much slower than that of the rougher step or the kink faces. This will affect the crystal shape due to the differences between the growth rates of the different faces. The rapidly growing faces get smaller and smaller then tend to disappear. As a result, the surrounding faces of crystals are those characterised by the relatively slow growing flat faces.

2.5.3.1 Diffusion reaction theory

There are many factors including the three-dimensional crystal structure, crystal defects, temperature, supersaturation, solvents and the presence of impurities which affect crystal growth [64]. Noyes and Whitney [65] assumed that the crystallisation process is

the reverse process of dissolution. The driving force for crystallisation is the difference between the concentration in the bulk of solution and at the solid surface.

$$\frac{dm}{dt} = k_m A(c - c^*) \quad (2.31)$$

where m is crystal mass deposited in time t ; A is surface area of crystal; C is solute concentration in the solution; C^* is equilibrium concentration; and k_m is coefficient of mass transfer.

$$\frac{dm}{dt} = \frac{D}{\delta} A(c - c^*) \quad (2.32)$$

where D is coefficient of diffusion of the solute and δ is the thickness of the stagnant film.

Crystal growth is a combination of two processes: diffusion and surface adsorption. Firstly, solute molecules are transported from the bulk of the supersaturated liquid phase to the surface of a crystal (diffusion process). Secondly, the solute molecules are incorporated into the crystal surface to extend the crystal lattice (adsorption) (Figure 2.17). Hence, the overall growth rate of a crystal reflects the relative rates of these stages.

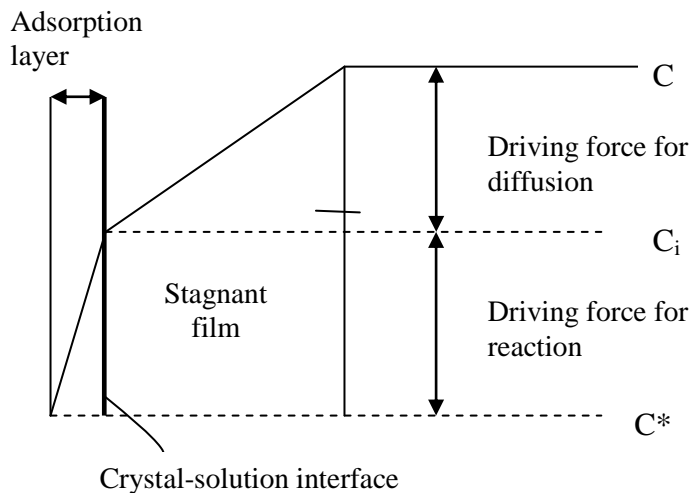


Figure 2.17 Concentration driving forces of two stages (diffusion and adsorption) in crystal growth from the solution [26].

Diffusion:

$$\frac{dm}{dt} = k_d A(C - C_i) \quad (2.33)$$

Adsorption:

$$\frac{dm}{dt} = k_r A(C_i - C^*) \quad (2.34)$$

where k_d is the rate constant associated with diffusion; k_r is the rate constant associated with incorporation of growth units into the crystal.

When the diffusion of materials between the bulk solution and the surface of a crystal is slow compared to the surface absorption (surface diffusion, integration, and the adsorption and desorption of the crystallising units), this is known as mass transport (diffusion) controlled. When the surface adsorption is slow compared to the diffusion, this is a surface controlled process. However, it is difficult to apply in above calculations since the interfacial concentration is not easy to measure.

2.5.3.2 Crystal growth mechanisms

Different crystal faces show different surface chemistry, thus the growth of individual faces depends on crystallising conditions such as supersaturation, solvent and impurities due to the interactions at the interface. Hence, the growth rate of each face is expected to be different resulting in a change of size and morphology of the crystal. The growth mechanisms that show the relationship between the crystal growth rate and supersaturation level will be described and discussed in the following section. The behaviour of growth rate of a crystal face is dependent on its underlying growth mechanism [66]. The growth mechanism controls molecular attachment onto the growing crystal surface [67]. There are three dominant crystal growth mechanisms expected to be active for a particular supersaturation region (Figure 2.21).

(a) Screw dislocation mechanism (Burton, Cabrera and Frank (1951)): This mechanism was developed by Burton, Cabrera and Frank to explain experiments which observed crystal growth at very low supersaturation where the transport of solute molecules from the bulk solution to the crystal surface is unfavourable. According to Burton, Cabrera and Frank at low supersaturations, the crystal growth process occurs via 2-dimensional diffusion of solute molecules over the crystal surface. The incorporation of growth units onto the face of the dislocation protrusion leads to the formation of a growth spiral over the crystal surface. Screw dislocations provide a

continuous source of kink sites which allow easy attachment of growth units onto the surface and facilitate the subsequent growth of the surface (Figure 2.18).

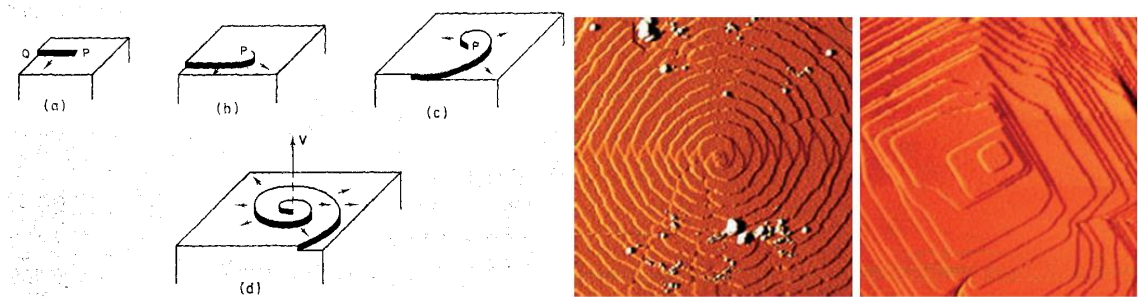


Figure 2.18 Crystal grown by the BCF mechanism shows the surface of the crystal with a screw dislocation and development of a spiral [60].

The resulting growth rate expression is given by:

$$R = A\sigma^2 \tanh\left(\frac{B}{\sigma}\right) \quad (2.35)$$

where A and B are complex temperature-dependent constants.

(b) Two-dimensional Birth and Spread mechanism [68, 69]: At higher supersaturation, nucleation can occur without the need for edge and kink sites and takes place anywhere on the crystal surfaces. These develop through creating a growing monolayer. After this initial stage, further growth units integrate into the existing monolayer to spread over the surface (Figure 2.19). The relationship between the face growth velocity and supersaturation can be expressed by:

$$R = A_1\sigma^{5/6} \exp\left(\frac{A_2}{\sigma}\right) \quad (2.36)$$

where A_1 and A_2 are constants .

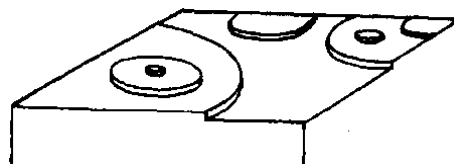


Figure 2.19 Crystal grown by birth and spread mechanism in which nucleation may occur at the edges, corners, or on the faces of the crystals [26].

(c) **Continuous growth (rough interface) model** [70]: At very high supersaturation, surface roughening provides abundant sites for surface integration with more kink sites resulting in a much higher growth rate. At this region, the energetics of growth unit attachments are the same regardless of the growth direction producing morphologies which result in spherulitic or dendritic crystals (Figure 2.20).

$$R = A\sigma \tag{2.37}$$

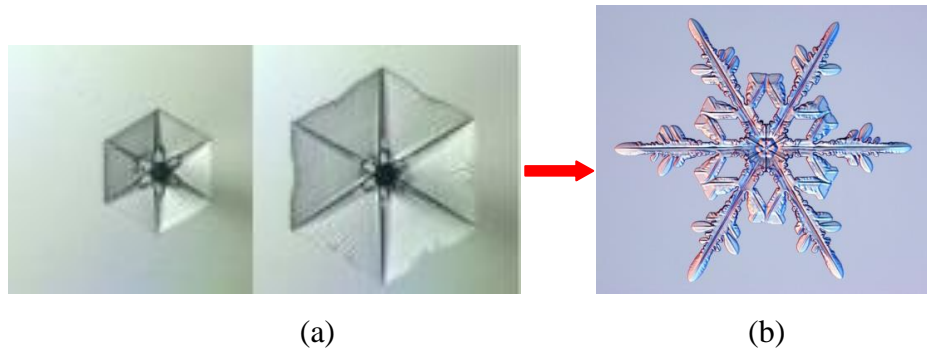


Figure 2.20 (a) Ice (snow) crystal morphology changes by roughening occurring at the corner of a crystal; (b) Dendritic ice crystals [71].

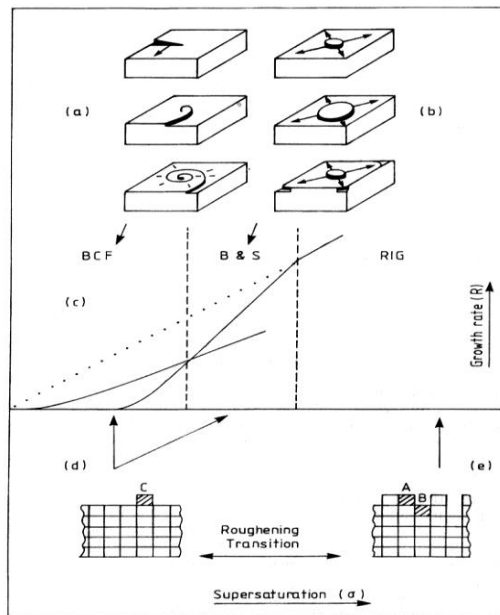


Figure 2.21 Schematic showing the crystal growth rate mechanism taking place at the crystal/solution interface, involving screw dislocation (a) 2D surface nucleation (b) together with the expected crystal growth mechanisms as a function of solution supersaturation (c) and the transition between stable growth on a smooth surface to unstable growth at the roughened crystal/solution interface ((d) and (e)) [72].

2.5.3.3 The surface entropy factor and its relation to the entropy factor

Jackson (1958) and Bennema and van der Eerden [73] introduced the α factor as a surface entropy factor which can be used to predict the growth mechanism of a crystal face

$$\alpha = \xi_{hkl} \frac{L}{RT} = \frac{n_s}{n_t} \frac{\Delta H}{RT} = \frac{n_s}{n_t} \frac{\Delta S}{R} \quad (2.38)$$

where L is the molar heat of fusion for the melt growth calculation; in the case of crystal growth from solution, L must be replaced by enthalpy of dissolution; ξ_{hkl} is the surface anisotropy factor: $\xi = n_s/n_t = E_{sl}/E_{cr}$ with E_{sl} is the total energy in the slice of the crystal face and E_{cr} is the total crystallisation energy; ΔH and ΔS are the entropy and enthalpy of phase transition, respectively.

For solution growth, there are two most used expressions for calculation the surface entropy factor α_{hkl} [74]:

$$\alpha = \xi \frac{\Delta H_s}{RT} \quad (2.39)$$

$$\alpha = \xi \left(\frac{\Delta H_f}{RT} - \ln X_{seq} \right) \quad (2.40)$$

where ΔH_s and ΔH_f are respectively the heat of solution and the heat of fusion; X_{seq} is the mole fraction calculated from solubility.

According to Bennema and Gilmer [75] and Davey [76] (Table 2.4), the growth mechanism can be predicted by the values of α .

Table 2.3 Predicted growth mechanism according to the value of α

Bennema and Gilmer [75]	Davey [76]	Predicted growth mechanism
$\alpha < 3.2$	$\alpha < 2$	The interface is rough so all growth units can incorporate onto the growing surface (continuous growth).
$3.2 < \alpha < 4.0$	$2 < \alpha < 5$	The interface is smoother and the most probable mode of growth is B&S

$\alpha > 4$	$\alpha > 5$	The surface becomes very smooth and growth generally proceeds by screw dislocation (BCF).
--------------	--------------	---

When a face is growing at temperatures above T_R , the surface is rough and growing ‘continuously with a linear dependence of the growth rate on supersaturation showing non-faceted crystal morphology. Whilst a crystal grows below T_R , the surface is smooth and growing with a layer mechanism (B&S and BCF) and follows a non-linear relationship between the growth rate and the supersaturation [77]. Human et al [77] calculated the surface anisotropy ξ and the α_{hkl} and α_{hkl}^R for different faces (hkl) in various organic solvents and the melt using equation 2.38. For the (001) and (110) face, the α factors are above the critical value α_{hkl}^R so the face grows below the roughening temperature confirming a proper faceted crystal surface. However, for the growth from toluene and the melt, the α factors are slightly above α_{hkl}^R so kinetic roughening may happen which is in good agreement with the experimental observations. For the (11-1) face, non-faceted growth of this face is expected due to this face is growing above roughening temperature. However, the (11-1) face is much smaller or even not present so it is impossible to observe if this face growing faceted or not. Similarly, Jetten et al [78] calculated the α_{hkl} and α_{hkl}^R of important faces of naphthalene in toluene to determine if the (hkl) face is growing above or below the roughening temperature. The morphology of crystal growing at below and above the roughening temperature was shown from experiments. The experimental results were in good agreement with the calculated values of the α_{hkl} and α_{hkl}^R .

The critical values α_{hkl}^R of the α_{hkl} factors of crystal habit faces of biphenyl in methanol, toluene, and from the melt were calculated [77] and naphthalene in toluene [78] in Table 2.4.

Table 2.4. The critical values α_{hkl}^R of the α_{hkl} factors of crystal habit faces of biphenyl and naphthalene

	α_{hkl}^R
Biphenyl	2.6 – 3.4
Naphthalene	2.5 – 3.4

Bourne and Davey [79] [80] considered solvent effects and calculation of the α factor for the growth of hexamethylene tetramin (HMT) from vapour and from aqueous and ethanolic solutions from the heat of solution, from the entropy of solution and from the surface energy. The prediction of the growth mechanism from the α values are linked to the observed growth mechanism using data fitting. The α factor calculated from the vapour phase correctly predicted a BCF growth mechanism; however, the α value from aqueous solution agreed with linear kinetic mechanism; and a BCF mechanism from ethanolic solutions.

2.6 Design of crystal and particle properties by crystallisation

2.6.1 Background

Variation in the crystallisation process conditions can make a significant effect on the physical properties (thermodynamic, kinetic and mechanical properties) (Figure 2.22) of the resulting material.

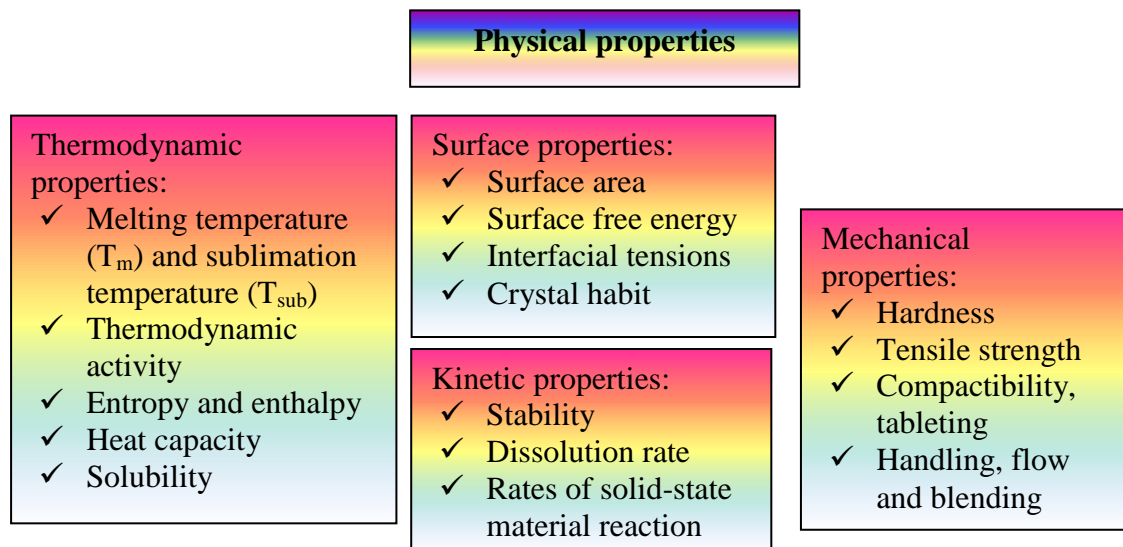


Figure 2.22 Summary of physical properties of a crystal.

In some cases, minor changes in crystallisation conditions, for example, the supersaturation, temperature, cooling or evaporation rate, and the presence of impurities

can provoke significant changes in the particle size, shape, purity, and defect structure (twinning). Changes of factors in the crystallisation processes can make major alterations in the thermodynamic and mechanical properties of a crystal. Hence, the supersaturation of solution needs to be controlled to obtain the crystal forms and size to meet the drug specifications, e.g. the dissolution rate and bioavailability. In addition, the size and morphology of crystals have effects on their downstream processing, e.g. separation, filtration, flowability, compaction etc. [81]. In the following sections, the effects of these crystallisation parameters on the properties of crystals (Figure 2.23) will be discussed in more detail.

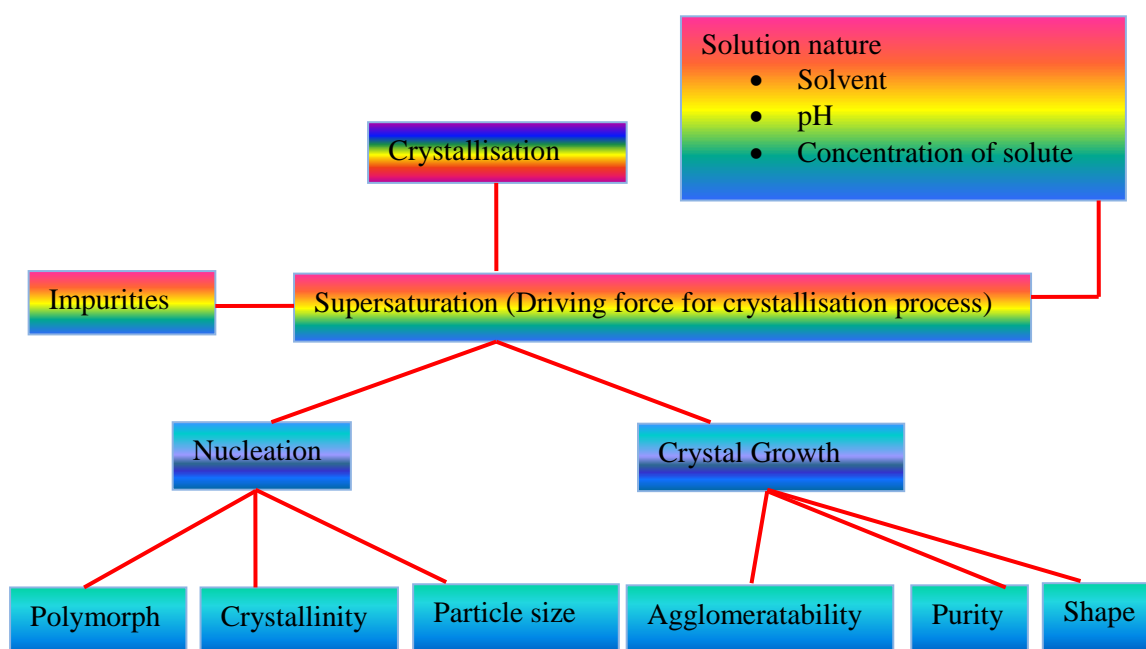


Figure 2.23 Diagrammatic route map of the influence of crystallisation conditions on crystal properties.

2.6.1.1 Supersaturation

The supersaturation of a solution can be generated by adjusting the solute concentration in the solution, i.e. solvent removal, addition of salts with ions which participate in precipitation, temperature change, pH change and addition of an antisolvent decreasing the solubility of the solute. Supersaturation can have a profound effect on the crystal growth, resulting in morphological changes in the crystallising compound over a range of supersaturation, e.g. Morphology of snow crystals exhibits various shapes under

different crystallising conditions and only shapes grow under specific conditions (Figure 2.24).

Tomozawa [81] studied the modification of octotiamine crystal habit under different crystallisation conditions (i.e., supersaturation ratio, pH, temperature, and impeller speed). With a pH value from 4.3 to 4.0, a decrease in the supersaturation ratio, and the impeller speed, octotiamine crystals for tableting powder showed a similar dissolution rate but an excellent flowability (less adhesive) and compressibility comparing to a conventional method. Kardum et al [82] studied the influence of cooling profile on an unseeded crystallisation process of pentaerythritol. The step and optimal cooling profile produced agglomeration and crystals with a wide crystal size distribution. For a linear cooling profile, crystals appeared with the wide crystal size distribution and without agglomeration. Optimal cooling profiles provide the narrow crystal size distribution without agglomeration. Supersaturations can influence the nucleation rate, thus changing the mean particle size. The number of nuclei produced was found to increase with increasing supersaturation with the size of crystals decreasing. However, large crystals are the most frequently produced at low supersaturation [83].

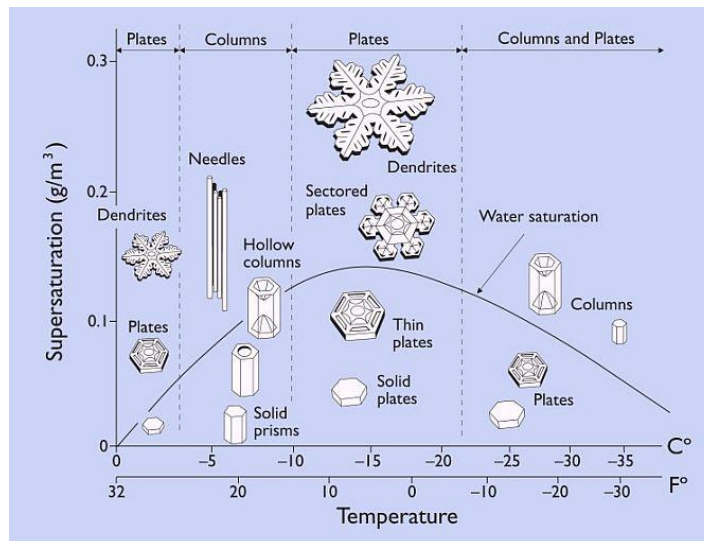


Figure 2.24 Morphology diagram of snow crystals showing various shapes under different crystallising conditions and only shapes grow under fixed conditions [84].

2.6.1.2 Solvent

The production of pharmaceutical compounds often involves crystallisation from organic solvents or mixtures of solvents. The solvent composition influences the

nucleation rate, the relative growth rate of each crystal face, and, thus, affects the shape and the size distribution of the product crystals, e.g. a solvent screening study was carried out by crystallising different crystal forms of tolbutamide from different solvents and studying the dissolution behaviour of its different crystal forms. Crystalline forms obtained from methanol and ethanol had the smallest particle size, plate-like shapes, and higher dissolution rates whilst crystals produced in acetone, ethyl acetate, and tetrahydrofuran had larger size with needle, cubic, and prismatic crystal habits, respectively, and had lower dissolution rates [85]. Carbamazepine crystallised from a drowning-out method using an anti-solvent has needle-like shape morphology. However polyhedral shapes were obtained from alcohol and thin plate-like shapes were found in acetone by reducing temperature and using solvent evaporation crystallisation methods [86]. Nokhodchi et al. [87] studied the effects of solvents and crystallisation temperature on the crystal habit of phenytoin. Variation in the crystallisation temperature was observed to change the crystal size. Needle-like crystals were obtained from recrystallisation of phenytoin in ethanol whilst rhombic morphologies were found in acetone solutions whilst the thin plates produced by the drowning-out method were found to have a higher compactibility when comparing to crystals formed using the other methods.

However, the understanding of the solvent effect on crystal form at the molecular level is still not completely resolved. Lahva and Leiserowitz [88] proposed that favourable interactions between solute and solvent on specific faces can lead to a reduction in the solid-liquid interfacial tension. Hence, the activation energy for nucleation on the crystal surfaces is reduced causing a transition from a smooth to a rough interface and a concomitant faster surface growth. Alternatively, it has been postulated that, solvent molecules can form strong bonding with the crystallising compounds, with the solute-solvent dissociation directing the nucleation and growth rates [89].

2.6.1.3 Impurities or additives

Impurities or additives can have a substantial effect on the kinetics of the nucleation and growth of a crystal. Some impurities can completely enhance or inhibit the crystal growth, whilst others act selectively or with a certain degree on specific crystal faces, consequently changing the crystal morphology [26]. Structurally-related substances

which are introduced into the crystallisation solution for specific purposes or compounds that have resulted from the synthesis or degradation of the desired product, represent the common impurities found in organic fine chemicals [90]. Additives are frequently used in pharmaceutical technology to modify crystal habits. The mechanisms of inducing crystal habit modification and/or the stabilization of polymorphs by additives related to the incorporation of additives into the crystal surfaces, thus changing the characteristics of the adsorption layer at the interface during the growth [26]. In this, additives can dock onto the crystal surface by adsorption, and subsequently block the absorption and incorporation of solute molecules on the crystal surface. Through this, they disrupt the crystal surface and/or the crystal lattice based on size, shape, position, structure and hydrogen bonding capability of their functional groups [90].

Beyond above mentioned examples, there are several other factors such as mixing intensity, crystalliser geometry on the crystals properties (shape, size and crystal size distribution) [91], pH effects on the impurity of final products [92].

2.6.2 The interrelationship among the structure, properties, performance and processing of crystalline material

Sun [28] analysed an inter-dependent relationship among the structure, properties, performance and processing of a drug (Figure 2.25).

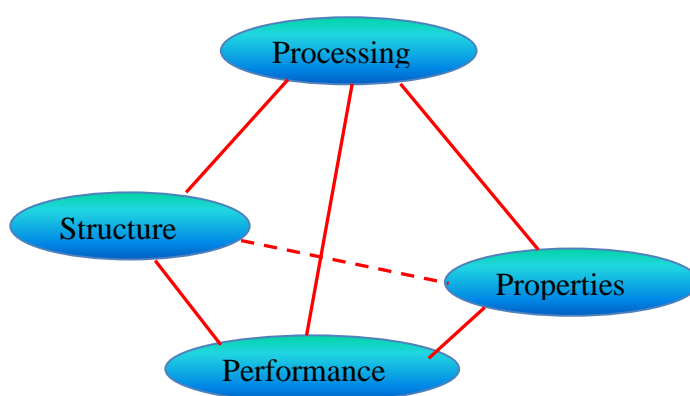


Figure 2.25 Inter-dependent relationship among the structure, properties, performance and processing of a drug [28].

This requires linking the disciplines and culture of material science-structure and property relationships, chemical engineering - processing, and manufacturing - quality management. The performance of a drug product including efficacy, safety, manufacturability, stability, solubility and bioavailability of a drug depend on its structure and properties. For example, solubility and dissolution rate are significant factors which rely on the selection of crystal forms (different packing and/or different conformations of the molecules) for the formulation of a drug since these properties can be expected to influence the absorption of the solid dosage form. Bioavailability is a measure of the rate and extent of the absorption of API and hence can be a decisive factor in terms of a drug's overall efficacy.

Moreover, the corresponding properties of a drug can be mechanical and physicochemical properties which are affected by structures at molecular, crystal, granular, bulk powder, and finished drug product levels. An example of a structure-property relationship is provided by acetaminophen (Figure 2.26). For the monoclinic form I crystals, molecules are hydrogen-bonded and form zigzag shaped layers which interlock and prevent sliding under the influence of a shear stress. For orthorhombic form II crystals, molecules are hydrogen-bonded forming flat layers with relative large spacing favouring plastic deformation and better tableting performance [93].

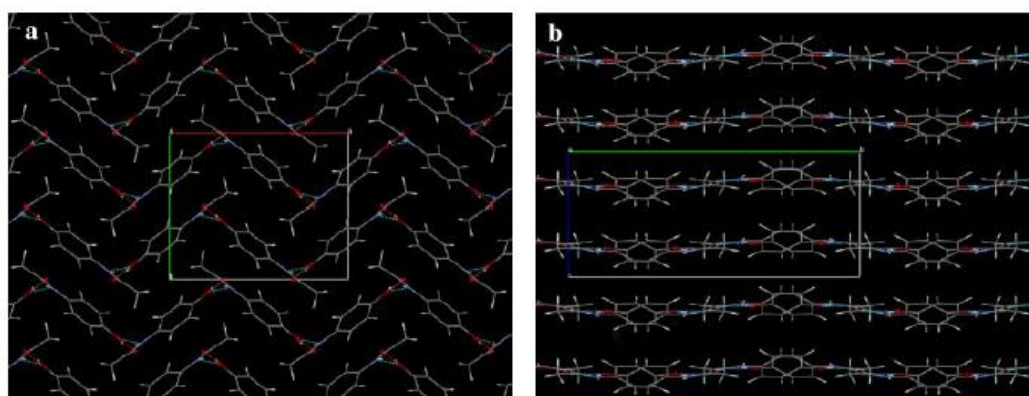


Figure 2.26 Molecular packing in crystal structure of acetaminophen (a) form I (monoclinic); (b) form II (orthorhombic) [28].

In addition, crystal structure and packing related to functional groups exposed on the surfaces and the elasticity of a crystal impact on the compressibility and powder compaction, which is an important aspect of tablet manufacturing. Tablet tensile

strength is affected by both bonding area and bonding strength over a unit bonding area [94]. Hence, despite identical molecular structure, the bonding strength over a unit bonding area may be slightly different due to the different functional groups exposed on crystal surfaces which is affect to the powder tabletability of a material [28] (Figure 2.27).

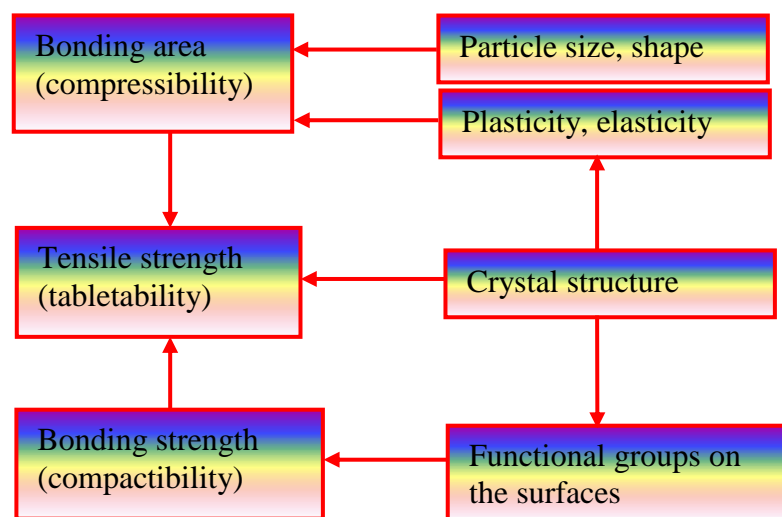


Figure 2.27 Relationship between crystal structures and the powder tabletability [28].

However, the structure affecting the properties and performance can be modified by processing such as chemical synthesis, crystallisation, milling, granulation, and compaction.

In summary, a minute change in crystallisation process or formulation can influence the final product quality. An understanding of the inter-dependant relationship among the structure, processing, properties and performance not only enables the high quality solid-form product to be more easily managed and controlled but also facilitates designing and optimizing a formulation and crystallisation process. Hence, a development of precision pharmaceuticals demands a detailed understanding of the structure, properties, performance and processing inter-relationships.

2.7 Crystallisation characterisation

Polymorphism and the shape of crystalline materials can be identified and characterized by a range of analytical methods such as microscopy, scanning electron microscopy,

transmission electron microscopy, differential scanning calorimetry (DSC), X-Ray diffraction (XRD), powder size distribution analysis (Malvern Instruments) and DVS etc. In addition, spectroscopic techniques such as FTIR spectroscopy, Raman spectroscopy which have afforded the detailed information on molecular structures and interactions in a solution have addressed the importance of solution clusters and precursors in determining the outcome of crystal polymorphs and morphology.

2.7.1 Optical microscopy

The simplest and most important tool used to characterize the crystal shape and crystal growth rate is using microscopy. There are two types of microscope that have been used widely for the characterisation of polymorphs: optical and electron microscopy. In optical microscopy using polarised light provides an excellent technique to improve the quality of the images obtained from birefringent crystals which have more than one refractive index which are doubly refracting [42]. In polarised microscopy, both a polariser positioned in the light path somewhere illuminating the sample together with an analyser are needed. When the polarisation direction of the polariser is aligned 90° with respect to the analyser, a situation known as using crossed polarisers, the empty field of view is black. When an anisotropic material is placed on the stage between the crossed polarisers, it will show bright contrast if it is not at the extinction position [42]. The differential interference contrast (DIC) and phase contrast techniques are complementary approaches for producing high contrast images of transparent objects.

2.7.2 Differential scanning calorimetry (DSC)

DSC is a popular technique to study polymorphs for their identification and characterization and to determine any phase transformation between forms. Since polymorphs have different crystal structures, their phase diagrams and melting points differ. DSC monitors the temperature difference between the sample and the reference during the heating or cooling cycle. It is based on the principle that the thermal event of melting or crystallisation will cause a temperature difference between the sample reference when latent heat is either absorbed or released. The difference in temperature between the sample and reference can be converted to the heat flow, which can be used to calculate the enthalpy of fusion. DSC data can provide information such as melting

point, crystallisation point, solid-solid phase transformation, chemical reactions, measurement of heat capacity and changes in heat capacity.

Reference and sample are heated up and cooled down to a temperature at a constant rate. DSC measures the difference between the sample and the reference and presents the differences in diagrammatic form. The peaks represent the crystalline and melting temperature respectively. The integration of the under curve area can give the energy of the thermal change.

2.7.3 Attenuated total reflection ultraviolet visible (ATR UV/Vis) spectroscopy

Ultraviolet-visible (UV-Vis) spectroscopy uses light in the ultraviolet and visible wavelength range. In this range of the electromagnetic spectrum, the absorption of this radiation makes a change in the electronic energy level of molecules which causes electronic transitions from the ground electronic state to the excited state. The absorbance of the attenuation of the reflected beam can be measured by the logarithm between the intensities of the incident light I_0 and of the reflect light I :

$$A_b = \log \frac{I_0}{I} \quad (2.41)$$

According to the Beer-Lamberts law:

$$A_b = \log \frac{I_0}{I} = \epsilon cb \quad (2.42)$$

where A_b is the absorbance; I is the transmitted intensity; I_0 is the incident intensity, b is the path length, C is the solution concentration (mol/L), and ϵ is the molar extinction coefficient (or molar absorptivity) which depends on the properties of the solute and solvent.

An UV-Vis spectrophotometer includes key components such as light sources, monochromator, detector and a holder for cuvettes containing samples (Figure 2.28). It can be either a single beam or dual beam. In a single beam, all of the light passes through the sample cell. I_0 must be measured by removing the sample. In a double-beam instrument, the light is split into two beams before it reaches the sample. One beam is used as the reference; the other beam passes through the sample. The reference beam

intensity is taken as 100% transmission (or 0 absorbance), and the measurement displayed is the ratio of the two beam intensities.

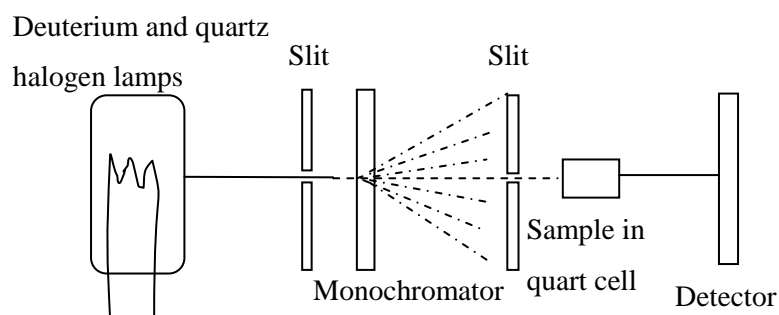


Figure 2.28 Schematic diagram of a UV-Vis spectroscopy.

The mechanistic working of ATR (Attenuated Total Reflection) based on light passing from a material with high refractive index (ATR crystal at the tip of the probe) to a material with lower refractive index (solution). The light enters the solution and can be partially absorbed by the solute before being reflected back into the ATR probe. The reflected light is therefore attenuated, resulting in a reduction in the output signal due to the absorbance of the solution (Figure 2.29). ATR can be practically implemented using a fibre optic immersion probe which can be inserted into a saturated or supersaturated solution to study solution concentration.

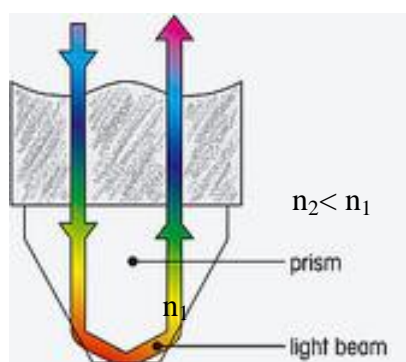


Figure 2.29 ATR probe using 3-bounce sapphire ATR crystal.

In this, the fibre-optics is used to transmit light to and from the probe from the UV/Vis spectrometer. ATR-UV probes are suitable for the direct measurement of strongly absorbing solutions (high solubility solutions) where standard transmission probes cannot be used. A combination of PAT tools and solid-state analytical techniques to

investigate the polymorphic transformations during the antisolvent crystallisation of sodium benzoate from IPA/water mixture to identify the form of the polymorph, hydrate, or solvate and investigate which forms exists under the conditions [95].

ATR-UV probes are suitable for the direct measurement of strongly absorbing solutions (high solubility solutions) where standard transmission probes cannot be used. The measurement approach has some significant advantages: (a) no sampling; (b) solutions need not be diluted; (c) applicable to measure high-solids content slurries on-line; (d) easy to set up with a flexible fibre-optics connection to the probe. However, a high concentration solution may cause a crystallisation process and the crystals may deposit on the ATR probe. Therefore it is necessary to clean the probe properly with solvent. For a particular material, a calibration model has to be built from a series of spectra recorded at various concentrations and then this calibration model can be used to obtain in-situ concentration and supersaturation in a reactor to monitor and control the crystallisation process.

2.8 Closing remarks

This chapter reviewed and discussed the fundamental theories of crystallisation including the basic crystallography, crystal chemistry, stages of crystallisation process explaining nucleation and growth process, particularly in the influence of crystallisation environmental conditions on crystal morphology and sizes. These theories are a foundation for the study and understanding of crystallisation processing, which will be used in chapter 6 and 7 in this thesis. The importance of polymorphism, size, shapes of particles, and the effects of crystallizing conditions, e.g. supersaturation, solvents, impurity etc. on the quality of final products have been reported and discussed. The concepts for the morphological simulation prediction in solid-state materials have been described. The chapter reviews some novel and important aspects in crystal science and engineering such as the interrelation among the structure, properties, performance and processing of materials and the possibility to predict and control final product properties from a very early stage of research and development at the molecular scale and the significance and potential applications of computational methods in crystal science and engineering.

3 Crystal growth rate kinetics and mechanism

Summary:

This chapter reviews research regarding the on-line measurement of crystal growth rates, together with aspects concerning crystal growth rate dispersion and describes the expected crystal growth kinetic mechanisms as a function of solution supersaturation.

3.1 Introduction

The physical properties of active pharmaceutical ingredients (API), such as particle sizes and shapes, can play a significantly important role in the downstream formulation of ingredients into the practical drug dosage forms. The growth rate of each crystallographically unique crystal face is likely to be different depending on the growth environment such as supersaturation, temperature, solvents and impurities etc. mindful that its surface chemistry will be different. This, in turn, result in a change of the morphology of crystals. There are various methods for the measurement of the growth rate of crystals [96] which can be either carried out on the measurement of the linear growth rate on specific faces of a single crystal or by estimating an overall linear growth rate from the mass deposition rates on the bulk mass of a large number of crystals. The single crystal measurement method avoids the impact of other physical phenomena such as the collision of crystals with other objects, e.g. the wall of the vessel or other crystals that may have an effect on the growth kinetics.

3.2 Expression of crystal growth rates

The crystal growth rate can be expressed as a mass deposition rate, R_G ($\text{kgm}^{-2}\text{s}^{-1}$) and a mean linear velocity (ms^{-1}) or an overall linear growth rate G (ms^{-1}) [26]:

$$R_G = K_G \Delta c^g = \frac{1}{A} \frac{dm}{dt} = \frac{3\alpha}{\beta} \rho_c G = \frac{3\alpha}{\beta} \rho_c \frac{dL}{dt} = \frac{6\alpha}{\beta} \rho_c \frac{dr}{dt} = \frac{6\alpha}{\beta} \rho_c \bar{v} \quad (3.1)$$

where L is the characteristic size of the crystal; r is the radius corresponding to the equivalent sphere; ρ_c is the crystal density; α and β is the volume and surface factors of the crystals; m and A is the mass and area of the crystal.

There is broad agreement in the literature that there are three main methods [96] to express the crystal growth rate:

- (a) The face growth rate (R_{hkl} or v_{hkl} , m/s) is the velocity of movement forward of the crystallographic faces in the direction perpendicular to the face (hkl) which can be measured on the individual crystal faces over time. These face-specific growth rates can

be related to their crystal growth mechanisms. Reflecting the fact that different faces of a crystal may have different growth rates under the same crystallisation condition. In particular, the higher index faces can normally be expected to grow much faster than the lower index faces. Therefore, the growth rates of the individual crystal faces cannot be considered as an effective measurement of the overall growth rate and the growth rate of individual faces (hkl) should be measured to assess the overall growth kinetics.

(b) Overall mass growth rate, R_G (kg/m²s) is the total mass flux to the crystallographic faces and is used to express the average growth rate of the whole crystal:

$$R_G = \frac{1}{A_C} * \frac{dM_C}{dt} \text{ or } R_G = \frac{\rho_c}{A_C} \sum v_{hkl} A_{hkl} \quad (3.2)$$

where M_C is the mass of crystal; A_C is the surface area of whole crystal; and A_{hkl} is the area of face hkl, v_{hkl} is the face growth rate and A_{hkl} is the area of the faces on a crystal.

Measurement of the bulk mass of crystals usually is used for calculation and design purposes for batch processes [96], in terms of determining the mass transfer rates under controlled conditions e.g. supersaturation, temperature; and for assessing size-dependent growth [26]. In this approach the determination of the overall growth rates can be conducted by a gravimetric method, i.e. through weighing the crystals mass formed as a function of time.

(c) Overall linear growth rate is the rate of change of characteristic dimension:

$$G = \frac{dL}{dt} \quad (3.3)$$

G and R_G can be related as follows:

$$R_G = \frac{1}{A_C} * \frac{dM_C}{dt} = \frac{1}{\beta \cdot L^2} \frac{d(\alpha \rho_c L^3)}{dt} = \frac{3\alpha \rho_c}{\beta} \frac{dL}{dt} = \frac{3\alpha \rho_c}{\beta} G \quad (3.4)$$

It is essential to characterise the shape of the crystal when using overall growth rate, where:

$$M_C = \alpha \cdot \rho_c \cdot L^3 \quad (3.5)$$

$$A_C = \beta \cdot L^2 \quad (3.6)$$

where α is the volume shape factor and β is the crystal surface shape factor. If crystals are spherical or cubic ($\beta/\alpha = 6$) then:

$$R_G = \frac{1}{2} \rho_c \cdot G \quad (3.7)$$

This expression is commonly applied for the population balance theory. The population balance method related to the crystal size distribution (CSD) was firstly applied to crystal kinetics by Randolph and Larson [97]:

$$\frac{\partial(nV)}{\partial t} + \frac{\partial(GnV)}{\partial L} = 0 \quad (3.8)$$

where n is the population density per unit volume, V is the total suspension volume of the crystallizer, G is the linear growth rate, L is the crystal size and t is the time.

3.3 Growth rate dispersion (GRD)

Growth rates of crystals of the same material and size, when exposed to identical conditions of supersaturation, temperature and fluid dynamics, do not grow at the same rate; this phenomenon is known as growth rate dispersion [21, 25, 98, 99]. Whilst Size Dependent Growth (SDG) is the phenomenon by which crystals of different sizes grow at different rates, growth rate dispersion (GRD) is a phenomenon where similar sized crystals grow at different rates under apparently identical conditions of supersaturation, temperature and hydrodynamics.

This phenomena was first reported by White and Wright [99] who found that an initially seeded crystal sample which possessed a narrow size distribution of sucrose (size 500 μ m) and aluminium trihydroxide crystals (size 55 μ m) showed a dispersion of growth rates when the population of seeded crystals grew. This occurrence has also

been observed in many other cases with different crystal materials and sources. Their results revealed that when seed crystals with a narrow size range were grown for a period of time, the resulting product crystals showed a very wide size distribution. This was demonstrated by Wang and Mersmann [100] and Mitrovic [101] also shown that there may be a correlation between the initial crystal sizes and the growth rates. The growth rate dispersion was also observed for primary nucleated ADP crystals [20]. With individual crystals having their own growth rates and retaining their initial growth rates over a long period of time.

Garside and Larson [102] studied the growth rate dispersion of potash alum crystals. The number of crystals with an initial size bigger than 10 μm was found to be dependent of the supersaturation, while particles with initial sizes smaller than 10 μm was shown to be independent of the supersaturation level. Rusli et al. [103] generated potash alum crystals in the size range of 2 -25 μm through attrition, e.g. by contacting a large potash alum crystal with a steel rod and fracturing small particles off the large crystal. Particles below 4 μm grew at a very small rate whilst crystals larger than 25 μm presented a strong dependence of growth rate on the initial sizes. Sherwood and Ristic [104] studied the influence of mechanical stress on the growth rate of materials suggesting that there was a competition between stress reduction and dislocation enhancement of the growth rate of secondary nuclei causing the growth rate dispersion.

Because the incidence of the variations of growth rate of the uniform sized crystals affects the CSD of the product crystals and hence product quality, much research has been performed to study the source of GRD. There are three types of factors which are able to describe experimental data, the Constant Crystal Growth model (CCG), the Random Fluctuation model (RF) [105] and a ‘fast-growers’, ‘slow-growers’ model (FGSG) [106].

The CCG model [20] which proposes the constant relative growth rate of each crystal along the growth periods, with different growth rates for the different crystals which might differ even for crystals of the same size growing under identical conditions. In this mechanism, nuclei are formed with a distribution of growth rates and at constant crystallising conditions, with each nucleus showing a constant but different rate.

The RF model proposed the growth rate of a crystal fluctuates around an average constant growth rate which might be caused by the change of surface structure versus time resulting in a growth rate deviation on a particular crystal surface [105].

Daudey [106] proposed the FGSG model in which proposed two types of growth rate that have an influence on the population of secondary nuclei crystals to interpret these growth rate dispersions. The larger crystals produced by a surface breeding mechanism by which the surface growth features such as macrosteps are removed by attrition. The smaller crystals, produced by a mechanical breeding mechanism, are likely to contain more strain, thus growing with low growth rate. Ristic et al [19] studied the growth rate of sodium chlorate crystals (size 5-150 μm) grown from secondary nuclei showing the growth rate of crystals depended on the degree of lattice strain. The most strained crystals grow at the slowest rates and the strain focused on or in the surface of very small crystals might play a leading role in growth rate dispersion.

3.4 Techniques for studying crystal growth rate

Currently, there have been various techniques studied previously for the characterisation of in-line crystallisation processes and for monitoring and measuring of the crystal growth rates using optical light microscopy techniques, on-line high speed imaging, atomic force microscopy (AFM), interferometry, laser polarization-interference techniques, laser confocal microscopy with differential interference contrast etc. However, different systems and applications require different methods. For example, transmission light microscopy is used for the growth rate determination of crystal faces while interference contrast or phase contrast microscopy is applied for measuring step velocities where steps are small [96].

These techniques are described in the following sections.

Table 3.1 Microscopy techniques for studying crystal growth kinetics and mechanisms

Technique	Applications
Optical light microscopy	<ul style="list-style-type: none"> ✓ Characterisation of crystal morphology and size as a function of crystallising environment. ✓ Measurement of crystal growth rates of individual crystal habit faces and identification of growth mechanisms ✓ Determination of nucleation and crystal growth kinetics in-situ
On-line high speed imaging	<ul style="list-style-type: none"> ✓ Measurement of crystal growth rate in agitated vessel by measuring CSD ✓ Monitoring of shape evolution and polymorph transformations ✓ Investigation of the effect of hydrodynamic, agitated speed, supersaturation, impurities etc. on the nucleation and growth kinetics
AFM	<ul style="list-style-type: none"> ✓ Examination of surface topography to study crystal growth mechanism due to its imaging capability at high resolution ✓ Measurement of grow rates of crystal habit faces through observing the growth of steps on the surface ✓ Study of solvent or additive molecules interactions with crystals faces
Interferometry	<ul style="list-style-type: none"> ✓ In situ examination of surface steepness, surface ✓ Measurement of step velocities and growth rate of crystal face, and identification of growth mechanisms

3.4.1 Microscopy technique

Optical microscopy employs a series of objective lenses and a visible light to magnify the images of a sample. Microscopy techniques equipped with a video camera and

commercial image capturing and analysis software has been employed to measure *in situ* the velocity of the moving step and the growth rate of individual faces during growth process [5-8, 98, 107, 108]. For example, Davey studied the effect of the supersaturation on the growth of the (100) faces of ammonium dihydrogen phosphate (ADP) [7] and the effect of ionic species ($\text{CrCl}_3 \cdot 6\text{H}_2\text{O}$; FeCl_3 and AlCl_3) on the growth of the (101) and (100) faces of ammonium dihydrogen phosphate (ADP) [7, 8] and the growth kinetics of the (001) and (100) face of urea in two cases: pure solution and with presence of biuret as an impurity [6].

The use of digital video-microscopy together with computational methods for analysis of captured images has also been demonstrated so far, a hot stage adapted to a polarizing light digital video-microscope accompanied by a computational method to investigate the growth rate [11]. An algorithm method was used to extract growth and nucleation data by subtracting grey pixel values corresponding to positions on pictures which can relate to the new growth of either nuclei or of growing crystals [16].

From the growth rate data as a function of supersaturation, the mechanism of crystal growth was investigated [10, 66, 108].

Furthermore, the estimation of growth rate for different crystal faces through in-process imaging and image analysis in multi-dimensional population balance modelling (PBM) to study the growth behaviour of crystal sizes in a reactor [14]. The morphological population balance model has been used to simulate the dynamic evolution of the shape distribution as well as size distribution by incorporating crystal shape information with faceted growth kinetics data. This has been demonstrated on L-glutamic acid [109], protein [110], [27].

A microscopy system has been employed for the study of kinetics and growth rate of the crystallisation process efficiently and conveniently, particularly in the growth rate of crystal habit faces.

3.4.2 On-line high speed imaging

This technique is able to capture high resolution images of particles in agitated reactors and propose the possibility of real-time particle analysis using online high-speed camera systems in [14, 17, 18]; Process Vision and Measurement (PVM) of Lasentec and Mettler Toledo Ltd [111]; In Situ Particle Viewer (ISPV) of Perdix. Wang et al [17] the growth rates of β form needle-shaped L-glutamic acid crystals in 2D using on-line imaging and imaging analysis (Figure 3.1). Calderon De Anda et al. [12] characterized the crystal morphology, size and shape together with the crystal growth rate of (L)-glutamic acid which exhibits two polymorphs, alpha and beta using the on-line and automated techniques for the real-time shape measurement via analysing the segmented images.

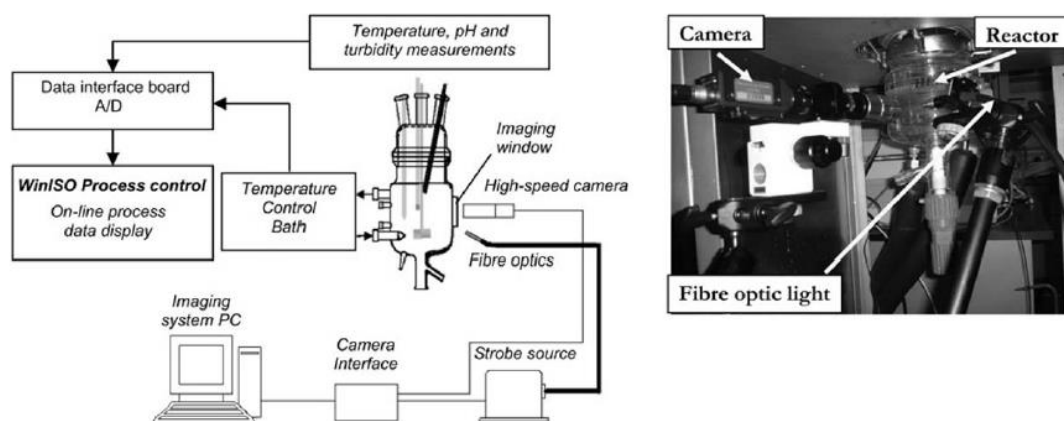


Figure 3.1 An example of the experiment set-up for measurement of the growth rate of L-glutamic acid using online imaging system [17].

The above examples of in-process digital video microscopy for process monitoring and measurement of crystal growth rate proved that this technique has been developed and improved. However, Wang et al. [17] reported that though on-line imaging has shown to be the most promising technique for on-line measurement of crystal shape within reactors, however it was limited in 2D imaging. Hence, future research and developments should investigate imaging techniques that provide the capability for direct 3D information. Li et al. [13] studied a new method for integrating crystal morphological modelling with *in-situ* shape measurement using on-line microscopy. The 3-D shape obtained from morphological modelling was rotated to get 2-D images and then matching was carried out between these 2-D images and real 2-D images acquired from an on-line imaging instrument (Figure 3.2).



Figure 3.2 2D projected image of L-glutamic acid generated through predicted 3-D shapes [22].

The use of in-process digital video microscopy for process monitoring and potentially control of product form is highly desirable so far. A recent development in on-line crystal morphology measurement and control is using on-line imaging and image analysis to measure crystal growth rate for each individual crystal within crystallisation reactors, which could open the way for the development of precision *in-situ* control of the growth process and final product quality control.

3.4.3 Focus beam reflectance measurement (FBRM)

FBRM employs a laser light source and a set of lenses to focus the laser light to a small spot (a focal spot). Particles will be located in the scanning focused spot and backscatter distinct pulses of reflected light. These pulses of backscattered light are detected and translated into chord lengths based on the simple calculation of the scan speed multiplied by the pulse width (time). The chord length is distant from one edge of the particle to another edge. In this technique, a correlation between the numbers of counts per second, the cord-length distribution of particles and particle size can be achieved (Figure 3.3) [112].

This technique integrated with FTIR/ATR can provide a real time measurement of dimension and number of crystals for the nucleation rate and crystal growth rate measurements as a function of supersaturation [22, 23] and studying growth kinetics and growth mechanisms [24]. Markande [23] used Lasentec focused beam reflectance measurement (FBRM) and an in-line process refractometer for monitoring aqueous crystallisation of dextrose monohydrate to evaluate the kinetic constants from the

growth and nucleation as a function of supersaturation level. The chord length distribution is related to the crystal size but it does not provide information on the crystal shape.

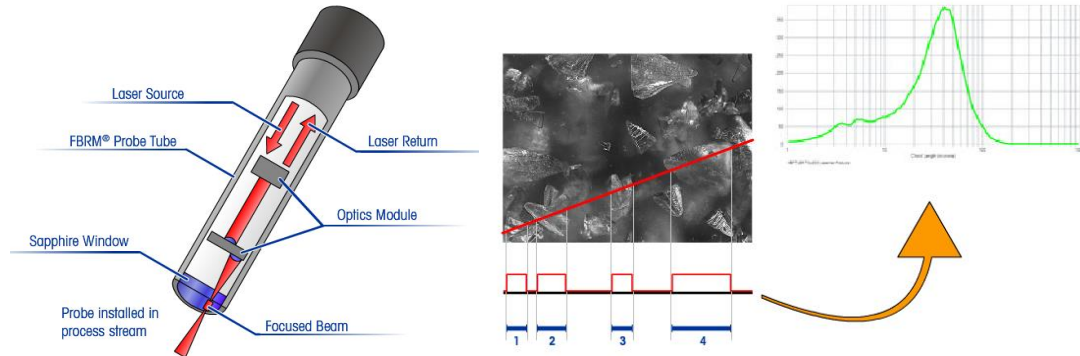


Figure 3.3 Focused Beam Reflectance Measurement [112].

3.4.4 AFM

AFM has been a powerful technique in the nanoscale investigation of growth rate and growth mechanism. It is able to image material surface with high resolution in aqueous environments, hence facilitating the study of solid-liquid interface [113]. An AFM probe mounted at the end of a short, flexible cantilever is impressed on the surface of the studied material and then scanned over the sample along a continuous sequence of raster lines. As the probe tip translates over the surface, it interacts with the structural features on the surface, through collective atomic forces including mechanical contact force, van der Waals forces, capillary forces, chemical bonding, electrostatic forces, magnetic forces causing the probe to be deflected. These deflections are amplified by the deflections of a laser beam and subsequently detected by a position-sensitive split photodiode (Figure 3.4). Photoelectric circuitry converts the laser beam deflections into height information [113] and AFM has been applied in studying the growth of crystals from solution both in-situ and ex-situ and the data can be recorded as a topological image and presented in different visual forms [114]. This technique has been successfully used to investigate the crystallization of proteins [114-116], barium nitrate [117], calcite [118] and viruses [119].

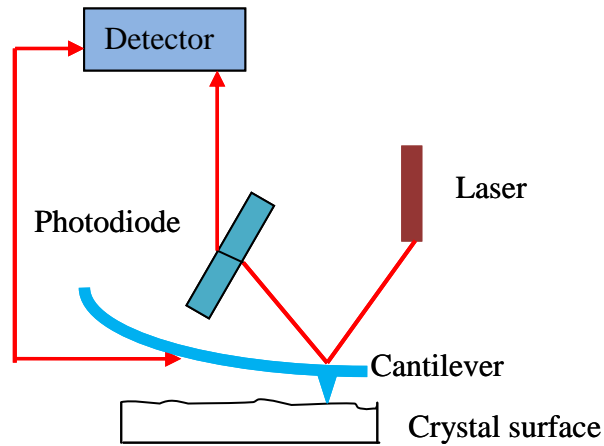


Figure 3.4 Diagram of atomic force microscope (redraw after [120]).

3.4.5 Interferometry

In interferometer system, an illuminating coherent light beam is split into two beams. One is reflected by a mirror and another one is reflected by the sample. The reflected beams recombine in a detector and interfere with each other. The basic set-up of an interferometer is shown in Figure 3.5. The interferometric patterns provide topographic information on a growing crystal surface. Such microtopographic observations can reveal the growth kinetics and growth mechanisms of crystal habit faces under various crystallising growth conditions. Interferometric studies have been performed on paracetamol crystals to investigate the growth kinetics of straining brittle paracetamol and plastic sodium nitrate crystals [121], the growth rate and growth mechanism of the (101) face of protein at various supersaturation [122], crystal defects [123], and the influence of additives [124, 125].

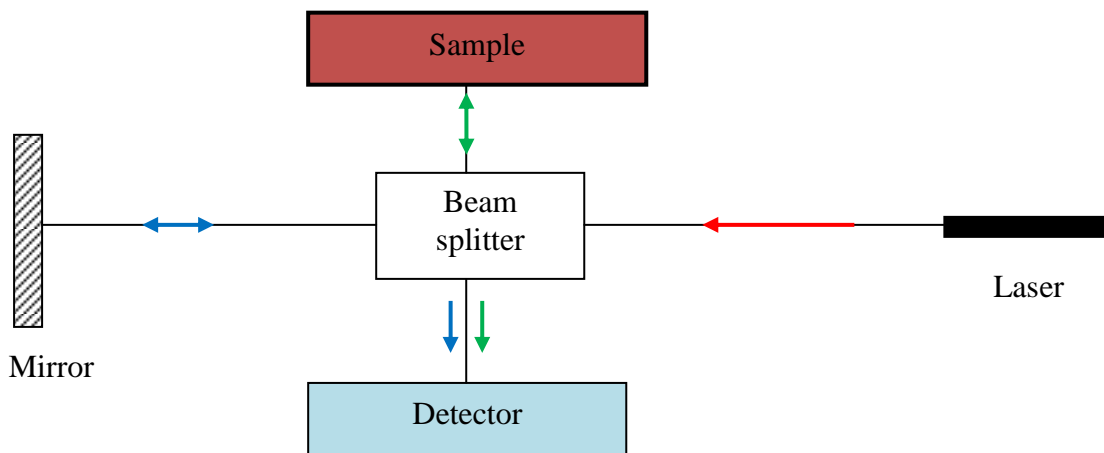


Figure 3.5 Schematic diagram of interferometry system (redraw after [121]).

There are also other techniques such as laser polarization-interference techniques and laser confocal microscopy with differential interference contrast microscopy. Liu [126] employed laser polarization-interference techniques for the measurement of the growth kinetics of (100) KDP crystal faces in the presence of polyphosphate as the function of various supersaturation and at different concentration of impurities. Experimental data was correlated to a two-dimensional nucleation model for a pure system and Kubota and Mullin's model for the case with presence of impurities.

Alexander [127] compared three observation techniques (AFM, Michelson interferometry, and laser confocal microscopy with differential interference contrast microscopy) through the growth rate measurement of protein crystallisation for the investigation of crystal growth kinetics. Growth rate measurements were carried out on the same system under identical experimental conditions using the three above different techniques showing differences up to 5-fold in growth rate and a different behaviour of the growth rate as a function of supersaturation. The explanations for these differences are differences in mass transport at the crystal interface during data acquisition and data acquisition rate.

In summary, a field of application of these techniques was provided for the choice of the optimal measurement technique in crystal growth studies. The growth rate measurement of a population of crystal in stirred reactors is usually employed using on-line high speed imaging or the FBRM to investigate the size distribution as a function of time. In this study, the microscopy technique was suitable and mainly used throughout to measure the growth rate of individual crystal faces of spontaneously nucleated single crystals at relatively high supersaturation, and the detailed methodology for crystal growth rate measurements is described in chapter 4.

3.5 Choice of experiment system for measuring crystal growth

3.5.1 Crystallography structures

Ibuprofen (2-(4-isobutyl-phenyl) propionic acid, $C_{13}H_{18}O_2$ $M = 206.28\text{g/mol}$, melting point: 76°C) is known as a non-steroidal anti-inflammatory drug (NSAID) that has been used to relieve pain, cold, fever and inflammation. Ibuprofen has one stereocentre so it can exist in two enantiomeric forms S(+)-ibuprofen and R(-)-ibuprofen. The commercially available product is usually the racemate since it is difficult to separate the two enantiomers. Cheminor Drugs have developed a process for production of the pure S-Ibuprofen (the active form of ibuprofen) that could decrease by almost half of the regular ibuprofen dosage and associated side effects. The inactive R form is unfortunately converted to the biologically active S form within the body so this process is unlikely to have commercial development [128]. Racemic ibuprofen contains both S(+) and R(-) ibuprofen in equal amounts. The solubility and dissolution rate of S(+)-ibuprofen and racemic ibuprofen are effected significantly by the temperature and the pH value of the solvent [129].

3.5.2 RS-ibuprofen

The racemic (R)-(S) ibuprofen crystals belong to the space group $P2_1/c$ (four molecules in a monoclinic system) and the unit cell with the lattice parameters $a = 14.667\text{\AA}$, $b = 7.886\text{\AA}$, $c = 10.730\text{\AA}$, $\beta = 99.3628^\circ$. The crystal chemistry of RS-ibuprofen molecules involves the packing of pairs of hydrogen-bonded (R)-(S) dimers [130] (Figure 3.6).

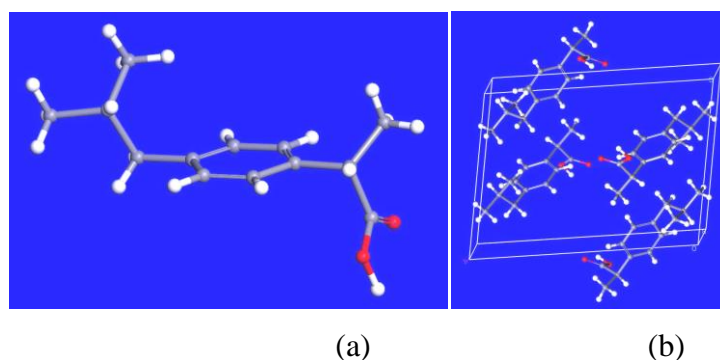


Figure 3.6 Molecular diagram showing (a) structure and (b) packing in the crystallographic unit cell of the ibuprofen molecule.

The crystal structure of Ibuprofen was first analysed by Shankland et al. [130]. It consists of centro-symmetric dimers, in which two molecules are linked by a pair of hydrogen bonds between their carboxyl groups (Figure 3.7). The O-H...O hydrogen

bonding parameters show a medium strength hydrogen bond with an O-H distance of 0.963 and a O-H...O angle of 179.5°. The hydrogen bonding affects the ibuprofen crystal shape by favouring growth in the b direction. The carboxylic acid dimers form about inversion centres; in this case the inversion centre is at the body centre of the second unit cell up along the b axis. The two molecules shown in Figure 3.7 forming a dimer are the asymmetric unit and its inversion object two cells up along the b axis.

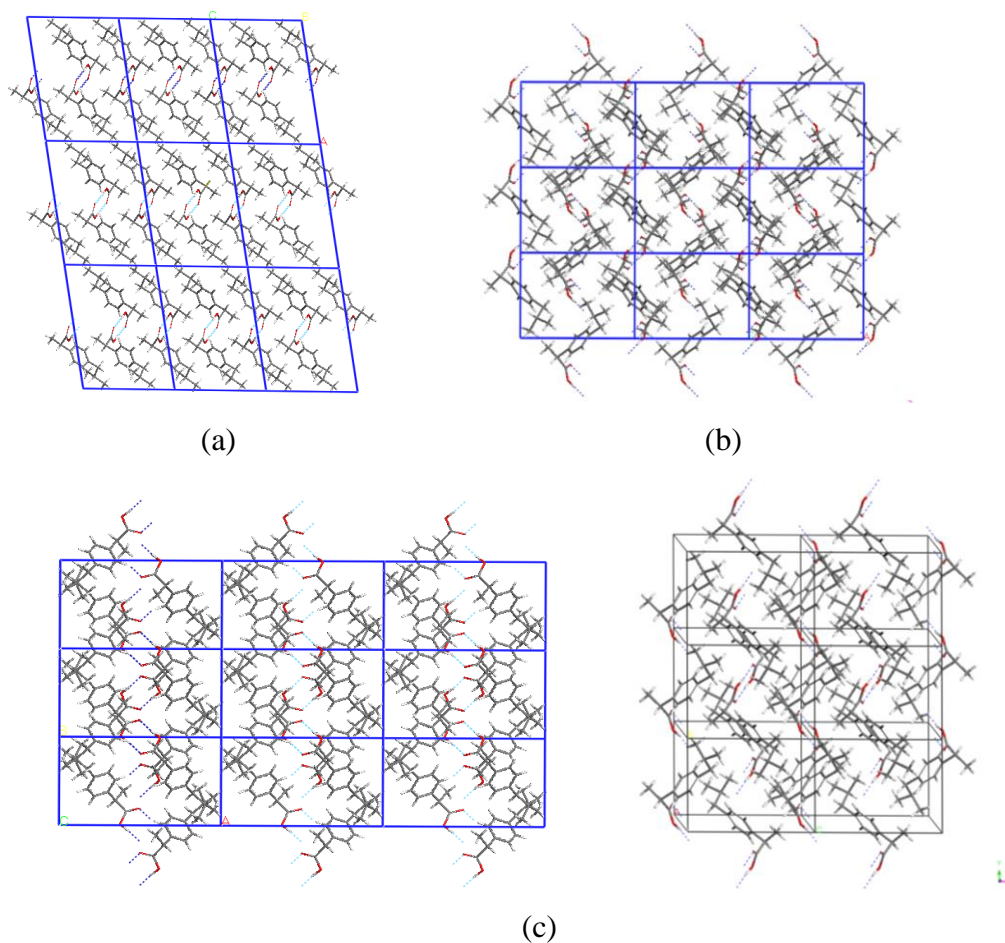


Figure 3.7 Molecular packing of ibuprofen (a) in the xz plane; (b) in the yz plane and (c) in the xy plane. A slightly tilted projection close to the yz plane reveals that hydrogen bonds are formed across the unit cell and between molecules 1 and 3 in the unit cell of the first row and the unit cell in the third row.

The pharmacological mechanism of action of ibuprofen is to reduce the effect of irritant chemicals, produced by the body, that cause inflammation and high temperature. Ibuprofen was first produced in the UK in 1969 by Boots under the trade name Brufen. It has a powdery white appearance and has been sold in the form of capsules, tablets, or powder on the market.

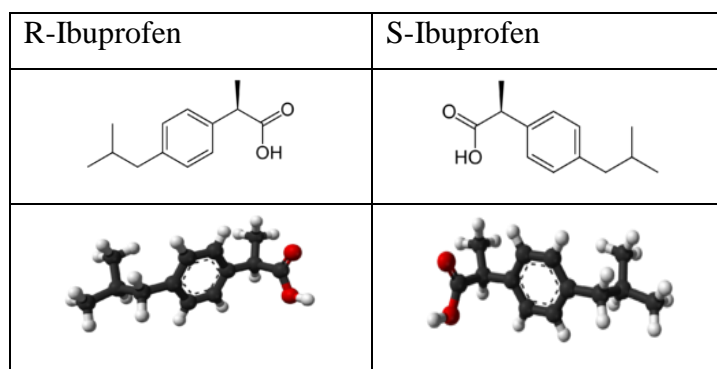


Figure 3.8 Molecule structures of R-ibuprofen and S-ibuprofen.

However, a new polymorphic form of ibuprofen can be obtained by specific re-crystallisation of the supercooled liquid ibuprofen. The nucleation of this polymorphic form is obtained by keeping the temperature at least 60°C below that of the glass transition temperature T_g of Ibuprofen ($T_g = 228^{\circ}\text{C}$). This new polymorph melts at 290K which is below the conventional form [131].

3.5.3 S-ibuprofen

(S)-Ibuprofen crystals belong to the space group $P2_1$ with four molecules in a monoclinic, a unit cell with parameters ($a = 12.462\text{\AA}$, $b = 8.035\text{\AA}$, $c = 13.539\text{\AA}$, $\beta = 112.89^{\circ}$) and a needle-like crystal morphology when recrystallised from methanol. S-(+)-Ibuprofen crystallizes with two independent molecules in the asymmetric unit with the molecules packing as cyclic hydrogen-bonded dimers in which each molecule adopts an S configuration [132] (Figure 3.9).

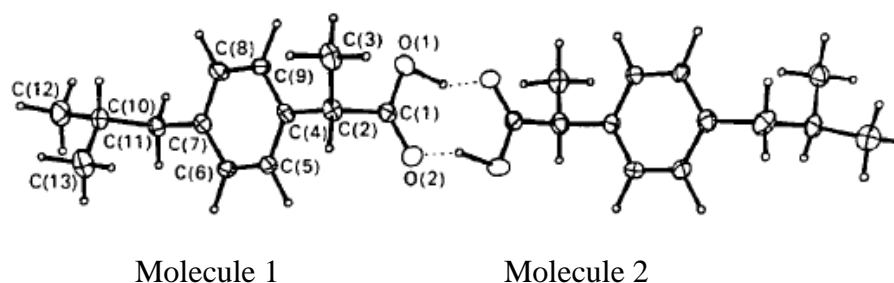


Figure 3.9 Two molecules of S-(+)-ibuprofen in the asymmetric unit form a cyclic hydrogen-bonded dimer [132].

3.5.4 Solubility

S-Ibuprofen shows higher solubility, higher dissolution rate and a lower melting temperature compared with the racemic form [133, 134]. In the crystal structure of ibuprofen, the hydrophilic parts (-COOH) are mutually bonded which results in a hydrophobic crystal structure [134]. Hence, Ibuprofen is slightly soluble in water and more soluble in organic solvents such as methanol, acetone, ethyl acetate, and hexane. The solubility of Ibuprofen in various solvents at the temperature range 10°C-40°C were reported and found that the dissolution enthalpies, ΔH , for these systems (ibuprofen in ethanol/ethyl acetate) correspond to 24.7 and 25.4 KJ/mol⁻¹ and both systems show a nearly ideal solubility behaviour [5].

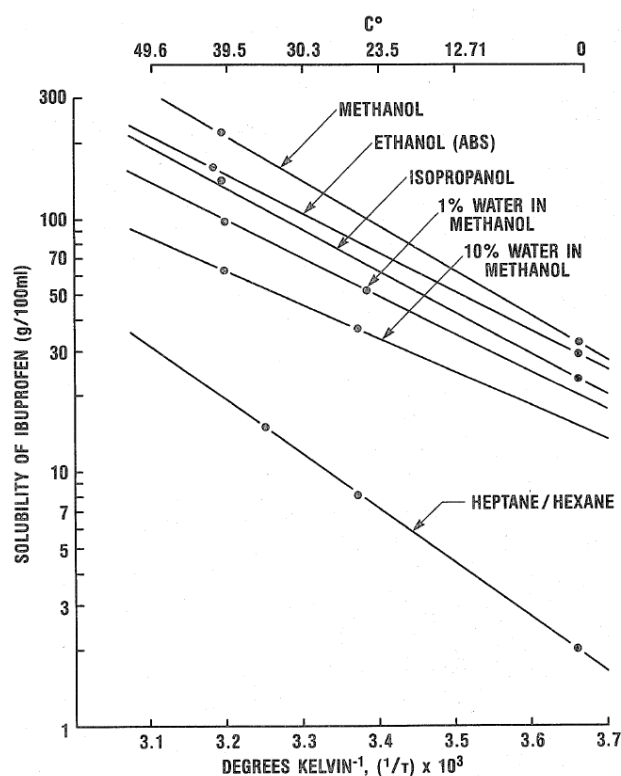


Figure 3.10 Solubility of ibuprofen in various solvents [135].

3.5.5 Crystal morphology

Crystals of racemic ibuprofen exhibit different crystal habits from prisms to needles and plates depending upon the different crystallising conditions (Figure 3.11) such as solvent type, temperature and the presence of additives. This material mostly has a plate-like crystal morphology dominated by a large (100) face with smaller {001} and

{011} side faces. Changes in crystal habit have been reported many times [5, 136-141]. Gordon et al. [135] reported that ibuprofen then crystallised at the commercial scale from hexane and heptane solutions was needle-like and had poor processing properties. This stimulated pharmaceutical and processing researchers to investigate potential process change to obtain equant (cube, sphere, grain) crystals with a higher bulk density, lower bulk volume and improved flowability.

It has been demonstrated that in different solvents it is only the crystal morphology that changes and the crystal structure remains after recrystallising [137] [141]. While crystals produced from methanol and ethanol shows a polyhedral crystal habit, crystallisation from hexane results in needle-like crystals at similar conditions. However, there are no polymorphic modifications confirming by X-ray powder diffraction (XRD) and differential scanning calorimetry (DSC) studies.

Different crystal forms including cubic, needle-shaped, and plate-shaped crystals were obtained from the different solvents, leading to differences in the physicochemical [138] and mechanical properties [137] impacting on compressibility, flow rate, bulk density and dissolution rate. An explanation for these phenomena was that changes in the intermolecular packing in the crystal surfaces altered the hydrogen bonding and other intermolecular interactions.

The properties of ibuprofen were optimized in the solvent change technique using the presence of different water-soluble additives [140]. These additives were only present during the crystallisation process and were removed after precipitation by a washing process. Ibuprofen molecules can form hydrogen bonds and the additives that are able to interact with these hydrogen bonds during the crystallisation process may alter the properties of the product crystals.

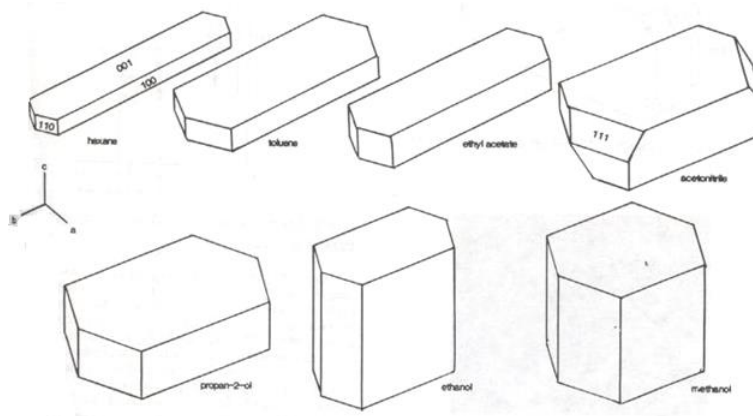


Figure 3.11 Morphologies of ibuprofen in various solutions [136].

3.5.6 Crystal growth rates

It has been acknowledged that the different morphologies or shapes of ibuprofen crystals are formed by different growth rates of certain faces mediated by the effect of the growth solvent or additives. Hence, the morphology of ibuprofen can be understood through the measurement of growth rate of the individual faces surrounding the ibuprofen crystal. Both theoretical and experimental studies of the morphology have shown that the important faces are the $\{002\}$ and $\{100\}$ faces. Calculation of the relative growth rate using the attachment energy method has shown that attachment at the $\{100\}$ face is the least energetically favourable. Since E_{att} is assumed to be directly proportional to the relative growth rate, $\{100\}$ is predicted to be the slowest growing face, and therefore dominates the theoretical morphology [130]. The theoretical morphology of ibuprofen can be predicted from the intermolecular potential calculations and attachment energy calculations. The experimental morphology can be explained by the relative growth rates of crystal faces of Ibuprofen through the interaction of solvents and growing crystals surfaces obtained from different solvents [5, 136].

So far there have been quite limited studies of this material's crystallisation kinetics. Rashid et al. [15] studied growth rates of ibuprofen crystals grown from ethanol by adding size proportional growth seed crystals to an isothermal non-nucleating batch crystallization vessel and sampling the resultant crystals during the batch. They found that Ibuprofen crystallising from ethanol exhibits significant growth rate dispersion. Cano, et al. [5] measured the growth rates of the $\{100\}$, $\{001\}$ and $\{011\}$ faces in a

single ibuprofen crystal using a crystal-growth flow cell. During these measurements, a crystal was secured within the cell with the crystal faces of the seed crystal being oriented with respect to the solution flow in order to obtain reproducible growth conditions at $\sigma = 0.013$. However, this work did not provide information on the growth rates for spontaneously nucleated crystals nor were variation in the crystal growth rate between different crystals studied.

3.6 Closing Remarks

There are many methods and techniques for crystal growth rate measurement which can be applied for different systems and material models. Despite this, little information has been provided regarding the growth rate at high supersaturations of spontaneously nucleated crystals nor has the growth rate variations of crystal faces between different crystals been studied. There have been several simulation and morphological modelling works for ibuprofen crystal and there is no molecular scale understanding on crystal morphology and the growth rate of individual faces. This PhD was focused on investigating the influence of solvent type (ethanol 95%, ethyl acetate, acetonitrile and toluene) at relative supersaturation σ from 0.55 to 1.3 on the growth rate of the {001} and {011} surfaces of nucleated single (RS)-ibuprofen crystals in a stagnant solution at two crystallizer volume scale-sizes; 0.5 ml and 15ml using a microscopy technique, and the growth mechanisms were assessed through the growth rate data versus supersaturations. Furthermore, molecular modelling, intermolecular bonding analysis and crystal habit surface chemistry analysis and calculation of solvent-mediated attachment energy was examined to enhance the understanding of the observed morphology and effect of solvents on the growth rate of crystal habit faces. The computational and experimental work is presented in chapter 4.

4 Materials, instrumentation and methodology

Summary:

The molecular and crystal structure of ibuprofen, together with a description of the instrumentations and the experiment and computation methods are presented in this chapter.

4.1 Introduction

This chapter describes the material examined in this study and the instrumentation and methodologies employed for its examination. Firstly it presents a brief overview of the physical properties and structure together with the details of molecular and crystallographic modelling and morphological prediction including methodologies for conformational analysis, conformer distribution in solvents and morphological prediction. Next the experimental set-up and methodology used for polymorph screening, solubility measurements, and experimental studies on measuring face growth rates at different scale sizes is presented. The latter includes a 0.5 ml cuvette crystallisation cell, a 15ml jacketed vessel and a 7ml agitated batch vessel (Avantium Crystalline platform).

4.2 Materials

Ibuprofen (melting point 75-77°C, purity \geq 98%) was obtained from Sigma Aldrich and Tokyo Chemical Industry UK Ltd.

Table 4.1 Solvents used in studying polymorphism

Solvents	Purity	Manufacture
Acetone	For residue analysis	Across Organics
Acetonitrile	99.9%	LC-MS
Ethanol	95%	Sigma Aldrich
Ethyl acetate	>99.5%	Acros Organics
Hexane	> 99%	Reagent Plus
Diethyl ether	>99%	Fisher Scientific
Methanol	99.5%	Sigma Aldrich
Toluene	> 99.8%	Sigma Aldrich
Propanol	>99%	Sigma Aldrich
Xylene	> 99%	Sigma Aldrich
Isopropyl ether	> 99%	Acros Organics

The solvents used for the growth rate determinations were: Ethanol 95% (the azeotropic composition of a binary mixture of ethanol and water) from Sigma Aldrich, Ethyl

acetate 99.5% Acros Organics, Acetonitrile 99.9% from LC-MS and anhydrous Toluene 99.8% from Sigma-Aldrich, acetonitrile.

Case study in Pfizer, UK: The material under study was a pharmaceutical compound A. The material was recrystallised and provided by Pfizer. Solvents used in this case study were 2-Methyltetrahydrofuran (2-MeTHF) ($\text{CH}_3\text{C}_4\text{H}_7\text{O}$) from Sigma-Aldrich.

4.3 Computational methods

4.3.1 Conformational analysis

The CONFORMER in Material Studio [142] was employed to analyse the conformational flexibility of the ibuprofen molecule. The molecular structure for an isolated ibuprofen molecule was downloaded from the Cambridge Structure Database (refcode: IBPRAC). Examination of the molecular structure revealed eight significant torsion angles which were examined to investigate the flexibility of ibuprofen as in Figure 4.1.

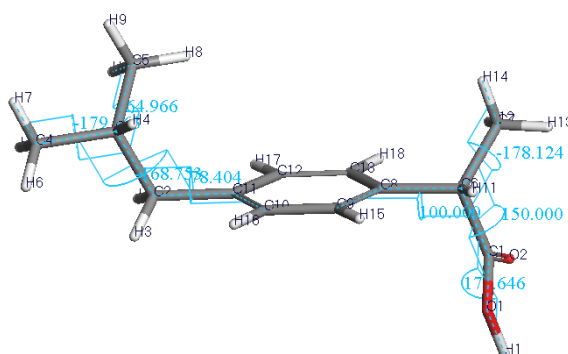


Figure 4.1 Structure of an ibuprofen molecule highlighting the potential torsion angles involved in double bonds and bonds terminated with hydrogen (not including bonds in benzene rings).

In order to have a good representative selection of torsion angles in the ibuprofen structure, an investigation of the extent of flexible torsion angles was carried out using systematic grid search of CONFORMER in Material Studio. The extent of change of the total energy after optimisation was studied when each of the torsion angles was varied from -180 to 180 degrees with step-angle of 20 degrees and the molecular energy profiles were calculated using the Dreiding [143] force field. After selecting representative torsion angles, two torsion angles were varied from -180 to 180 degrees with a step-angle of 10 degrees and the torsion energy was calculated using a molecular

mechanics force field in CONFORMER module in Material Studio. The torsion angles were kept constrained and the rest of molecule was relaxed and optimized. The contour maps (torsion energy maps) for conformational energy of ibuprofen were plotted and the conformers of an ibuprofen molecule before and after geometry optimisation were marked on this energy map. The simple set-up procedure for this conformational search method is shown in Figure 4.2.

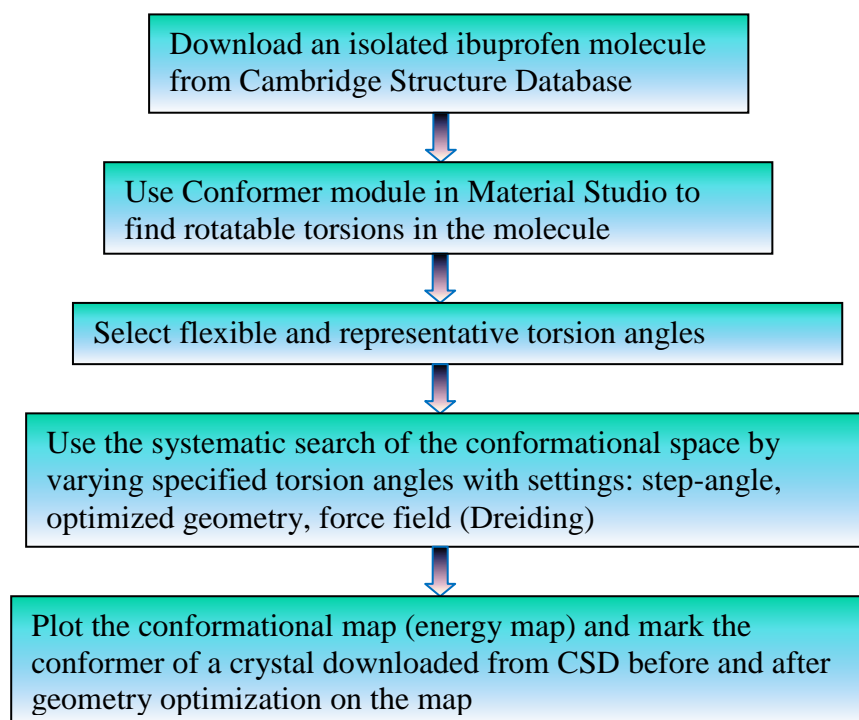


Figure 4.2 Schematic diagram of conformational analysis using CONFORMER in Material Studio.

4.3.2 Conformational propensity as a function of solvents

Ibuprofen conformers were optimised within the COSMO solvent dielectric environment for ethanol, ethyl acetate, acetonitrile and toluene and statistical thermodynamics COSMO-RS calculations were implemented to calculate the population of conformers in the solution. These calculations reveal the preferential conformer structure of the early stage clustering of crystallisation of ibuprofen in these solvents and the important building blocks in the formation of these crystal structures.

The calculation of the propensity of conformers is shown in Figure 4.3. In the first step, a conformational analysis was performed using the CONFORMER software package in

Material Studio in section 4.3.1. After the conformational search was complete, the 10 lowest energy conformations generated were further optimized using aqueous media using GGA/PBE/DNP/COSMO calculations (PBE functional and DNP basis set) in Dmol3 [144] which is a unique density functional theory (DFT) quantum mechanical code. The gradient-corrected potentials are PBE functional (developed by Perdew, Burke and Enzerhof) [145, 146]. The Conductor-like Screening Model (COSMO) [147], a continuum solvation model, was used to analyse the stability of the lowest energy conformers in solution. In the second step, the *.COSMO files generated from Dmol3 were used to calculate the propensity of conformers in ethanol, ethyl acetate, acetonitrile and toluene at 25°C using the COSMOtherm software package [148]. The conformers will be weighted internally by COSMOtherm using their COSMO energies and their chemical potentials. Normalized weight factor of molecule in compound was shown % conformer in mixture of conformer. The equilibrium propensity of conformers was calculated according to:

$$p(i) = \frac{\bar{\omega}(i)\exp\left(-\frac{G(i)}{RT}\right)}{\sum_j \omega(j)\exp\left(-\frac{G(j)}{RT}\right)} \quad (4.1)$$

where $\bar{\omega}(i)$ is a multiplicity of the conformer (i); R is the gas constant; T is the temperature in Kelvin and $G(i)$ is the free energy of conformer (i) in the solution.

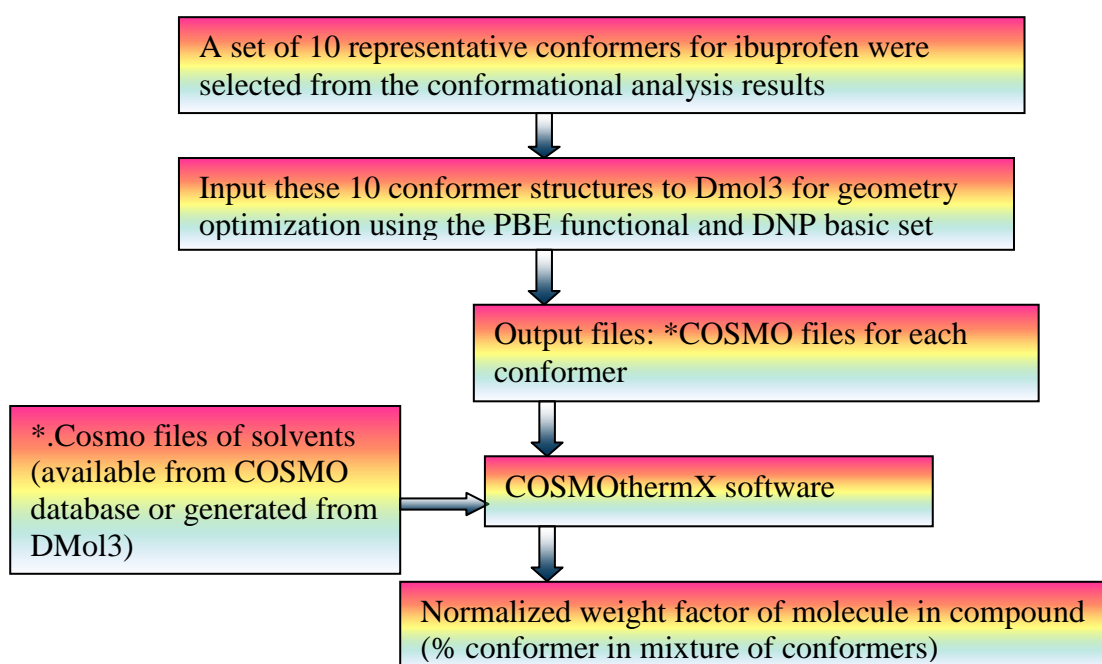


Figure 4.3 Schematic diagram of the examination of the conformer distribution in solvents.

4.3.3 Intermolecular force calculations

The slice and attachment energies were calculated using the program HABIT98 [52] by summing pair-wise the potential energy involved in the intermolecular interactions between a central molecule and all molecules within and outside the slice, respectively. Habit98 can operate in several modes: LATT, FULL etc. with bonding options (0, -1, -2, DM (each intermolecular interaction is assigned a particular number known as DM number)). The LATT mode is used for calculation of lattice energy and the FULL mode is employed for attachment energy calculations associated with morphological prediction.

4.3.3.1 Lattice energy and intrinsic synthon classification

Firstly, molecular crystal structures were downloaded from the CSD containing essential crystallographic data which are used to calculate the partial atomic charges using the semi-empirical quantum mechanics program MOPAC [149]. In order to obtain accurate lattice energy, a suitable potential function is chosen to calculate the intermolecular interactions involved. The force field was selected according to the structure and bonds within the molecule. In this study, the energy of each atom-atom bond is calculated using Momany [50] and Lifson [51] force fields. Lifson force field is a force field which provides partial charges for the carboxylic group and the alkyl chain of the ibuprofen molecule, but there are no parameters and partial charges for the aromatic ring, just considering aromatic portion as aliphatic one. Momany force fields contain only non-bonded terms switching between the van der Waals and the hydrogen bonded terms, depending on the atom-atom distance and the type of the atoms, and a separate electrostatic interactions term. The total crystallisation energy (lattice energy) per mole is calculated by summing the energy of all atom-atom bonds within a certain defined radius and then divided by two. The input file contains crystallography information for calculating the lattice energy at a series of limiting radius of 5, 7, 9, 11, 20, 30, 40 Angstroms. The appropriate potential function chosen is investigated through comparison of the calculated lattice energy with the experimental calculated lattice energy derived from experimental sublimation enthalpy.

$$V_{\text{exp}} = \Delta H_{\text{sub}} - 2RT \quad (4.2)$$

The procedure for morphological prediction is shown in Figure 4.4.

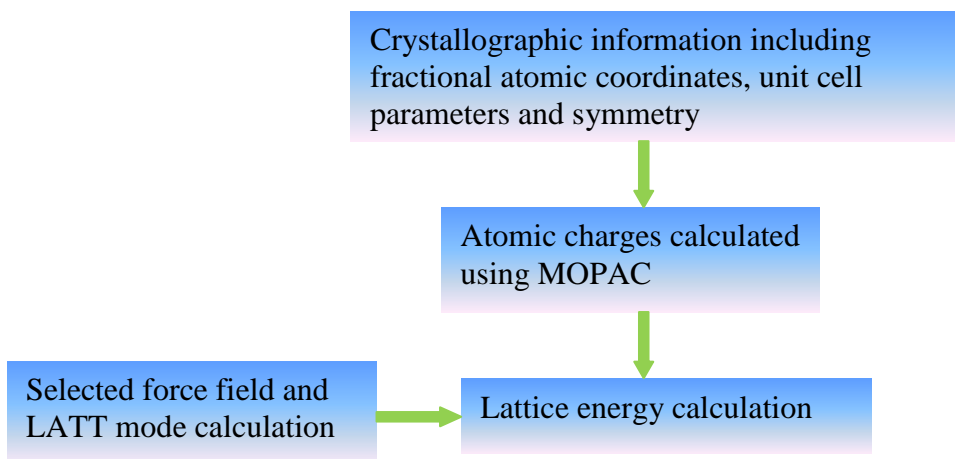


Figure 4.4 Flowchart describing the calculation of lattice energy from crystallographic information.

The examination of the intrinsic synthons, referred to as inter-molecular interactions which take place within a material, was carried out using the bonding options to identify the strong bonds and, particularly constituent atom-atom or atom type contributions.

Bonding (or Debug) analysis -1 in LATT mode was used for the analysis of the intermolecular interactions (its breakdown energy into the attractive, repulsive and electrostatic contributions) in the crystal lattice. The energy contribution of each atom in the lattice energy (%) and its breakdown in each different type and atom-atom pair were also examined by Debug-2.

The bonding analysis -1 in FULL mode was employed to analyse the assignments of the intermolecular bonding (including the direction and strength of these bonds) on each crystal surface. The display of the intermolecular interaction of interest, e.g the strongest bonds or hydrogen bonds associated with dimer formation of carboxylic groups was performed through Debug-DM.

4.3.3.2 Morphological prediction and determination of extrinsic synthons

The attachment energies were calculated for all the dominant crystal faces generated using the geometrical BFDH principle [48, 150, 151] which states that the larger the inter-planar spacing d_{hkl} , the more morphologically important the crystal (hkl) face will be. From this, a number of faces which are most likely to be dominant in the crystal morphology were chosen. The calculated attachment energies related to the relative growth rate of individual faces were used to generate a three-dimensional models of predicted morphology of the crystal using the SHAPE software [152]. The procedure for morphological prediction is shown in Figure 4.5.

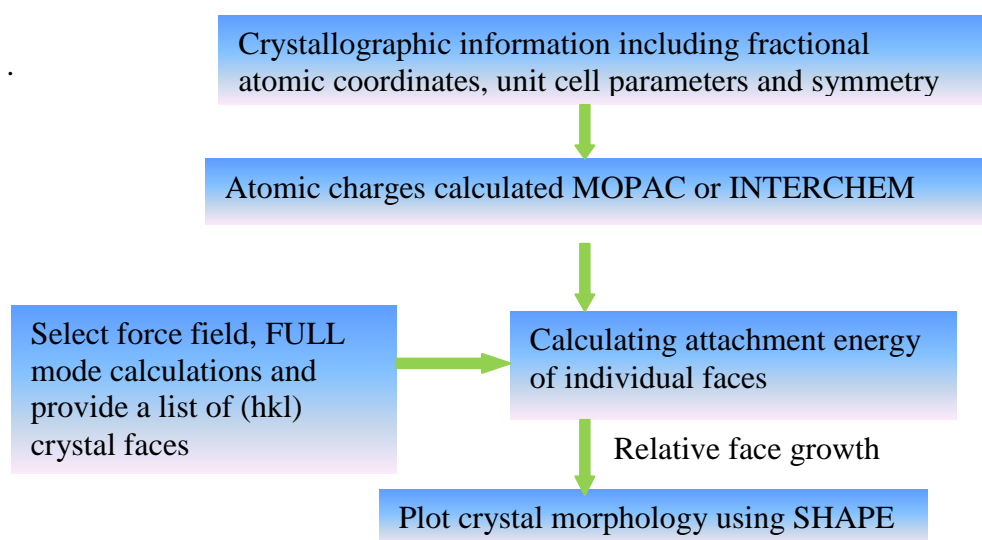


Figure 4.5 Flowchart describing crystal morphology predictions from calculated attachment energies.

Extrinsic synthons referred to as inter-molecular interactions taking place at interfaces of the material were also analysed in this study. Accelrys Material Studio [142] was used for cleaving a crystal in a specific plane to create crystal surface habits. This enabled to examine the molecular arrangement and the properties of the surfaces (e.g. hydrophobicity, polar or hydrogen-bonding) on dominant crystal habit surfaces. The interfacial molecular interaction of ibuprofen-solvent molecules e.g. the potential of the hydrogen bonding formation between solvent molecules and COOH functional groups of ibuprofen was utilised to rationalise the growth rate of the individual crystal surface habits in various solvents.

4.4 Experimental method

4.4.1 Polymorph and solvent screening

Experiments of (RS)-ibuprofen polymorph screening were carried out in a shaker MaxQ 2000 Barnstead/Lab-line with a temperature controlled Julabo F25. A set of slurry solutions of (RS)-ibuprofen in various solvents including polar protic, polar aprotic and non-polar (ethanol, methanol, propanol, ethyl acetate, acetonitrile, acetone, diethyl ether, isopropyl ether, toluene, hexane and xylene) were prepared in vials. These vials were agitated in a shaker for a period of about 2 days. The solutions were heated up to 70°C then cooled down and kept constant at 0°C to recrystallise. The final solutions were dried carefully in a vacuum oven to collect crystals and observe their shape under a light microscope. The DSC data were determined using a differential scanning calorimeter (DSC 820, Mettler) (Figure 4.6). Each sample was heated from 25 to 85°C at 5°C/min in aluminium pans under nitrogen atmosphere. The onsets of the melting points and enthalpies of fusion were determined using STAR^c software.

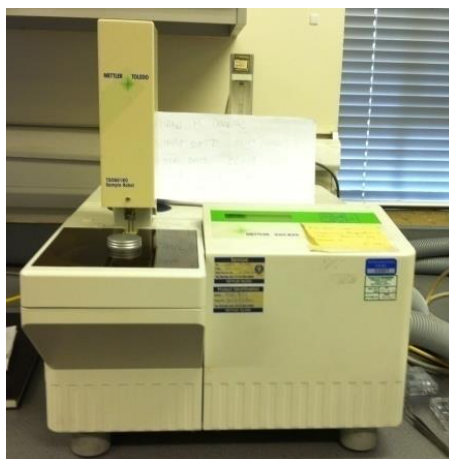


Figure 4.6 DSC 820 Mettler used to determine melting points of ibuprofen recrystallised from series of solvents.

4.4.2 Solubility measurements

4.4.2.1 Equipment

An ATR UV/Vis spectroscopy system comprising a Cary 50 from Varian spectrophotometer and an ATR probe from Hellma Analytics (Figure 4.7) was

employed for solubility determinations of solutions of ibuprofen in all solvents except toluene where gravimetric methods were used. The material of construction of the ATR probe tip is sapphire and the barrel material is made from titanium with an outer diameter of 6.35 mm. This operates at over the wavelength range from 240 - 1100nm and is optimal for the direct measurement of strongly absorbing solutions where standard transmission probes cannot be used. This measurement approach had the advantage: in that it involved no sampling; the solutions need not be diluted; it was applicable for the measurement of high-solids content slurries on-line; and it was easy to set up with a flexible fibre-optics connection to the probe.

Unfortunately the depth of penetration for toluene at the critical angle increases indefinitely at 319 nm so a limiting value of the refractive index is reached at 319 nm [153] and hence this technique could not be used for measurements in toluene and in this case this solubility was determined by gravimetric methods.



Figure 4.7 ATR UV-Vis spectroscopy Cary 50 from Varian employed to measure solubility of ibuprofen. The inset shows the probe.

4.4.2.2 Procedure

A set of saturated solutions with excess, suspended solids of (RS)-ibuprofen in various solvents was prepared in vials and put in a shaker MaxQ 2000 Barnstead/Lab-line with a temperature controlled Julabo F25. The vials were agitated for 24 hours then allowed

to settle for 6 hours to ensure all solids were separated from the saturated solvent. The saturated solutions were separated from solid phase for solubility measurement.

ATR UV-Vis spectroscopy method: Calibration curves were obtained by scanning a series of known concentrations of Ibuprofen in solvents over the wavelength range from 300 to 250nm (the characteristic ibuprofen absorbance peak is at 264nm). Saturated solutions at different temperatures were also scanned to obtain absorbances and hence the solubility of ibuprofen at various temperatures was determined from the calibration curve.

Gravimetric method: One gram of saturated solution at different temperatures 15°C, 20°C, 25°C, 30°C, 35°C was withdrawn and transferred to vials, the solvents were then allowed to evaporate at room temperature for approximately one week until the remaining mass of solid-material was constant with time and then the solubility, expressed in gram of solutes/gram of solvent, was calculated by the equation (g/g_{solvent}).

$$s = \frac{m_{solid}}{1 - m_{solid}} \quad (4.3)$$

4.4.2.3 Data analysis

The ideal solubility of crystalline materials can be calculated by:

$$\ln X = \frac{\Delta H_m}{R} \left(\frac{1}{T_m} - \frac{1}{T} \right) \quad (4.4)$$

where ΔH_m is the enthalpy of fusion and T_m is the melting temperature, obtained from DSC.

For real solutions equation (4.4) is not valid and the van't Hoff equation provides the enthalpy and entropy of dissolution through the plots of $\ln X$ versus $1/T$:

$$\ln X = -\frac{\Delta H_{dis}}{RT} + \frac{\Delta S_{dis}}{R} \quad (4.5)$$

where X is the mole fraction of solute in solution; ΔH_{dis} and ΔS_{dis} are the enthalpy and entropy of dissolution, respectively; T is the temperature of solution; T_m is the melting point of the solute; and R is the gas constant.

According to Raoult's law, the activity coefficient of the solute in the saturated solution, γ_i^{sat} , is defined as:

$$a_i^{sat} = x_i^{sat} \gamma_i^{sat} \quad (4.6)$$

where a_i^{sat} is the activity of the solute i in the saturated solution and is given by:

$$a_i^{sat}(T) = \exp \left[\frac{\Delta H}{R} \left(\frac{1}{T_{fus}} - \frac{1}{T} \right) \right] \quad (4.7)$$

where x_i^{sat} denotes the mole fraction experimental solubility; T_{fus} and ΔH_{fus} obtained from DSC in section 4.4.1.

Activity coefficients are calculated from the ratio of ideal solubility at a given temperature and the experimentally measured solubility at that temperature. The logarithm of activity coefficient γ in ethanol 95%, ethyl acetate, acetonitrile and toluene versus saturation temperature T can be fitted as:

$$\ln \gamma = aT + b \quad (4.8)$$

4.4.3 Polythermal and isothermal crystallisation

4.4.3.1 Equipment

The Avantium Crystalline platform consists of a multi-reactor crystallisation platform which can fit 7ml crystallisers equipped with three-blade marine impeller (34 x 10 mm) and overhead and bottom magnetic stirring (8 independent temperature blocks from -15°C up to 150°C controlled by a microprocessor controlling a heat and peltier element. Crystalline provides an inlet for a dry purge gas (typically nitrogen) to prevent condensation on the reactor blocks and electronics (Figure 4.8). The high quality digital visualisation probes are independent of each other, and can be synchronised with the turbidity measurements and temperature profile of each independent reactor.

In this equipment, there are 2 blocks equipped with a 2.0 x magnification lens and 1 block equipped with a 1.0x magnification lens. There are two operation modes: standard

mode (only temperature and turbidity probe) and particle viewer (temperature, turbidity and camera for on-line particle viewing).

For these experiments to measure MSZW, the blocks were only operated in standard mode to record the temperature and turbidity of solutions.

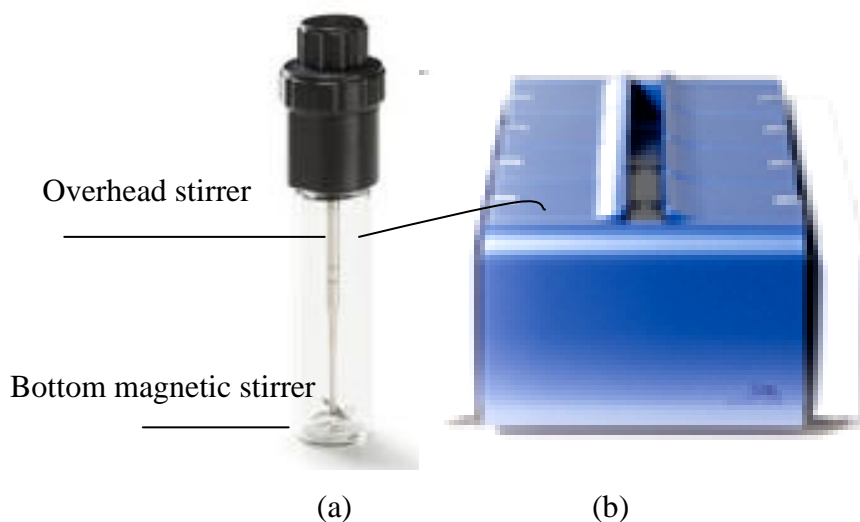


Figure 4.8 (a) A 7ml crystalliser with overhead and bottom magnetic stirring which can be fitted in blocks of Avantium Crystalline platforms ; (b) Multi-reactor Avantium Crystalline platforms with parallel 7ml crystallizers with overhead and bottom stirring [154]

4.4.3.2 Procedure

The MSWZ studies were carried out for solutions in ethanol 95% (1.4g/ml and 0.98g/ml), ethyl acetate (0.72 g/ml) and acetonitrile (0.28g/ml) and toluene (0.65g/ml). Solutions were heated to 50°C at various heating/cooling rates ranging from 0.1- 0.5 °C/min. The system was held at 50°C for 30 mins and cooled to -15°C at the specific heating/cooling rate with a stirring speed of 500 rpm overhead and 100rpm bottom stirred throughout the experiment. These runs were repeated from 3-4 times for each cooling rate.

The induction time determinations were carried out for solutions in ethanol 95% (1.4g/ml), ethyl acetate (0.98 g/ml) and acetonitrile (0.40 g/ml) and toluene (0.87 g/ml). The vials were stirred at a stirring speed of 500 rpm overhead and 100 rpm bottom stirred throughout the experiment and were heated at 55°C and held for 30 mins to make sure that the crystals were dissolved. The solution was drastically cooled to the desired

temperature at a rate of 20°C/min and kept constant at that temperature until the onset of nucleation. The time at which the solution reached the saturated temperature was set as time zero. The percentage of the light transmission decreased at the onset of nucleation and the difference between the time at which the transmittance started to decrease and time zero was recorded as the induction time, τ_{ind} . Several runs were repeated from 4-8 times for consistency and reproducibility of the results.

4.4.3.3 Data analysis

The dissolution and crystallisation temperatures were obtained at the different heating/cooling rates. Figure 4.9 shows an example of a turbidimetric profile for polythermal studies: (a) transmittance and temperature as a function of time and (b) a plot of transmittance as a function of temperature. The temperature of crystallisation is determined at the point at which the transmittance starts to drop significantly.

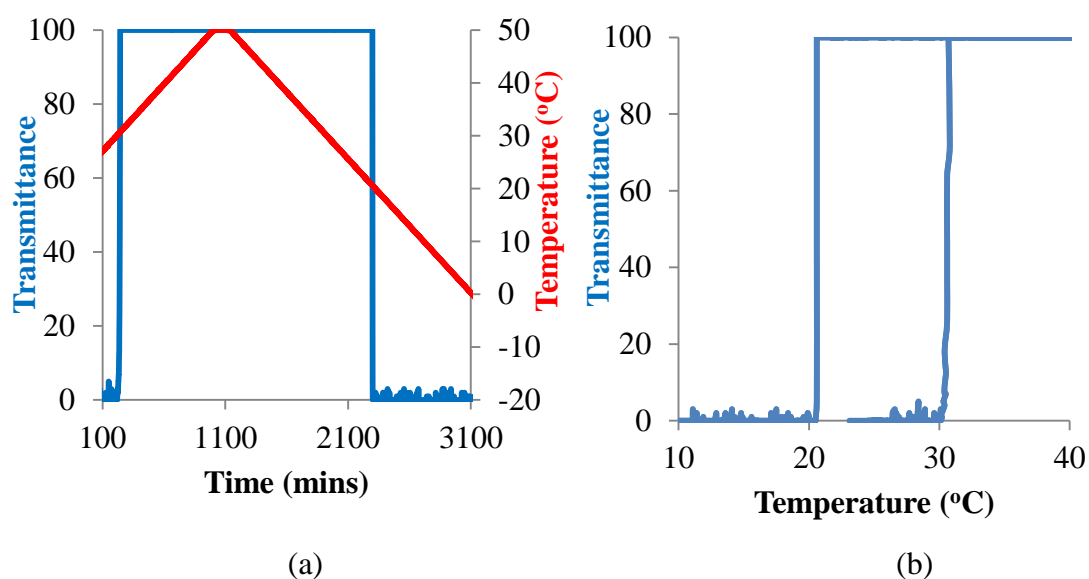


Figure 4.9 A sample turbidimetric profile for polythermal studies of 0.72g/ml of ibuprofen in ethyl acetate at the heating/cooling rate 0.1C/min: the transmittance and temperature as a function of time (a); plot of the transmittance as a function of temperature (b). From these plots, temperature of dissolution and temperature of crystallisation at different heating/cooling rates were investigated.

The equilibrium MSZW is the difference between the dissolution and crystallisation temperature and it was obtained at infinitely slow cooling rate. The dissolution

temperature (T_{dis}) and crystallisation temperature (T_{crys}) versus heating/cooling rate was plotted and T_{dis} and T_{crys} extrapolated at $0^\circ\text{C}/\text{min}$ to estimate the MSZW.

$$MSZW = T_{dis} - T_{crys} \quad (4.9)$$

The order of the nucleation (m), reflecting the cooling rate dependence of the process was determined using Nyvlt's equation

$$\log b = (m - 1) \log \frac{dc}{dt} - \log \varepsilon + \log k_n + m \log \Delta T_{max} \quad (4.10)$$

where b is cooling rate, m is the order of nucleation; c is the equilibrium concentration; k_n is the nucleation rate constant, ε is associated with the molecular weight and ΔT_{max} is the MSZW.

Plotting $\log b$ against $\log \Delta t_{max}$ yields a straight line with slope equal to the order of nucleation m . The nucleation rate constant can be obtained from the intercept value.

Induction time is a parameter measuring the metastability of the crystallisation system like the MSZW of slow cooling. The induction time is considered as the time elapsed between the achievement of saturation and the appearance of the first crystals (see Figure 4.10).

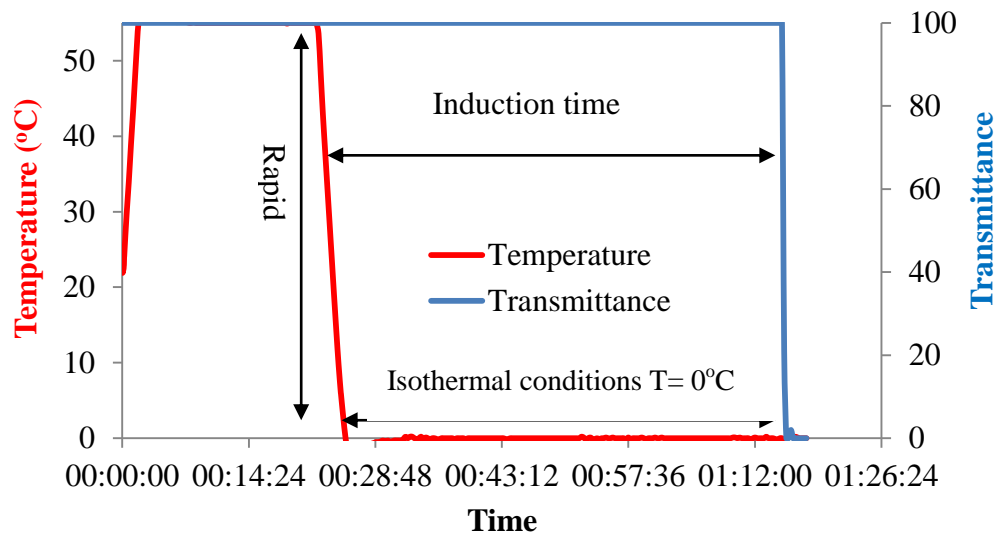


Figure 4.10 An example of isothermal crystallisation for ibuprofen crystallising from acetonitrile: Induction time is the period of time between the solution being saturated at a given temperature and the appearance of first nuclei of ibuprofen (the transmittance drops indicating the onset of crystallisation).

The interfacial energy was calculated using classical nucleation theory

$$\ln\tau = \left[\frac{16\pi\gamma^3\vartheta^2}{3k^3T^3(\ln\sigma)^2} \right] - \ln A \quad (4.11)$$

The slope of the straight line plot of $\ln(\tau)$ vs. $1/T^3(\ln\sigma)^2$ was used to determine the interfacial energy/tension.

The radius of a critical nucleus can be derived by the equation

$$r^* = \frac{2k_A\vartheta\gamma}{3k_v k T \ln S} \quad (4.12)$$

where the shape factors are $k_A = 4\pi$ and $k_v = 4\pi/3$ for the spherical nuclei.

4.4.4 Single crystal growth rate measurements

4.4.4.1 Equipment

The diagram of instrumentation employed in this study is shown in Figure 4.11.

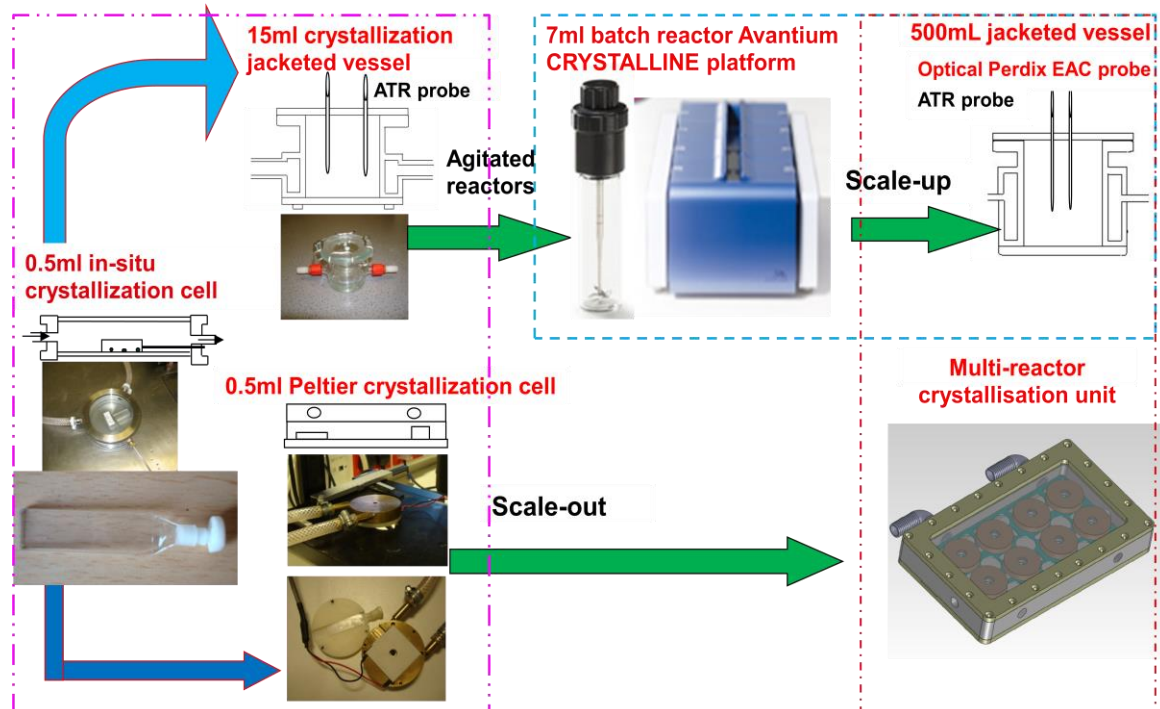


Figure 4.11 Diagram of scale-up crystallisation instrumentation for measurement of crystal growth rate at single particle level (pink block); for measurement of crystal growth rate in a population of crystals (blue block).

The growth rates of faces habit planes $\{001\}$ and $\{011\}$ for individual single crystals as a function of the growth solvent used and the solution supersaturation were measured at two scale sizes: a 0.5ml crystallisation cuvette cell (Figure 4.12) and a 15ml jacketed-vessel (Figure 4.13). The crystallisation setup employed for this comprises an inverted optical polarizing microscope (Olympus Optical IMT-2 or Leica/ Leitz DM IL 090-131-002) integrated with a CCD Lumenera Infinity 3.3 megapixel camera, a PC with Image Capture and Image Analyze Software to capture pictures during crystal growth. The crystallisation vessels comprised of:

- A UV cuvette cell 0.5ml (54 x 10 x 1 mm) submerged in a shallow tank of water whose temperature was controlled by a Haake F3 recirculation bath.
- A 15ml jacketed vessel (34 (mm) ID diameter x 17(mm) height), with flat optical glass discs at the top and the bottom connected to a Huber ministat chiller. The jacketed vessel was equipped with an ATR UV/Vis spectrometer immersion probe to monitor the solution concentration and hence the level of supersaturation during crystallisation.

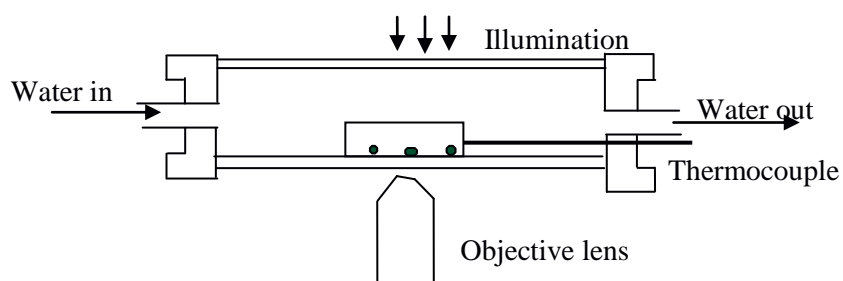


Figure 4.12 Prototype cell for measurement growth rate of individual faces of ibuprofen.

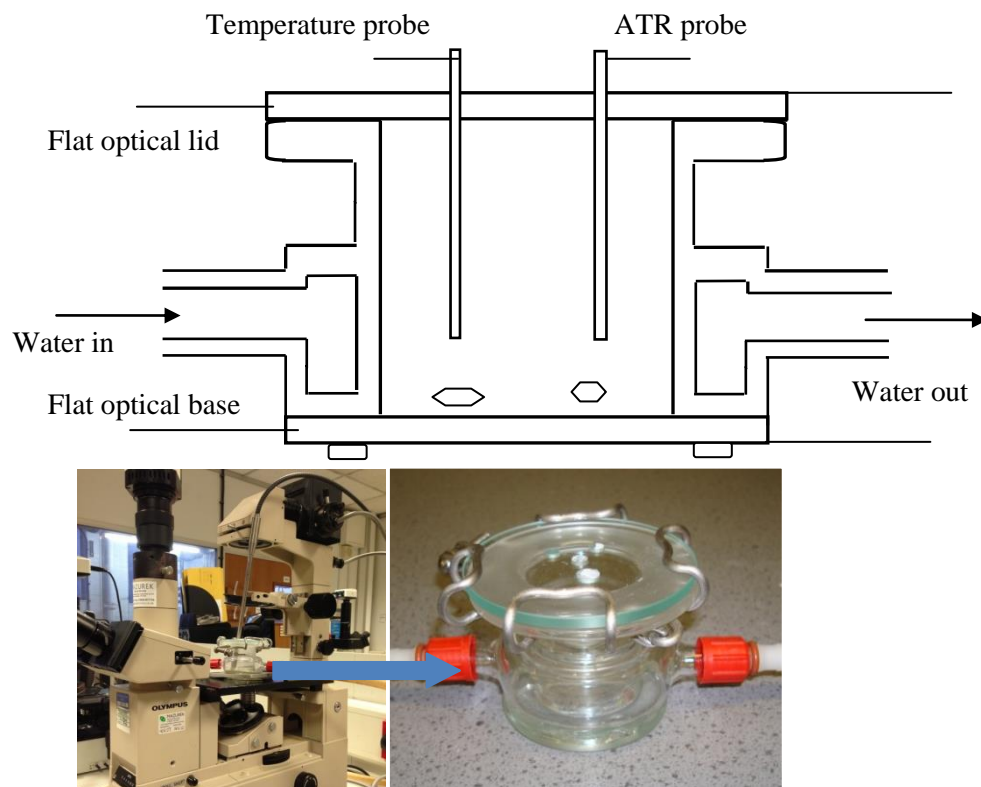


Figure 4.13 Crystallisation system set up for measurement of crystal growth rate in a 15ml jacketed vessel.

4.4.4.2 Procedure

RS-ibuprofen solutions were prepared by dissolving solute in ethanol 95% (1.4g/ml), ethyl acetate (1g/ml), acetonitrile (0.4g/ml) and toluene (0.87g/ml).

For the 0.5ml scale, a pipette was used to transfer the prepared solution into the cuvette cell which was sealed and fixed to the bottom of the water tank.

For the 15ml scale, the prepared solution was transferred into the vessel.

The ibuprofen/solvent solutions were heated to 50°C to completely dissolve all ibuprofen crystals, then the solutions were cooled down to a constant temperature such as 20, 23, 25 and 27°C to maintain a specific supersaturation as monitoring using ATR UV/Vis spectroscopy and the system was monitored until crystals were found to appear. The Image Analyze Software was used to capture a temporal sequence of images of the crystals as they developed.

Procedure for growth rate measurement for a case study in Pfizer: The cuvette cell was employed to study the morphology of this compound in pure 2-MeTHF and a mixture of 99% of 2-MeTHF and 1% of water. Compound A solutions were prepared by dissolving compound A in 2-MeTHF (30mg/ml) and in a mixture of 99% 2-MeTHF 1% and water (18mg/ml). The prepared solution was transferred into the 0.5ml glass cuvette crystallisation cell immersed in a tank of water. This cuvette was sealed and secured at the bottom of the glass surface of the water tank, whose temperature was controlled using a Huber recirculation bath.

The solutions were heated to 40°C to completely dissolve the solid material, and then the solutions were cooled down to a set temperature corresponding to a specific supersaturation level and held the temperature constant. The experiments were carried out in 2 conditions: (a) in a stagnant condition (the cuvette cell was placed at a fixed position in the water tank, without tilting or shaking) or (b) in a turbulent condition (the cuvette cell was placed at a fixed position in the water tank, with random tilting or shaking to accelerate the nucleation). When crystals are nucleated and grown, an inverted, polarizing video microscope Carl Zeiss together with the Image Capture and Image Analyze Software was used to capture a sequence of images of the crystals in order to observe morphology and determine the growth rate of crystals along the length (longer direction) and the width (shorter direction).

4.4.4.3 Image analysis

The dominant faces of ibuprofen crystals can be indexed by comparing the predicted morphology and experimental morphology. A titled predicted morphology for ibuprofen showing the {011} and {111} are oriented in the similar direction. The crystal is lying flat on one of its {100} faces therefore it is impossible to state whether the {111} face is present in the experimental morphology or not. However, the {011} face is much more dominant compared to the {111} face so it is reasonable to assume the growth rate in b direction was measured for the {011} face.

The growth rates of faces {001} and {011} were measured using two different methods as shown schematically in Figure 4.14.

- Either the length of a line from the centre of the crystal and perpendicular to the projection of the crystal edges for (001) or (00-1) and (011) or (0-11) or (01-1) or (0-1-1) faces (assuming crystals are symmetric was measured).
- Or the separation distance between two opposite parallel faces of crystals was measured and then divided by two.

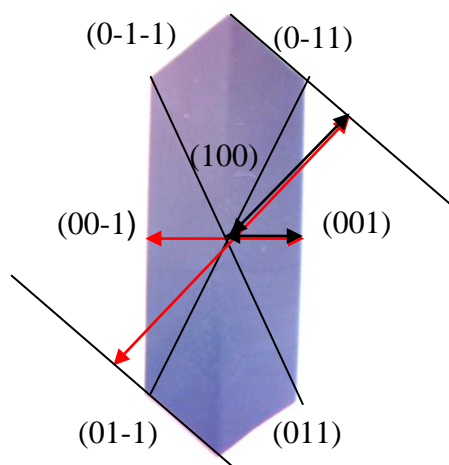


Figure 4.14 Image of crystal with overlaid annotations highlighting the methodology for the measurement of growth rate of the individual faces.

Assuming the crystal is lying flat on one of its {100} faces, the in-plane measurements were geometrically corrected with the aid of MORANG [155] to allow for the tilt of the {001} and {011} planes (80.64° and 84.42° respectively) with respect to the sample's dominant {100} habit plane to be taken into account. Because the face is slightly tilted, it is seen as an area rather than a single line. Therefore, the edge of the face needs to be chosen consistently for a series of crystals. Growth rates of crystal faces were determined by capturing images at user-defined time-intervals (typically ranging 1-10 minutes, depending on the growth rate) and then by plotting the distance from the centre of the crystals to the faces as a function of time. The slope of the line corresponds to the measured growth rate of the face. Mean growth rates, together with standard deviations, were obtained from between five to eight growth rate measurements on individual single crystals under equivalent conditions. The coefficient of variation for the growth rate of each crystal face in each solvent and two scale-sizes was calculated by the standard deviation divided by the growth rate of the crystal faces.

4.4.4.4 Growth mechanism investigation

The growth mechanism was assessed through user-defined fitting functions using the appropriate growth kinetic models. Birth and Spread (equation 3.6) and BCF (equation 3.7) to plots of mean growth rate versus range of supersaturation to evaluate which model gives the better fit. Data fitting was carried out using nonlinear curve-fitting in Origin [156]. The quality of regression was measured by the coefficient of determination R^2 . In this, if the value of adjusted R^2 (adj. R^2) is found to be close to 1, the plot calculation can be regarded as being very strong, i.e. showing a high degree of confidence in the regression model. The adj. R^2 can be negative when the fit is poor [156].

4.4.5 Comparison of the growth rate in non-agitated vessel and in agitated-vessel

There were two techniques used to measure the growth rate of ibuprofen crystal in ethanol in this section. In the first technique, the growth rate of number of crystals in agitated reactors as a function of supersaturation. Crystal size was analysed by Image analysis software. The diameter of the particle was then calculated as a diameter of a sphere with equivalent area. In the second technique, the growth rate of individual crystals was estimated by direct observation from an inverted microscope.

4.4.5.1 Growth rate measurement in agitated vessel using Avantium platforms

These growth rate measurements in agitated reactors were carried out in The Avantium Crystalline platform (see Figure 4.8). For these particle size measurements, the 2 blocks quipped with a camera (2x magnification lens) were employed and the system was operated in particle viewer mode (temperature, turbidity and camera for on-line particle viewing).

The growth rate of ibuprofen was determined from seeded batch saturated solutions. 0.98g/ml ($T_{\text{sat}} \approx 30^\circ\text{C}$) of ibuprofen in ethanol 95% was prepared. The prepared vials were placed in the CRYSTALLINE and were heated 10°C above the saturation temperature for an hour. The temperature was then brought down to 27°C and 28°C with

10°C/min cooling rate and after 20 minutes the ibuprofen seed crystals were added to the vials and the system was left at constant temperatures. The images were obtained at every 5-15 seconds and analysed using Process Image Analysis Expert [157] software in order to obtain particle size distribution and hence the overall crystal growth rates.

A fundamental limitation of image analysis reflects the difficulty in terms of segmenting crystal images from the diffuse background presented from within a concentrated solution. The image analysis software calculates the diameter of a circle that has the same number of pixels detected for the particle, and is referred to as an area equivalent diameter. The supersaturation ratios used were 0.157 and 0.105.

This was done by calculating the area of the crystal and converting into area equivalent diameter of a circle.

4.4.5.2 Growth rate measurement in non-agitated vessel using microscopy

The growth rates of faces and of single crystals as a function of solvents and supersaturation were measured using a 15 mL jacketed-vessel which was connected to a Huber Ministat circulation water bath to control the temperature of the solution (Figure 4.13).

The growth rate of ibuprofen in ethanol was determined from seeded batch undersaturated solutions. 7ml of ibuprofen in ethanol at concentration 0.98g/ml was prepared and transferred into the vessel. Solutions were kept at a constant temperature 27°C and 28°C in 30 minutes to ensure the temperature of solution was homogenous. Seed crystals were introduced to a stagnant solution in a 7mL jacketed vessel. When seed crystals were grown, an inverted, polarizing video microscope together with the Image Capture and Image Analyze Software was used to capture a sequence of images of the crystals in order to analyse the overall growth rate. At each supersaturation, each experiment was repeated twice to check the reproducibility of the data.

In order to obtain crystal growth rate, further analysis described below must be followed on each captured image. Firstly, the centre of a crystal is defined by drawing two

diagonal lines from two adjacent corners to the opposite end. Then the distance from the centre of the crystal to the specific faces were measured by drawing lines perpendicular to each face (Figure 4.15).

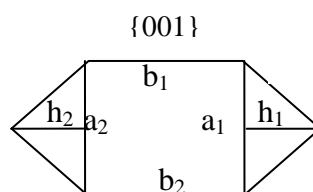


Figure 4.15 Sketch for the calculation of an area of a crystal; from this the equivalent diameter can be calculated.

The area of a crystal can be calculated by

$$A = \frac{1}{2} * a_1 * h_1 + \frac{1}{2} * a_2 * h_2 + \left[\frac{1}{2} (a_1 + a_2) \right] * \left[\frac{1}{2} (b_1 + b_2) \right] \quad (4.13)$$

From the calculated area of crystals during the period of time, the overall growth rate (equivalent diameter) can be estimated.

4.5 Conclusions

This chapter shows materials used in this study together with a general description of its crystal and molecular structures, the instrumentation and methods for computational and experimental works were presented in this chapter.

The basic computational method for crystal morphological prediction using the attachment energy method together with intermolecular bonding analysis of the important faces; conformational population in different solvents and solvent-mediated effect on crystal morphology are summarized in this chapter.

The experimental crystallisation study involved polymorph screening, solubility measurements, MSZW determination, and a study of the growth rate of individual faces of ibuprofen as a function of solvent type, supersaturation and scale-sizes. The methods for the nucleation kinetics of ibuprofen in ethanol, ethyl acetate, toluene and acetonitrile were examined MSZW and induction time measurements were presented. The measurement of crystal growth rate for the {001} and {011} face were performed in a

0.5ml cuvette crystallisation cell and a 15mL jacketed vessel. In addition, the methodology for measuring the overall growth rate of single crystals in stagnant solution compared to the data recorded on the population of crystals crystallised in an agitated 7ml reactor are presented.

5 Modelling the molecular and crystallography structure and its mediation by its solution state environment

Summary:

This chapter presents the outcomes of molecular modelling including conformational analysis for an isolated ibuprofen molecule, morphological prediction with both monomer and dimers as the growth unit and intermolecular bonding analysis on the dominant faces {100}, {001} and {011}.

5.1 Introduction

Computer modelling based on crystal structures offers a powerful technique for assessing the correlation between crystal structures, conformational energy space of a molecule, crystallising conditions and crystal morphology and shape. The purpose of the work in this chapter, therefore, is to link the subsequent chapters involving polymorphism screening crystal morphology observations and crystal growth rate of individual faces in various solvents (in chapter 7). This involves the analysis of conformational flexibility as related to polymorphism, the prediction of the theoretical morphology using BFDH and attachment energy models using HABIT simulations, and to compare these observations with experimentally derived morphologies aided by a detail analysis of the including intermolecular interactions both within the bulk structure and on the crystal habit faces. This is complemented by molecular-scale visualization of the bulk and surface chemistry. The morphological predictions of solvent-mediated morphologies are compared with the *in-situ* observations of ibuprofen crystal morphology in various solvents. The theory behind these calculations is given in chapter 2 and methodology is given in chapter 4.

5.2 Conformational analysis for a free ibuprofen molecule

Conformer analysis of the torsions using Materials Studio revealed eight potential torsion angles including double bonds and bonds with terminal hydrogen atoms (disregarding bonds in the benzene rings) in a free ibuprofen molecule. To investigate and select the most flexible torsion angles associated with significant energy changes, the energy of the molecule when rotating each torsion angle are shown in Table 5.1.

Table 5.1 Total energy changed when rotating each torsion angle using the Conformer module in Material Studio

Torsion angles	Atoms involved in torsion angle	E_{\min} and E_{\max} (kcal/mol)
T1	C2-C3-C4-H7	27.06
T2	C2-C3-C5-H10	27.06 - 31.12
T3	C11-C2-C3-C4	27.07 - 33.23
T4	C10-C11-C2-C3	27.24 - 33.03
T5	C9-C8-C6-C1	27.35 - 32.27
T6	C1-C6-C7-H14	27.06 - 31.17
T7	C7-C6-C1-O1	27.04 - 28.8
T8	C6-C1-O1-H1	27.06 - 52.24

This initial analysis revealed that four of these torsion angle rotations, T3, T4, T5 and T8 resulted in the greatest change of energy. These were selected to characterise the conformational flexibility of ibuprofen. An example of the molecular structure reveals: T3 affects the twist of the carbon chain, T4 and T5 involve a twist of the carbon chain with respect to the benzene ring and T8 is associated with the orientation of the carboxylic group with respect to the carbon chain (Figure 5.1). Based on this, torsion energy maps were built and are shown in Figure 5.3. Ibuprofen molecules with measured torsion angles T3, T4, T5 and T8 before and after geometry optimisation are shown in Table 5.2.

Table 5.2 Measured torsion angles T3, T4, T5 and T8 from the structure of an ibuprofen molecule before and after geometry optimisation, which were used to mark on the energy map

	Torsion angles	T3	T4	T5	T8
RS-ibuprofen	Before Optimization	-168.7	78.0	96.5	176.6
	After optimization	-173.6	68.1	114.6	-179.7
S-ibuprofen	Molecule 1	-170.3	86.0	92.5	175.5
	Molecule 2	171.5	-79.1	-95.0	-172.5

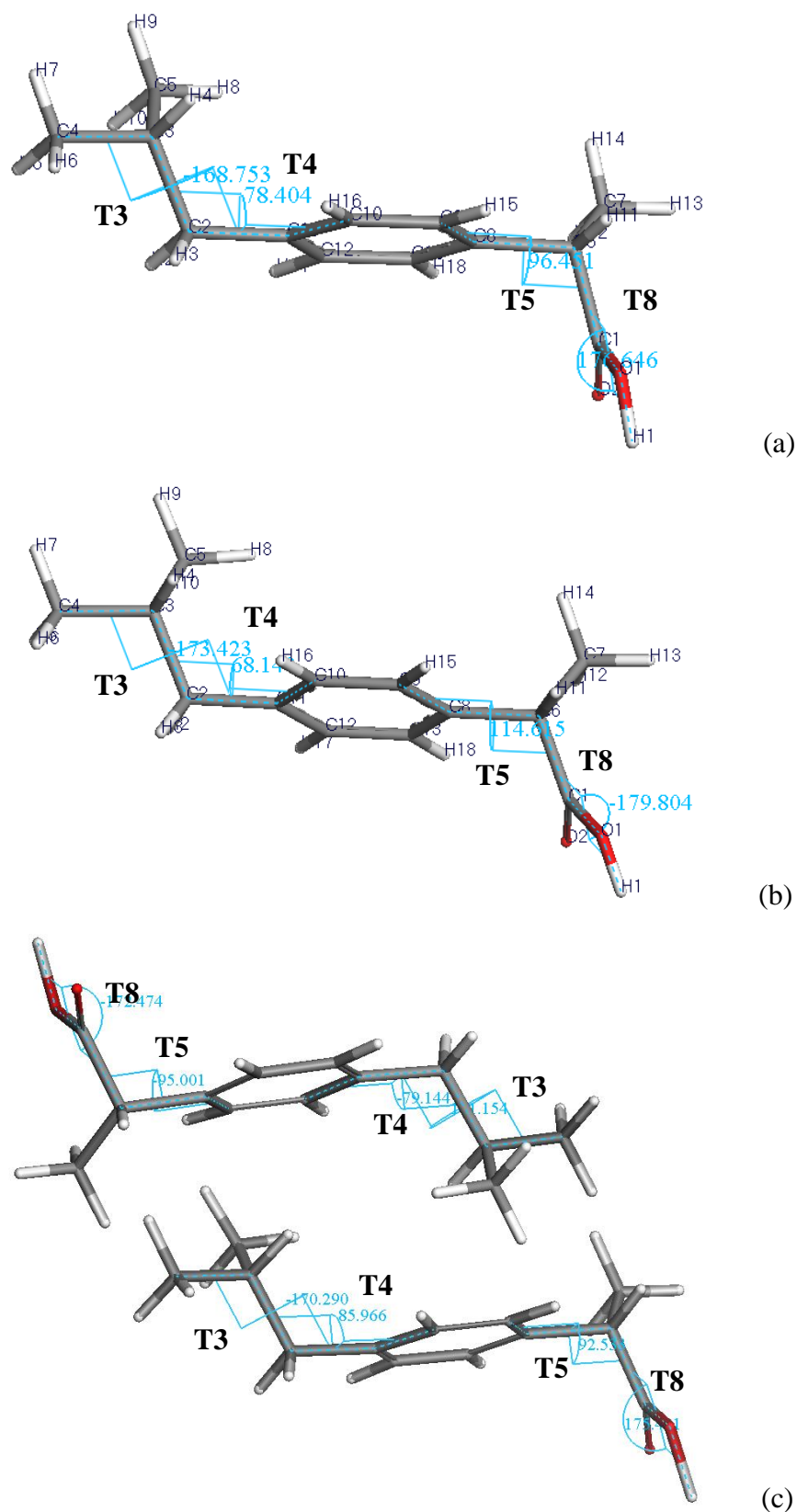


Figure 5.1 RS-ibuprofen molecules with measured torsion angles T3, T4, T5 and T8 (a) before geometry optimization; (b) after geometry optimization and (c) S-ibuprofen molecules.

The study reveals the not so surprising result that ibuprofen is not a very flexible molecule. This is shown by the fact that the torsion angles, before and after geometry optimization, do not change significantly, for example, the torsion angle T3 changed from -168.7° to -173.6° , T4 from 78° to 68° etc. in which the total energy of the molecule decrease to its lowest value (Figure 5.2).

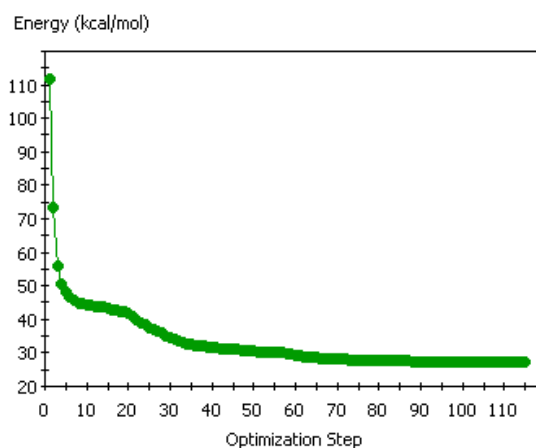


Figure 5.2 Energy minimisation using the Geometry Optimization in Material Studio.

The effect of conformational change on the molecular energy of ibuprofen is summarized in table 5.1. The range of energy change (kcal/mol) when rotating these torsion angles (T3-T4), (T3-T5), (T3-T8), (T4-T5), (T4-T8) and (T5-T8) from -180 to 180 degree is shown in Table 5.3 and Figure 5.3 (a, b,c, d, e, f).

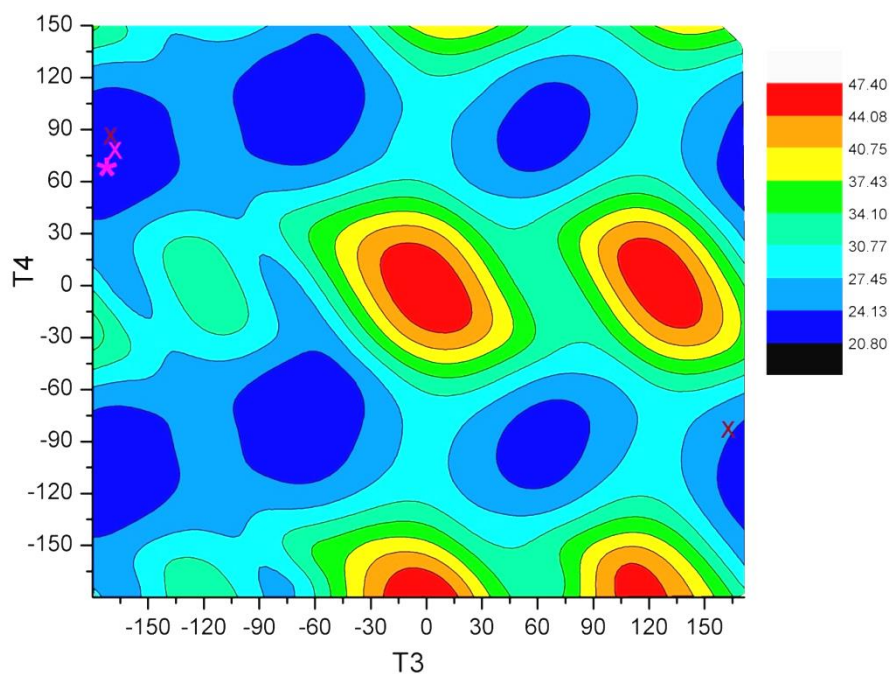
Table 5.3 Energy change when rotating two torsion angles (T3-T4), (T3-T5), (T3-T8), (T4-T5), (T4-T8) and (T5-T8) from -180 to 180 degree (kcal/mol)

Torsion angle	E_{\min} and E_{\max} (kcal/mol)
T3-T4	21 - 48
T3-T5	29.8 - 41
T3-T8	30- 60
T4-T5	29.8 - 4.2
T4-T8	30 – 60
T5-T8	29.8 - 35.0

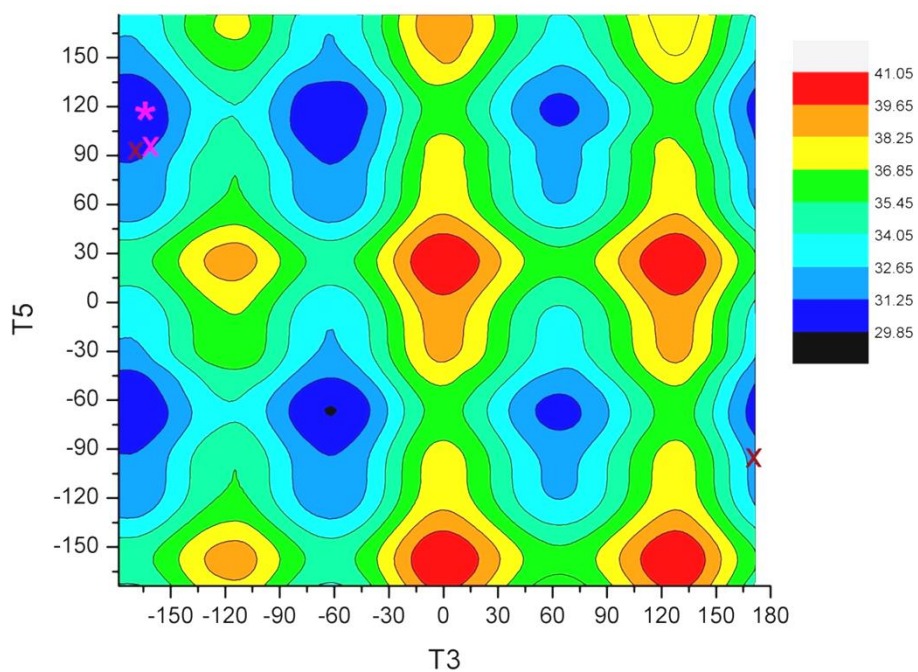
x: Racemic-ibuprofen molecule (1 molecule in asymmetric unit) before optimisation

*: Racemic-ibuprofen molecule after optimisation

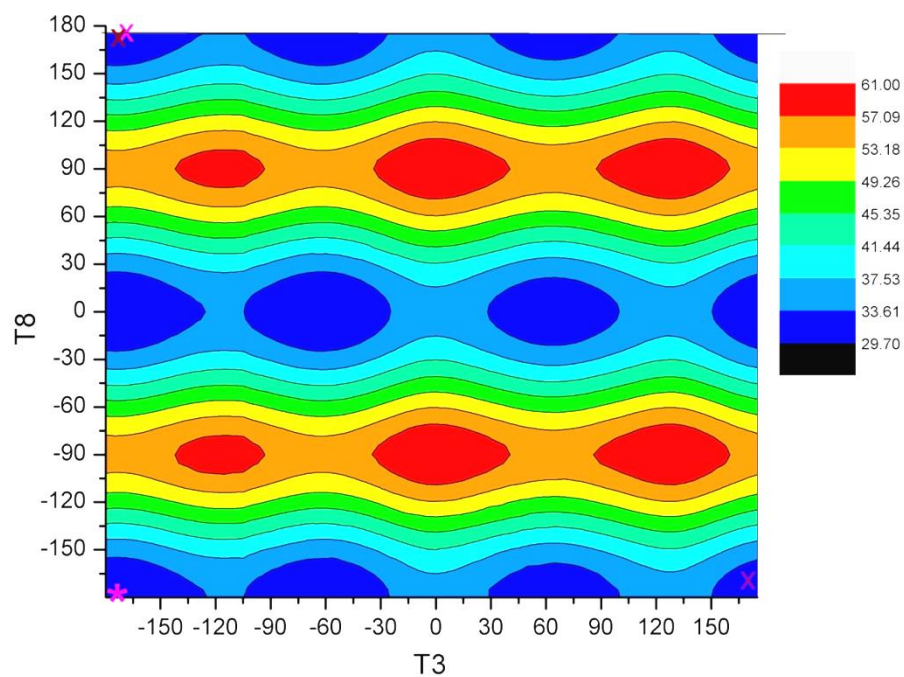
x: S-ibuprofen molecules (2 molecules in asymmetric unit)



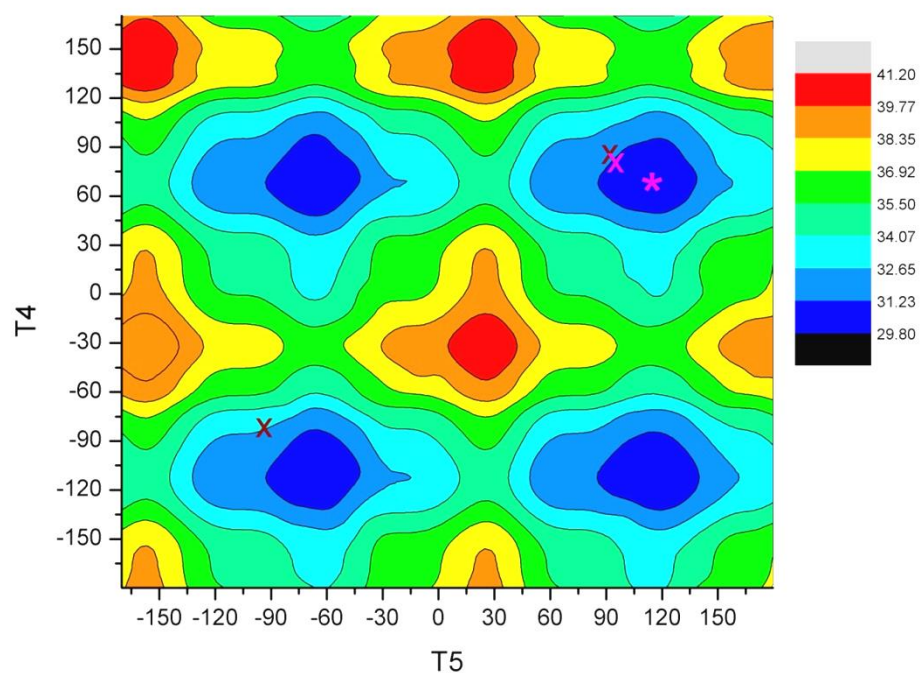
(a) The torsion angle T3 (C11-C2-C3-C4) and T4 (C10-C11-C2-C3) reflects the conformation of the carbon chain.



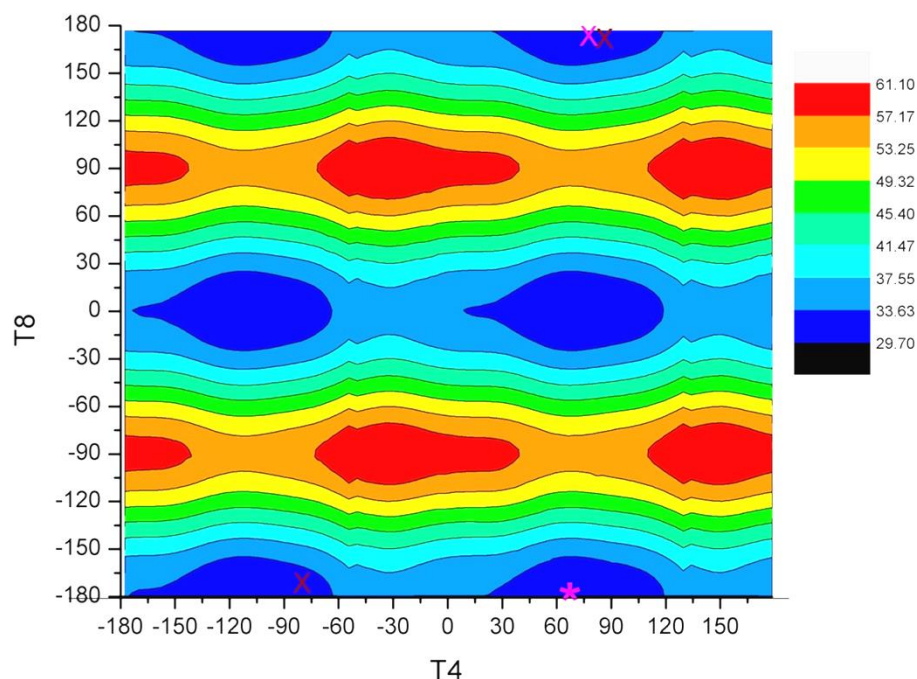
(b) The torsion angle (T3) and (T5) reflects the twist of the carbon chain which is involved in C4-C3-C2-C11 and C9-C8-C6-C1.



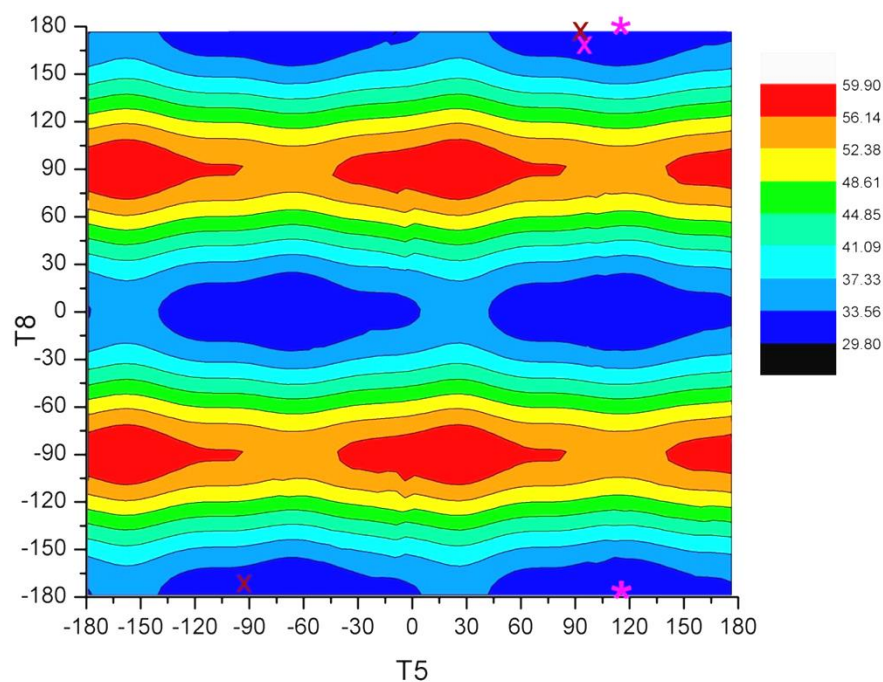
(c) T3 (C11-C2-C3-C4) reflects the conformation of the carbon chain and T8 (C6-C1-O1-H1) is a torsion angle associated with the position of the carboxylic group with respect to the carbon chain.



(d) T4 (C10-C11-C2-C3) and T5 (C9-C8-C6-C1) reflect the twist of the carbon chain with the benzene ring.



(e) T4 (C10-C11-C2-C3) reflects the twist of the carbon chain with the benzene ring and T8 (C6-C1-O1-H1) is a torsion angle associated with the position of the carboxylic group with respect to the carbon chain.



(f) T5 (C10-C11-C2-C3) reflects the twist of the carbon chain with the benzene ring and T8 (C6-C1-O1-H1) is a torsion angle associated with the position of the carboxylic group with respect to the carbon chain.

Figure 5.3 Energy map of a free ibuprofen molecule together with marked torsion angles for an isolated racemate-ibuprofen molecule before and after geometry optimization and S-ibuprofen molecules.

The torsion energy map shows that the crystal structure downloaded from the database before and after geometry optimisation was marked in the torsion energy minimum of a free molecule. The success of this method in mapping out the favoured conformational space of the molecule which was studied and assessed by comparing CONFORMER search output with the minimum conformational energy on an isolated ibuprofen molecule. The values of the two torsion angles of the ibuprofen molecule were marked on this map indicating the torsion angles for molecules in the crystal structure (observed structure) which is close to the calculated torsion energy minimum. This is consistent with there being little recorded evidence for polymorphism in this material when recrystallised at non-extreme conditions. It is in good agreement to published literature.

In this study, the BFDH and attachment energy model were employed for the prediction of ibuprofen morphology. The simulation calculations were performed to obtain attachment energies for a growth unit based on a monomer and dimer, as ibuprofen molecules pack in the crystal lattice as dimers by forming hydrogen bonds between the carboxylic groups so it is likely that the dimer growth unit is present in the crystal lattice.

5.3 Predicted morphology compared to experimental morphology

In this study, the BFDH and attachment energy model were employed for the prediction of ibuprofen morphology. The simulation calculations were performed to obtain attachment energies for a growth unit based on a monomer and dimer, as ibuprofen molecules pack in the crystal lattice as dimers by forming hydrogen bonds between the carboxylic groups so it is likely that the dimer growth unit is present in the crystal lattice.

5.3.1 Attachment energy morphological simulation for a growth unit based on a monomer

5.3.1.1 Force field and charges

The tested force fields used in this work were Momany and Lifson force fields for carboxylic acid. The atomic co-ordinates of the resultant crystal structure of ibuprofen together with the atomic partial charges as calculated using MOPAC or INTERCHEM are tabulated in Table 5.4.

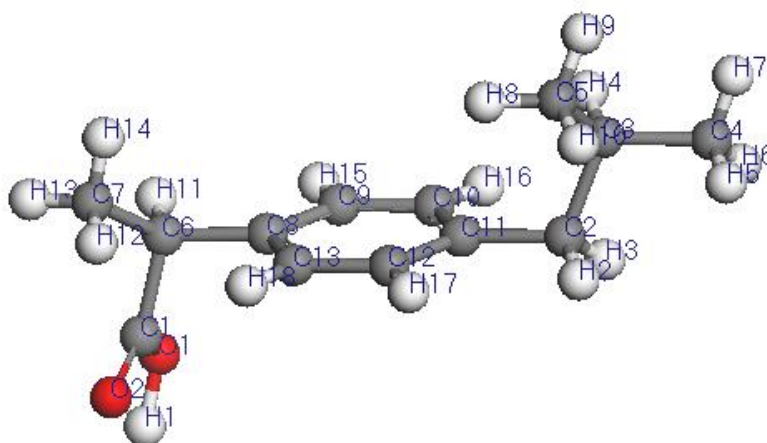


Figure 5.4 Numbering of the atoms in an ibuprofen molecule structure.

Table 5.4 Atomic charges of all atoms in the ibuprofen crystal structure

Atomic number	Atomic type	X coordinate	Y coordinate	Z coordinate	Charges
1	C1	0.4166	0.34642	0.3982	0.2983
2	C2	0.17355	-0.13553	0.7004	-0.1033
3	C3	0.09846	-0.26027	0.6429	-0.1223
4	C4	0.04237	-0.40949	0.7423	-0.1866
5	C5	0.13806	-0.31984	0.5818	-0.191
6	C6	0.35072	0.22129	0.3253	-0.0539
7	C7	0.40131	0.10904	0.2436	-0.1657
8	C8	0.3042	0.1251	0.4211	-0.0923
9	C9	0.2185	0.1740	0.4460	-0.0989
10	C10	0.1770	0.0901	0.535 1	-0.1137
11	C11	0.2197	-0.0405	0.6035	-0.0606

12	C12	0.3059	-0.092	0.5798	-0.1237
13	C13	0.3475	-0.0085	0.4900	-0.0933
14	H1	0.4309	0.5642	0.4715	0.2582
15	H2	0.2182	-0.2042	0.7642	0.0829
16	H3	0.1449	-0.0572	0.7495	0.0796
17	H4	0.0548	-0.2010	0.5755	0.0811
18	H5	0.0864	-0.3885	0.8066	0.0639
19	H6	0.0182	-0.2258	0.7821	0.0739
20	H7	-0.0045	-0.3992	0.7029	0.0715
21	H8	0.1797	-0.3746	0.5198	0.08
22	H9	0.0850	-0.4811	0.5417	0.0727
23	H10	0.1768	-0.4706	0.6520	0.0628
24	H11	0.3060	0.2896	0.2733	0.101
25	H12	0.4503	0.0429	0.2974	0.0926
26	H13	0.4223	0.1811	0.1808	0.0723
27	H14	0.3609	0.0314	0.1946	0.0708
28	H15	0.1895	0.2663	0.3970	0.1204
29	H16	0.1169	0.1266	0.5524	0.1207
30	H17	0.3403	-0.1892	0.6333	0.1281
31	H18	0.4075	-0.0473	0.4762	0.1258
32	O1	0.3801	0.4935	0.4163	-0.2821
33	O2	0.4969	0.3118	0.4402	-0.3692

5.3.1.2 Lattice energy

With the chosen force field and calculated charges for each atom, the lattice energy was calculated and the contribution of van der Waals and coulombic intermolecular interactions into the lattice energy are shown in Figure 5.5.

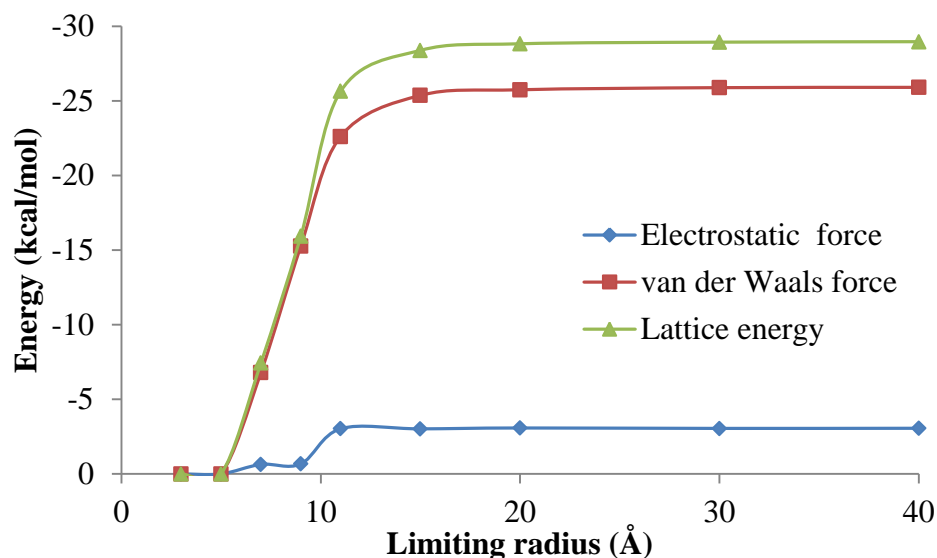


Figure 5.5 Lattice energy which is a sum of the van der Waals and electrostatics interactions which converges at 20 Å. The van der Waals and electrostatic contributions also converge with distance.

The calculated value of lattice energy was found to be -28.93 (kcal/mol) with the lattice convergence taking place at ca 20Å as shown Figure 5.5. This provides a reasonable agreement with the experimental lattice energy calculated from the heat of sublimation for ibuprofen; 30.10 kcal/mol [136]. It suggested that these force fields; Momany and Lifson chosen, are appropriate for this calculation. It was shown that the van der Waals and Coulombic intermolecular energies increase rapidly and converge as the limiting radius increases because only molecules within a fixed distance from the central molecule contribute to the lattice energy. This occurs at a distance of 20Å from the central molecule. The van der Waals interactions 25.1 kcal/mol contributing to the overall lattice energy were found to be much higher than the Coulombic interactions, which was around 3.8 (kcal/mol).

5.3.1.3 Analysis of strong intermolecular interactions (synthons) on the crystal lattice

The bonding analysis features were used for the analysis of the intermolecular interactions in the crystal lattice (see Table 5.5). Analysis of interatomic interactions: Further calculations (Table 5.6) showed the most important atom-atom interactions within all the intermolecular interactions.

Table 5.5 Five strongest intermolecular interactions on the crystal lattice corresponding to the different molecular distance

Bond type	Multi plicity	Dist. (Å)	Attractive energy	Repulsive energy	Coulombic	Total (kcal/mol)
a	4	9.81	-47.4	42.15	-2.22	-7.47
b	8	6.28	-3.72	1.24	-0.11	-2.58
c	4	6.69	-3.14	1.31	-0.43	-2.26
d	8	7.08	-3.00	0.76	-0.02	-2.25
e	4	8.04	-1.67	0.33	0.01	-1.33

Table 5.6 Contributions of different type of atoms in the asymmetric unit to the lattice energy (%)

Atom	Attractive energy	Repulsive energy	Coulombic	Total	Percentage
C1	-2.41	1.06	-0.36	-1.71	7.8
C2	-1.02	0.29	0.26	-0.46	2.1
C3	-0.76	0.14	0.15	-0.48	2.17
C4	-0.87	0.30	0.24	-0.34	1.53
C5	-1.13	0.42	0.29	-0.42	1.93
C6	-1.15	0.43	0.17	-0.56	2.54
C7	-1.36	0.60	0.59	-0.17	0.87
C8	-1.01	0.23	0.14	-0.64	2.93
C9	-1.25	0.44	0.05	-0.76	3.45
C10	-1.20	0.49	0.00	-0.71	3.24
C11	-1.10	0.48	0.09	-0.54	2.46
C12	-1.39	0.58	0.44	-0.38	1.71
C13	-1.30	0.51	0.28	-0.52	2.39
H1	0.00	0.00	-3.33	-3.33	15.23
H2	-0.43	0.08	-0.45	-0.79	3.62
H3	-0.35	0.06	-0.12	-0.4	1.82
H4	-0.30	0.07	0.04	-0.19	0.88
H5	-0.45	0.21	-0.25	-0.49	2.26

H6	-0.26	0.04	-0.06	-0.29	1.31
H7	-0.20	0.02	0.02	-0.15	0.70
H8	-0.44	0.09	-0.14	-0.48	2.20
H9	-0.30	0.05	0.02	-0.23	1.07
H10	-0.47	0.13	-0.22	-0.56	2.57
H11	-0.61	0.39	-0.53	-0.75	3.43
H12	-0.34	0.05	-0.27	-0.56	2.56
H13	-0.63	0.28	-0.42	-0.77	3.50
H14	-0.54	0.15	-0.18	-0.56	2.57
H15	-0.48	0.11	-0.06	-0.43	1.98
H16	-0.37	0.07	0.04	-0.26	1.20
H17	-0.58	0.17	-0.79	-1.2	5.49
H18	-0.61	0.32	-0.64	-0.93	4.27
O1	-2.66	1.97	1.43	0.74	-3.38
O2	-2.79	2.43	-2.20	-2.56	11.69

Table 5.6 shows the constituent intermolecular interactions partitioned with respect to their contributing atomic sites in the molecule. This reveals that atom carbonyl oxygen O2 in (C=O) and hydroxyl oxygen H1 in (O-H) contribute the most to the lattice energy and that the strongest intermolecular interactions are those related to hydrogen bond O--H interactions.

5.3.1.4 BFDH selection of slices and the attachment energy

From the BFDH rule based on the cell dimensions, molecular positions, and with an assumption that the slowest faces possess the highest density of material and largest d_{hkl} , the miler indices and morphology of the ibuprofen crystal was obtained. The calculated surface attachment energies for the individual faces are given in Table 5.7 with the predicted morphology, based on these values, given in Figure 5.6 and the experimental morphology shown in Figure 5.7.

Table 5.7 Interplanar spacing (in Å) and attachment energies (in kcal/mol) for a growth unit based on a monomer

Face	Multiplicity	d_{hkl}	E_{att} (Momany)	E_{att} (Lifson)	E_{att} (Bunyan, 1991)
100	2	14.47	-4.27	-4.75	-4.76
110	4	6.92	-15.84	-15.46	-17.85
011	4	6.32	-18.30	-16.13	-18.04
11-1	4	6.01	-17.14	-16.93	-17.40
111	4	5.60	-16.46	-16.19	-16.70
210	4	5.33	-18.25	-18.26	-18.76
002	2	5.29	-14.79	-16.22	-8.29
10-2	2	5.25	-16.59	-18.18	-17.20
21-1	4	5.00	-19.46	-19.67	
102	2	4.73	-15.26	-16.74	-15.86
20-2	2	4.65	-25.91	-24.76	
211	4	4.54	-18.16	-18.26	
0 1 2	4	4.39	-21.93	-20.09	
1 1 -2	4	4.37	-20.63	-20.73	
3 1 0	4	4.11	-19.67	-19.97	
1 1 2	4	4.06	-19.34	-19.30	
E_{latt} (kcal/mol)			-28.93	-28.04	-28.94

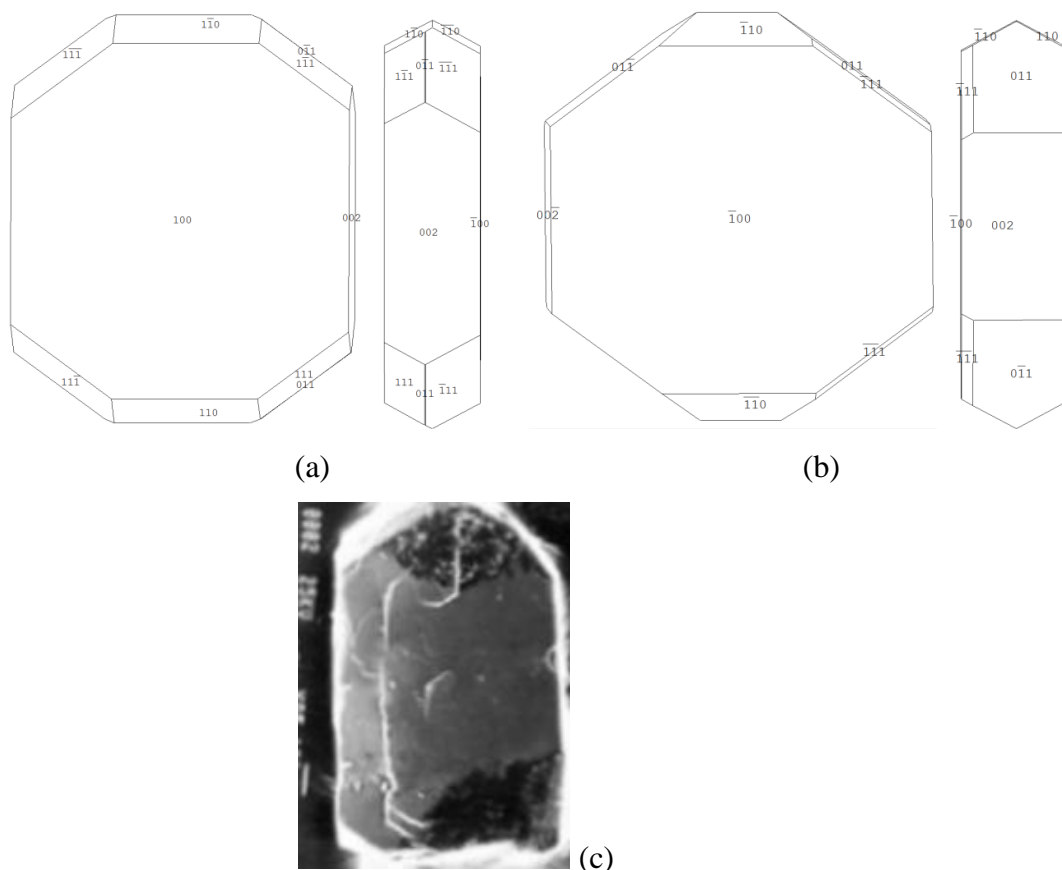


Figure 5.6 Morphology of ibuprofen calculated using (a) Lifson force field; (b) Momany force field; and (c) ibuprofen crystal grown from vapour phase [136].

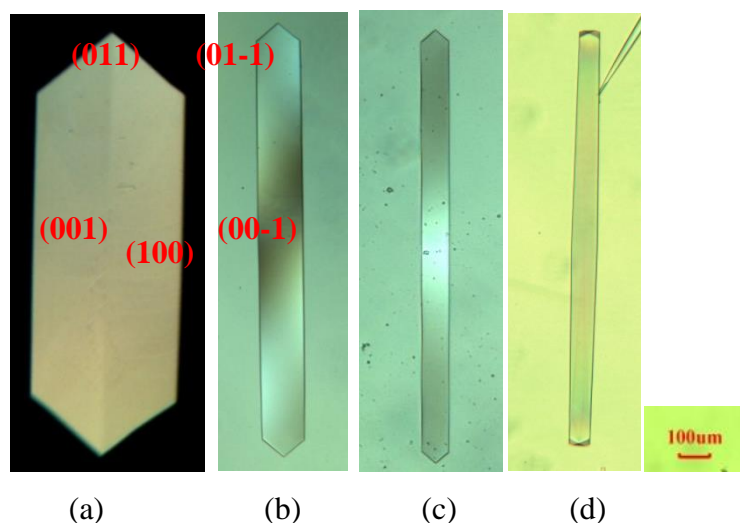


Figure 5.7 Morphology of ibuprofen recrystallised in ethanol (a), ethyl acetate (b); acetonitrile (c); toluene (d).

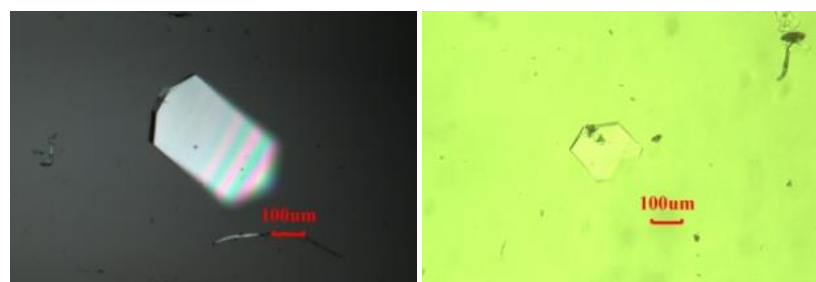


Figure 5.8 Thin crystal morphology of ibuprofen recrystallised in ethanol solutions

The crystal morphology obtained from the morphological simulation from both force fields was found to be in good agreement with published literature [5, 136, 158] and with the optical micrographs taken of the crystals grown from various solvents in this study, apart from the aspect ratios of the crystals (Figure 5.7). The {100} face has smallest attachment energy so it is the slowest growing face of ibuprofen which is in good agreement with the observed morphology (thin crystals) (Figure 5.8). Ibuprofen crystals are quite thin and the {100} face is the dominant face. Larger {110} and {111} faces and smaller {011} faces present in the morphology calculated from Momany force field whilst larger {011} face and a smaller {110} face present in the theoretical morphology calculated from Lifson. However, the morphology calculated from the Momany force field is slightly thinner than that calculated from the Lifson force field.

The simulated morphology for ibuprofen crystals revealed that the {100}; {001} and {011} are the dominant faces which is also in relatively good agreement with experimental results and previous observations from the literature [136, 159]. However, the {110} face is not present in the experimental crystals and the aspect ratio of ibuprofen crystals vary with crystallising environments.

5.3.1.5 Analysis of the strongest bonds on the {001}, {011} {100} and {110} face

Intermolecular bonding for ibuprofen in terms of the most important bond types, multiplicity, distance and strength of bonds (Table 5.8) and the display of these intermolecular interactions (Figure 5.9) were discovered and analysed to give details on the strongest bonds on dominant crystal surfaces {011}, {001} and {100}. For example, to examine the strength and direction of hydrogen-bonds and contributions of these strongest bonds on the slice and attachment energy and surface chemistry to rationalise the growth rate of these faces.

Table 5.8 Bonding analysis for the {011}, {001} and {100} faces with for a growth unit based on a monomer

Bond type	Multiplicity	Dist. (Å)	ATT	REP	COU	Total	Face {011}	Face {001}	Face {100}	Face {110}
a	4	9.81	-47.4	42.15	-2.22	-7.47	(+/-)	(SL)	(SL)	(+/-/SL)
b	8	6.28	-3.72	1.24	-0.11	-2.58	(SL/+/-)	(+/-)	(SL)	(SL)
c	4	6.69	-3.14	1.31	-0.43	-2.26	(SL)	(SL)	(SL)	(+/-/SL)
d	8	7.08	-3.00	0.76	-0.02	-2.25	(+/-/SL)	(+/-)	(SL)	(+/-)
e	4	8.04	-1.67	0.33	0.01	-1.33	(SL)	(SL)	(+/-)	(+/-/SL)

(SL): slice energy bond

(+): attachment energy bond: molecule lies above the slice centre and contributes to Eatt(+)

(-): attachment energy bond: molecule lies below the slice centre and contributes to Eatt(-)

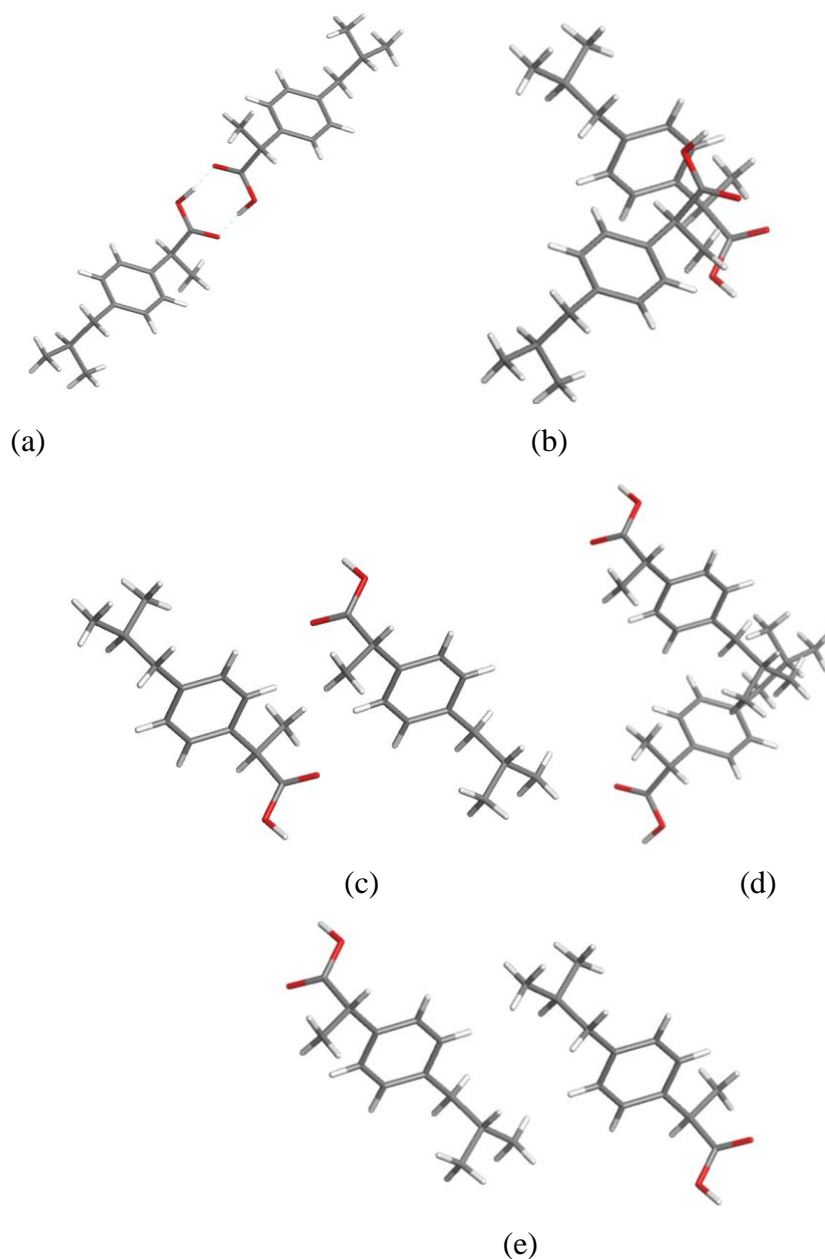


Figure 5.9 Molecular interaction of the 5 strongest bonds (a) The strongest bond type a (-7.47 kcal/mol) is a hydrogen-bond between carboxylic acid -COOH groups of ibuprofen (homosynthon); (b) Second strongest bond type b (-2.58 kcal/mol); (c) Third strongest bond type c (-2.26 kcal/mol); (d) Fourth strongest bond type d (-2.25 kcal/mol); (e) Fifth strongest bond type e (-1.33 kcal/mol).

The intermolecular bonding results on dominant faces for ibuprofen are dominated by strong bonds of -7.47 kcal/mol (van der Waals contribution of -5.25 kcal/mol is much higher than columbic contribution). These are hydrogen-bonded molecules between molecule number 1 and molecule number 3 which continue along the [010] direction so crystals are expected to grow more significantly in the b direction more so than in the a

and c direction which is in good agreement with the observed morphology. In addition, it was also shown that most of the strong bonds (hydrogen bonds) for the {100} face are inside the slice, thus E_{slice} for this face is high making this face one of the most morphologically important. The strongest bonds (type a: -7.47 kcal/mol) contributes to the attachment energy on the {011} face both above and below the slice centre and contributes to slice energy on the {001} face, which envisage the growth rate of the {011} face being greater than the growth rate of the {001} face.

5.3.2 Attachment energy morphological simulation for a growth unit based on a dimer

5.3.2.1 Force field and charges

The force fields used in this work were Momany and Lifson force fields for carboxylic acid. The atomic co-ordinates of the resultant crystal structure of ibuprofen together with a set of atomic partial charges for the dimer using MOPAC with the AM1 method are tabulated in Table 5.9.

Table 5.9 Atomic charges of two molecules for the dimer calculation

	Atom	X	Y	Z	Charges		Atom	X	Y	Z	Charges
1	C1	0.417	0.347	0.398	0.329	34	C1	0.583	0.653	0.602	0.329
2	C2	0.174	-0.136	0.700	-0.103	35	C2	0.826	1.136	0.300	-0.103
3	C3	0.099	-0.260	0.643	-0.122	36	C3	0.902	1.260	0.357	-0.122
4	C4	0.042	-0.320	0.742	-0.187	37	C4	0.958	1.320	0.258	-0.187
5	C5	0.138	-0.410	0.582	-0.191	38	C5	0.862	1.410	0.418	-0.191
6	C6	0.351	0.221	0.325	-0.056	39	C6	0.649	0.779	0.675	-0.056
7	C7	0.401	0.109	0.244	-0.168	40	C7	0.599	0.891	0.756	-0.168
8	C8	0.304	0.125	0.421	-0.093	41	C8	0.696	0.875	0.579	-0.093
9	C9	0.219	0.174	0.446	-0.095	42	C9	0.781	0.826	0.554	-0.095
10	C10	0.177	0.090	0.535	-0.113	43	C10	0.823	0.910	0.465	-0.113
11	C11	0.220	-0.045	0.604	-0.060	44	C11	0.780	1.045	0.397	-0.060
12	C12	0.306	-0.092	0.580	-0.124	45	C12	0.694	1.092	0.420	-0.124
13	C13	0.348	-0.009	0.490	-0.095	46	C13	0.652	1.009	0.510	-0.095
14	H1	0.431	0.565	0.472	0.301	47	H1	0.569	0.436	0.529	0.301
15	H2	0.218	-0.204	0.764	0.083	48	H2	0.782	1.204	0.236	0.083
16	H3	0.145	-0.057	0.750	0.080	49	H3	0.855	1.057	0.251	0.080
17	H4	0.055	-0.201	0.576	0.081	50	H4	0.945	1.201	0.425	0.081
18	H5	0.087	-0.389	0.807	0.064	51	H5	0.914	1.389	0.193	0.064
19	H6	0.018	-0.226	0.782	0.074	52	H6	0.982	1.226	0.218	0.074

20	H7	-0.005	-0.399	0.703	0.072	53	H7	1.005	1.399	0.297	0.072
21	H8	0.180	-0.375	0.520	0.080	54	H8	0.820	1.375	0.480	0.080
22	H9	0.085	-0.481	0.542	0.073	55	H9	0.915	1.481	0.458	0.073
23	H10	0.177	-0.471	0.652	0.063	56	H10	0.823	1.471	0.348	0.063
24	H11	0.306	0.290	0.273	0.105	57	H11	0.694	0.710	0.727	0.105
25	H12	0.450	0.043	0.297	0.092	58	H12	0.550	0.957	0.703	0.092
26	H13	0.422	0.181	0.181	0.073	59	H13	0.578	0.819	0.819	0.073
27	H14	0.361	0.031	0.195	0.071	60	H14	0.639	0.969	0.805	0.071
28	H15	0.190	0.267	0.397	0.122	61	H15	0.810	0.734	0.603	0.122
29	H16	0.117	0.127	0.552	0.121	62	H16	0.883	0.873	0.448	0.121
30	H17	0.340	-0.189	0.633	0.128	63	H17	0.660	1.189	0.367	0.128
31	H18	0.408	-0.047	0.476	0.125	64	H18	0.592	1.047	0.524	0.125
32	O1	0.380	0.494	0.416	-0.306	65	O1	0.620	0.506	0.584	-0.306
33	O2	0.497	0.312	0.440	-0.420	66	O2	0.503	0.688	0.560	-0.420

5.3.2.2 Lattice energy

The calculated energy for ibuprofen for a growth unit based on a dimer is 42.95 kcal/mol which contribute from electrostatic and van der Waals forces (Figure 5.10).

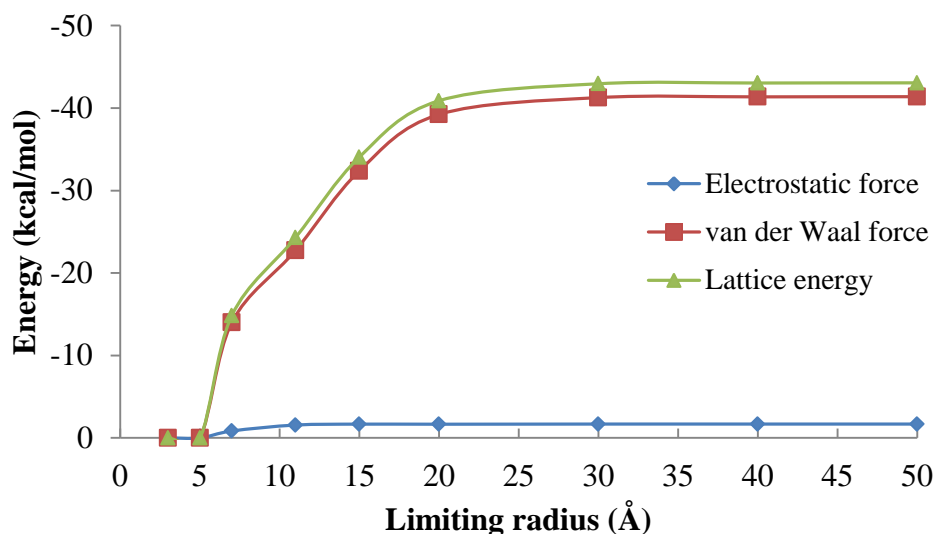


Figure 5.10 Lattice energy which is a sum of the van der Waals interaction and electrostatics which converges at 20 Å in the dimer calculation.

It was shown that the van der Waals and coulombic intermolecular energies increase rapidly and converge as the limiting radius increases. This occurs at a distance of 20 Å from the central molecule. The van der Waals interactions - 41.38 kcal/mol ($\approx 96\%$ of the lattice energy) contributing to the overall lattice energy were found to be much higher than the coulombic interactions, which was around - 1.68 kcal/mol.

5.3.2.3 Attachment energy and predicted morphology

The calculated surface attachment energies for the individual faces are given in with the Table 5.10 predicted morphology, based on these values, given in Figure 5.11.

Table 5.10 Attachment energies (kcal/mol) calculated for a growth unit based on a dimer

Face	Multi plicity	d_{hkl} (\AA°)	E_{att} (using Momany)	E_{att} (using Lifson)	E_{att} (Win and Doherty) [159]
100	2	14.47	- 8.53	- 9.50	-9.59
110	4	6.92	- 32.55	- 35.87	
011	4	6.32	- 32.21	- 36.59	-35.20
11-1	4	6.01	- 33.55	- 37.00	-35.61
111	4	5.60	- 32.27	- 35.63	-34.23
210	4	5.33	- 34.21	- 37.67	
002	2	5.29	- 29.59	- 32.45	-31.45
10-2	2	5.25	- 33.19	- 36.38	-35.35
21-1	4	5.00	- 34.58	- 38.11	
102	2	4.73	- 30.53	- 33.50	
20-2	2	4.65	- 33.68	- 36.97	
211	4	4.54	- 34.55	- 38.09	
012	4	4.39	-35.72	-39.50	
11-2	4	4.37	-31.38	-34.73	
310	4	4.11	-35.00	-38.56	
112	4	4.06	-33.89	37.56	
E_{latt} (kcal/mol)			- 42.95	- 47.43	

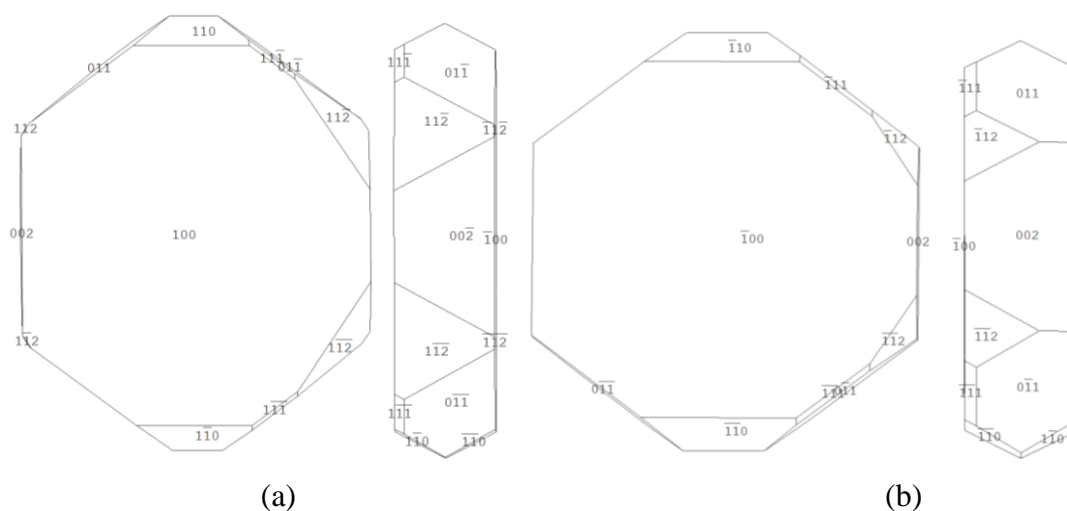


Figure 5.11 Predicted crystal shapes of (RS)- ibuprofen in a dimer using Momany (a); Lifson force field (b).

Both of the monomer and dimer models gave the predicted shape similar to the sublimation crystal with plate-like morphology, dominated by the {100} face. However, it showed that the dimer calculation seems to give a better prediction of ibuprofen morphology with the {011} face present as the dominant form to grow in the b axis direction which agrees with the literature published by Winn and Doherty [159]. Particularly, the dimer model using Momany force field provides a thinner crystal and more elongated in the b direction compared to the monomer model. Also, the smaller {110} faces appear in the dimer model. However, there were less numbers of crystal faces considered from the dimer calculation compared to that in this study.

5.3.2.4 Analysis of the strongest bonds on the {011}, {001}, {100} and {110} faces

Intermolecular bonding and the display of these intermolecular interactions on crystal surfaces {011}, {001} and {100} are shown in Table 5.11 and Figure 5.12.

Table 5.11 Full calculation mode analysis for the {011}, {001}, {100} and {110} faces with for a growth unit based on a dimer

Bond type	Multiplicity	Dist. (Å)	ATT	REP	COU	Total	Face {011}	Face {001}	Face {100}	Face {110}
a	4	7.89	-5.96	1.82	-0.35	-4.49	(+/-)	(SL)	(SL)	(+/-)
b	8	6.66	-4.98	1.248	-0.21	-3.71	(SL/+/-)	(+/-)	(SL)	(+/-/SL)
c	8	12.99	-3.03	0.76	-0.02	-2.29	(+/-)	(+/-)	(SL)	(SL)
d	4	16.65	-1.69	0.33	0.00	-1.36	(+/-)	(SL)	(+/-)	(+/-)
e	8	16.88	-1.26	0.46	0.01	-0.79	(SL/+/-)	(+/-)	(+/-)	(+/-/SL)

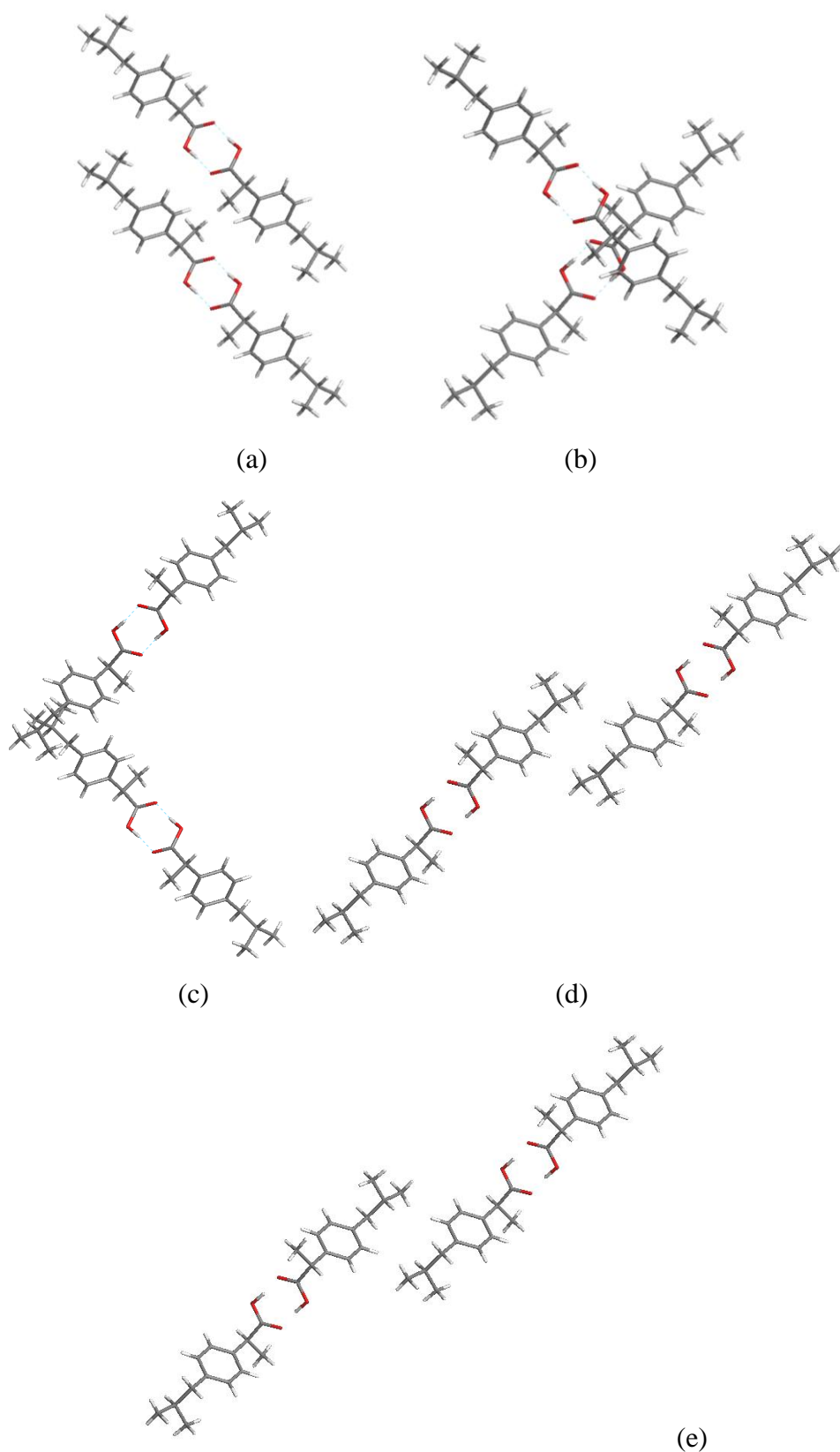


Figure 5.12 Molecular interaction of the 5 strongest bonds in (a) The strongest bond type a (-4.49 kcal/mol); (b) Second strongest bond type b (-3.71 kcal/mol); (c) Third strongest bond type c (-2.29 kcal/mol); (d) Fourth strongest bond type d (-1.36 kcal/mol); (e) Fifth strongest bond type e (-0.79 kcal/mol).

For growth units based on a dimer, it showed the similar trend of intermolecular interactions for the calculations with the growth unit based on a monomer. The strongest bond type (-4.49 kcal/mol) contributes to attachment energy on the {011} and {110} face both above and below the slice centre and contributes to slice energy on the {001} face and the first three strongest bonds contribute to slice energy on the {100} face. This indicates that the {011} face is the fast growing face and the {100} is the slow growing faces.

The ratio of calculated attachment energy of the {011} and {001} face for the growth unit as a monomer and as a dimer is quite similar which is around 1.1 to 1.3 respectively. However, the ratio of attachment energy of the {011} and {001} of observed crystals grown in ethanol, ethyl acetate, acetonitrile and toluene simulated from SHAPE software [152] are 3, 10.5; 15.2; and 16.5 respectively. It showed discrepancies between the attachment energy values in the vacuum morphology and the experimental morphology. The attachment energy of the {011} is much greater than that of the {001} face in these solvents, which was linked to the relative growth rate and the crystal habit surface chemistry analysis and to the dominant synthons on the {001} and {011} face and the surface synthon analysis provided in the previous section..

Interfacial angles of dominant faces of grown ibuprofen crystals and of predicted morphology was measured from optical micrographs to allow indexing of the faces on the experimental morphology (Figure 5.7) for the measurements of the crystal growth rate of the individual faces. It showed the interfacial angles on the dominant faces of grown ibuprofen matched those calculated from morphological prediction. The {011} faces were obviously present in growth solution morphology. However, the crystals were lying flat on the {001} face and the crystals were too thin for identification of the {011} and {-111} face.

5.4 Detailed surface chemistry analysis of the {001}, {011}, {100} and {110} face

The chemistry analysis for the crystal habit faces $\{001\}$, $\{011\}$, $\{100\}$ and $\{110\}$ was performed to examine the crystal surface chemistry of these important faces. Molecular packing on the $\{001\}$ face shows a non-polar property with $-\text{CH}_3$ groups projecting out of the surface. The $-\text{COOH}$ groups are quite restricted in position and the hydrogen bonds formed between $-\text{COOH}$ groups are only in one direction (Figure 5.13). The cleaved surface revealed the hydrogen bonds formed contribute to construct a crystal lattice which agrees with the analysis of the strongest bonds on the ibuprofen crystal surface of the $\{001\}$ face where bond a (the hydrogen bonds) and bond c contribute to lattice energy whilst bond b and d contribute to attachment energy.

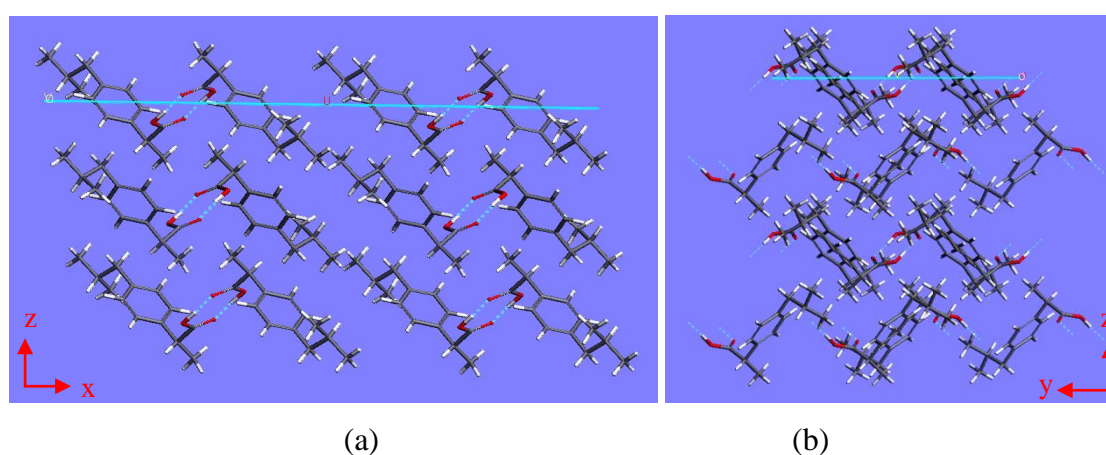


Figure 5.13 Molecular packing diagrams based upon the crystallographic structures of the $\{001\}$ face viewed along the y axis (a) and along the x axis (b) showing its hydrophobic nature with $-\text{CH}_3$ groups exposed at the surface with the $-\text{COOH}$ groups exposed in one direction and in a quite restricted position.

The $\{011\}$ face is more polar and $-\text{COOH}$ groups on the $\{011\}$ face are more exposed and more easily accessible than $-\text{COOH}$ groups on face $\{001\}$. The intermolecular hydrogen bonds appear in two different directions (see Figure 5.14) contributing to slice energy and attachment energy resulting in much faster growth compared to the $\{001\}$ crystal face. This fact can be used to envisage or rationalise the relative growth rate of the $\{011\}$ and $\{001\}$ face. As the $\{011\}$ face exhibits great hydrophilicity on which carboxylic acid groups provide good binding sites for polar solvent molecules which are more easily accessible to form hydrogen bonds.

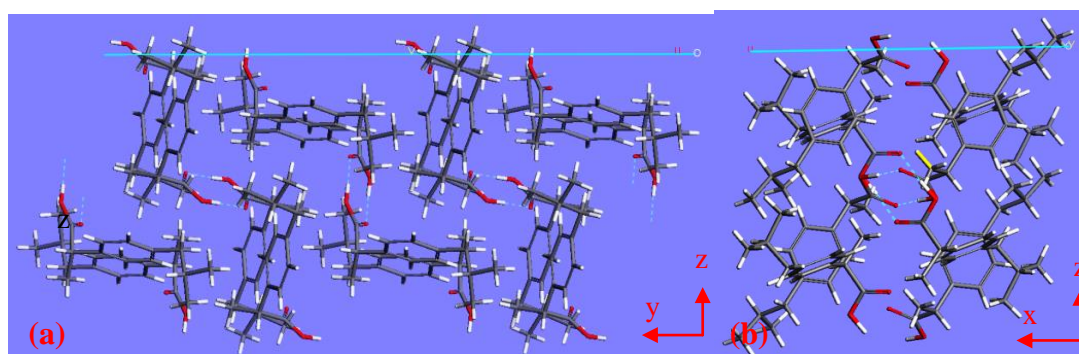


Figure 5.14 Molecular packing diagrams based upon the crystallographic structures of the $\{011\}$ face viewed along the x axis (a) and along the y axis (b) showing a more polar surface with exposed $-\text{COOH}$ groups at the surface with two different directions.

Figure 5.15 shows the molecular model of the $\{100\}$ crystal surface of ibuprofen which has layers of dimers formed by hydrogen-bond between carboxylic groups. The surface possesses two different natures as the molecular arrangements have two distinct molecular structure terminations, which can be either polar (with $-\text{COOH}$ groups) or non-polar (with alkyl-groups). The approach associated with two modes of termination of the $\{100\}$ face for ibuprofen crystals. Carboxylic acid groups projecting out from the surface are free to interact with solvent molecules in surrounding environment so the adsorption of solvent on the crystal surface may inhibit the growth rate of face $\{100\}$. Interactions of the alkyl portions of neighbouring layers result in weak attachment energy. Hence, this face is predicted to be a slow growing face.

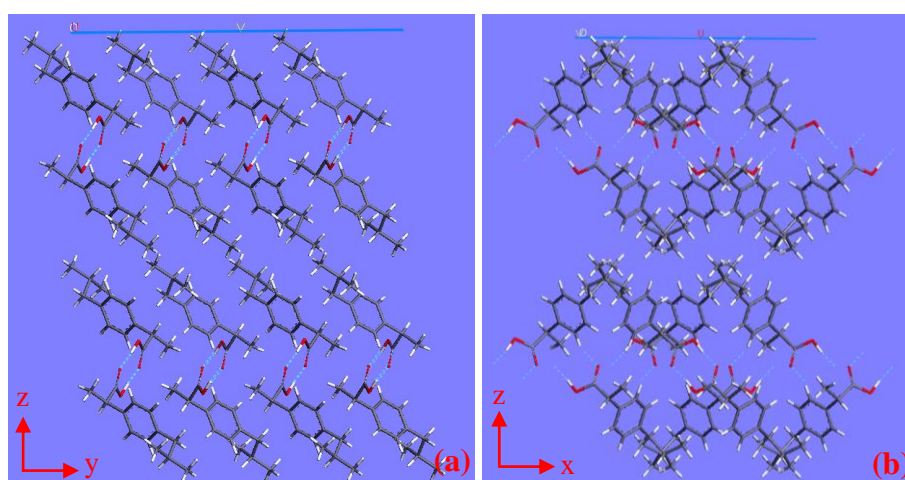


Figure 5.15 Molecular packing diagrams based upon the crystallographic structures of the $\{100\}$ face viewed along the x axis (a); viewed along the y axis (b).

The $\{110\}$ face exposed with $-\text{COOH}$ groups and alkyl groups shows intermolecular hydrogen bonds appearing in different directions. COOH groups on the $\{100\}$ face are more exposed and more accessible. Hydrogen bonds are involved both in the formation of a crystal lattice and in the attachment of the crystal lattice on the crystal habit surface (Figure 5.16). This agrees with the analysis of the strongest bonds on the ibuprofen crystal surface of the $\{110\}$ face.

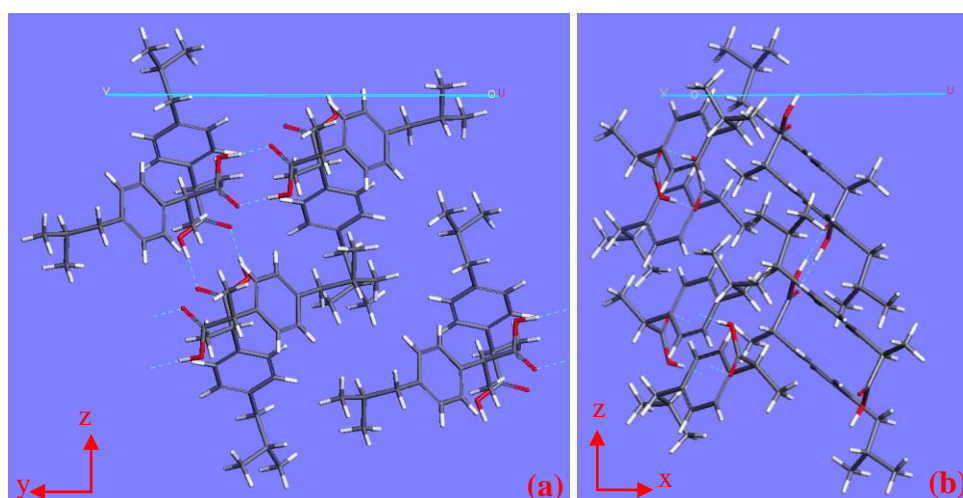


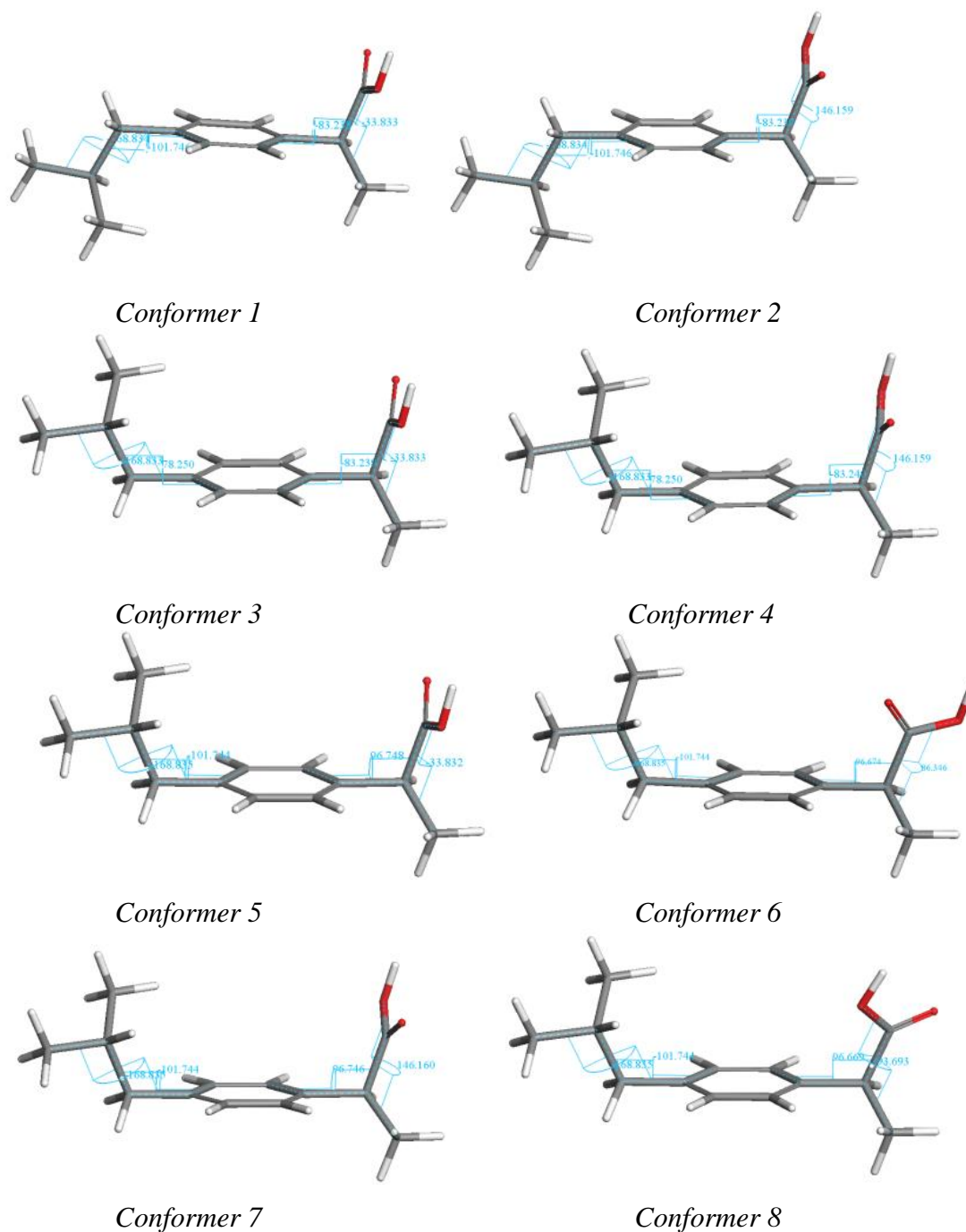
Figure 5.16 Molecular packing diagrams based upon the crystallographic structures of the $\{110\}$ face viewed along the x axis (a) and viewed along the y axis (b).

The surface chemistry analysis for the dominant crystal habit faces was carried out to relate to the bonding analysis on these faces and envisage and/or to rationalise the growth rate of face $\{001\}$ and $\{011\}$ in chapter 7. Surface chemistry analysis, where the properties of the surfaces (e.g. hydrophobicity, polar or hydrogen-bonded) was examined and from this, relative qualitative binding interactions between solvents and solute and the associated inter-molecular interaction on specific growing faces can be analysed to interpret the growth rate. For example, polar solvents are found to inhibit the growth rate of faces which contain available binding sites for hydrogen bond formation. Hence, ibuprofen morphology grown from solvents can be explained by molecular arrangement at the $\{011\}$ and $\{001\}$ surface and hydrogen bonds can be formed between solvents and COOH functional groups of ibuprofen. It can be predicted that the $\{100\}$ is a very slow growing face, and the $\{011\}$ face grows faster than the

{001} faces; however the relative growth rate between {011} and {001} depend on the growth environments.

5.5 Conformer population in solutions

The 10 optimized ibuprofen conformations using GGA/PBE/DNP/COSMO calculations (PBE functional and DNP basis set) in Dmol3 are shown in Figure 5.17.



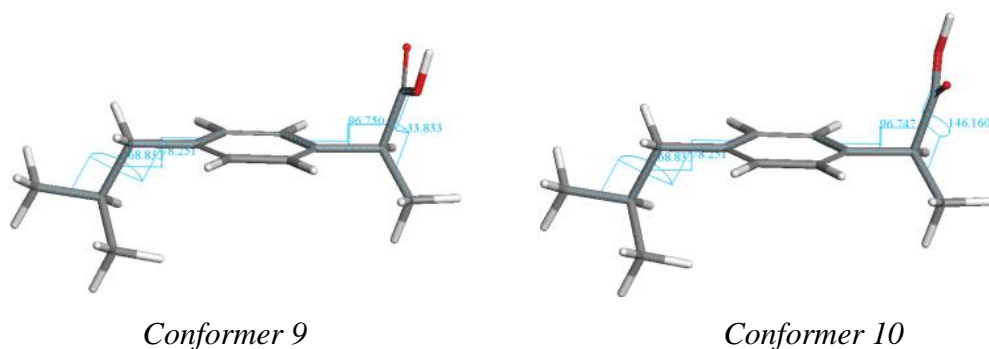


Figure 5.17 10 lowest energy and optimised conformers were chosen for the conformational distribution study.

The conformation distribution of the 10 conformer in ethanol, ethyl acetate, acetonitrile and toluene at 25°C are shown in Table 5.12.

Table 5.12 Percentage of ibuprofen conformer in solvents (%) calculated from COSMOtherm software package

Conformer	Ethanol	Ethyl acetate	Acetonitrile	Toluene
1	4.27	4.27	4.29	4.30
2	19.77	21.12	20.60	20.87
3	5.55	4.52	4.98	4.46
4	19.69	21.5	20.32	21.47
5	4.87	3.93	4.31	3.90
6	2.1	2.62	2.50	2.73
7	17.77	18.2	17.70	18.26
8	1.63	1.71	1.84	1.74
9	6.65	5.49	5.82	5.46
10	17.69	16.63	17.64	16.80

There was no significant solvent effect on the conformer distribution in different solvents. The population of four conformers (conformer 2, 4, 7 and 10) has a highest percentage in the range of 17-21% in all four solvents compared to other conformations in the population. There were only a very slightly change in the percentage of the conformer 2, 4, 7 and 10 in different solvents (Figure 5.18). The torsion angles of favoured conformations of ibuprofen in all solvents are shown in Table 5.13. This indicates there is no conformational polymorphism in different solvents for ibuprofen.

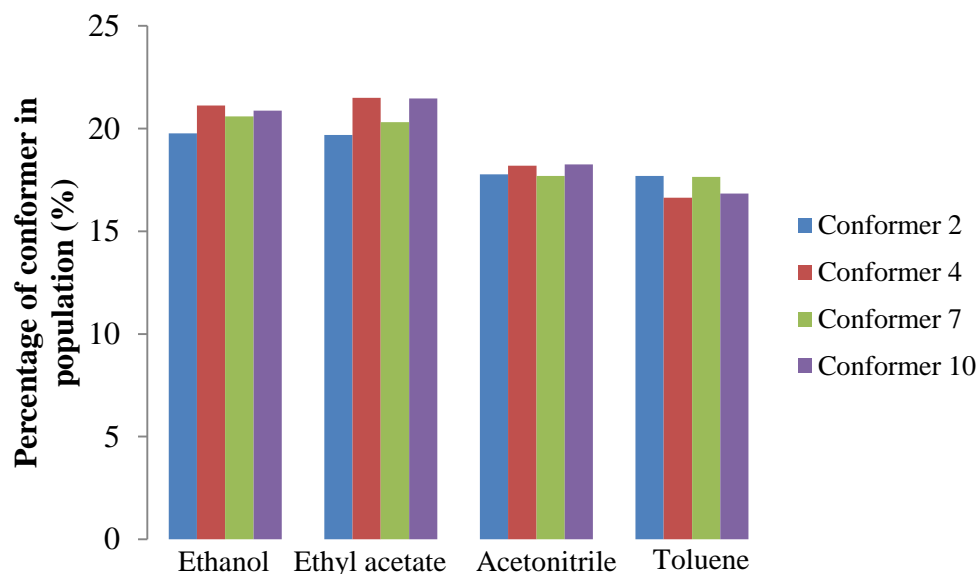


Figure 5.18 Population of four conformers (2, 4, 7 and 10) in solvents.

Table 5.13 Torsion angles of preferred conformations in solutions

Conformer	T3	T4	T5	T8
2	-168.83	-101.75	-83.24	146.16
4	-168.83	78.25	-83.24	146.16
7	-168.83	-101.74	96.75	146.16
10	-168.83	78.25	96.75	146.16

This methodology has also been used for calculation of conformation populations of form A and B of famotidine, tatieline, ritanovir and S-ibuprofen [160] showing relative conformation distribution can be used to predict conformational polymorphs based on the trend of conformation distribution in different solvents. For example, form B of famotidine was found in water solution with high initial concentration independence of cooling rate whilst form A of famotidine was recrystallised from methanol and acetonitrile. The calculated population of conformer A and B in these solvents revealed that conformer A presents the highest population in methanol and acetonitrile and conformer B has the highest population in water. Furthermore, this method can be used for solvent screening and selection based on the relative population of conformers in solvents.

5.6 Conclusions

This chapter reported a modelling study applied to examine the conformation of an isolated molecule, the morphology, intermolecular interactions and crystal habit surface chemistry for ibuprofen. CONFORMER in Material Studio was successful in analysing the flexibility of the ibuprofen molecule. The energy of a free molecule before and after geometry optimisation does not change much indicating ibuprofen is a rigid molecule. The molecule is located within a minimum energy space or is close to the minimum energy in the energy map which is a validation for the known crystal structures of a given molecule in the CSD.

The calculated values of lattice energy based on a monomer growth unit of -28.9 (kcal/mol) revealed a reasonable agreement with the experimental lattice energy calculated from the heat of sublimation for ibuprofen of 30.10 kcal/mol [136]. The simulated crystal habit for ibuprofen revealed a prismatic plat-like crystal shape, shown to be in good agreement with expected shapes from experimental observations and previous studies [5, 136]. The habit prediction for racemate-ibuprofen revealed a flat crystal morphology with predominance of the {001} crystal habit face. Both of the Momany and Lifson force fields gave a good prediction for the ibuprofen morphology in vacuum.

Both of the monomer and dimer models gave the predicted shape similar to the sublimation crystal with plate-like morphology, dominated by the {100} face. However, the dimer model using Momany force field provides the better predicted morphology, a thinner crystal and more elongated in the b direction compared to the monomer model. The smaller {110} faces appear in the dimer model.

From atom-atom bond analysis, carbonyl oxygen (C=O) and hydroxyl hydrogen (O-H) atoms were found to account for the highest energy per atomic site in the lattice energy. The strongest intermolecular interactions are hydrogen bond chain O---H. Intermolecular bonding analysis revealed the strength and direction of the strongest bonds on each of the {011}, {001} and {100} surface which was used to rationalise and validate

the growth rates of the {011}, {001} and {100} faces (reported in chapter 7). The strongest bonds are the hydrogen bonds which contribute to the attachment energy on the {011} face and to the slice energy on the {001} face, which verifies the growth rate of the {011} face is greater than the growth rate of the {001} face. Most of the strongest bonds located on the {100} face are inside the slice thus this face is one of the most morphologically important. The strength and direction of hydrogen-bonds was also viewed through Material Studio. Moreover, cleaving the surfaces of these faces were also shown as validation, by analysing the properties of the surfaces e.g. hydrophobicity, polarity or hydrogen-bonded and relative binding interactions between solvents and solute and the associated inter-molecular interactions involved on specific growing faces.

The attachment energy model used in this chapter takes into account the effect of crystal internal structure on the morphology; however these predictions can be improved by taking into account the crystallising environment (such as solvents, supersaturation etc.). Both of the models (monomer and dimer) did not predict accurately the solvent-grown shapes. Hence, prediction of ibuprofen morphology in growth solutions using systematic grid search should be performed to compare with the experimental crystals.

6 Crystallisation process characterisation and analysis

Summary:

Polymorph screening, solubility determination, and the nucleation kinetics of ibuprofen in ethanol 95%, ethyl acetate, toluene and acetonitrile were examined involving MSZW and induction time measurements.

6.1 Introduction

Polymorphism screening, solubility determination and assessment of nucleation kinetics are all important components for characterising crystallisation behaviour. To study the crystal growth kinetics of ibuprofen, it is essential to measure the solubility together with nucleation kinetics associated with the crystallisation behaviour of ibuprofen. From solubility data, supersaturation, a concentration driving force for the crystallisation process, a fundamental and key parameter in designing and controlling the crystallization process in terms of product yield and the nucleation and crystal growth rates can be calculated. In addition, solubility is a very important parameter to the understanding and study of nucleation manners.

Hence, this chapter presents the results of the polymorph screening, and then the solubility measurement for ibuprofen in ethanol 95%, ethyl acetate, acetonitrile and toluene measured by ATR UV/Vis spectroscopy, which will be used to calculate the supersaturation of solutions. Solubility data are also discussed from the perspective of molecular aspects of solute-solvent interactions and van't Hoff plots to assess if it is ideal or non-ideal solubility in these solvents, activity coefficients were also calculated for each solvent to reveal the affinity of the ibuprofen molecule to solvent molecules. The basic kinetics parameter, the MSZW and induction time were also obtained through polythermal (slow cooling) and isothermal (crash cooling) methods, respectively. The polythermal experimental results were associated with the empirical relationship between the undercooling temperature and the cooling rate derived by Nyvlt [58] to determine nucleation parameters such as the nucleation order and the nucleation constant. Another crucial parameter in nucleation theory is the interfacial energy between the nucleus and liquor surrounding environment within the concept of classical homogeneous nucleation theory which can be estimated from the isothermal experimental results showing the relationship of induction time and supersaturation.

6.2 Polymorphism screening

Polymorphism screening was performed to verify whether different polymorphic forms appear in different solvents following recrystallisation at room temperature. The

melting points and enthalpy of melting of ibuprofen crystals recrystallised from various solvents are reported in Table 6.1 and Figure 6.1.

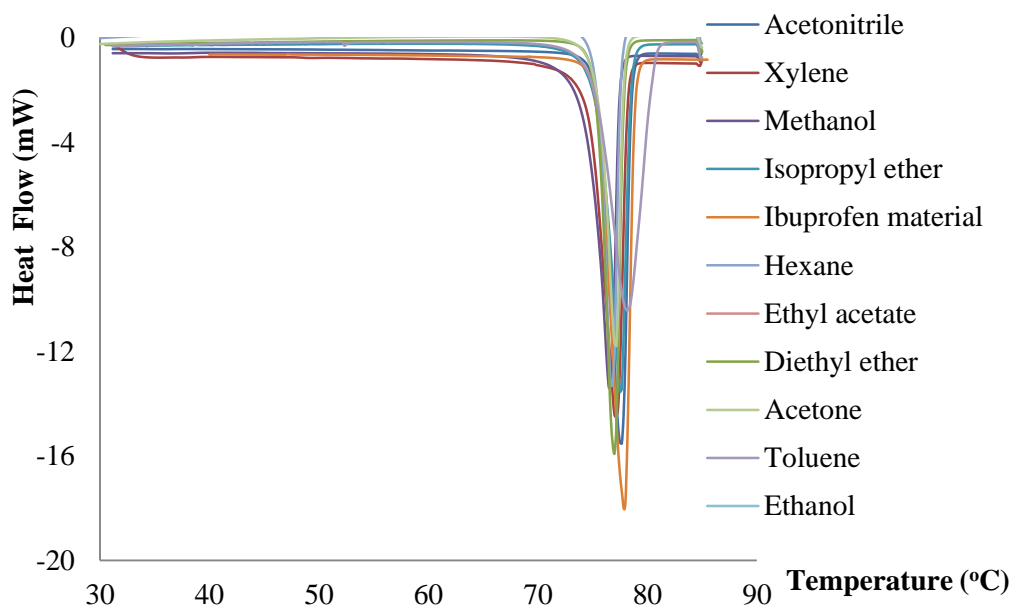


Figure 6.1 DSC data of ibuprofen raw material together with ibuprofen recrystallised from solvents showing similar melting points and melting peak shapes.

Table 6.1 DSC data: onset of melting point, melting point peak and enthalpy of fusion

Solvents	Polarity	Onset of melting point (°C)	Melting peak (°C)	ΔH_{fus} (kJ/mol)
Methanol	Polar protic	74.51 ± 0.5	76.13 ± 0.4	24.01 ± 0.5
Ethanol	Polar protic	74.51 ± 0.3	76.13 ± 0.5	23.87 ± 0.4
Propanol	Polar protic	74.52 ± 0.5	75.72 ± 0.3	25.97 ± 0.4
Acetonitrile	Polar aprotic	75.62 ± 0.4	77.05 ± 0.4	24.45 ± 0.5
Ethyl acetate	Polar aprotic	74.93 ± 0.3	77.41 ± 0.5	25.43 ± 0.3
Acetone	Polar aprotic	75.43 ± 0.5	76.68 ± 0.4	25.84 ± 0.4
Diethyl ether	Non-polar	75.30 ± 0.7	76.46 ± 0.4	23.73 ± 0.5
Hexane	Non-polar	75.34 ± 0.7	76.29 ± 0.3	23.58 ± 0.5
Isopropyl ether	Non-polar	75.46 ± 0.6	77.12 ± 0.4	26.21 ± 0.5
Toluene	Non-polar	75.02 ± 0.4	77.81 ± 0.5	24.21 ± 0.4
Xylene	Non-polar	74.56 ± 0.5	76.59 ± 0.4	25.39 ± 0.5
Ibuprofen		75.25 ± 0.5	77.30 ± 0.4	25.28 ± 0.3

Based on the onset of melting points and melting peaks given by DSC, it can be concluded that there is no polymorphism in ibuprofen recrystallised from various solvents which agrees with previous studies [137]. There were single melting peaks and no other endotherms or transitions were observed as illustrated in Figure 6.1. The onsets of melting points are around 74.5°C - 75.6°C, melting peaks are in the range 75.7°C - 77.8°C and the value of enthalpy of fusion 23.8 - 26.2 kcal/mol. From the data published, the molar enthalpy were to be 26.65 kJ mol⁻¹ obtained by adiabatic calorimetry [161] and 25.5 kJmol⁻¹ from DSC [162, 163]. There was a small difference in the melting point and heat of fusion between ibuprofen crystals recrystallised from different solvents. This may be due to a difference in the degree of structural order within the samples, the variance of degree of structural perfection when recrystallised from different solvents and/or samples were not completely free from solvents.

It is likely that only the external shape of the ibuprofen crystal exhibits morphological changes from prisms to needle-like and plate-like [135, 136] which is affected by the different growth rates of the individual faces, without changing the internal structure. The only known crystal structure for ibuprofen has been published [130] with the exception of an evidence for a new crystalline phase of (RS)-ibuprofen [131], however the crystal structure has still not been revealed yet.

6.3 Solubility measurements

In this study the solubility of (RS)-ibuprofen in ethanol 95%, ethyl acetate, acetonitrile and toluene measured by ATR/UV-Vis spectroscopy at the range temperature range of 10, 15, 20, 30, and 35°C are reported. Spectra of ibuprofen in solvents at various concentrations are shown in Figure 6.2. Calibration curves for ibuprofen in three solvents were obtained using the specific absorbance peak of ibuprofen at 264 nm (Figure 6.3).

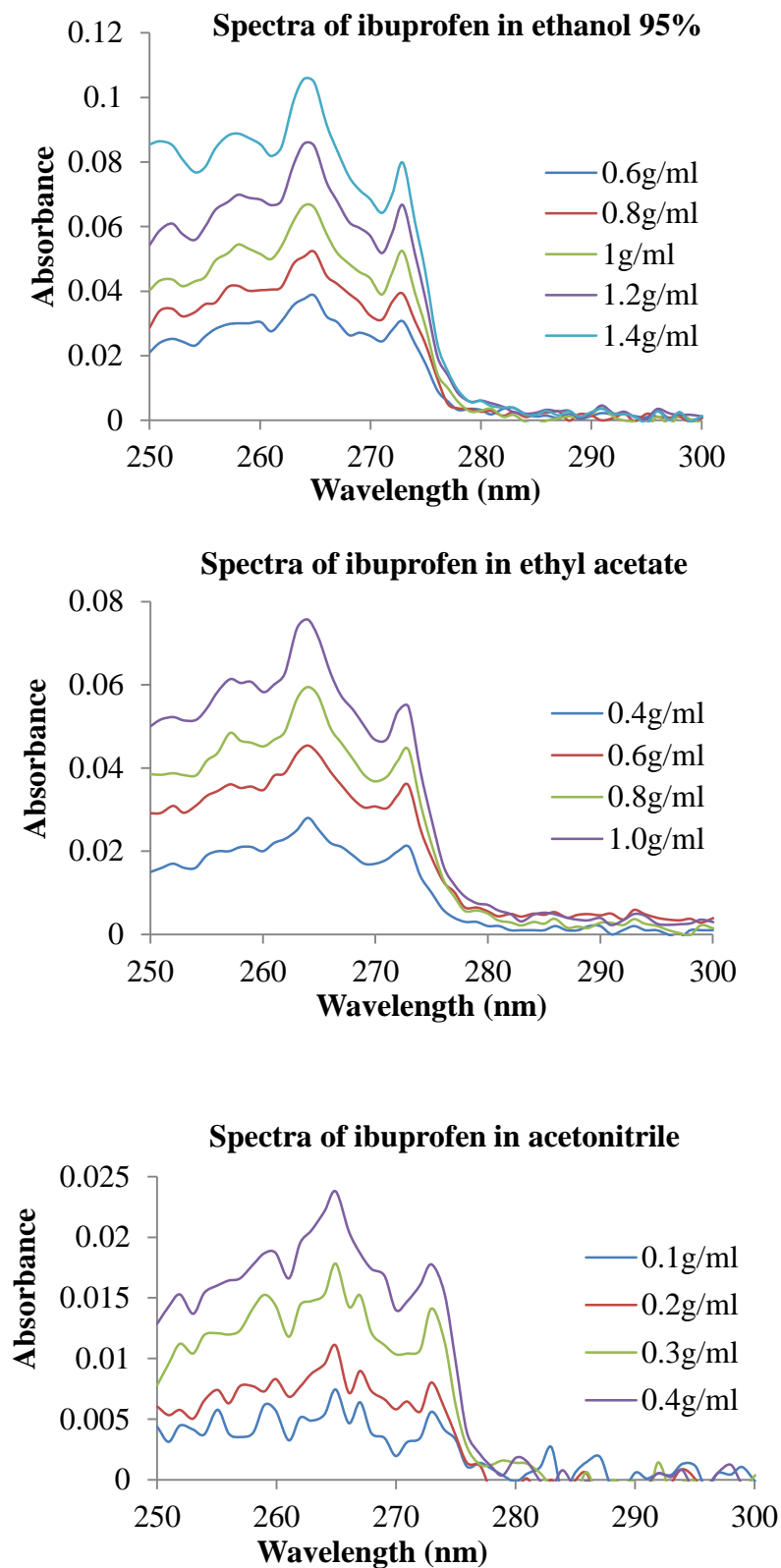


Figure 6.2 Spectra of ibuprofen in ethanol 95%, ethyl acetate and acetonitrile showing absorbance at 264 nm increase with increasing concentration of solutions.

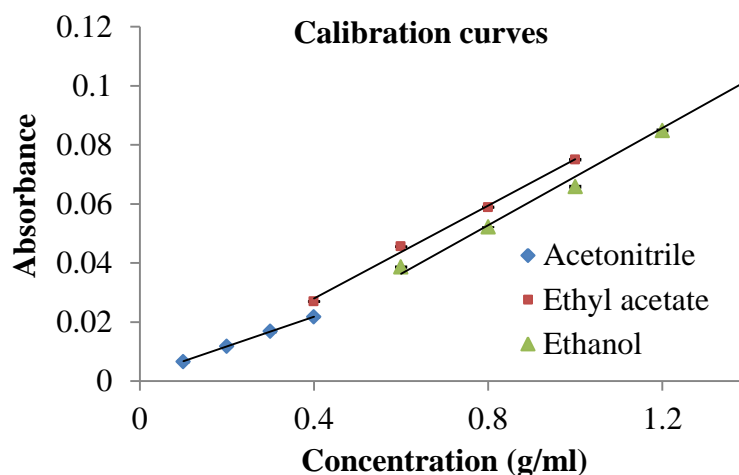


Figure 6.3 Calibration curves were obtained from the absorbances at 264 nm of the known concentration solutions.

The Beer-Lambert law states that the absorbance of a solution is directly proportional to the concentration of the absorbing species in the solution and the path length. Hence, ATR UV/Vis spectroscopy was employed to determine the concentration of ibuprofen in a solution for a fixed path length. The calibration curve of ibuprofen was determined by measuring the specific absorbance peak of ibuprofen at 264nm versus a range of concentrations with the fitting parameters summarised in Table 6.2.

Table 6.2 Calibration line of ibuprofen in ethanol 95%, ethyl acetate and acetonitrile at temperature from 15-35°C

Solvents	Calibration line
Ethanol 95%	$y = 0.0823x - 0.013$
Ethyl acetate	$y = 0.0786x - 0.0034$
Acetonitrile	$y = 0.0503x + 0.0017$

Using these calibration curves, the solubility of ibuprofen in solvents over the temperature range 15-35°C was calculated from the measured ATR UV/Vis curves. These ibuprofen solubility values (g/ml) in ethanol, ethyl acetate and acetonitrile were then fitted by polynomial functions which obey the above equations for the temperature range 15-35°C.

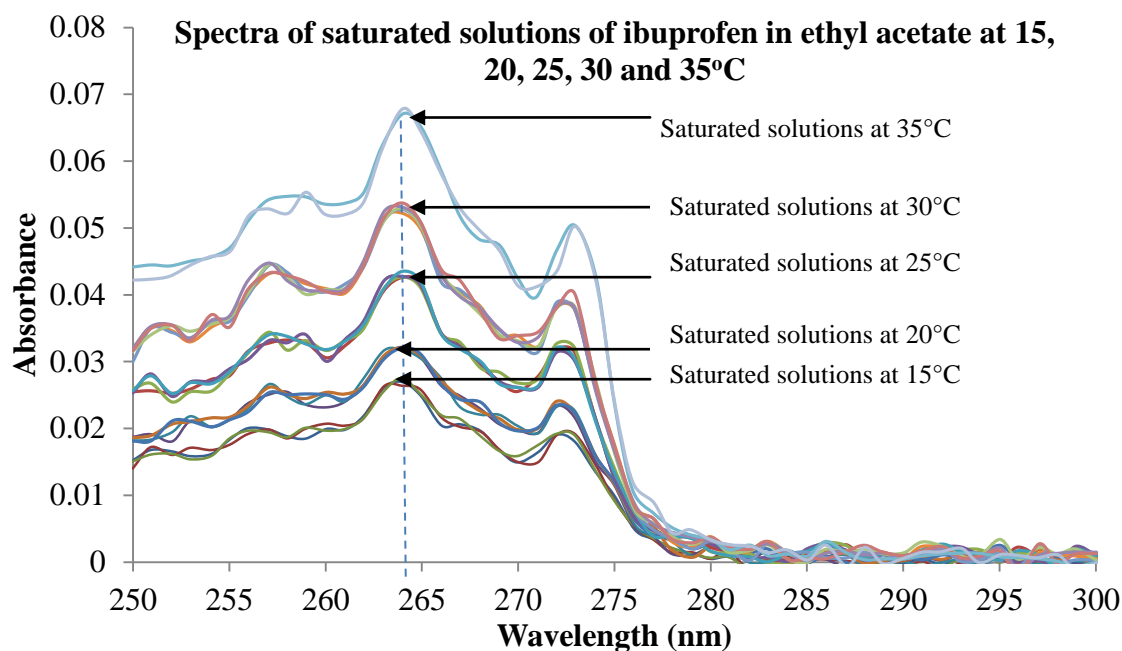


Figure 6.4 Spectra of ibuprofen in ethyl acetate showing solubility increase with increasing temperature and λ_{\max} does not shift with temperature. The λ_{\max} was not found to shift even in different solvents and concentration nor even as a function of temperature.

From the absorbance of saturated solutions and the obtained calibration curves, the solubility of ibuprofen in ethanol, ethyl acetate, acetonitrile (using ATR UV/Vis spectroscopy) and toluene (from gravimetric method) was calculated and shown in Table 6.3.

Table 6.3 Solubility of ibuprofen in ethanol, ethyl acetate, acetonitrile and toluene (g/ml)

T (°C)	Ethanol 95%	Ethyl Acetate	Acetonitrile	Toluene
15	0.54 ± 0.011	0.38 ± 0.009	0.09 ± 0.001	0.31 ± 0.001
20	0.65 ± 0.007	0.45 ± 0.005	0.12 ± 0.001	0.40 ± 0.000
25	0.78 ± 0.011	0.59 ± 0.005	0.19 ± 0.006	0.51 ± 0.002
30	0.98 ± 0.029	0.72 ± 0.007	0.28 ± 0.009	0.65 ± 0.001
35	1.26 ± 0.009	0.94 ± 0.053	0.40 ± 0.005	0.82 ± 0.015

The theoretical solubility of ibuprofen in ethanol 95%, ethyl acetate, acetonitrile and toluene were calculated based on the Hilderbrand equation assuming ideal solution behaviour and compared to the data collected from experiments. The onset of melting

point temperature was obtained by DSC in section 6.2. The enthalpy and entropy of dissolution of Ibuprofen in various solvents were calculated; summarised in Table 6.5. The solubility of ibuprofen is high in ethanol, ethyl acetate and toluene and low in acetonitrile which can be rationalized on the basis of solvent polarity and the like-dissolves-like rule of thumb. e.g. a non-polar compound will be dissolved by non-polar solvents and vice versa. The polarity can be based on the dipole moment parameter. Ibuprofen is an organic compound with medium polarity due to the presence of both polar (-COOH group) and non-polar portions (benzene ring and substituted group -C₂H₆ attached to benzene ring). The dipole moment of ethanol, ethyl acetate and toluene is lower than that of acetonitrile (shown in Table 6.5) thus ibuprofen has a higher solubility in ethanol, ethyl acetate and toluene than in acetonitrile (Table 6.3).

The theoretical solubility of ibuprofen in ethanol 95%, ethyl acetate, acetonitrile and toluene were calculated based on the van't Hoff equation assuming ideal solution behaviour and compared with the data collected from experiments. The solubility of ibuprofen in ethyl acetate, ethanol 95%, acetonitrile and toluene have a discrepancy from the ideal behaviour with the experimental solubility. In the ideal case, the solubility is independent of the chemical composition of the solvent since the solute-solute, solvent-solvent and solute-solvent interaction are equal so there is no favour of any particular interaction and enthalpy of mixing is zero. However, in the less than ideal case of acetonitrile, it is shown that the intermolecular interaction energy between two solute molecules is stronger than between solvent and solute molecules. The enthalpies of solutions are all positive so they are endothermic in all cases. The solubility of a solute is determined by the properties in equilibrium with the solvents and the conditions for the solute in solution.

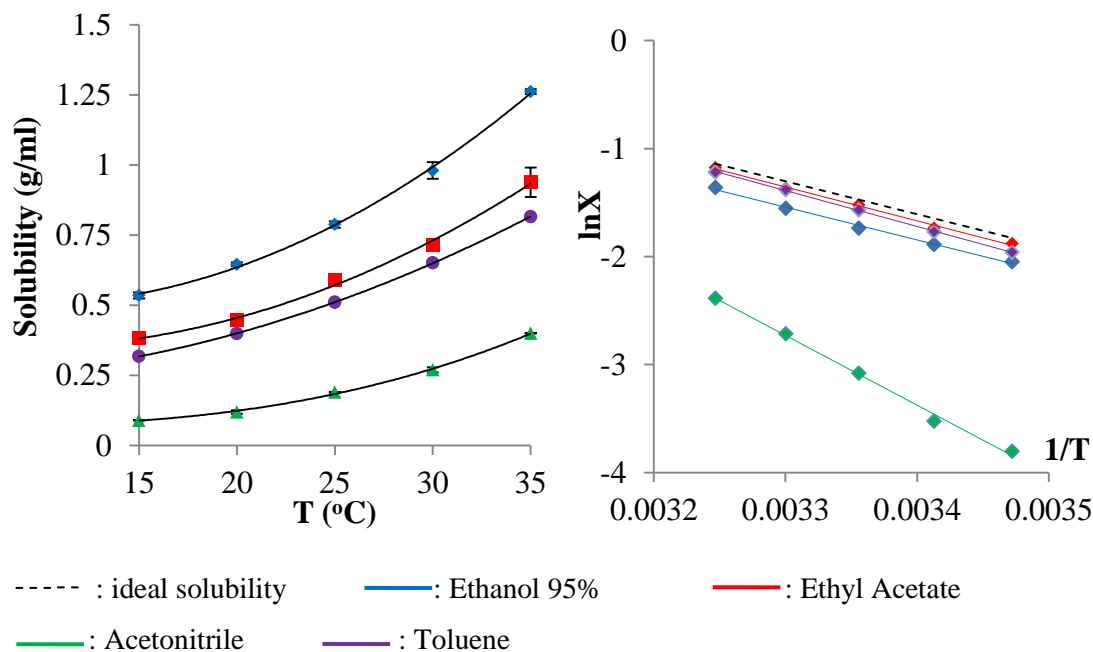


Figure 6.5 Polynomial regression lines of the solubility of ibuprofen in ethanol, ethyl acetate, acetonitrile and toluene at temperatures from 15-35°C (left); and plot of $1/T$ versus $\ln X$ of the ideal solubility and the real solubility (right).

The activity coefficient γ as a function of temperature is shown in Table 6.4. The values of γ in acetonitrile are from 3.57-7.69 which is higher than that in ethanol, ethyl acetate and toluene. When examining the solubility of a solute in different solvents, the activity coefficient completely accounts for the effect of solvent [162]. Ibuprofen is found to behave differently in various solvents according to the values of γ . In acetonitrile, where γ values are much greater than 1.0, the solution behaviour becomes more nearly ideal as the temperature increases. The high values of γ in acetonitrile are due to a consequence of weaker interactions between ibuprofen molecules and acetonitrile, whereas the almost ideal values of γ in ethyl acetate, ethanol and toluene are due to stronger interactions between ibuprofen and these solvent molecules. This indicates that ibuprofen molecules generally do not exhibit much affinity for acetonitrile or maybe rather that acetonitrile does not have affinity for ibuprofen molecule. Therefore, the results presented here, as well as those presented previously [164], support the fact that ibuprofen is principally a lipophilic compound.

Table 6.4 Calculated activity coefficients of ibuprofen in various solvents as a function of temperature

Activity Coefficients γ	15	20	25	30	35
Ethanol 95%	1.41	1.42	1.44	1.40	1.35
Ethyl Acetate	1.05	1.09	1.05	1.07	1.04
Acetonitrile	7.60	6.84	4.95	4.24	3.57
Toluene	1.24	1.22	1.18	1.15	1.14

The solubility data were validated either from the gravimetric method or from the literature. Possible uncertainties in the solubility measurements in this study could be due to the errors in the weighing materials, evaporation of solvents when dissolving the materials, variations in water bath temperature when preparing the saturation solution and any incomplete settling of the excess ibuprofen solids in the gravimetric method. However, the solubility and activity coefficient of ibuprofen measured in this study is quite similar with literature data [162, 165].

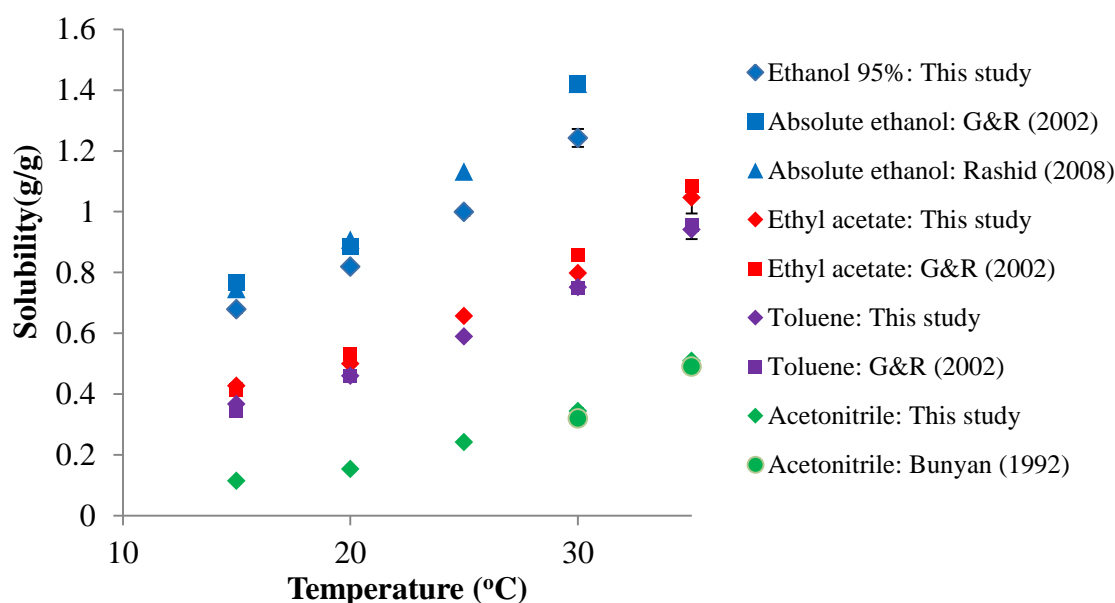


Figure 6.6 Comparison of the solubility (a) in ethanol; (b) in ethyl acetate; (c) in toluene; (d) in acetonitrile in this study with published data.

There are a few solubility data of ibuprofen in the solvents studied are available in the literature but they are obtained from the gravimetric method which consumes more time and labour compared to using the ATR UV/Vis spectroscopy. Solubility data for

ibuprofen in absolute ethanol [5, 158, 162, 166] and a mixture of ethanol and water [158, 166] are available in the literature.

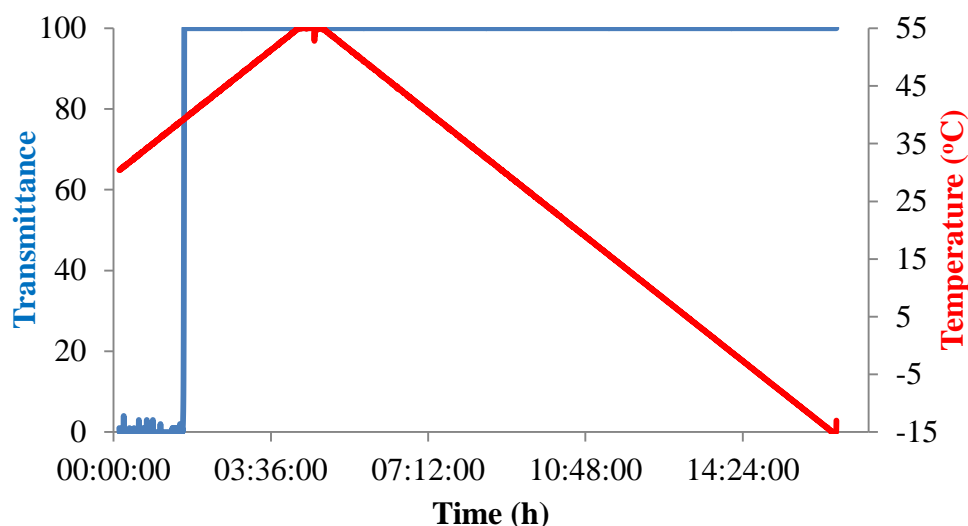
Table 6.5 Enthalpy of dissolution, ΔH , and entropy of dissolution, ΔS , derived from solubility data, together with calculated activity coefficient and temperature dependence fitting parameter. Logarithm of activity coefficients of as a function of saturation temperature ($\text{Ln}\gamma = aT + b$)

Solvents	Ethanol 95%	Ethyl Acetate	Acetonitrile	Toluene
Dipole moment	1.69	1.78	3.92	0.36
Solubility (g/ml) 20°C	0.65	0.45	0.12	0.4
ΔH (KJ/mol)	25.23	26.16	53.76	27.6
ΔS (KJ/K ⁻¹ mol ⁻¹)	0.07	0.075	0.154	0.08
γ (T = 15-35°C)	1.35-1.44	1.04-1.09	3.57-7.60	1.14-1.24
a	-0.002	-0.0008	-0.0398	-0.0045
b	0.3897	0.077	2.6482	0.2837

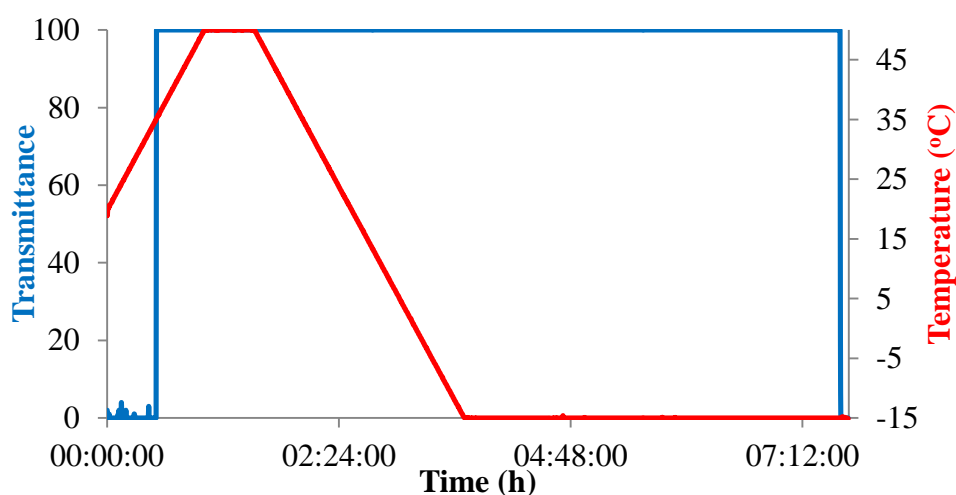
6.4 Polythermal crystallisation as a function of solvent

The polythermal crystallisation of ibuprofen in ethanol (1.4g/ml and 0.98g/ml), ethyl acetate (0.72g/ml), acetonitrile (0.28g/ml), and toluene (0.65g/ml) as a function of solution cooling/heating rate were carried out to investigate the MSZW. The raw data of MSZW measurements for ibuprofen in ethyl acetate, acetonitrile and toluene are shown in Appendix A1.

The crystallisation temperature for ibuprofen in ethanol 95% at the different concentrations 1.4 (g/ml) ($T_{\text{sat}} \approx 38^\circ\text{C}$) and 0.98 (g/ml) ($T_{\text{sat}} \approx 30^\circ\text{C}$) was not obtained since the solutions barely crystallised at the cooling rates 0.1; 0.2; 0.3; 0.4 and 0.5°C/min (see Figure 6.7).



(a)



(b)

— : Temperature; — : transmittance

Figure 6.7 Experimental polythermal data for ibuprofen in ethanol 95% solution illustrating that (a) ibuprofen (1.4g/ml) does not crystallise under polythermal crystallisation at a heating/cooling rate of $0.1\text{ }^{\circ}\text{C}/\text{min}$ when cooling from 55°C to -15°C ; (b) ibuprofen (0.98g/ml) does not crystallise under polythermal crystallisation at heating/cooling rate $0.5^{\circ}\text{C}/\text{min}$ when cooling down from 50°C to -15°C . Crystallisation only occurs during the hold segment of the program i.e after the cooling stage is complete.

It was also shown that the less concentrated solution (0.98g/ml) was likely to have higher probability to nucleate than the more concentrated solution (1.4g/ml). This perhaps reflects the fact that the solutions in ethanol require longer induction time for cluster aggregation and to form the nuclei which can grow into crystals.

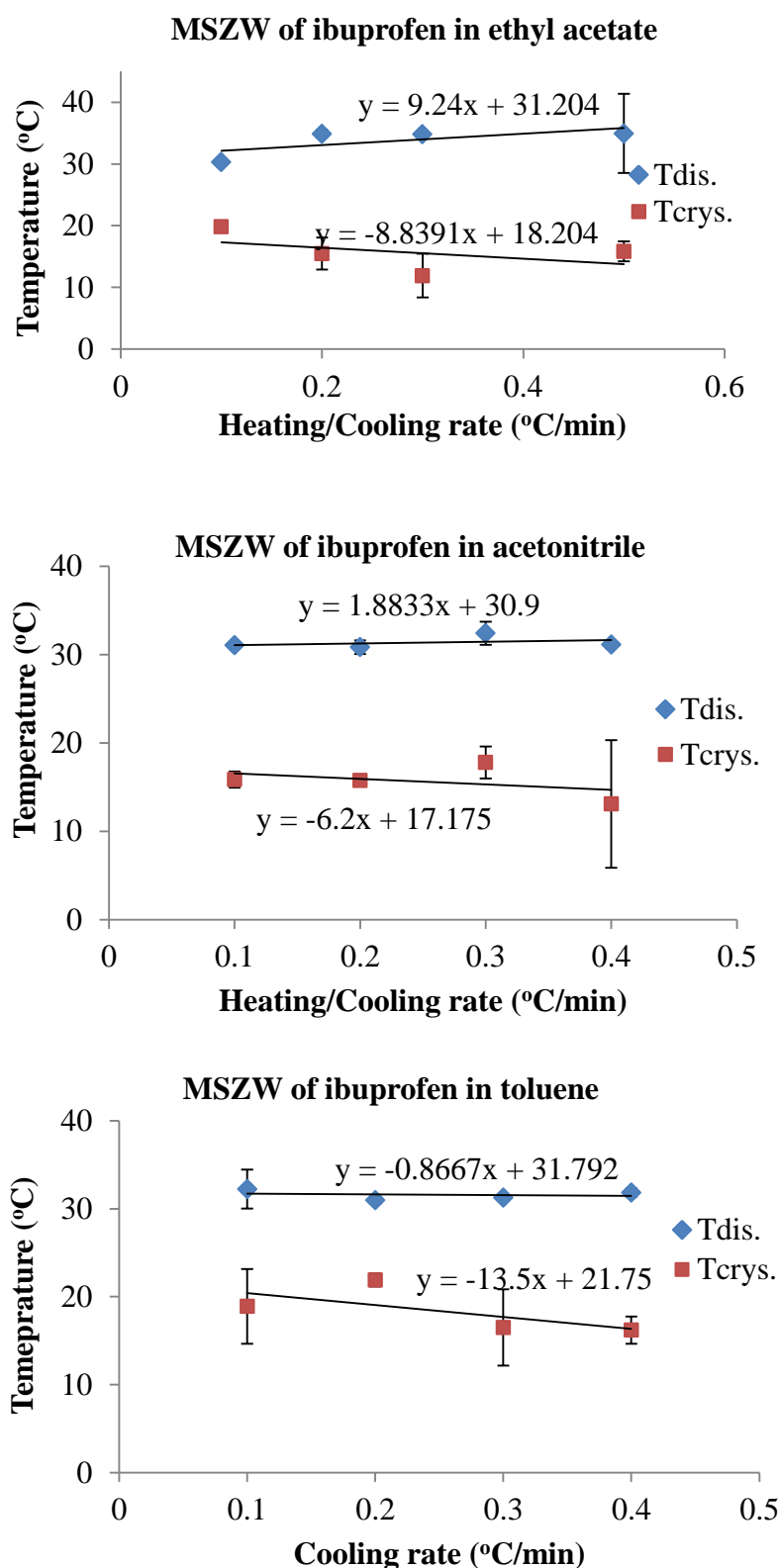


Figure 6.8 Plots of the dissolution and nucleation on-set temperatures for ibuprofen in ethyl acetate (0.72g/ml), acetonitrile (0.28g/ml), and toluene (0.65g/ml) as a function of solution cooling/ heating rate. The dissolution and crystallisation temperature are determined from the intercepts.

The plots of temperature versus the cooling rates are presented in Figure 6.8 showing the dissolution/crystallisation temperature dependency on the heating and cooling rates. The undercooling temperature decreases with decreasing heating/cooling rate. The MSZW is a parameter to indicate how deep the solution has to be undercooled before the nucleation process starts to occur. It is quite obvious with slow cooling rate, the size of clusters in solution can follow the change in the solution state so that the MSWZ is narrower; whilst the structure changes in solution are slower than the change of the temperature with the rapid cooling (high cooling rate) so the MSZW becomes wider [96]. Table 6.6 summarises the MSZW of ibuprofen in ethyl acetate, acetonitrile and toluene and the relationship between $\text{Log}(b)$ vs $\text{Log}(\Delta T)$.

Table 6.6 MSZW of ibuprofen in ethyl acetate, acetonitrile and toluene solutions and the relationship between $\text{Log}(b)$ vs $\text{Log}(\Delta T)$

Solvents	T_{dis} ($^{\circ}\text{C}$)	T_{crys} ($^{\circ}\text{C}$)	MSZW ($^{\circ}\text{C}$)	$\text{Log}(b)$ vs $\text{log}(\Delta T)$
Ethyl acetate	31.2	18.2	13.0	$y = 1.549x - 2.54$
Acetonitrile	30.9	17.2	13.7	$y = 3.268x - 4.563$
Toluene	31.8	21.8	10.0	$y = 0.939x - 1.700$

The MSZW is not very big compared to many pharmaceutical compounds. It was also shown that the slopes of dissolution and crystallisation temperature lines are rather flat suggesting the intrinsic barrier but it does not really depend on cooling/heating rates.

It was seen that the dissolution temperature does not fluctuate much while crystallisation temperature is quite susceptible to the cooling or heating rate. The crystallisation temperature generally decreases with increasing cooling rate. It can be elucidated by the assumption that the higher the cooling rate is, the formation of nuclei and clusters are expected to occur faster due to high supersaturation being reached quickly. A large number of smaller and unstable nuclei are generated which are likely to dissolve or rearrange themselves to achieve the stable crystals. On the contrary, the slow cooling with lower cooling rate is associated with the lower rate of supersaturation production. Hence, it is possible that there are a small amount of nuclei which possess excess the critical size and these nuclei grow directly into mature crystals, which results in nucleation occurring at a higher temperature.

In this study the crystallisation temperature of ibuprofen in these solvents was found to be quite scattered due to the high solubility of ibuprofen in organic solvents. Solutions were very viscous, in particular in ethanol, resulting in higher interfacial tensions and potentially unstable nucleation. Any foreign material or the molecular ordering or embryo still present somewhere in the reactor such as the cap of crystallisers or the wall of the reactor, or the stirrer can cause heterogeneous nucleation. Thus it is difficult to state which solvent produces the widest MSZW. In summary it can be concluded that the MSZW of ibuprofen is from 10°C to 13.7°C. Ibuprofen in toluene has a smallest MSZW and in ethanol scarcely crystallises even though experiments were implemented at two different concentrations (1.4g/ml and 0.98g/ml).

The polythermal (slow cooling) crystallisation experiments were performed on Ibuprofen systems to find the kinetics of the nucleation process including nucleation order and nucleation constant from the Nyvlt equation and MSZW. The nucleation order determined by the slope of these straight lines is 1.55, 3.27 and 0.94 in ethyl acetate, acetonitrile and toluene respectively which indicated that ibuprofen nucleated easier in toluene and ethyl acetate solutions than in acetonitrile solutions.

6.5 Isothermal crystallisation as a function of solvent

The raw data of induction times of ibuprofen in acetonitrile, toluene, ethanol 95% and acetonitrile are shown in Appendix A2. An example of induction of ibuprofen in acetonitrile is shown in Figure 6.9.

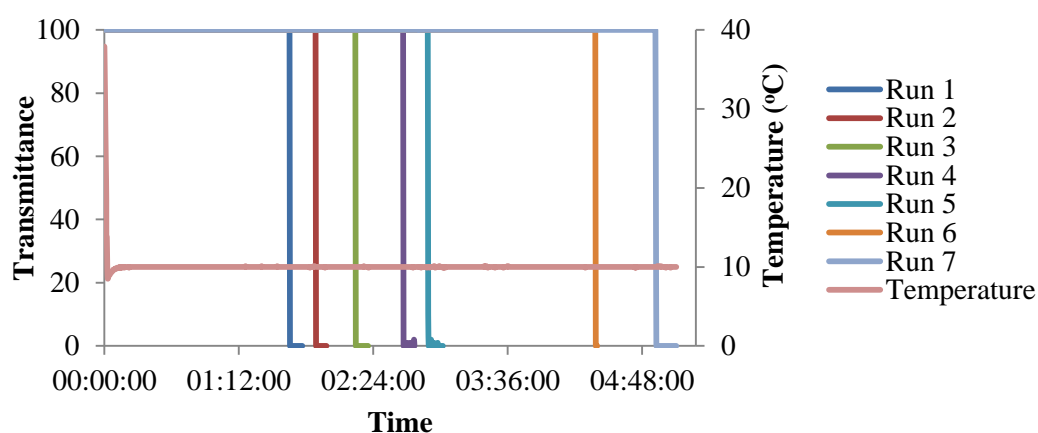


Figure 6.9 An example of the measured induction time of ibuprofen in acetonitrile (0.4g/ml) at $S = 6.86$.

The induction time experiments were repeated in many isothermal crystallisation runs and summarized in Table 6.7 and Figure 6.10.

Table 6.7 Induction times of acetonitrile, toluene, ethanol 95% and ethyl acetate

Acetonitrile			
T	S	Induction time (mins)	Average
-5°C	24.9	25; 26; 76	42.3 ± 29.2
0°C	15.9	52; 83; 85, 98; 109 and 107	89 ± 21.1
5°C	10.4	76; 101; 102; 112; 142; 197	121.7 ± 42.6
10°C	6.86	99; 113; 134; 160; 173; 263; 295	176.7 ± 74.9
Toluene			
T	S	Induction time (mins)	Average
0°C	5.52	20; 31; 35; 38	31 ± 7.9
5°C	4.84	34; 87; 92; 115; 135; 136; 161	108.6 ± 41.9
10°C	3.84	38; 41; 45; 46; 56; 142; 48; 55	55.9 ± 34.2
15°C	2.91	91; 98; 110; 112; 135; 141; 168; 173	128.5 ± 30.9

Ethanol 95%			
T(°C)	S	Induction time (mins)	Average
0°C	5.02	42; 117; 208; 222; 27; 324	156.7 ± 115.3
5°C	4.04	94; 49; 289; 489; 580	300.2 ± 234.3
10°C	3.26	424; 608; 140; 205; 834; 967; 101; 679	494.8 ± 328.4
Ethyl acetate			
T(°C)	S	Induction time (mins)	Average
15°C	2.68	12; 18; 48; 107; 34; 38; 82; 96	54.4 ± 36.4
20°C	2.14	70; 99; 82; 19	67.5 ± 34.5
25°C	1.71	73; 124; 262; 104	140.8 ± 83.5

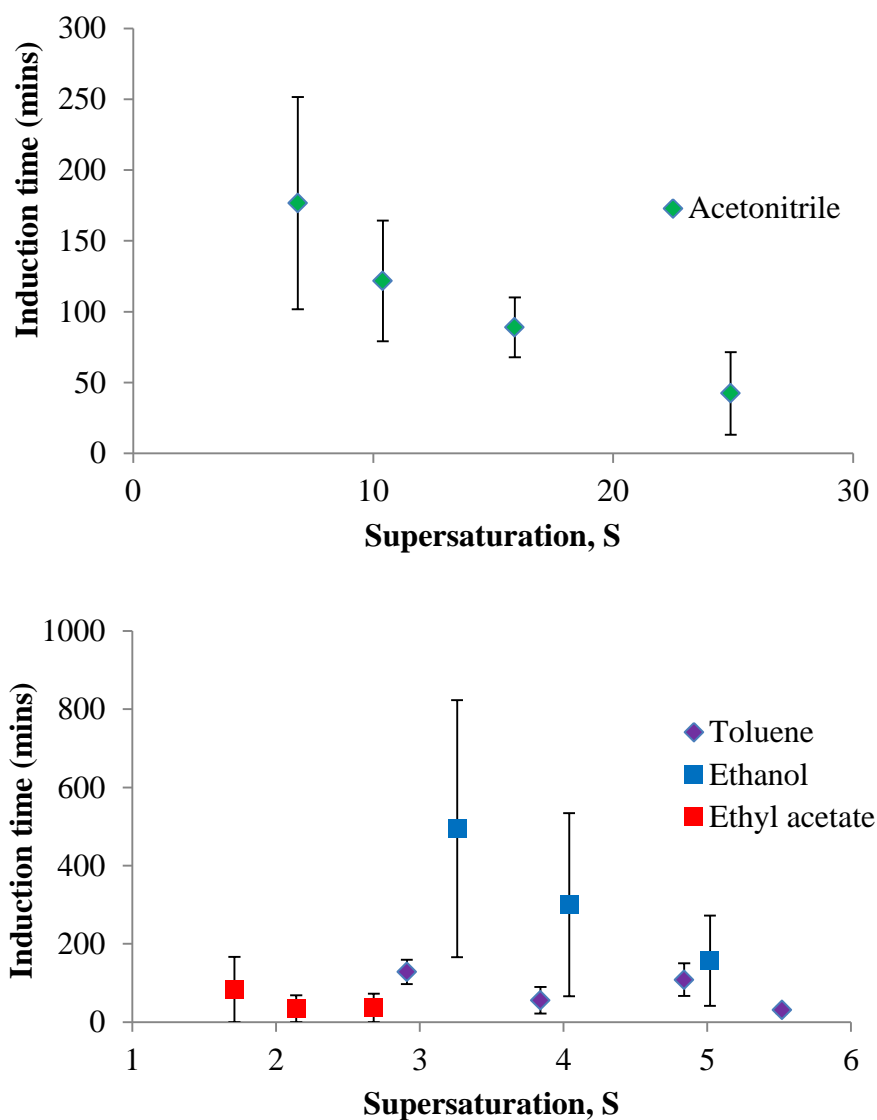


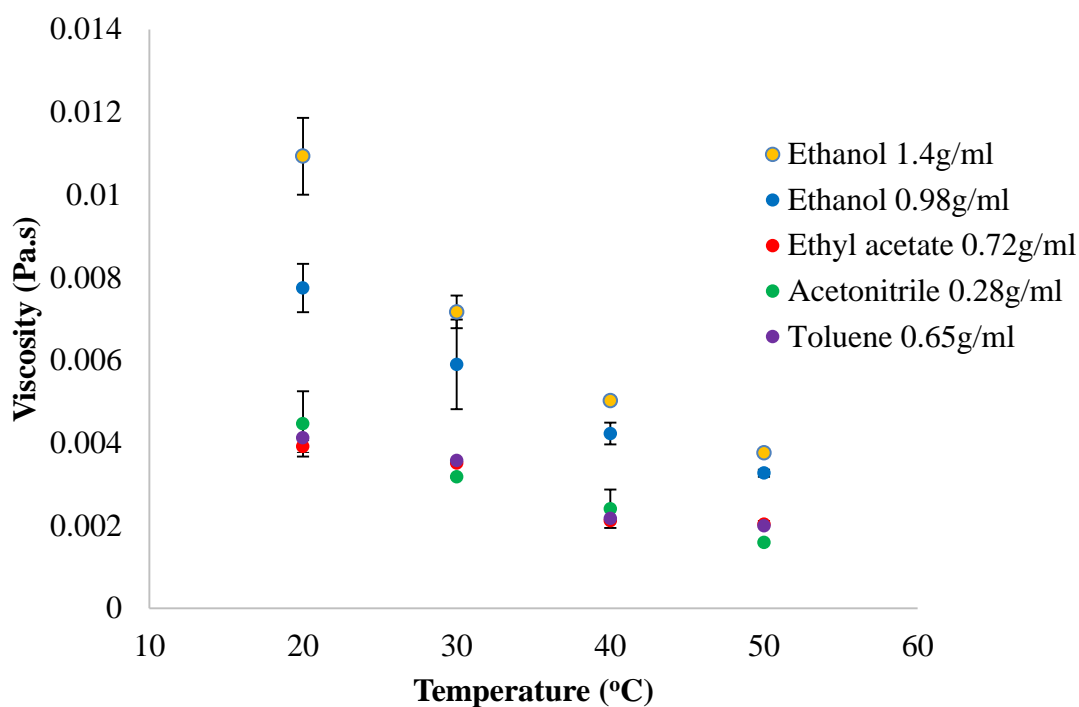
Figure 6.10 Induction time of acetonitrile, toluene, ethanol 95% and ethyl acetate at different supersaturation ratios.

The isothermal (crash cooling) crystallisation experiments for the ibuprofen system was attempted to investigate the induction time. From the data it is apparent that the induction times increase, as expected, with higher temperatures (lower supersaturations) and vice versa. Comparing the MSZW and induction time data, it is likely that ibuprofen in toluene and ethyl acetate solvents would have a smaller MSZW and induction time when compared to acetonitrile and ethanol. However, the data has high variation in all systems, very large for the ethyl acetate and ethanol 95% systems so many repetitions should be carried out to obtain probability distributions of induction times in the cases of ethanol 95% and ethyl acetate. Similarly, the induction period of aqueous solution of KCl scattered rather large [167] which is often found and arise from

the stochastic character of nucleation. This is anticipated as nucleation is considered to be a random stochastic process [26]. Jiang and ter Horst [168] have developed a method for determination of nucleation rates from an examination of the cumulative probability distributions of induction times in agitated solutions due to the stochastic nature of nucleation process; this reflects the variation of the nucleation time. The appearance of a nucleus can be considered as a random process at a constant supersaturation level. The effective nucleation rate varies so widely from one sample to another, defining a typical nucleation rate or time is not trivial. Hence, a measure of the average nucleation time or the distribution of induction time might be required [169].

Ibuprofen in ethanol 95% is a viscous solution. High viscosity has a tendency to prevent nucleation [96]. Therefore, high viscosity results in less freedom and space for solute molecules to diffuse and aggregate together to form molecular clusters and then nuclei in supersaturated solutions according to classical nucleation theory. Myerson et al. [170, 171] measured the diffusion coefficients in a number of systems in aqueous supersaturated solution. The diffusion coefficient was shown to decrease rapidly with increasing concentration in the supersaturated region.

Hence, in this study the viscosity of supersaturated solution was examined as a function of solvents and temperatures at the temperature range 20°C-50°C using the Bohlin Gemini rheometer and viscosity calculated using the Newtonian model fit is presented in Figure 6.11.



Ethanol 95% 1.4g/ml : $T_{\text{sat}} = 38^{\circ}\text{C}$

Ethanol 95% 0.98g/ml, ethyl acetate 0.72 g/ml, acetonitrile 0.28g/ml and toluene 0.65g/ml: $T_{\text{sat}} \approx 30^{\circ}\text{C}$

Figure 6.11 Viscosity of ibuprofen solution examined as a function of solvents and temperature.

It is clearly shown that the saturated solutions at $T = 30^{\circ}\text{C}$ of ibuprofen in ethanol 95% (0.98g/ml) has much higher viscosity compared to ibuprofen in ethyl acetate (0.72g/ml), acetonitrile (0.28g/ml) and toluene (0.65g/ml) solutions. The higher concentration of ibuprofen in ethanol shows a much higher viscosity. The system has demonstrated whilst viscosity of ibuprofen in ethanol showed a strong dependence on temperature, viscosity in ethyl acetate, acetonitrile and toluene are quite similar and showed less dependence on temperature. The viscosity of ibuprofen in ethanol increased significantly when the solution was cooled down to 30-20°C (see Figure 6.11) which might result in increasing difficulty of the solutions to crystallise at low temperature at any cooling rate 0.1-0.5°C/min and the less concentrated solutions in ethanol associated with the lower viscosity have a higher probability to nucleate than the more concentrated solutions.

The interfacial energy, a parameter involving the growing crystal and the surrounding mother liquor, can be estimated from a plot of $\ln\tau_{\text{ind}}$ versus $T^{-3}(\ln S)^{-2}$. This uses equation

2.26 in chapter 2 with the molecular volume of ibuprofen taken as $306\text{\AA}^3 \approx 3.06 \cdot 10^{-28} \text{ m}^3$ (the volume of a unit cell $V = 1224.54 \text{\AA}^3$ and the number of molecules in a unit cell $Z = 4$; assuming 4 molecules occupied the whole volume of the unit cell and from this the volume of an ibuprofen molecule was calculated); the Boltzmann constant $K = 1.3805 \cdot 10^{-23} \text{ J/K}$. The calculated interfacial energy from the slopes of the straight lines is shown in the Figure 6.12 and results in the value shown in Table 6.8 and the plots of the dependence of the size of the critical nucleus as a function of temperature and supersaturation are shown in Figure 6.13.

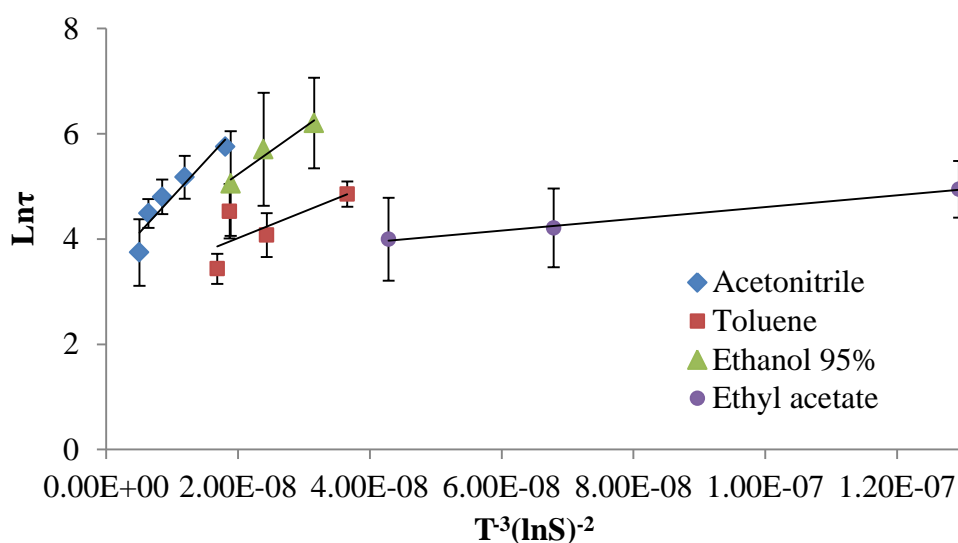


Figure 6.12 Plot of $\text{Ln}\tau_{\text{ind}}$ versus $T^{-3}(\text{lnS})^{-2}$ of ibuprofen in 4 solvents. Interfacial tension can be calculated from the slope of the line.

Table 6.8 The interfacial energy calculated from the slopes of the straight lines $\text{Ln}\tau_{\text{ind}}$ versus $T^{-3}(\text{lnS})^{-2}$

	$\text{Ln}\tau_{\text{ind}}$ versus $T^{-3}(\text{lnS})^{-2}$	Interfacial energy (J/m^2)
Acetonitrile	$y = 1\text{E}+08x + 3.436$	$5.52 \cdot 10^{-3}$
Toluene	$y = 5\text{E}+07x + 3.0103$	$4.38 \cdot 10^{-3}$
Ethanol	$y = 9\text{E}+07x + 3.4576$	$5.33 \cdot 10^{-3}$
Ethyl acetate	$y = 1\text{E}+07x + 3.4913$	$2.56 \cdot 10^{-3}$

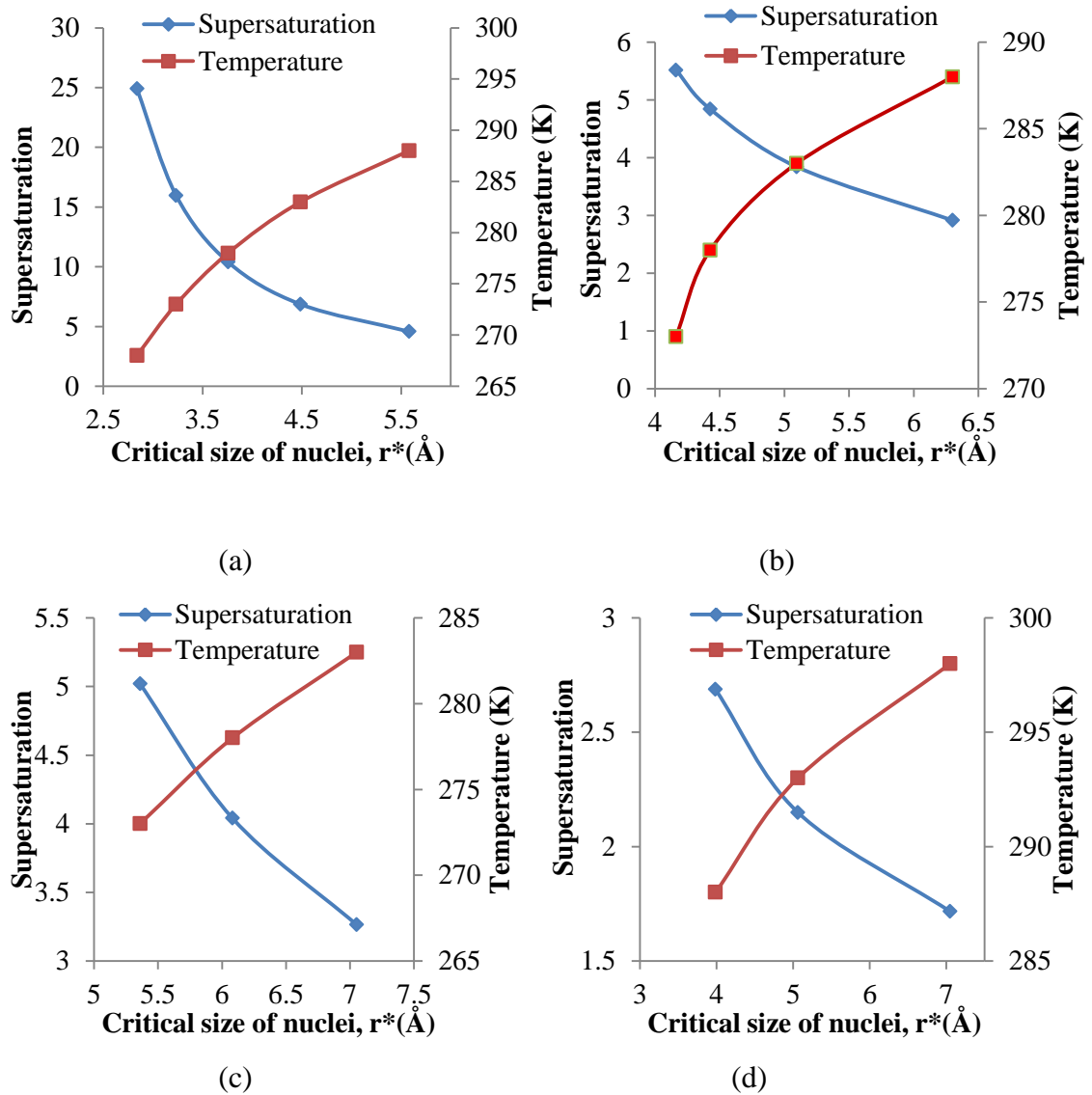


Figure 6.13 The size of the critical nucleus as a function of temperature and supersaturation (a) in acetonitrile; (b) in toluene; (c) in ethanol 95% and (d) in ethyl acetate.

It is clearly shown that, as expected, the radius of the critical nuclei increases with decreasing the degree of supersaturation and increasing temperature. This is consistent with homogeneous nucleation theory as discussed in chapter 2. If the solutions are maintained at higher temperature associated with the lower supersaturation, the size of the critical nuclei will increase. At each concentration and temperature of solution a particular size of cluster for the nucleation process is expected. If the state of solution varies, the size of critical cluster also changes resulting in a wider or smaller MSZW; hence, MSWZ depends on many parameters such as supersaturation, temperature, cooling rate, agitation speed etc.

6.6 Conclusions

This chapter presented the DSC data including melting points and enthalpy of dissolution of ibuprofen, solubility data, MSWZs and induction times for ibuprofen of RS-ibuprofen in a range of solvents. The solubility, enthalpy and entropy of dissolution and activity coefficient of ibuprofen at different temperatures were compared to the published data showing quite similar values. The experimentally measured solubility of ibuprofen is lower than calculated by the van't Hoff equation showing discrepancy from the ideal behaviour with the real solubility, consistent with strong solute-solute interactions, particularly in the case of acetonitrile. ATR UV/Vis spectroscopy was found to be a rapid and efficient technique for the measurement of solubility for strong absorbing materials but was found to have some limits in terms of the refractive index of some solvents.

It was also found that the MSZW of ibuprofen is relatively small. This is not typical for many organic crystallising systems where the induction of the nucleation process can be slow and limited. Though the MSWZs and the induction times for ibuprofen scatter quite widely in all solvent systems, it was shown that ibuprofen has the smallest MSZW in toluene. Ibuprofen in ethanol is not a good system for studying MSZW due to the high viscosity of solution. The viscosity increases more rapidly with increasing of concentration in the supersaturated region. This retards the cluster diffusion in solutions and the formation of nuclei. In this system, higher concentration and holding solutions at lower temperatures make even solution harder to crystallise. The induction times increase with decreasing supersaturation, which are in quite good agreement with classic nucleation theory. The critical nucleus diameter and thus size decreases as the supersaturation increases. The nucleation order and the calculated interfacial energy is summarised in Table 6.9.

Table 6.9 The nucleation order and calculated interfacial energy calculated from MSZW

	Ethanol	Ethyl acetate	Acetonitrile	Toluene
Nucleation order	-	1.55	3.27	0.94
Interfacial energy (J/m ²)	5.33*10 ⁻³	2.56*10 ⁻³	5.52*10 ⁻³	4.38*10 ⁻³

The solubility and MSZW results are essential and useful for the design of a crystallisation process for the measurement of crystal growth rate. The solubility and MSZW indicates that the measurement of the growth rate of spontaneously nucleated single crystals should be performed in the range of $\Delta T > 13^{\circ}\text{C}$ in this research and the seeding experiments can be carried out within the MSZW ($\approx 13^{\circ}\text{C}$).

7 Growth kinetic and mechanism

Summary:

The growth rate on the {001} and {100} faces versus supersaturation for spontaneously nucleated single crystals in stagnant solutions is measured as a function of solvent type and reactor scale-size (0.5mL and 15mL) and the interface growth mechanism assessed. This is compared to the data recorded on the population of crystals crystallised in an agitated 7mL reactor.

7.1 Introduction

Crystals of racemic ibuprofen exhibit different crystal habits as a result of varying crystallisation conditions [5, 135-139, 141]. This material primarily exhibits a plate-like crystal morphology dominated by a large {100} face with smaller {001} and {011} side faces. So far there have been limited studies of this material concerning the crystallisation kinetics [5, 15]. Despite this, little information has been provided regarding the growth rate of spontaneously nucleated crystals nor has crystal growth rate variation of the individual faces been studied. This chapter reflects upon the growth kinetic and growth mechanism of the {001} and {011} surfaces of spontaneously nucleated single (RS)-ibuprofen crystals under diffusion limited conditions (stagnant solutions) at two scale sizes; 0.5mL and 15mL, as a function of solvent (ethanol 95%, ethyl acetate, acetonitrile and toluene) and relative supersaturation, σ , from 0.55 to 1.30 is presented.

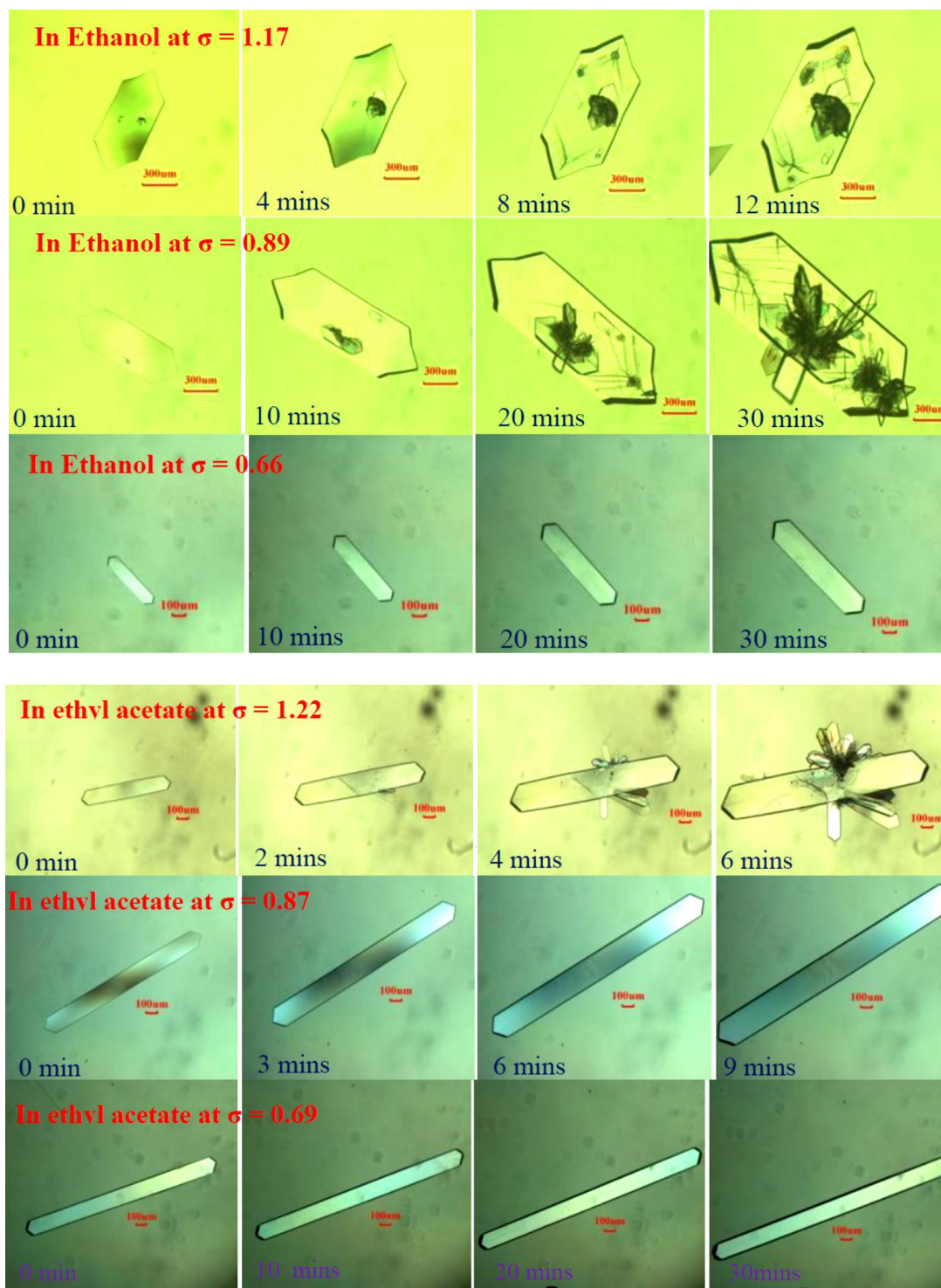
The growth mechanism of these faces was investigated by fitting growth rate data to growth kinetic models notably B&S and BCF. The growth rate of single crystals in non-agitated vessel is compared to the measurements made on a population of crystals crystallising in a 7 mL agitated vessel.

7.2 Mean growth rate of the {001} and {011} faces as a function of growth environment

A full set of the experimental growth rate data provided in this thesis is given in the Appendix B. The data comprises a total of 125 single ibuprofen crystals, spontaneously nucleated in 120-130 growth runs measured in ethanol 95%, ethyl acetate, acetonitrile and toluene over a supersaturation range from 0.54 to 1.31 at 2 scale sizes 0.5 and 15 mL.

A sequence of images of crystals grown in a 0.5mL cuvette crystallisation cell in different solvents is shown in Figure 7.1. An example of the plot the distance from the centre of the crystals along the growth normal as measured for 5 crystals in the 15ml growth cell to the faces as a function of time are shown in Figure 7.2. Simultaneously,

the ATR UV/Vis spectra and calculated solute concentration and relative supersaturation of ibuprofen in ethanol collected during crystallisation experiments to monitor the supersaturation of solution are shown in Figure 7.3 The mean growth rates of the {001} and {011} faces of single ibuprofen crystals spontaneously nucleated in ethanol, ethyl acetate, acetonitrile and toluene in 0.5 mL and 15 mL are shown in Table 7.1 and Figure 7.4.



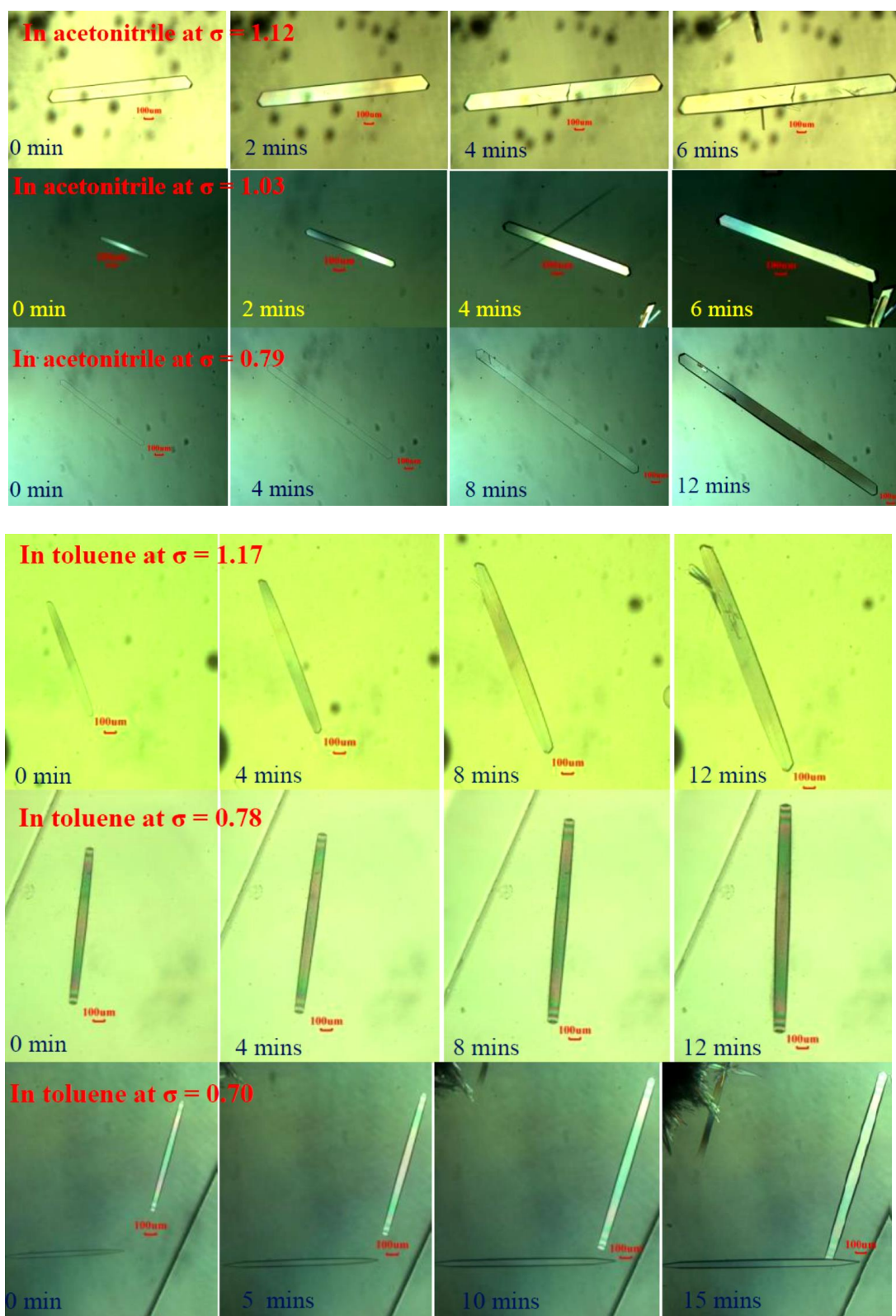


Figure 7.1 Series of optical micrographs of ibuprofen crystals grown in ethanol 95% between $\sigma = 1.17$ and $\sigma = 0.66$ (a), in ethyl acetate between $\sigma = 1.20$ and $\sigma = 0.69$ (b), in acetonitrile between $\sigma = 1.12$ and $\sigma = 0.79$ (c) and in toluene between $\sigma = 1.17$ and $\sigma = 0.70$ (d) at the 0.5ml scale size showing the growth of the crystals and their morphology as a function of solvent, elapsed time and solvent supersaturation.

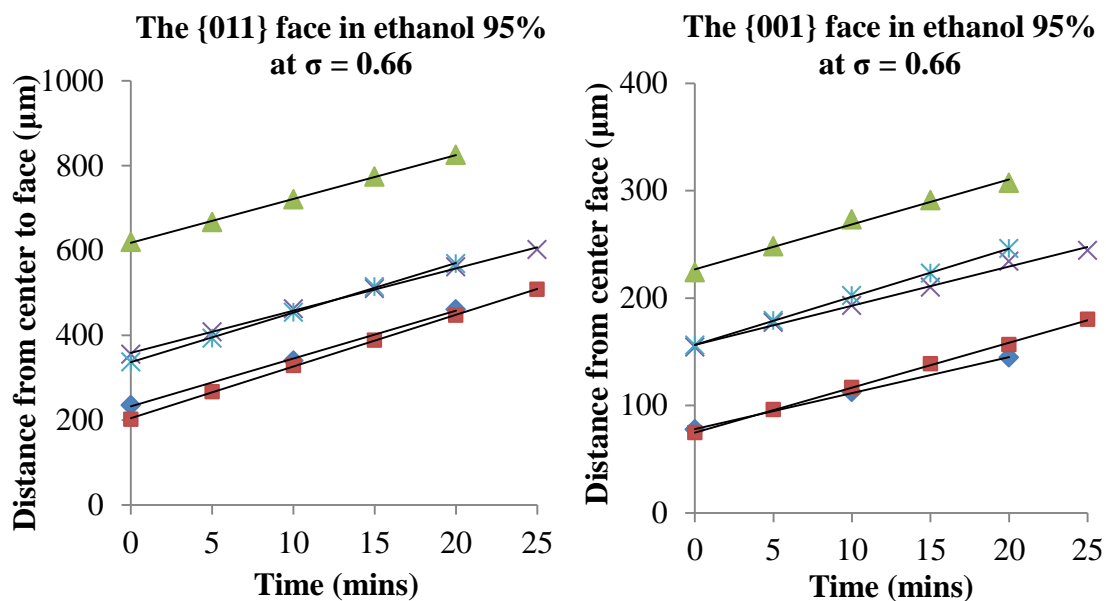


Figure 7.2 The distance from the centre of the crystals to the faces was plotted as a function of time. The slope of the line gives the measured growth rate of the face measurement for the estimation of the growth rate for the {011} and {001} face.

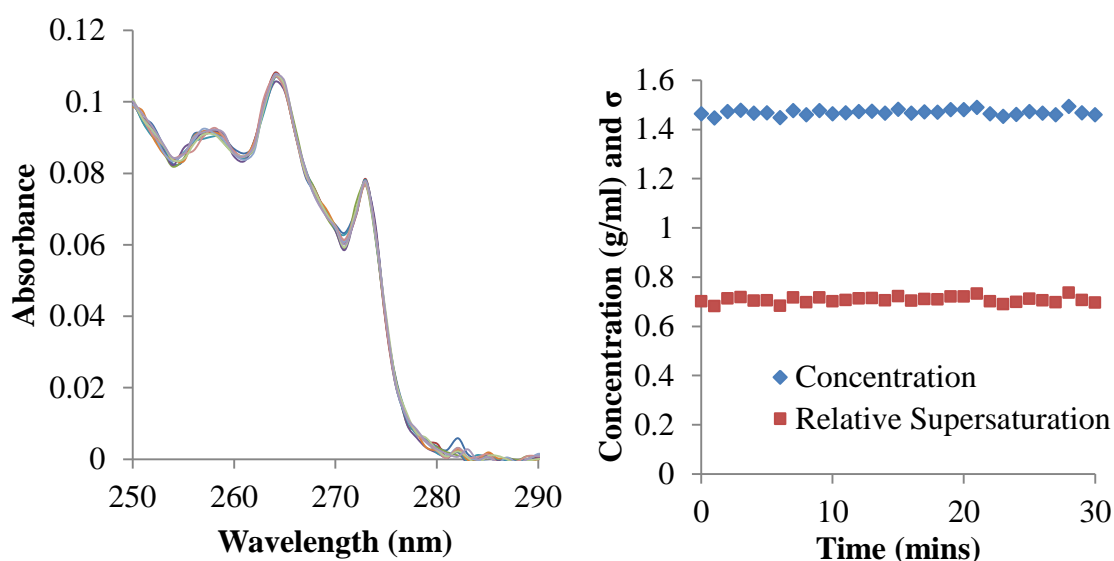
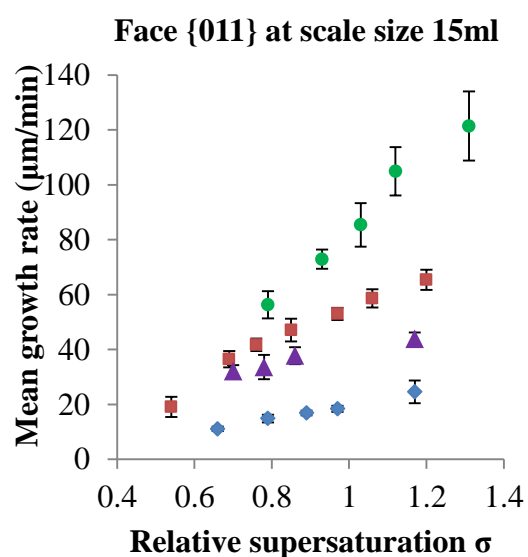
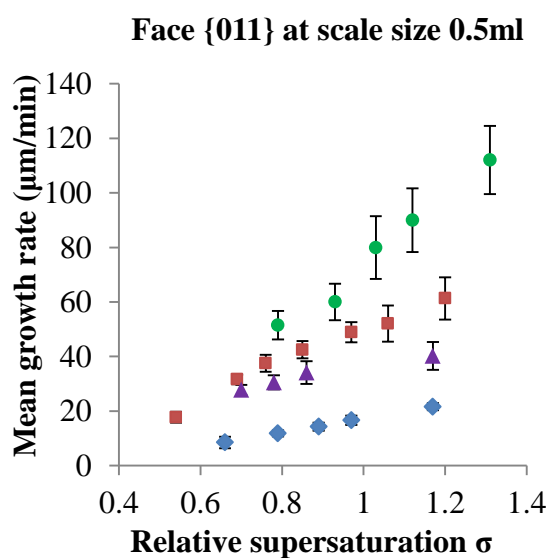


Figure 7.3 ATR UV/Vis spectra of ibuprofen in ethanol during crystallisation obtained every minute in 50 mins (left); Solute concentration and relative supersaturation calculated from the UV/Vis absorbance calibration model in 15mL jacketed vessel (right).

Table 7.1 Mean growth rate of face {011} and {001} of ibuprofen in ethanol 95%, ethyl acetate, acetonitrile and toluene in prototype cell 0.5 mL and jacketed-vessel 15 mL

Choice of solvents	σ	Number of crystals	Mean Growth Rate R($\mu\text{m}/\text{min}$)			
			$R_{\{001\}}$		$R_{\{011\}}$	
			0.5mL scale	15mL scale	0.5mL scale	15mL scale
Ethanol 95%	0.66	5	3.6 ± 0.7	3.8 ± 0.5	8.5 ± 2.1	11.1 ± 0.8
	0.79	8	4.6 ± 0.4	5.6 ± 1.0	11.8 ± 1.1	14.9 ± 1.4
	0.89	5	6.2 ± 0.8	7.2 ± 0.8	14.3 ± 1.5	16.9 ± 0.9
	0.97	5	8.0 ± 0.9	8.9 ± 0.4	16.6 ± 1.7	18.4 ± 1.1
	1.17	5	13.2 ± 1.6	13.2 ± 0.7	21.6 ± 1.3	24.6 ± 4.1
Ethyl acetate	0.54	6	1.8 ± 0.3	1.9 ± 0.3	17.7 ± 2.0	19.1 ± 3.7
	0.69	5	3.4 ± 0.4	3.9 ± 0.9	31.6 ± 1.8	36.5 ± 3.0
	0.76	6	4.4 ± 0.6	5.8 ± 0.4	37.5 ± 3.1	41.7 ± 4.1
	0.85	7	6.3 ± 0.4	6.6 ± 0.7	42.5 ± 3.2	47.1 ± 2.1
	0.97	7	8.3 ± 0.8	10.1 ± 0.8	48.9 ± 3.7	53.0 ± 2.2
	1.06	7	9.7 ± 0.8	12.6 ± 0.5	52.1 ± 6.6	58.6 ± 3.3
	1.20	7	12.2 ± 2.6	13.8 ± 1.2	61.3 ± 7.7	65.4 ± 3.7
Acetonitrile	0.79	6	3.6 ± 0.7	4.8 ± 1.0	51.5 ± 5.2	56.3 ± 5.0
	0.93	5	5.0 ± 0.3	5.8 ± 0.3	60.0 ± 6.7	72.9 ± 3.5
	1.03	6	7.4 ± 2.0	9.3 ± 0.6	79.9 ± 11.5	85.4 ± 7.9
	1.12	6	10.7 ± 2.0	12.7 ± 1.4	90.0 ± 11.7	104.9 ± 8.8
	1.31	6	14.6 ± 2.6	16.9 ± 1.4	112 ± 12.5	121.4 ± 12.6
Toluene	0.7	6	1.8 ± 0.2	2.4 ± 0.5	27.8 ± 1.8	32.0 ± 2.3
	0.78	5	2.1 ± 0.2	2.8 ± 0.5	30.5 ± 2.6	33.6 ± 4.4
	0.86	6	3.2 ± 0.6	3.5 ± 0.8	34.1 ± 4.2	38.7 ± 3.1
	1.17	6	4.4 ± 1.7	5.0 ± 0.4	40.2 ± 5.1	43.8 ± 2.4



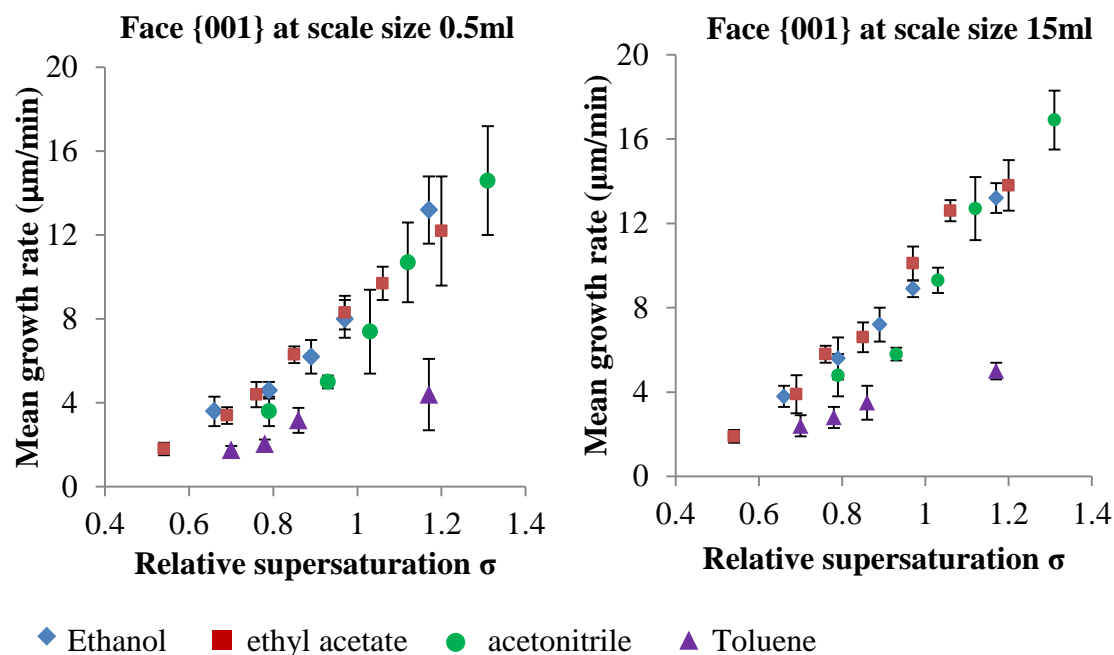


Figure 7.4 Mean growth rate of the {011} and {001} face versus supersaturation of crystals grown in ethanol 95%, ethyl acetate, acetonitrile and toluene.

The growth rates of ibuprofen crystals grown in absolute ethanol at different temperatures using stirred seeded batch crystallization were reported in [15] showing the growth rate in ethanol followed a first order dependence on supersaturation. i.e. $G = k_G \sigma^n$ where G is the linear growth rate of crystals (in $\mu\text{m}/\text{min}$), n is the kinetics order ($n = 1$), k_G is the growth rate coefficient ($k_G = 15$) and σ is the supersaturation.

Table 7.2 Comparison of the mean growth rates of face {011} and {001} of ibuprofen in ethanol with the growth rate calculated from $G = k_G \sigma^n$ (with $k_G = 15$, $n=1$) [15]

Supersaturation σ	This study		Data after Rashid [15]
	Face {001}	Face {011}	
0.66	3.6 - 3.8	8.5 - 11.1	9.9
0.79	4.6 - 5.6	11.8-11.9	11.85
0.89	6.2 - 7.2	14.3 - 16.9	13.35
0.97	8.9 - 8.9	16.6 - 18.4	14.55
1.17	13.2	21.6 - 24.6	17.55

The mean growth rates (R) of the $\{001\}$ and $\{011\}$ faces increase quite significantly with increasing relative supersaturation. $R\{001\}$ and $R\{011\}$ are responsible for defining the shape of crystals. For the solvents studied, $R\{011\}$ is greater than $R\{001\}$, in particular for crystals grown in ethyl acetate, acetonitrile and toluene. This results in shapes with a higher aspect ratio in these solvents (elongated crystals), e.g. in ethanol the ratio of $R\{011\}$ and $R\{001\}$ ranges from 1.6 to 2.6 whilst that in ethyl acetate ranges from 5.0 to 9.8 with even higher values in acetonitrile and toluene.

Considering the four solvents, for solutions at the same supersaturation level, $R\{011\}$ in acetonitrile is the highest and $R\{011\}$ in ethanol is the lowest. $R\{001\}$ of ibuprofen crystals in ethanol and ethyl acetate are nearly similar and $R\{001\}$ in acetonitrile is lower than $R\{001\}$ in ethanol and ethyl acetate. $R\{011\}$ in acetonitrile increases much more with increasing supersaturation compared to the other solvents (Figure 7.4). The rate of change of growth rate with changing supersaturation, $dR/d\sigma$, for the $\{001\}$ and $\{011\}$ faces in four solvents was not found to follow a linear relationship, for example, in ethyl acetate the gradients of $R\{011\}$ with supersaturation ($dR\{011\}/d\sigma$) at $\sigma > 0.76$ were found to be lower than those measured for $\sigma \leq 0.76$. At $\sigma < 0.76$ $dR\{011\}/d\sigma$ is 90.4 and $dR\{001\}/d\sigma$ is 11.6 but at $\sigma > 0.76$ $dR\{011\}/d\sigma$ is 50.7 and $dR\{001\}/d\sigma$ is 17.4.

At the 15 mL scale, the measured $R\{001\}$ and $R\{011\}$ are slightly greater than that found for the measurements at 0.5 mL scale. According to Noyes and Whitney [65], the driving force for crystal growth is the difference between the concentration in the bulk of solution and at the solid surface. As crystals start to grow in a supersaturated solution, the concentration drops across the stagnant film of liquid adjacent to the growing crystal faces and thus the diffusion process, in which solute molecules move from the bulk of the liquid phase to the thin stagnant film, occurs. It was reported that film thickness measured on stationary crystals in stagnant aqueous solutions is up to 150 μm whilst this rapidly drops to zero in vigorously agitated systems [26]. It is postulated that probably the mass transfer is greater for the larger scale size where the solution volume is greater hence suggesting that the diffusion rate is greater at the 15 mL solution compared to that at the 0.5 mL cuvette, thus the driving force for the crystal growth should be less in the 0.5 mL cuvette. With the same small amount of material

crystallized out, the local supersaturation levels should decrease faster in the 0.5 mL solution when compared to that in the 15 mL cell. However, examination of the ATR UV/Vis data measured in-situ shows the supersaturation level to be comparatively constant during crystallisation process. This probably due to the small numbers of nucleated single crystals in the unagitated vessel resulting in a modest un-measurable supersaturation change. When the crystals are growing, the supersaturation levels are likely to decrease locally within the solution adjacent to the growing crystal faces, and this change in concentration is not likely to be detectable by the ATR UV-Vis probe given its location some distance away (~8 mm). In addition, the temperature in the 15 mL vessel may not be completely homogeneous, while crystals which settle on the flat optical disc at the 15 mL vessel base may be at a slightly lower temperature when compared to that of the bulk solution due to a lack of coolant circulation around the disc. In contrast, the thin 0.5 mL cuvette is totally immersed in a water tank and thus the temperature should be controlled within $\pm 0.1^{\circ}\text{C}$.

7.3 Crystal morphology as a function of growth environment

The {001}, {011} and {100} faces are the dominant external morphological forms for ibuprofen crystals. The morphology of ibuprofen crystals grown from ethanol, ethyl acetate, acetonitrile and toluene at both scale sizes (cuvette 0.5mL and jacketed vessel 15mL) were found to be quite consistent from crystals to crystals and between two scale sizes in good agreement with previous studies [5, 136]. Plate-like hexagonal shaped crystals are obtained from ethanol whilst more elongated forms are found in ethyl acetate, acetonitrile and toluene. Crystal prepared from toluene and acetonitrile solutions were found to grow with the most needle-like morphology. The former exhibited some curvature on the {001} faces which might be with kinetics roughening. Changes of relative growth rate of the {001} and {011} faces with solvent type and supersaturation result in a variation of the crystal aspect ratios (the ratio of the length and the width of a crystal) reflecting the fact that the crystals tended to be more elongated in the less polar and non-polar solvents and with decreasing supersaturation, as shown in Figure 7.5 and Figure 7.6.

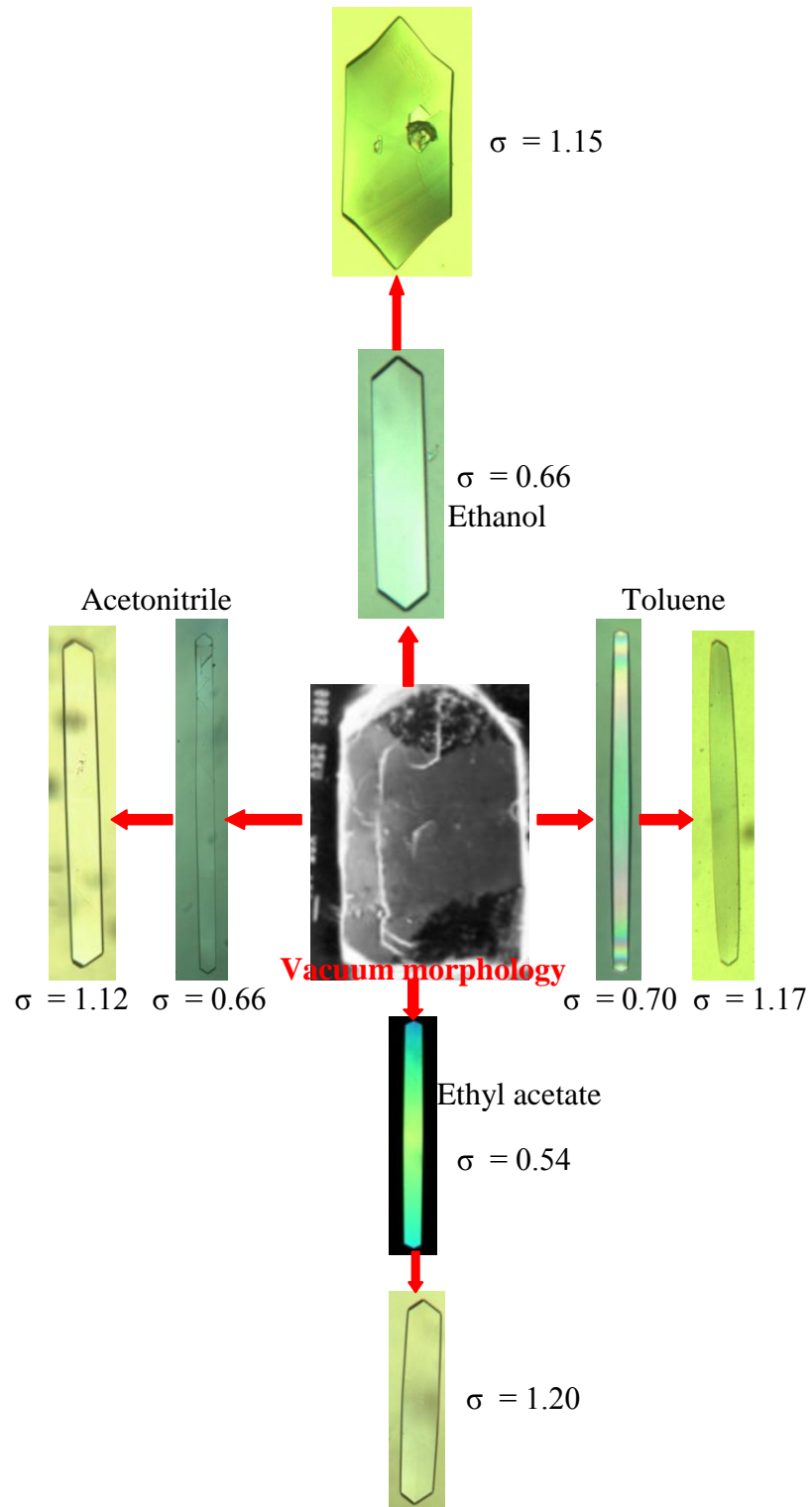


Figure 7.5 Photographs of aspect ratios (the ratios of the length and the width of crystals) of ibuprofen crystal grown from ethanol, ethyl acetate, acetonitrile and toluene versus relative supersaturation together with the vacuum morphology figure from Bunyan [136]. Note that the aspect ratios mostly tend to increase with decreasing supersaturation.

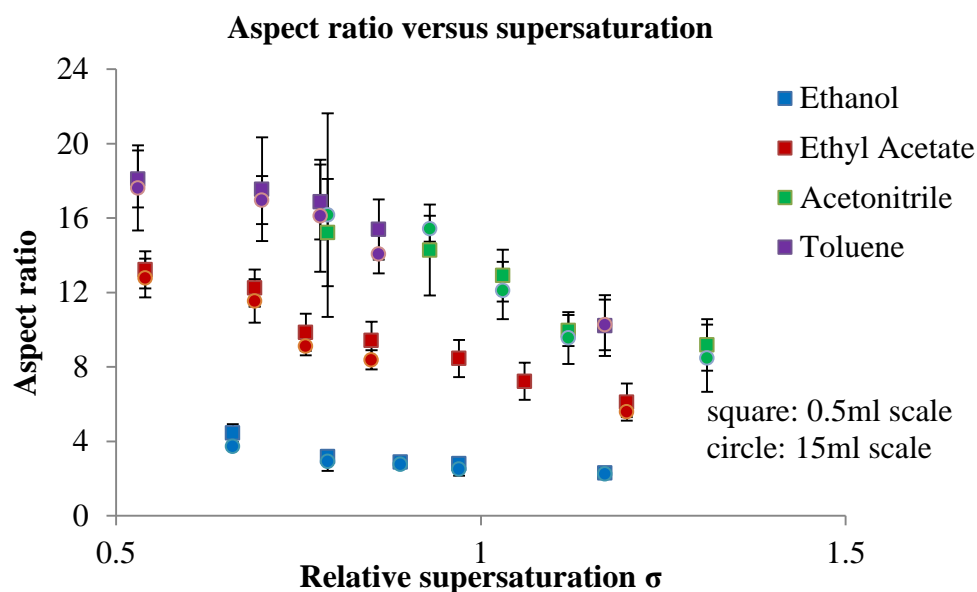


Figure 7.6 Aspect ratios of ibuprofen crystals grown from ethanol, ethyl acetate, acetonitrile and toluene versus relative supersaturation at two scale-sizes: 0.5ml and 15ml.

Similar effects were reported by Ristic, et al. [9] who observed that the growth morphology of monoclinic paracetamol from pure aqueous solution at different supersaturations exhibited a strong supersaturation-dependence associated with a change from a columnar to a plate-like habit with increasing supersaturation.

7.4 Variation in growth rates crystal by crystal

Each crystal growth rate data point reported here represents a mean value between five and eight individual crystals for which the growth rate was measured. Figure 7.2 illustrates the growth of the {001} and {011} face over time for five individual crystals. The face specific growth rates were found to display a good linear fit for each crystal surface indicating that these surfaces follow the constant crystal growth model. This model proposes the constant growth rate of each crystal along the growth periods. However, different crystals have different growth rates. The growth rate variations of ibuprofen in various solvents are summarised in Table 7.3.

Table 7.3 The coefficient of variation for the growth rate of the crystal faces

Solvent type	The {001} face		The {011} face	
	0.5mL	15mL	0.5mL	15mL
Ethanol	0.12	0.103	0.12	0.09
Ethyl acetate	0.123	0.10	0.095	0.07
Acetonitrile	0.177	0.103	0.12	0.083
Toluene	0.193	0.173	0.092	0.084

The average standard deviation of these particular crystal measurements was found to be about 12%. Caution should be exercised in interpreting this data as errors e.g. due to the blurring of the crystal boundaries, minor errors from manual measurements etc. could be introduced. Nonetheless, the standard deviations of the measured growth rates are broadly representative of the variation in growth rates of crystal habit faces in individual crystals. According to observations of sequence of single crystals grown during a period of time, there were different growth rate between four similar faces (011), (0-11), (01-1) and (0-1-1) faces and each crystal grows at slightly different rate in the same conditions. Given that the initial size of crystal studied is very similar, these observations are more consistent with the growth rate dispersion (GRD) effect than one of size dependant growth (SDG).

In this study, the growth rate data shows a lower growth rate variation for the growth of spontaneously nucleated crystals in stagnant, supersaturated solutions compared to the GRD observed in a stirred batch crystallizer which was measured from size distribution of crystals from seeding [15]. The latter study showed ibuprofen growth in absolute ethanol and water-ethanol mixtures at the 1L stirred seeded batch crystallisation vessel size exhibits GRD with a log normal distribution of growth rates having a spread of the coefficient of variation CV_v which is calculated by the standard deviation/mean size of volume based distribution of the growth rate on a volume basis. The distribution spread CV_v versus experimental growth time at 25°C in absolute ethanol) had the value of 0.5 (Figure 7.7).

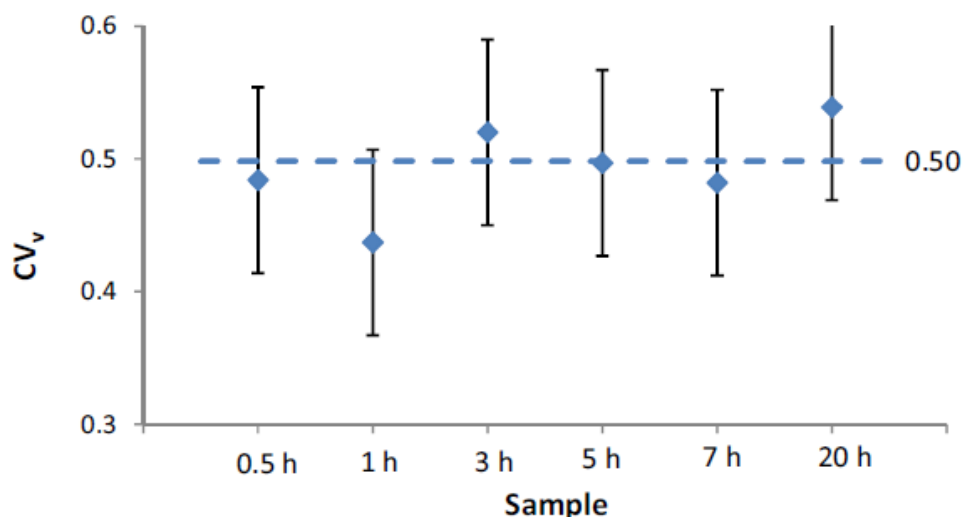


Figure 7.7 Distribution spread CV_v versus experimental growth time at 25°C in absolute ethanol) (reproduced with permission from Rashid et al [15]).

Similarly, studies of the growth rate behaviour of anhydrous sodium sulphate crystals revealed that the GRD of single crystals grown in a flow cell was less than that found among a population of crystals prepared in a batch crystallizer [172]. This was rationalised in terms of crystal collisions occurring in the agitated crystalliser producing greater numbers of faster growing nuclei.

Whilst a significant number of studies have been carried out, the mechanism of GRD is still a matter of some debate. The GRDs of ibuprofen was compared with some other organic and inorganic materials in Table 7.4.

Table 7.4 Growth Rate Dispersion of some other organic and inorganic materials

Materials	The coefficient of variation	References
Lysozyme (face {110})	0.05 - 0.2	Judge et al. [21]
Lysozyme (face {101})	0.05 - 0.33	Judge et al. [21]
Paracetamol (face {110})	0.061 - 0.141	Finnie et al. [173]
Sucrose	0.28	Berglund and Murphy [174]
Citric acid monohydrate	0.35	Berglund and Larson [175]
ADP	0.37	Garside and Ristic [20]
Ibuprofen	0.07- 0.19	This study

The GRD for the growth rate of the {001} and {011} of ibuprofen is quite similar to that of the {110} direction of paracetamol and slightly lower than other materials.

The GRDs of both faces in this study was found to increase with increases in the mean growth rate when crystals grow at the high supersaturation. The growth rate of the {001} and {011} faces showed a trend of higher GRD at the higher supersaturations and the GRD in the 15 mL vessel is less than the GRD in the 0.5 mL cuvette. It is similar to the case of citric acid monohydrate [175], sucrose [174], and fructose and protein [21]. At the higher supersaturations, the nucleation rate was found to be greater, which means more crystals are generated in the in-situ cell which grow at the same time in solution resulting in a more rapid desupersaturation of the growth solution at the smaller scale size (0.5 mL). The GRD do not vary greatly between the solvents except the GRD for toluene. This is might due to the very needle-like crystals with curvy {001} faces which were found in toluene.

7.5 Rationalisation the growth rates with intermolecular bonding and surface chemistry

In these four solvents, the growth rate of face {011} was found to be greater than the growth rate of face {001} in particularly crystals grown in ethyl acetate, acetonitrile and toluene. This resulted in a higher aspect ratio for the crystals formed in these solvents. The morphology, the growth rate of face {011} and {001} and aspect ratio of crystals can be rationalised and understood at the molecular scale through morphological prediction, analysis of the intermolecular bonds on the ibuprofen crystal surface of the {011}, {001} and {001} faces and the chemistry of the crystal habit surfaces.

The analysis of the strongest bonds on the ibuprofen crystal surface of the {011}, {001} and {100} faces showed that the strongest bond type (-7.47 kcal/mol) are hydrogen-bonded molecules between molecule number 1 and molecule number 3 which continue along the b direction so crystals are expected to grow more in this direction. The hydrogen bonds contribute to attachment energy on the {011} face and contributes to the slice energy on the {001} face, which can be used to verify the growth rate of the

{011} face being greater than the growth rate of the {001} face. This is in good agreement with the growth rate data of the measured {011} and {001} face in studied solvents. On the contrary, most of the strongest bonds on the {100} face are inside the slice thus this face is expected to grow slowly and become the most morphologically important. This agrees with the predicted and experimental morphology of ibuprofen, apart from the aspect ratio of crystals. It is likely due to the fact that the growth conditions effect the relative growth rate of the {011} and {001} faces resulting in changes of aspect ratio of crystals. The more detailed analysis of solution-crystal surface interactions, in this case solvent type, is considered.

The morphology of a crystal in different growth environments depends, collectively, on the relative growth rates associated with its constituent crystal habit faces. Mechanistically, these rates reflect the balance between the rate of desolvation of solvent molecules and the rate of solute adsorption at the different crystal growth interfaces. Ultimately these rates are linked to the respective interaction energies associated with the solute and solvents molecules on these surfaces. Hence, the growth rate of an individual habit face can be rationalised as being determined by interactions between solute and solvents on specific faces through either a reduction or an increase in interfacial tension and concomitant growth rate. Hence, the ibuprofen morphology grown from solvents can be explained by molecular arrangement at the {011} and {001} surface and hydrogen bond can be formed between solvents and the COOH functional group of ibuprofen.

Figure 5.13 and Figure 5.14 showed molecular packing diagrams which highlight the basic surface chemistry of the {001} and {011} growth surfaces. On the {011} face the molecules are arranged alternatively nearly parallel and perpendicular to the surface and intermolecular hydrogen bonds appear in different directions contributing to slice energy and attachment energy. Moreover, if considering the effect of solvent (polar, less polar and non-polar) on the growth rate of the {001} and {001} face, in particular the growth rate of the {011} face significantly varies among ethanol, ethyl acetate, acetonitrile and toluene. The {011} face exhibits great hydrophilicity because the carboxylic acid groups are more easily accessible so the use of polar solvents (ethanol which can act either as a hydrogen bond donors or acceptors) would inhibit the growth of {011} resulting in shortened crystals (plate-like crystals). On the contrary, a more

apolar solvent (ethyl acetate or acetonitrile) or non-polar (toluene) which interact to a lesser extent to the {011} face thus obtaining more elongated crystals. Moreover, interactions of less polar solvents with alkyl groups on the {001} face hinders the growth of this face.

In summary, the molecular modelling was quite successful in qualitative interpretation and supporting for the experimental data, particularly the growth rate of {011} and {001} in various solvents. The different shapes are formed by the differences in the relative growth rates of specific faces of ibuprofen crystals due to the interaction of solvent molecules and the structures of specific growing faces. Hence, the computational calculations using attachment energy and the BFDH approaches accurately predict the shapes of crystals grown in vacuum; they are not very accurate for crystal grown in the solution.

7.6 Growth rate mechanism of {001} and {011} at two scales 0.5mL and 15mL

The microscopy observations reveal that the crystal growth was clearly planar in nature. This, together with the appearance of crystals which are bounded by well-defined crystallographic surfaces which are not roughened would suggest that the growth mechanism would be either due to the BCF or B&S mechanism. This supposition is confirmed through examination of data presented in Figure 7.8 which show that there is a strong and non-linear dependence of the relative growth rates, on supersaturation ruling out models, such as the rough surface model for which a linear dependence of growth rate on supersaturation fitting would be expected. Data fitting has been carried out using nonlinear curve fit in Origin with user define functions (Birth and Spread model $A \cdot (x^{5/6}) \cdot \exp(B/x)$ and BCF model $A \cdot (x^2) \cdot \tanh(B/x)$). Plots of the measured crystal growth rate versus relative supersaturation together with fitting against these models are shown in Figure 7.8, summarised in Table 7.5. From this, an assessment was made to which model gave better fitted.

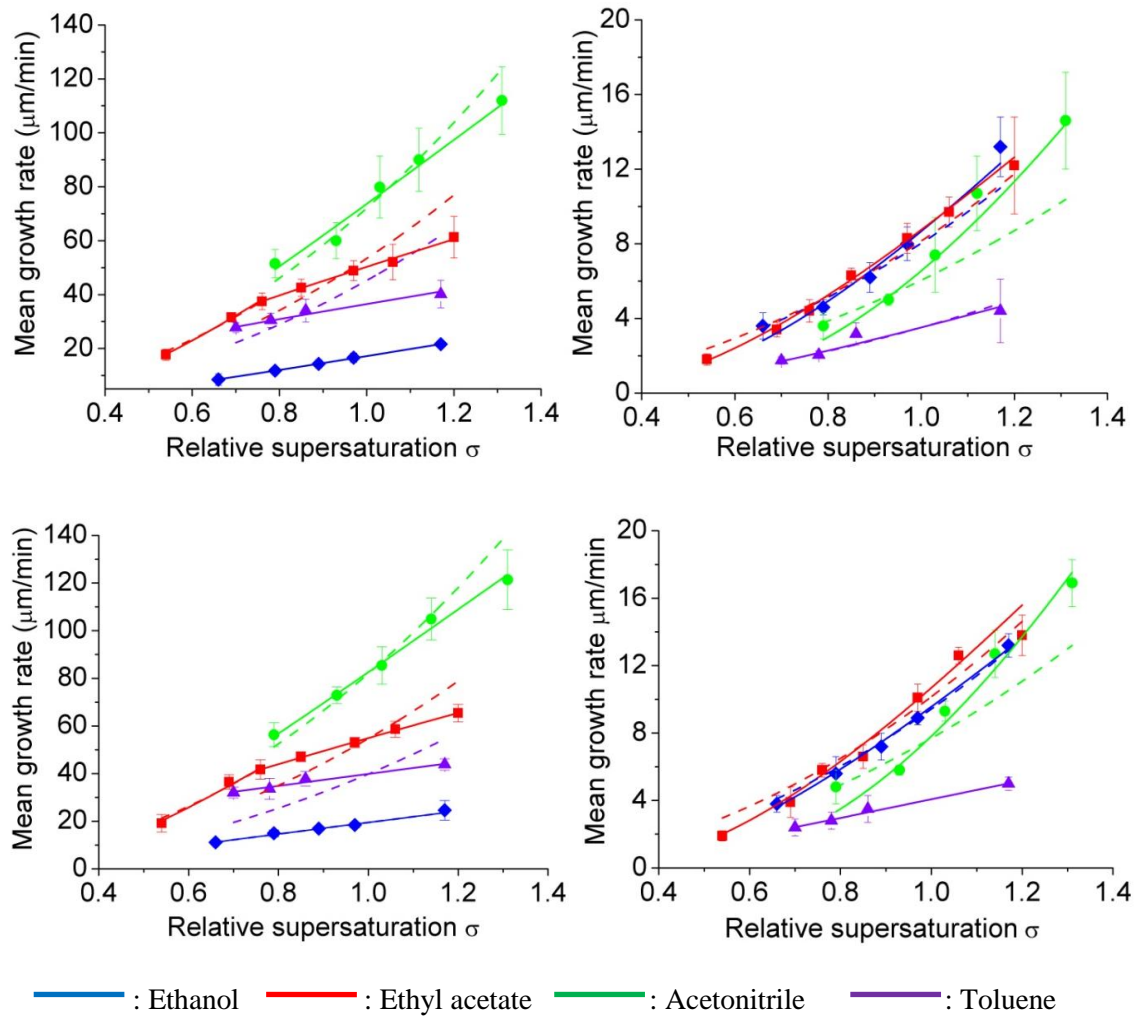


Figure 7.8 Plots of the growth rate versus supersaturation together with fitted B&S and BCF mechanism models for both {011} face (left) and {001} face (right) and for both 0.5mL (top) and 15mL (bottom).

Table 7.5 Fitting parameters for the faces {011} and {001} of ibuprofen grown in ethanol 95%, ethyl acetate, acetonitrile and toluene with B&S model and BCF models together with the adjusted coefficient of determination adjusted R^2 (adj. R^2)

		Vessel 0.5 mL				Vessel 15 mL			
		Face {011}		Face {001}		Face {011}		Face {001}	
		B&S	BCF	B&S	BCF	B&S	BCF	B&S	BCF
Ethanol 95%	A	41.782	16.540	39.41	8.03	29.13	33.97	32.28	9.42
	B	-0.962	8.79E8	-1.51	4.2E11	-0.40	0.65	-1.22	3.30E8
	Adj. R^2	0.986	0.966	0.94	0.94	0.99	0.99	0.996	0.992
EA ($\sigma =$ 0.54-0.76)	A	152.62	65.02	31.94	8.15	162.55	72.95	41.57	10.16
	B	-0.88	63.46	-1.29	2.2E9	-0.85	61.89	-1.36	8.31E12
	Adj. R^2	0.996	0.973	0.994	0.95	0.97	0.95	0.986	0.941
EA ($\sigma =$ 0.76-1.20)	A	61.53	53.41			63.56	54.75		
	B	-0.20	49.22			-0.15	48.74		
	Adj. R^2	0.995	-0.22			0.998	-0.28		

Acetonitrile	A	167.66	72.09	70.88	6.05	175.15	82.03	91.95	7.69
	B	-0.81	37.45	-2.38	2.0E8	-0.75	32.75	-2.47	1.91E6
	Adj.R ²	0.937	0.872	0.891	0.70	0.99	0.88	0.932	0.707
Toluene	A	33.76	45.25	9.56	3.51	32.46	39.82	6.902	5.858
	B	0.078	24.89	-1.00	4.62E6	0.21	8.07	-0.528	0.857
	Adj.R ²	0.958	-5.77	0.77	0.76	0.97	-5.86	0.994	0.994

Figure 7.4 shows that there is a strong dependence of the relative growth rates, between the {011} and {001} faces, which control the crystal's aspect ratio, on supersaturation ruling out models, such as the rough surface model [70] that predicts a linear dependence of growth rate on supersaturation. Table 7.5 shows the fitting parameters A and B (see equation (2.35) and (2.36)) and the adj. R² for the faces {011} and {001} grown in various solvents with the B&S model and the BCF model. Generally, the B&S model provides a better fit to the data than that for BCF model for most data measured. The main exception are for R{011} and R{001} in ethanolic solutions, which provided similar values for the fitting adj. R² (0.97-0.99) for both models.

In the case of ethanol, the increased viscosity of the solution inhibited mass transfer of the solute from solution to the crystal face thus it might contribute to reducing the crystal growth rate and the growth mechanism. According to Sherwood, there is a relationship between the mass transfer coefficient and diffusivity or diffusion coefficient and viscosity:

$$k_d = \frac{D}{L} \left(2 + 0.8 \left(\frac{\varepsilon_p L^4}{\nu^3} \right)^{1/5} Sc^{1/3} \right) \quad (7.1)$$

where D is the diffusion coefficient, L is crystal size, ε_p is the average power input and ν is the kinematic viscosity, and Sc is the Schmidt number ($Sc = \nu/D$). The diffusion coefficient, D , can be estimated using the Stokes-Einstein equation:

$$D = \frac{KT}{3\pi\mu d_m} \quad (7.2)$$

where K is the Boltzmann constant, T is temperature (K), μ is dynamic viscosity of the solution, and d_m is the molecular diameter.

Similarly, the effect of solvent composition on the growth kinetics and growth mechanism as a function of solvent composition associated with surface roughness, selective absorption, solubility gradient and viscosity of solution responsible for the decrease of growth rate with the solvent composition was reported for the antisolvent crystallization of paracetamol in methanol and water mixtures [176].

In ethyl acetate, the growth rate was studied at lower range of supersaturations, i.e. from 0.54 to 1.2. It was shown that at supersaturation σ from 0.54 to 0.76 $R\{011\}$ versus σ fits well for both BCF and B&S model (the adj. $R^2 = 0.996$ and 0.973 , respectively). However, at σ ranging 0.76 to 1.20 only the B&S shows acceptable fit (the adj. $R^2 = 0.995$ for B&S and -0.22 for BCF) consistent with the growth mechanisms where the BCF mechanism might be occur at low supersaturation.

In this study, ibuprofen crystals grown from four solvents follow the B&S mechanism at moderate and relative high supersaturation ($\sigma = 0.54 - 1.22$), except for some solvents and supersaturation BCF can equally fit and there is no mechanistic change with scale size.

7.7 Correlation between the calculated α factor and the growth mechanism

For a crystal face growing from solutions in different solvents, the value of the α factor might be expected to alter depending on the nature of solute-solvent interactions (interfacial roughness). The changes of the α factor due to the change of growth solvent can result in the change of the growth kinetics and growth mechanism of a crystal face and thus the growth rate of different crystal habit faces. These growth mechanisms are correlated to the values of the α factor given in Table 7.6 (ξ_{hkl} calculated from E_{crys} and E_{latt} for a growth unit based on a monomer) and Table 7.7 (ξ_{hkl} calculated from E_{crys} and E_{latt} for a growth unit based on a dimer). The surface entropy factor α_{hkl} of ibuprofen in ethanol, ethyl acetate, acetonitrile and toluene calculated in two methods using equation $\alpha = \xi \frac{\Delta H_s}{RT}$ at 25°C (1) and $\alpha = \xi \left(\frac{\Delta H_f}{RT} - \ln X_{seq} \right)$ (2) from $15 - 35^\circ\text{C}$.

Table 7.6 The surface anisotropy factors ξ_{hkl} calculated from E_{crys} and E_{latt} for a growth unit based on a monomer and the surface entropy factor α_{hkl}

Face	ξ_1	Ethanol		Ethyl acetate		Acetontrile		Toluene	
		(1)	(2)	(1)	(2)	(1)	(2)	(1)	(2)
100	0.83	8.9	9.4 – 10.5	9.0	9.2 – 10.4	18.4	10.2 – 12.0	9.45	9.3 – 10.4
110	0.45	4.7	5.0-5.7	4.8	5.0 – 5.6	9.9	5.5 - 6.4	5.01	5.0 – 5.6
011	0.42	4.4	4.8-5.4	4.6	4.7 -5.3	9.4	5.2 – 6.1	4.8	4.7 – 5.3
001	0.42	4.4	4.7- 5.3	4.5	4.7-5.2	9.3	5.2 - 6.1	4.8	4.7-5.3
012	0.28	2.5	3.2 – 3.6	2.6	3.1 – 3.5	5.4	3.5-4.1	2.7	3.1 – 3.6
112	0.31	3.4	3.5 – 3.9	3.6	3.4 – 3.9	7.3	3.8 – 4.5	3.8	3.5 – 3.9

Table 7.7 The surface anisotropy factors ξ_{hkl} calculated from E_{crys} and E_{latt} for a growth unit based on a dimer and the surface entropy factor α_{hkl}

Face	ξ_1	Ethanol		Ethyl acetate		Acetontrile		Toluene	
		(1)	(2)	(1)	(2)	(1)	(2)	(1)	(2)
100	0.80	8.3	9.0 -10.1	8.6	8.9 - 10.0	17.7	9.8 -11.5	9.08	8.9 - 10.0
110	0.24	2.5	2.8 - 3.1	2.6	2.7 - 3.0	5.3	3.0 - 3.5	2.74	2.7 - 3.0
011	0.23	2.4	2.7 - 2.9	2.4	2.5 - 2.8	5.0	2.8 - 3.3	2.57	2.5 - 2.9
001	0.32	3.3	3.7 – 4.0	3.3	3.5 - 3.9	6.9	3.8 - 4.5	3.52	3.5 – 4.0
012	0.17	1.7	2.0-2.1	1.8	1.9-2.1	3.7	2.1-2.4	1.9	1.9-2.1
112	0.21	2.2	2.4-2.6	2.3	2.3-2.6	4.7	2.6-3.0	2.4	2.3-2.6

The surface entropy factors α_{hkl} calculated from the dimer model are smaller than these calculated from the monomer model. For the ξ_{hkl} calculated from E_{crys} and E_{latt} for a growth unit based on a dimer (Table 7.7), the calculated surface entropy α factor for the {011} and {001} face has the value smaller than 5 (except for the case of acetonitrile using the method (1) so the B&S mechanism on these faces is expected to occur in these solvents, which agrees with the measured and fitted growth mechanisms from the experimental data.

For the ξ_{hkl} calculated from E_{crys} and E_{latt} for a growth unit based on a monomer, the values of α calculated for the {001} and {011} face using the method (1) are smaller than 5 and the α values calculated using the method (2) are between 4.7 - 5.3 (except for

the case of acetonitrile). For these faces whose α factor are nearly 5 or slightly higher than 5, which is in the border of B&S and BCF growth mechanism, both mechanisms were fitted (see Table 7.6).

The surface alpha factor α calculated using (2) is slightly higher than from (1) and the α values of the {011} face is higher than that of the {001} face which indicates the surface of the {001} face is smoother than that of the {011} face. This agrees with the growth rate of the {011} face which is higher than that of the {001} face in this study. It has been shown that the assessment of the surface entropy factor α from the heat of solution and from the heat of fusion was in quite good agreement to the observed growth mechanism for ibuprofen in this study. The calculated surface entropy α factor has a value of smaller than or equal to 5 so the B&S mechanism on the {011} and {002} face is expected to occur in these solvents, which agrees with the measured and fitted growth mechanism from experimental data. Except for the α values for acetonitrile calculated from (1) using the heat of solution from the solubility curve did not agree with the experimental data.

Actually the heat of solution often depends on the solution composition which can be measured through the differential heat of solution using small amounts of solute in large volumes of solution. Hence, the differential heat of solution can be measured as a function of solution composition. The extrapolation will give the value of heat solution at infinite dilution. In this study, the heat of dissolution was obtained through the slope of the solubility curve (the plot of $\ln X$ versus $1/T$) which gives the differential heat of solution at saturation. The plot $\ln X$ vs $1/T$ will give the true value of the enthalpy if the solution is ideal. For ethanol, ethyl acetate and toluene, the solutions are nearly ideal so the calculated α are quite accurate and reasonable for growth mechanism prediction. However, for the case of acetonitrile, the solution is negative ideality and the solubility showed a great dependence upon the temperature and thus resulting in the greater value of derived enthalpy of dissolution. Hence, the calculated α factor calculation using heat of solution failed to predict the observed growth mechanism.

The calculated α factors for the face {001} in all solvents indicated that this face follow the BCF growth mechanism which is in good agreement with the fact that this face is the dominant face associated with the slowest growing rate. The entropy surface α is a

useful data description for the effect of solute-solvent interactions and thus the nature of the surface based on the calculated α factor, which can be used to link the solution chemistry of the system and the growth mechanism of each surface. For a particular crystal face growing from solution in various solvents, the value of α may change depending on the solute-solvent interactions. The heat of solution might be expressed as $\Delta H_s = \Delta H_{\text{fus}} + \Delta H_{\text{mix}}$. The enthalpy of mixing ΔH_{mix} is negative when the dissolution process is exothermic and vice versa and thus the value of α calculated from the equation $\alpha = \xi \frac{\Delta H_s}{RT}$ increases as the solute-solvent interactions become weaker [79]. The calculated α factor for growth from acetonitrile was higher than the values calculated for the growth from ethanol, ethyl acetate and toluene indicating the weaker acetonitrile and ibuprofen interactions. This is in good agreement with the solubility, solution ideality and the measured growth rate of the $\{001\}$ and $\{011\}$ in the solvents studied.

7.8 Analysis of the re-entrant faces

It is interesting to note that crystals presenting re-entrant faces appear (Figure 7.9) for all 4 solvents at both 0.5mL and 15ml scale-size at high levels of supersaturation. These faces have been confirmed and proved as a crystallographic face by measuring the angles between these faces and the $\{011\}$ face. The measurements were carried out on 30 crystals and the mean interfacial angle and standard deviation were calculated. It was shown that the angle is fairly consistent which is around the value of $166^\circ \pm 2.7$. Standard deviation is quite low (1.6%) which can be due to the error of the manual measurements.

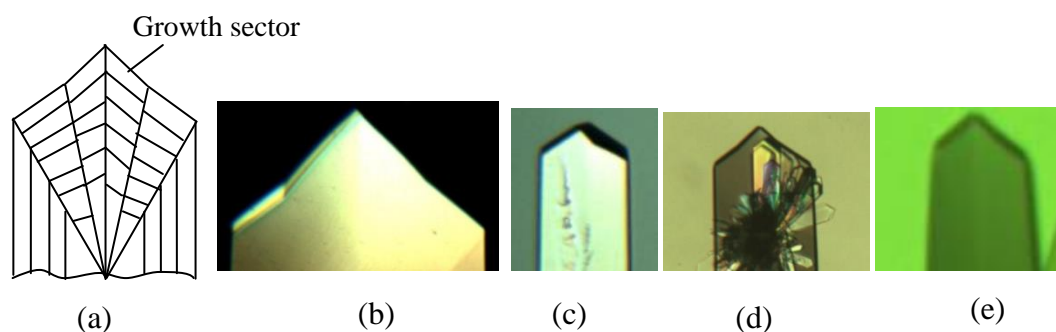


Figure 7.9 Schematic diagram (a) and ibuprofen crystals grown from ethanol (b), acetonitrile (c), ethyl acetate (d), and toluene (e) with high index re-entrant faces.

Also, it has been found that there is a critical supersaturation for this phenomenon occurring. The critical supersaturation for ethanol, ethyl acetate, acetonitrile and toluene are shown in Table 7.8. For acetonitrile and toluene these re-entrant faces are present at $\sigma_{\text{crit}} > 0.79$. However, more needle-like crystals are produced in these solvents particularly in toluene due to this the side $\{011\}$ faces are quite tricky to monitor the critical supersaturation for this phenomenon. Ibuprofen crystals with growing boundary sectors (Figure 7.10) show no evidence for substantial defects present like solvent inclusion, twinning etc.

Table 7.8 The critical supersaturation for the appearance of the re-entrant faces

	Ethanol	Ethyl acetate	Acetonitrile	Toluene
Critical supersaturation σ	0.66	0.69	> 0.79	> 0.79

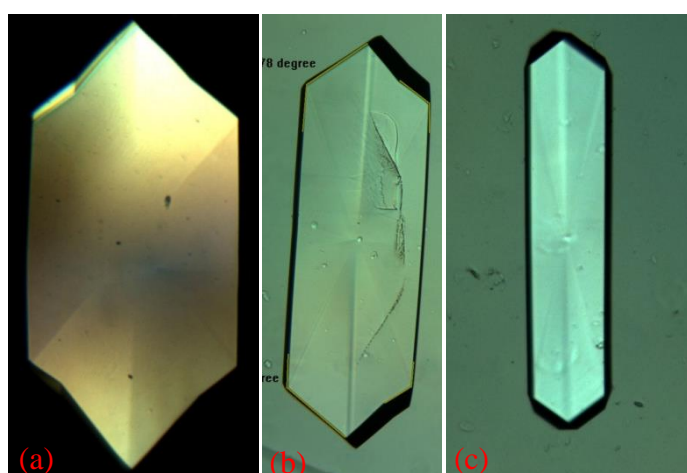


Figure 7.10 Ibuprofen crystal grown in ethanol at $\sigma = 0.97$ (a), $\sigma = 0.79$ (b) and $\sigma = 0.66$ (c) showing these re-entrant faces are likely appear at high supersaturation and not present at lower supersaturation.

In order to verify these crystals are twinned crystals or just single crystals, more detailed inspection of these crystals was performed using the crossed polarising microscopy technique which is powerful for the examination of twinned crystals due to changes in the optical properties [30]. It was shown that when crystals are rotated slowly in a clockwise direction in 360 degrees, the whole crystal body became darker or brighter, in which both parts are of equal brightness (Figure 7.11). Each half of the crystal (right or left) is not at extinction at any rotated angles or the individual crystals are at extinction

at the same time (for isotropic material). This, and the fact that the images showed well-resolved growth sector boundaries, is not consistent with any twinning mechanism. If there was a twin crystal, the extinction position for each crystal in twin crystals would be expected to be different (maybe several degrees of rotation) and there is a re-entrant angle which is a V-shaped groove [30].

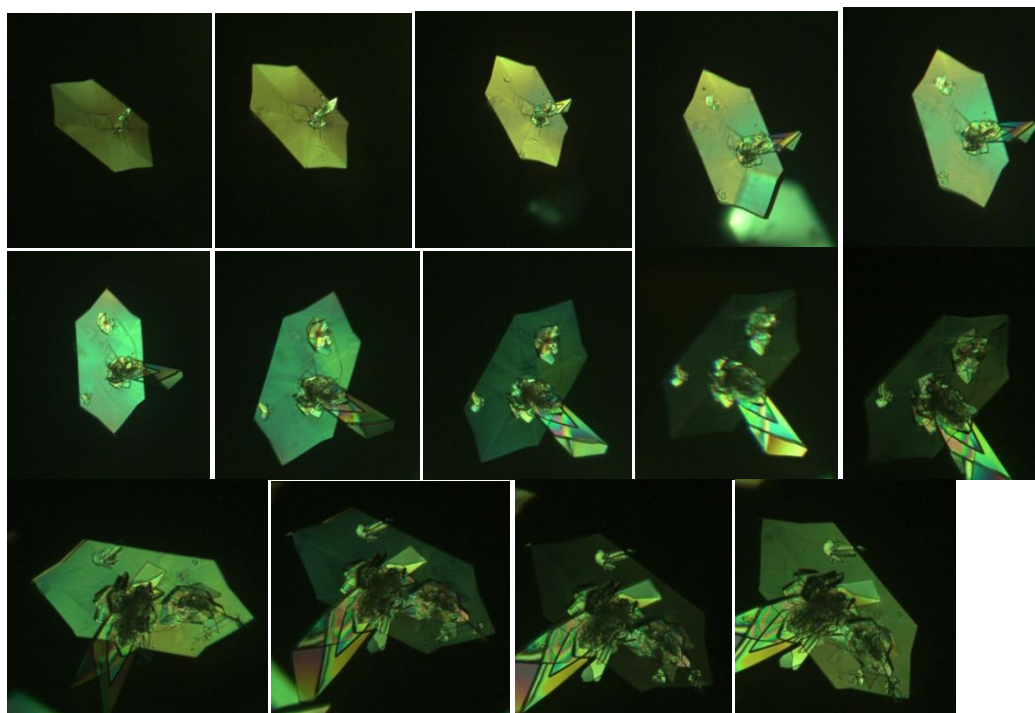


Figure 7.11 The series of polarized-light photographs of ibuprofen crystals in various optical rotation positions showing the whole crystal body became darker or brighter, in which both parts are of equal brightness. This proves that the re-entrant (concave) edges are not due to twinning.

From this evidence, it can be concluded that the re-entrant (concave) edges are not due to twinning. The interpretation is sketched in Figure 7.12. The $\{011\}$ and $\{012\}$ or $\{112\}$ are simply interchanged compared to the usual cases. Such interchange of faces, forming concave edges, is quite rare. This phenomenon has been observed in the case of lithium hydrazinium sulphate (point group mm^2) grown from aqueous solution [177]. In this ibuprofen work, however, re-entrant edges occur between symmetrically equivalent faces (011) and $(0-11)$. Analysis of the interplane angles for the experimental data using morphological simulation suggest that the high index face planes lies in a zone comprising the $\{012\}$ or $\{112\}$ and $\{100\}$ faces (see Figure 7.12 b and c). Obviously

the $\{100\}$ face is ruled out but it is hard to see which specific plane is involved. ($E_{\text{att}}(012) = -35.72$ (kcal/mol) and $E_{\text{att}}(112) = -33.89$ (kcal/mol)).

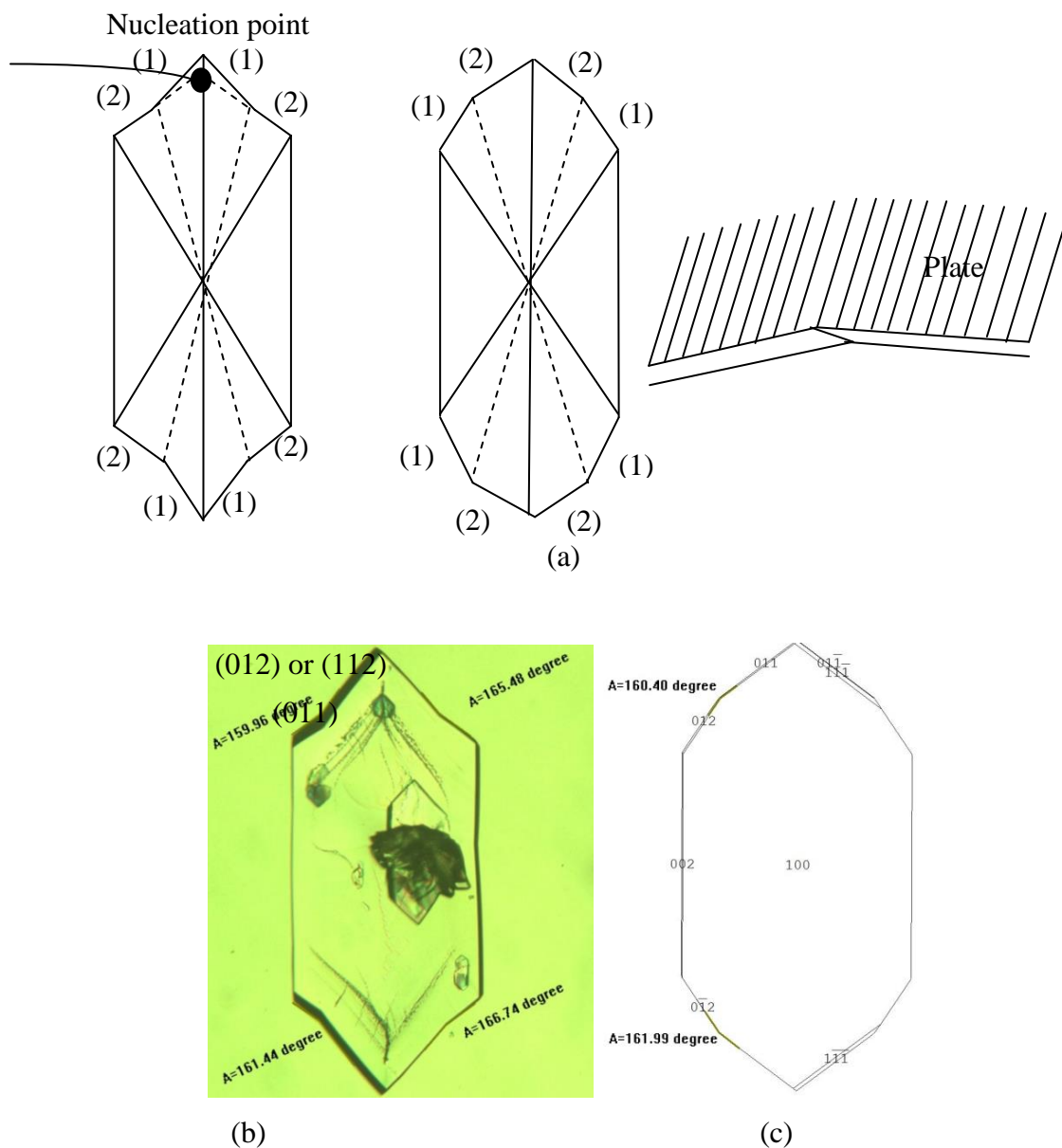


Figure 7.12 Schematic diagram showing the formation of re-entrant faces (a) The interfacial angle of the $\{011\}$ and $\{012\}$ face from the experimental morphology (b) and from morphological simulation (c).

The surface chemistry analysis for the $\{012\}$ and $\{112\}$ faces were analysed to examine the molecular packing on these surfaces and are shown in Figure 7.13 and Figure 7.14 respectively.

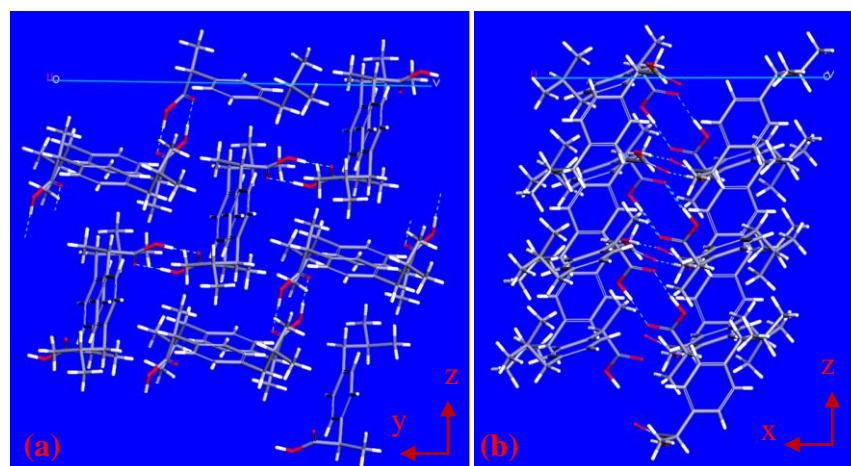


Figure 7.13 Molecular packing on the $\{012\}$ viewed along x axis (a) and along y axis (b).

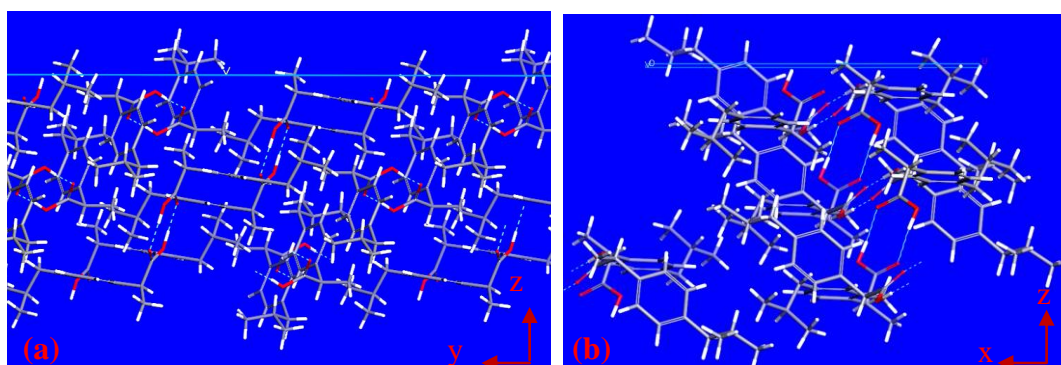


Figure 7.14 Molecular packing on the $\{112\}$ viewed along x axis (a) and along y axis (b).

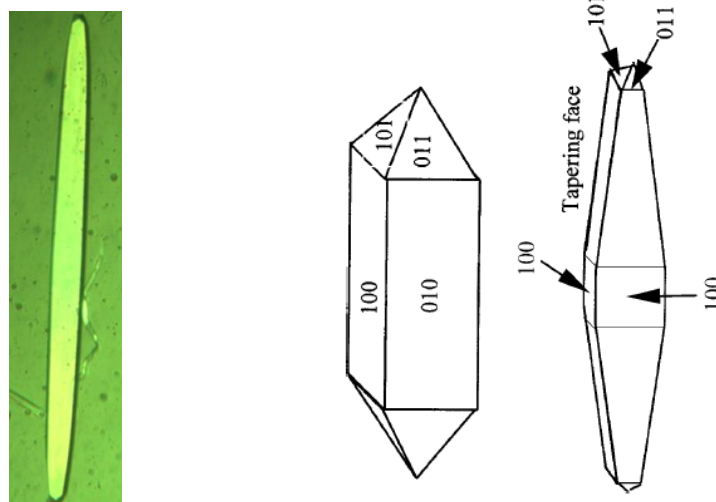
The properties of the $\{012\}$ and $\{112\}$ face are quite similar to the $\{011\}$ face in which $-\text{CH}_3$ and COOH groups are exposed on the surface. However, the $-\text{COOH}$ groups on the $\{112\}$ face are more exposed and more accessible than $-\text{COOH}$ groups on the face $\{012\}$. The intermolecular hydrogen bonds appear in two different directions on both of the faces and thus they are expected to be the fast growing faces.

7.9 Analysis of the curved $\{001\}$ faces of ibuprofen in toluene

Ibuprofen crystal morphology in toluene was found to be grown in an elongated shape and to develop a tapering $\{001\}$ face. Such behaviour is consistent with the blocking of surface terraces leading to a build-up of interfacial supersaturation close to the growing

surface. Given the narrow cross-section of the crystals it is hard to be specific on the origin of this effect but two scenarios are perhaps worthy of consideration:

- The (001) growth surface is curved which might suggest interface roughening [77, 78]. However, this effect is also observed at low supersaturation and anyway the kinetic analysis (see Figure 7.8) is not consistent with this.
- The (001) growth surface is tapered with respect to b-axis due to solvent-induced step poisoning having the effect of presenting the (001)/(011) growth sector boundary within the external morphology. Such effects have been previously observed in trivalent metal ion doping in ADP and KDP crystal [178-180] (Figure 7.15). These ions were identified as the factor responsible for the shape of KDP crystals from stubby to acicular due to the incorporation of ions on the prismatic (100) and (010) faces, resulting in these faces becoming tapered. This was clarified using X-ray absorption spectroscopy and molecular modelling showing the impurity occupied an interstitial site in the host crystal lattice associated with the formation of one hydrogen atom and two potassium ionic vacancies to maintain charge balance.



(a) Ibuprofen in toluene (b) KDP grown from pure KDP and impurity-doped KDP

Figure 7.15 (a) Morphology of ibuprofen in toluene was found to be grown in elongated shape with a tapering of the {001} face; (b) Schematic showing the typical growth morphology for KDP crystals with pure KDP and impurity-doped KDP. Crystal grow elongated associated with impurities, being preferentially incorporated into the (100) and (010) crystal growth sectors [178-180].

7.10 Crystal population growth rate measurements at 7mL reactor scale

7.10.1 Growth rate in 7mL non-agitated vessel

A sequence of images of crystals grown from ethanol in a 7ml non-agitated jacketed vessel at $\sigma = 0.157$ are showed in Figure 7.16 and the plots of equivalent diameter versus time are shown in Figure 7.17. Each line represents the growth rate of individual crystals over time.

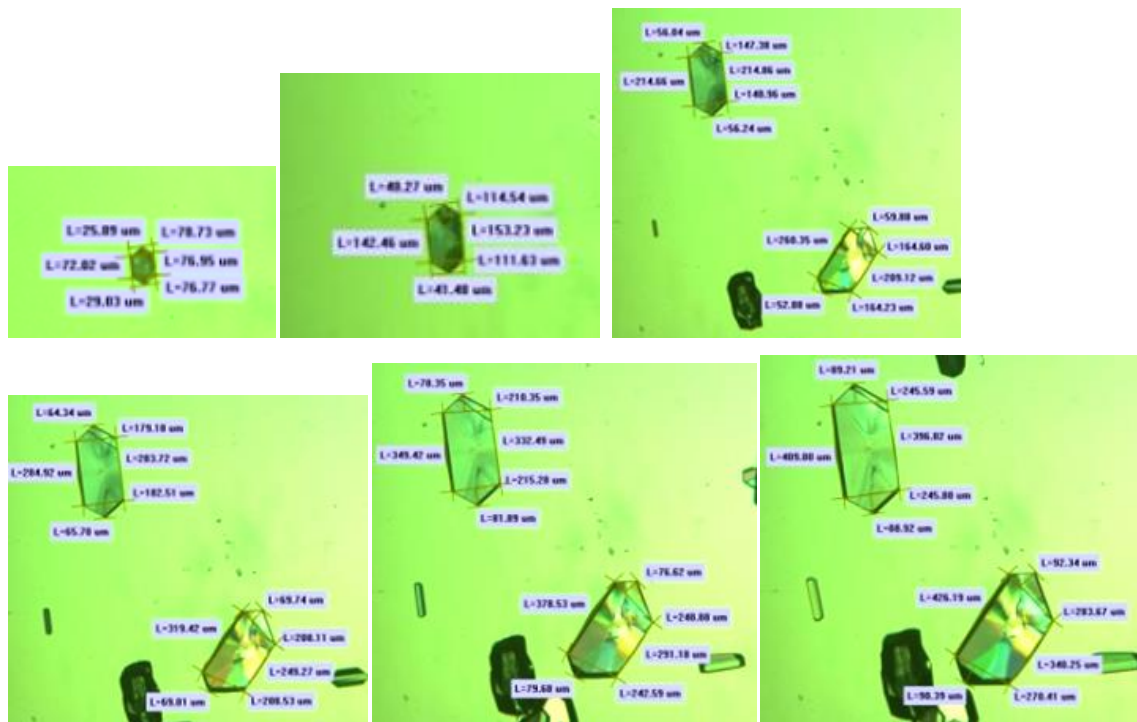


Figure 7.16 Ibuprofen single crystals growing in stagnant solution after seeding at $\sigma = 0.157$. From these images, the area of crystals can be calculated and then the equivalent diameter.

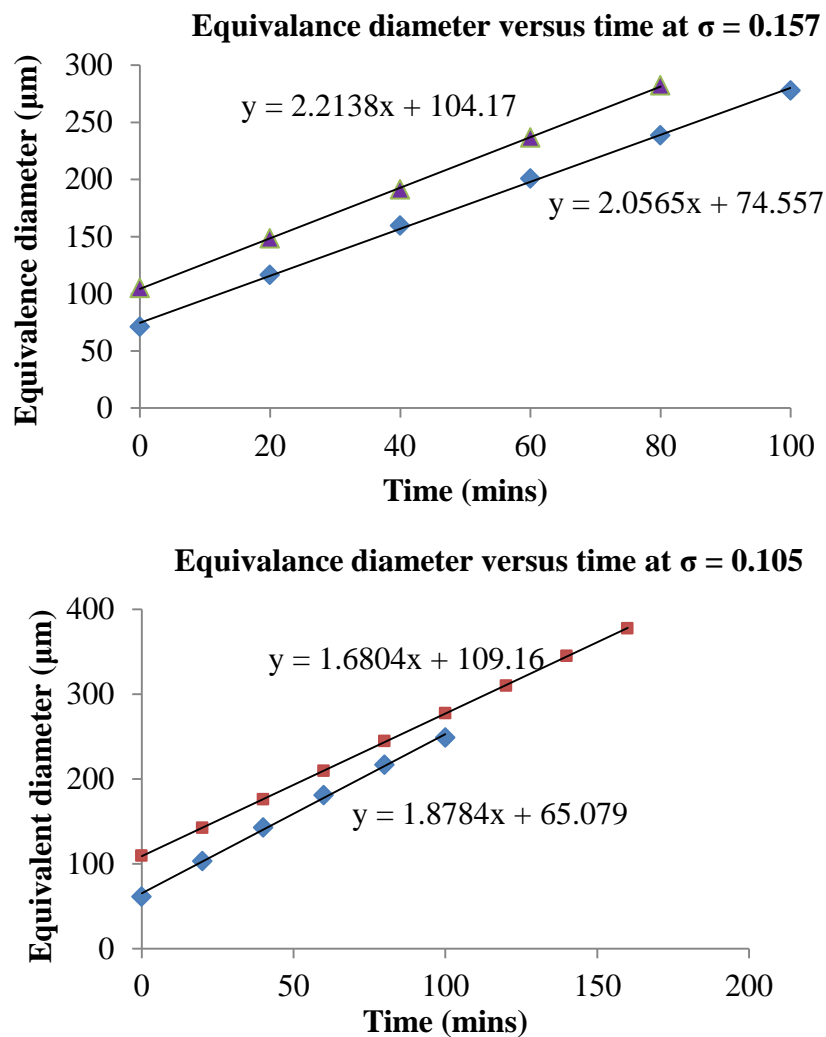


Figure 7.17 Growth rate (in equivalence diameter) in a 7mL non-agitated jacketed reactor at $\sigma = 0.157$ and 0.105 .

7.10.2 Growth rate in 7mL agitated vessel

A sequence of images of crystals grown in agitated 7ml crystallisers of CRYSTALLINE in ethanol is showed in Figure 7.18. Upon completion of the experiments, Process Image Analysis Expert software developed at the University of Leeds was used to extract the crystal growth rate. The fundamental limitation of image analysis is the difficulty of segmenting crystals in a concentrated solution due to overlapped crystals. In order to overcome this problem, images were captured frequently (every 10 seconds) so images which captured clear and sharp crystal edges can be selected for the growth rate estimation in the event that the particular crystal in question was obstructed by another crystal or shadowed by background noise (Figure 7.18b). The equivalence diameter of ibuprofen crystals in a population of crystals over time are shown in Figure

7.19. The summary results of the growth rate in stagnant and agitated solutions at a 7ml reactor scale are shown in Table 7.9.

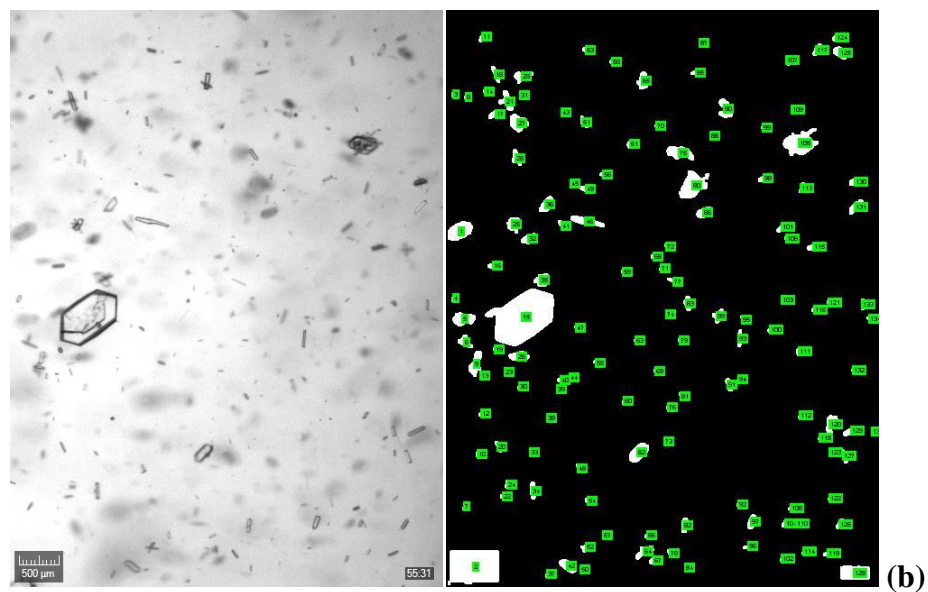
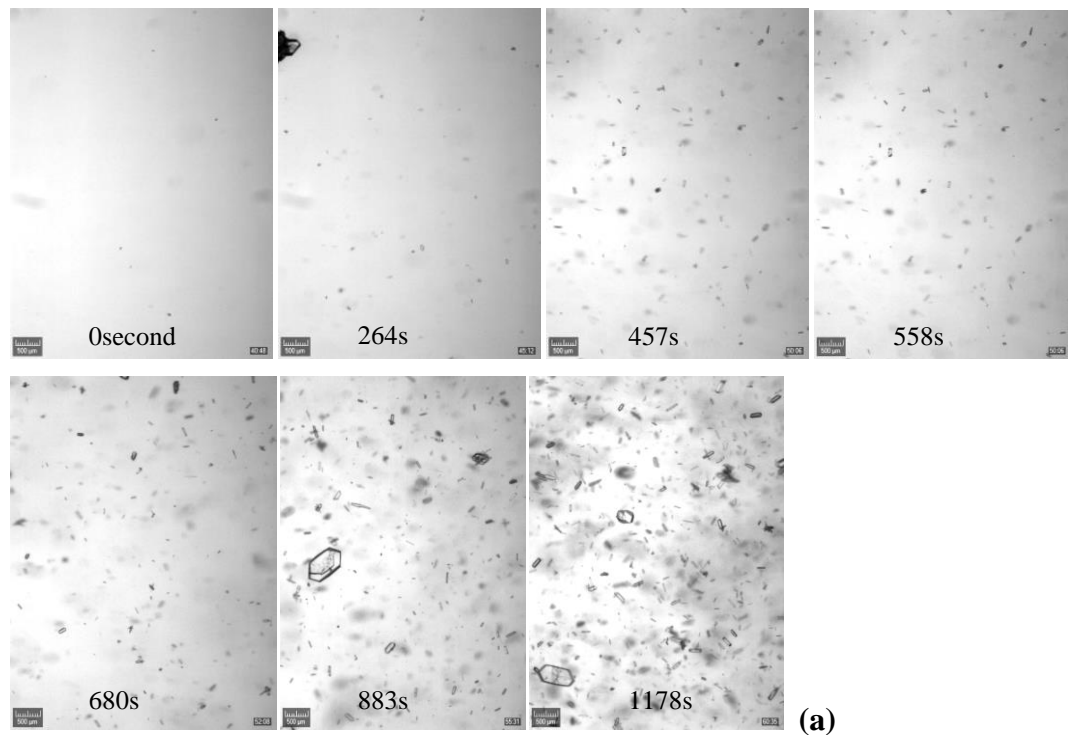


Figure 7.18 A sequence of crystals grown in ethanol after seeding at $\sigma = 0.157$ in an agitated reactor (a); the images of crystals before and after segmentation for image analysis (b).

Crystals are plate-like in shape and non-agglomerated. These single crystals are similar in appearance to crystal morphology obtained from single crystal growth rate

measurement and published images. The slopes of the straight lines give the values of the growth rate and show that the particle sizes are quite similar for both runs.

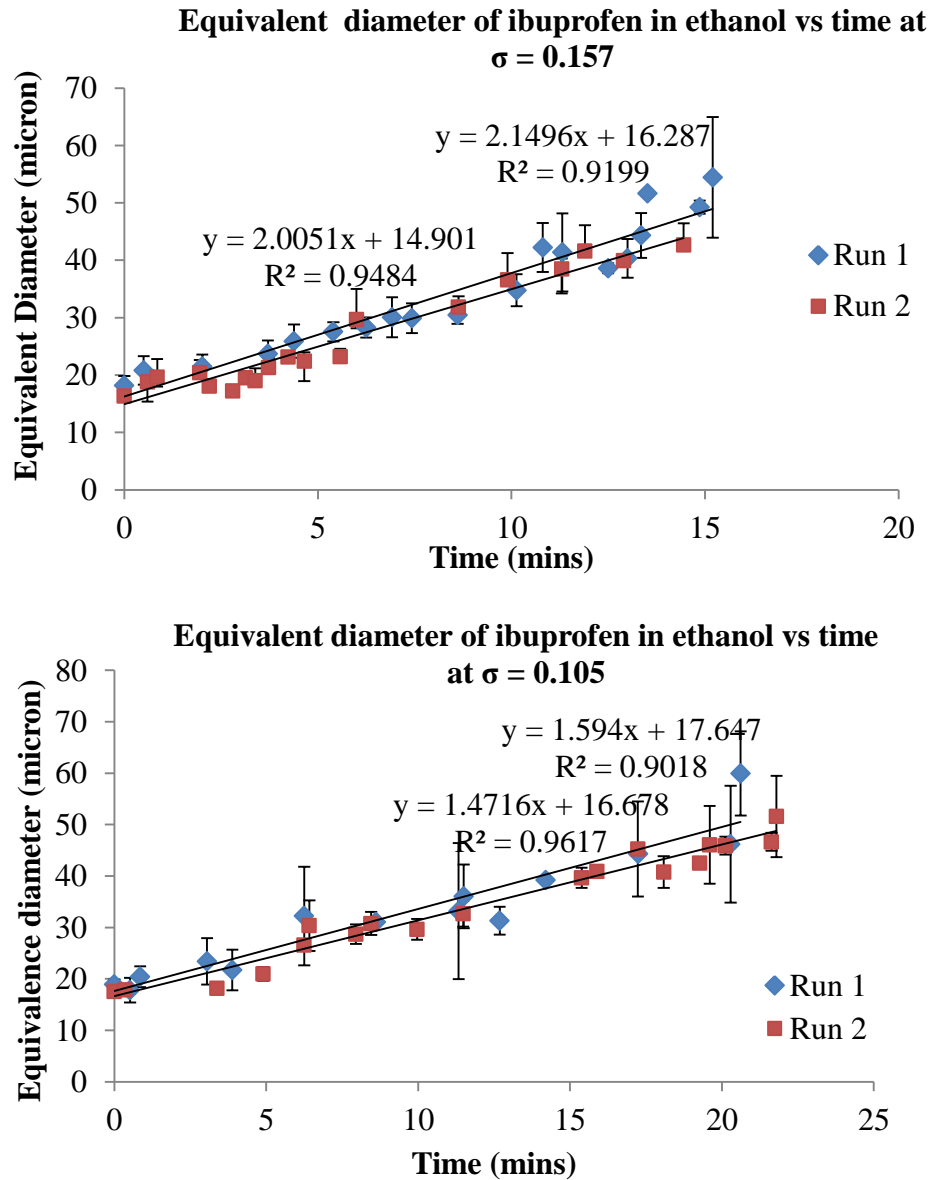


Figure 7.19 Plots of equivalent diameter of ibuprofen crystals grown in ethanol versus time at $\sigma = 0.157$ and 0.105 .

It was found that the overall growth rate increases as a function of supersaturation at $\sigma = 0.157$ and 0.105 . In order to compare the growth rate obtained from the two different techniques, a sequence of crystals captured from microscope method studies were used to calculate overall growth rates. From the plots and captured images, the first 4-6 mins after introducing seed crystals into the solutions in agitated reactors, the captured images hardly showed any crystals due to only a few seed crystals introduced into

solutions. After that period of time, an amount of new nuclei produced from an intense secondary nucleation. The secondary nucleation may have occurred by different mechanisms e.g initial breeding, needle breeding, fluid shear.etc. The secondary nucleation rate can be expressed as $B = K_b m_T^j N^k \Delta c^b$, where m_T is the concentration of crystals in suspension; N is the hydrodynamic interaction between the crystals and solution such as stirrer speed.

The secondary nucleation rate in the agitated reactor is expected to be much higher than that in non-agitated reactors. The results cannot be compared directly as one is single crystal measurements in stagnant solution (microscope) while the other is a population of crystals in agitated vessels (in CRYSTALLINE reactors) though they are measured at the same scale-size 7mL. However, the increase of growth rate trends as a function of supersaturation gives confidence that the data treatment were well-controlled in both techniques. The growth rate of ibuprofen in absolute ethanol was reported to follow a first order dependence on supersaturation . i.e. $G = k_G \sigma^n$ with $n = 1$ and $k_G = 15$. The growth of ibuprofen at $\sigma = 0.157$ and 0.105 was calculated from the first order growth kinetics shown in Table 7.9. It was obvious that the growth rate measured in CRYSTALLINE is slightly lower than the calculated data. The slightly lower growth rate obtained from the agitated batch crystalliser may be partly due to the fact that a high number of new nuclei (secondary nucleation) are formed which leads to a large number of small crystals, and thus resulting in faster desupersaturation of the solution. In addition, the breakage, collision of crystals can occur when agitated, and the growth rate analysis based on the equivalence diameter of a population of different-size crystals including seed crystals and nucleated and broken crystals (much smaller) in the agitated reactors contribute to the uneven particle size distribution and lower growth rate in agitated vessels.

Table 7.9 Overall growth rates obtained from microscopy method and CRYSTALLINE experiments at various supersaturation levels, σ

Supersaturation σ	Stagnant solutions	Agitated solutions	Data after Rashid [15]
0.157	2.14 ± 0.11	2.06 ± 0.11	2.35
0.105	1.78 ± 0.13	1.53 ± 0.09	1.57

7.11 Discussion

The solution mediated growth rates of the {011} and {001} faces of spontaneously nucleated ibuprofen crystals have been measured as a function of supersaturation and solvent under diffusion limited conditions at two scale sizes (0.5mL and 15mL). The results show that the mean growth rate of the {001} and {011} faces were found to increase with increasing relative supersaturation with $R_{\{011\}}$ being higher than $R_{\{001\}}$. This is found particularly to be the case for crystals grown in ethyl acetate, acetonitrile and toluene solutions at the two different scale sizes. At a similar supersaturation level σ , $R_{\{011\}}$ were found to be lowest in ethanol and highest in acetonitrile with $R_{\{001\}}$ lowest in toluene and highest in ethanol and ethyl acetate. The difference in growth rate between different surfaces of a crystal and the growth rate of the same surface in different solvents might be a result of the differences in the surface chemistry of the crystal and the interaction of these faces with solvent molecules. Changes of the relative growth rate of the {001} and {011} faces with solvent-type and supersaturation level cause variation of aspect ratios of the crystals. Ibuprofen crystals become more elongated in ethyl acetate, acetonitrile and toluene in comparison to the crystals grown in ethanol. Aspect ratios at two scale-sizes, 0.5 mL and 15mL, are quite similar or slightly higher at the 15mL scale-size.

The growth rate $R_{\{001\}}$ and $R_{\{011\}}$ in the 15mL vessel are greater than the growth rates in the 0.5mL cuvette cell due to the better temperature control in the 0.5mL cuvette and the supersaturation levels decrease quicker in the 0.5mL solution compared to that in the 15mL solution as crystals are nucleated and grow. However, the GRDs in the 15mL vessel are less than the GRDs in the 0.5 mL cuvette. At larger scale size, in the 15mL jacketed-vessel, integrated with an ATR/UV-Vis spectrophotometer based on an inverted microscope, highlights a good technique to monitor supersaturation levels during the crystallisation process. Studies at the larger 15mL scale in a jacketed-vessel revealed solution supersaturation to be fairly constant during the growth process thus confirming this methodology as being reliable for determination of the growth kinetics and mechanisms. However only the supersaturation of the bulk solution, not the stagnant film of liquid adjacent to the growing crystal faces, was monitored and

measured during the experiments. This drawback can be improved by integrating an overhead stirrer to provide gentle agitation to the solution.

The data also showed GRD occurs in both faces and at all supersaturation levels; however it is quite low (the average GRD is 12% of the mean growth rate) compared to the GRD in a stirred batch crystalliser measured from the crystal size distribution over time from the literature [15]. This study was carried out on single crystals in stagnant solutions so the growth process is mainly controlled by the volume diffusion. A volume diffusion controlled process should exhibit a low GRD. This might be due to stirred reactors which disturb the boundary layer (both the diffusion and the interface adsorption-boundary layer) leading to fluctuating mass transfer whilst single crystals grow in stagnant solutions at the constant rate because the boundary layer was not under disturbance during the growth process [181]. This explanation is supported on single crystal growth observations published in previous studies [20, 182].

The B&S model has been found to best description the dependence of the growth rate of the {011} face and {001} face on the supersaturations σ from 0.54 to 1.22, except for several cases both the B&S and the BCF mechanism are both well fitted. It was observed that the surface associated with the faster growth rate typically follow the B&S mechanism. These slower growth faces such as {001} of very needle-like crystals in toluene, {001} in ethyl acetate (1.8 - 4.4 $\mu\text{m}/\text{min}$) at σ from 0.54 to 0.76, both of the {001} and {011} in ethanol which can be fitted by both growth mechanisms. This agrees with the growth mechanism theory where B&S occurs when further growth units integrate into the existing monolayer to spread over the surface. The solubility in ethanol is highest resulting high viscosity and thus mass transport from solution to the surface is slow and surface diffusions plays an important role.

In ethyl acetate, the growth rate was studied at a wider range of supersaturation, from 0.54 to 1.2. It was shown that at σ from 0.54 to 0.76, $R_{\{011\}}$ versus σ fits well for both BCF and B&S model. However, at σ ranging 0.76 to 1.20 only B&S shows an acceptable fit (the adj. $R^2 = 0.995$ for B&S and -0.22 for BCF) which indicates agreement with the growth mechanism theory discussed in the chapter 2. The crystal growth rate mechanism taking place at the crystal/solution interface is expected to change as a function of supersaturation. The spiral growth mechanism might be occur

at low supersaturation [70]. Hence, at intermediate supersaturation (σ from 0.54 to 0.76) both B&S and BCF mechanisms were well fitted. However, at higher supersaturation (σ from 0.76 to 1.20) the two-dimensional nucleation mechanism is dominant.

Ibuprofen crystals grown from four solvents follow the B&S mechanism at moderate and relative high supersaturation ($\sigma = 0.54 - 1.22$) and there is no mechanistic change with scale size. The relation of growth mechanism and the surface entropy α factor was shown in this study. It has been shown that the assessment of the surface entropy factor α from the heat of solution was in quite good agreement to the observed growth mechanism. The B&S is the main growth mechanism on the $\{011\}$ and $\{002\}$ face, except for $R\{011\}$ and $R\{001\}$ in ethanol, $\{001\}$ in ethyl acetate and $\{001\}$ in toluene. The growth mechanism was in good agreement with the values of the calculated α factor in the range from 2 to 5.

The growth rate in the non-agitated jacketed vessel is quite similar or slightly higher than the growth rate in the agitated reactors which is counterintuitive due to the agitation accelerating the mass transfer and diffusion process. However it is understandable in this study because the agitated reactors retain higher secondary nucleation rates. Agitation causes the breakage of particles and the image analysis analysing the growth rate based on a population of uneven particle size distribution including seed crystals (big particles) and secondary nucleated and broken crystals (small particles). In the crystallisers, there are two growth kinetics proceeding simultaneously inside the reactor: the formation of new crystalline particles from secondary nucleation and their consequent increase in crystal size and the growth of seed crystals. Contacts between a growing crystal and walls of the crystalliser, the stirrer or other crystals result in the formation of contact nuclei. This nucleation is at quite a high rate, so a large numbers of nuclei were formed, resulting in broadening of the CSD.

Klug and Pigford [172] also showed a sensible agreement between the growth rate in batch and single crystal measurement for anhydrous sodium sulphate. Maharan et al [183] reported good agreement of the growth rate of L-asparagine in batch crystalliser, single crystals and MSMR.

The drawback of this PhD study was the supersaturation was not controlled, particularly in 0.5ml cuvette. However, the data in both scale sizes are quite similar. This drawback can be improved in industrial crystalliser by connecting a computer program to decrease the temperature as the solution was desupersaturated to keep supersaturation constant.

7.12 Conclusions

Several important points can be concluded from this chapter:

- The measured growth rate data in a series of solvents at both scale sizes; 0.5ml and 15ml, are quite consistent and showed a good methodology for studying the effect on crystallising conditions on the growth rate of single crystals as well as obtaining the fundamental kinetic data with taking into account of crystal shapes by measuring the growth rate of individual crystal habit faces.
- Single crystal growth measurements provide useful information for studying the basic growth kinetics of a solute system. They give more flexibility in investigating the influence of various key parameters such as temperature, supersaturation on the growth kinetics of crystal faces. However, industrial crystallisation is usually carried out in agitated batch reactors. In such crystalliser systems, the behaviour of individual particles in term of their velocity pattern and interactions with other crystals and the stirrer and the wall of reactors [183] as well as their nature in terms of shapes, crystal surface has not been well-understood. Hence, it is worthy to compare the growth kinetics obtained from single crystals and a population of crystals in agitated crystallisers.
- The agitation and scale-up do not invalidate the growth rate data and growth mechanism. The overall rate data was calculated to be slightly higher than that in agitated reactor and thus the data obtained from single crystals can be used for scale-up. This proposed that the results of single crystals growth rate experiments can be useful in representative for the growth rate of a population of crystals in agitated crystallizers for particular chemical systems.

8 Technology transfer: Growth rate measurements in an industrial R&D workstream

Summary:

This chapter presents the single crystal growth rate measurement technique for studying the effect of crystallising conditions on a new drug compound as part of the process research and workstream.

8.1 Introduction

The development of novel and effective platforms for studying the influence of crystallisation environment on the crystal growth in terms of crystal morphology and growth rates of individual crystal faces as a function of processing conditions is one of key aims of this research. This instrumentation has enabled derivation of the fundamental process crystal growth kinetics and to provide an understanding of the crystalline forms, shapes (aspect ratio) in order to control the final products. As such, this work addresses directly the industry-wide demand for refined research and development processes. The reliable processing of particles with controlled physical properties is able to reduce the manufacturing time and the overall number of unit operations. The 0.5ml cuvette crystallisation cell was employed as a technology transfer to a practical drug compound in development and it has been used as a routine and useful measurement tool for the pharmaceutical and chemical industry. It is an easy-to-use piece of equipment and consumes very small amount of materials, which is a suitable tool for developing drug compounds at the research and development stage. The case study shown here was compound A which appears as a mixture of needle-like and plate-like crystals of the same polymorph when it is recrystallised from batches at Pfizer pharmaceutical company.

These experiments were carried out in 7 working days during a short internship in Pfizer, Sandwich, UK and Pfizer, Groton, US. Also, this 0.5ml cuvette crystallisation cell has been used in other projects at the University of Leeds for different studies.

8.2 Solubility

The solubility of compound A was obtained as a function of temperature provided by Pfizer shown in Figure 8.1 .

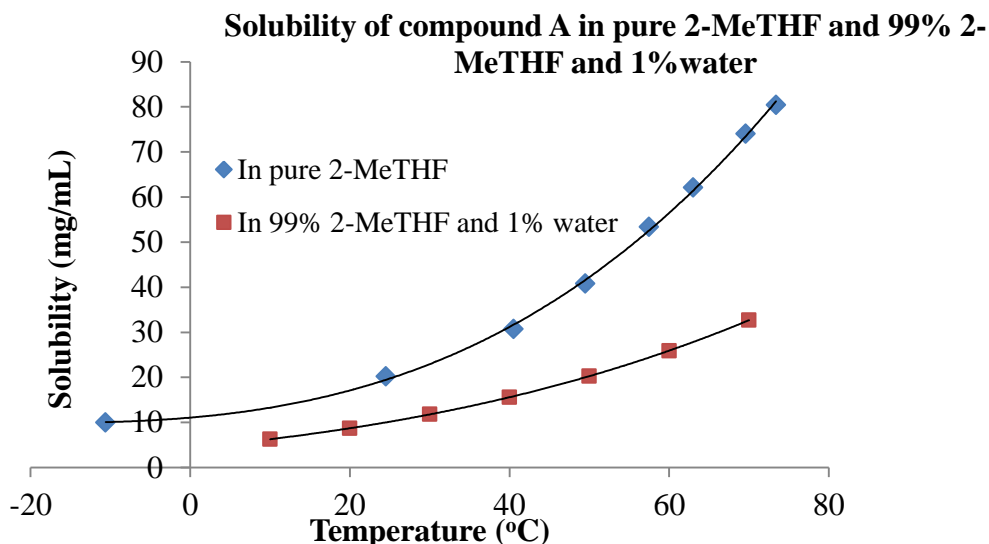


Figure 8.1 Solubility of compound A in 2-MeTHF and in a mixture of 99% 2-MeTHF and 1% water.

The solubility data of compound A in 2-MeTHF is experimentally measured data; however the solubility in 2-MeTHF 1% water was predicted from a quantitative validated model for the prediction of solubility as a function of water and temperature. It was shown that compound A is more soluble in 2-MeTHF than in the mixture of 99% 2-MeTHF and 1% water.

8.3 Growth rate determination for compound A

8.3.1 Growth rate in 2-MeTHF

A sequence of photomicrographs of spontaneously nucleated plate-like crystals grown in stagnant conditions at $\sigma = 0.65$ (Figure 8.2) and $\sigma = 0.52$ (Figure 8.3) and a sequence of needle-like crystals nucleated and grown after tilting the cuvette (turbulent conditions) at $\sigma = 1.00$ (Figure 8.4) and $\sigma = 0.38$ (Figure 8.5) together with an example of the plot of the length and width as a function of time (Figure 8.6) are presented to investigate the growth rates of compound A in 2-MeTHF.

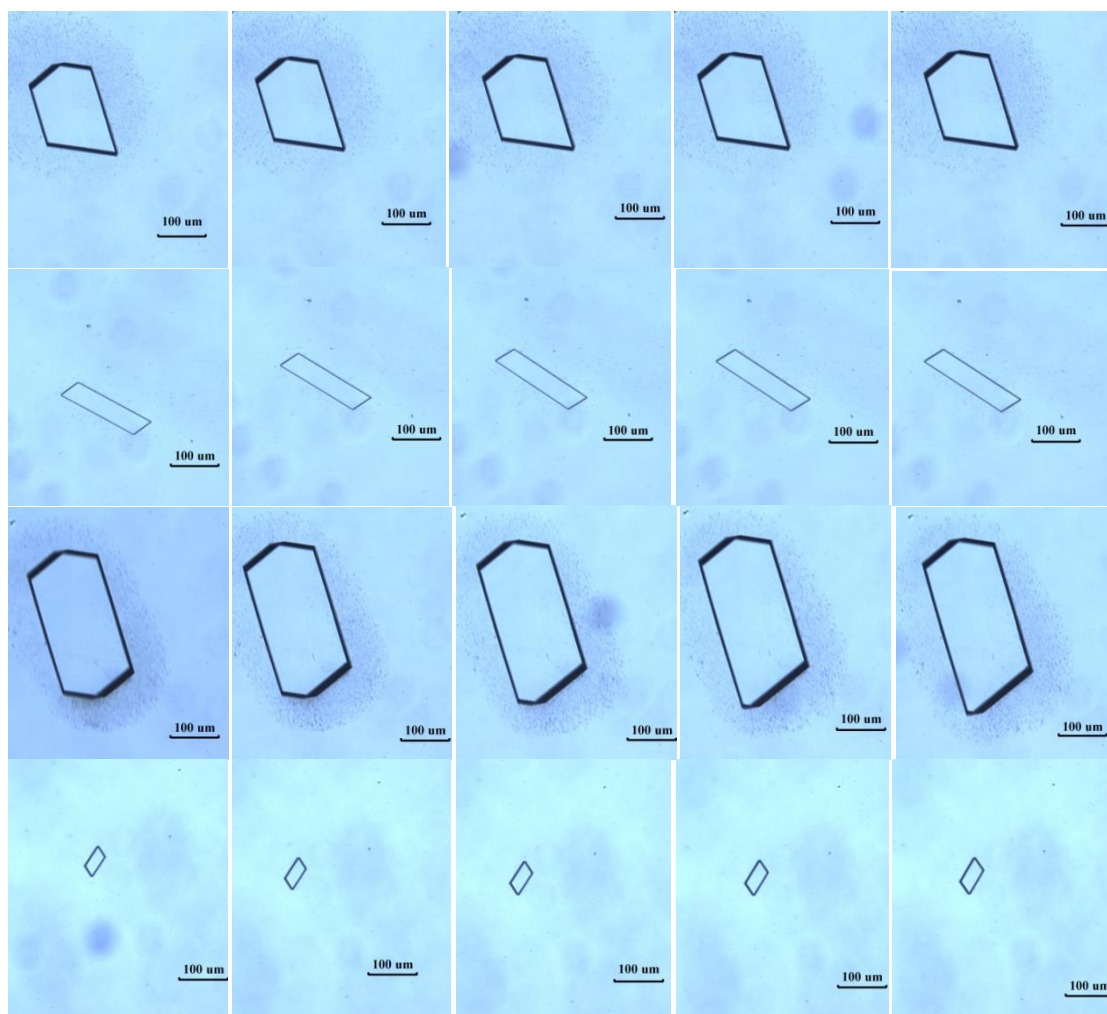


Figure 8.2 A sequence of in-situ crystal growth observations of 4 crystals grown from 2-MeTHF at $\sigma = 0.65$ with 10 minute intervals between images.

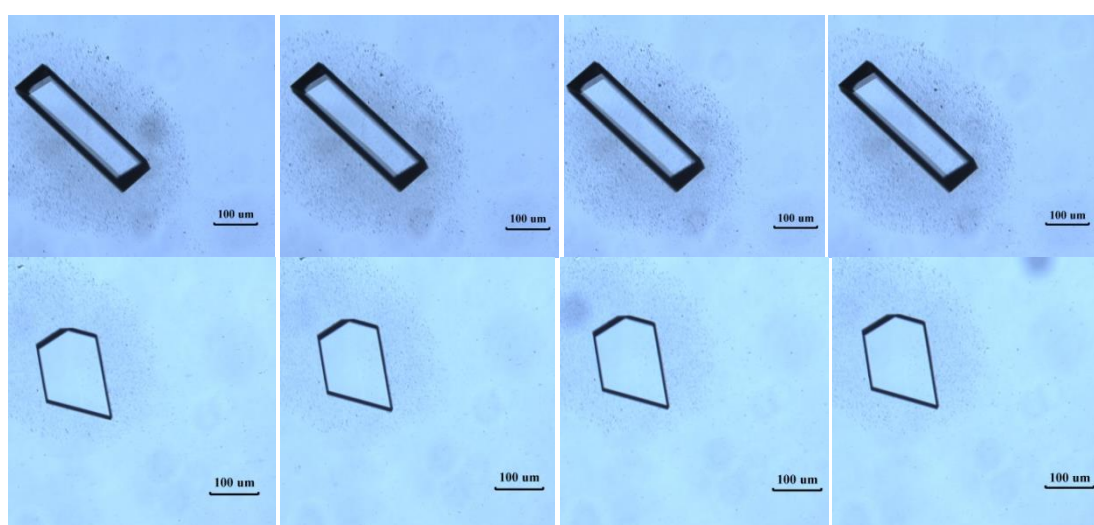


Figure 8.3 A sequence of in-situ crystal growth observations of 2 crystals grown from 2-MeTHF at $T = 25^{\circ}\text{C}$ ($\sigma = 0.52$) with 10 minutes interval between images.

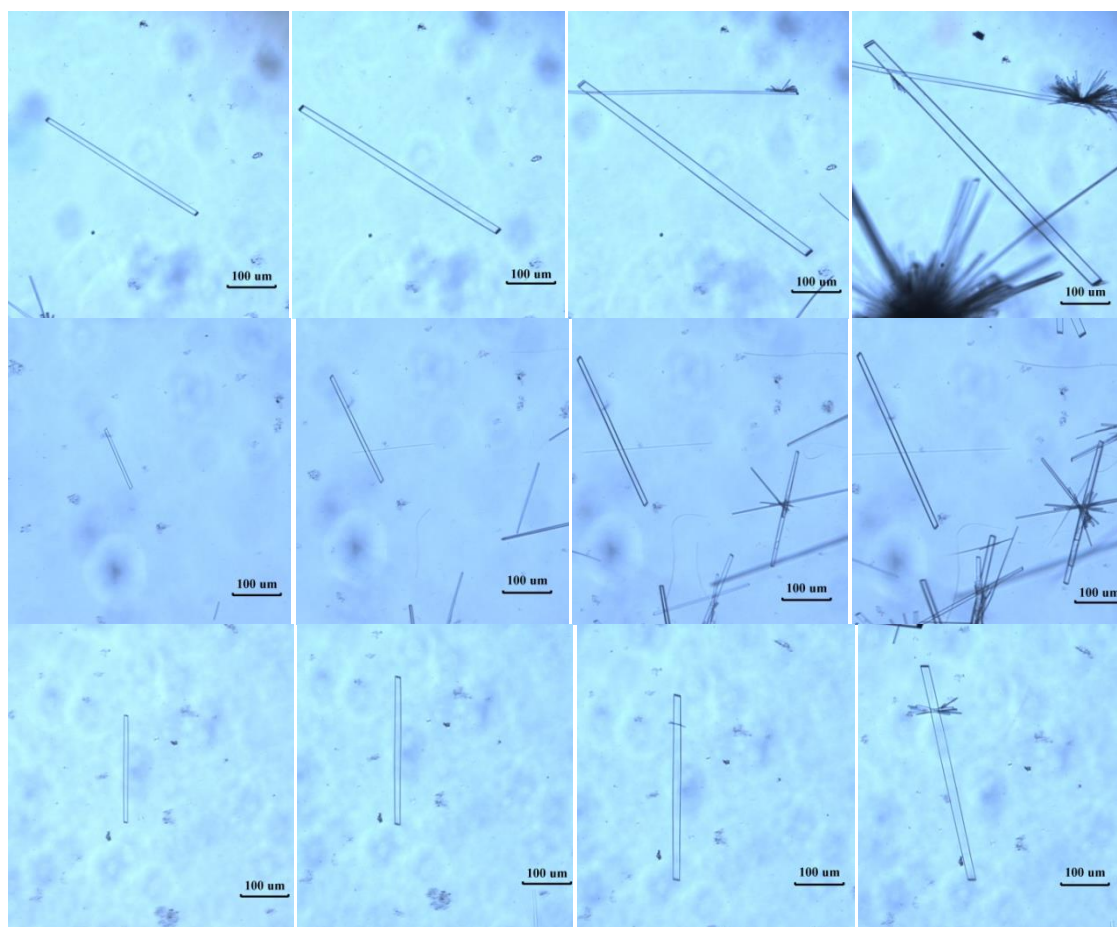


Figure 8.4 A sequence of in-situ crystal growth observations of 3 crystals nucleated and grown from 2-MeTHF isothermal at $T = 15^{\circ}\text{C}$ ($\sigma = 1.00$) after tilting the cuvette.

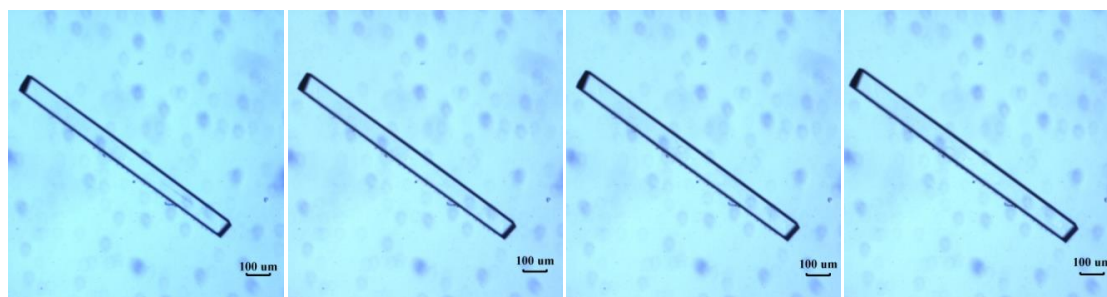


Figure 8.5 A sequence of in-situ crystal growth observations of a crystal nucleated and from 2-MeTHF isothermal at $T = 28^{\circ}\text{C}$ ($\sigma = 0.38$) after tilting the cuvette with 10 minutes interval between images.

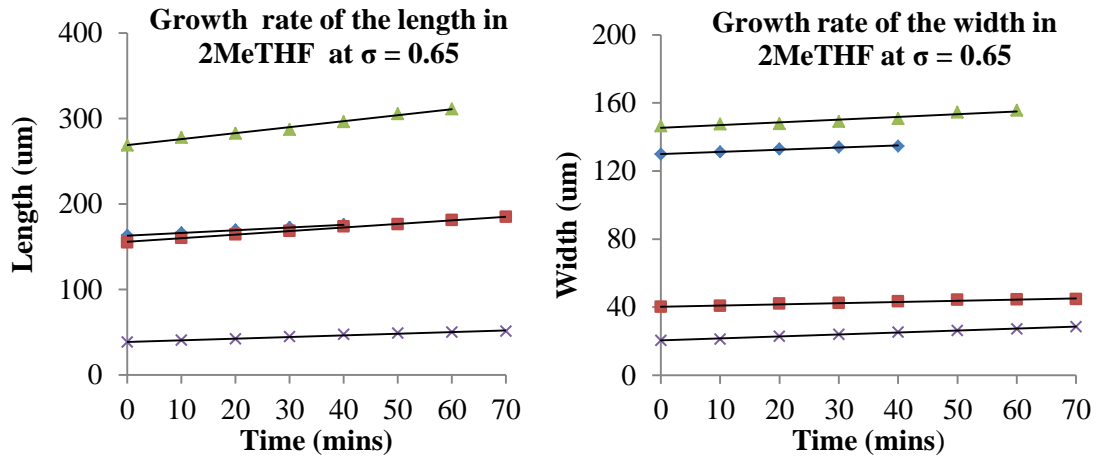


Figure 8.6 An example of the growth rate of the length and width of crystals grown from 2-MeTHF isothermal at $T = 22^{\circ}\text{C}$ ($\sigma = 0.65$) in stagnant conditions. Each line represents the growth rate of individual crystals over time.

Table 8.1 The growth rate of the length and width at $\sigma = 0.65$ and 0.52 in stagnant solutions

Supersaturation	$\sigma = 0.65$		$\sigma = 0.52$	
Plate-like crystals	Length	Width	Length	Width
Mean growth rate ($\mu\text{m}/\text{min}$)	0.41 ± 0.21	0.12 ± 0.04	0.23 ± 0.13	0.075 ± 0.03

Table 8.2 The growth rate of the length and width at $\sigma = 1.00$ and 0.38 in turbulent solutions

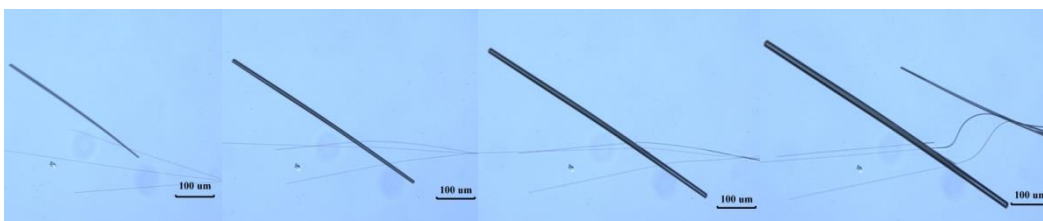
Relative supersaturation	$\sigma = 1.00$		$\sigma = 0.38$	
Needle-like crystals	Length	Width	Length	Width
Mean growth rate ($\mu\text{m}/\text{min}$)	10.17 ± 0.24	0.42 ± 0.02	2.21	0.31

It has been shown that compound A recrystallises as plate-like crystals in different shapes in stagnant solution and needle-like crystals in turbulent conditions. In both stagnant and turbulent conditions, the growth rates, both in the length and in the width, increase with increasing supersaturation. For example, in turbulent conditions, at $\sigma = 1.00$, the growth rate for the length and the width is 2.21 and 0.3 ($\mu\text{m}/\text{min}$) and at $\sigma = 0.38$, the growth rate for the length and the width 10.17 and 0.42 ($\mu\text{m}/\text{min}$). Comparing the growth rate at $\sigma = 1.00$ to the growth rate at $\sigma = 0.38$, is 4.6 times faster in the length and 1.35 times faster in the width indicating crystals have higher aspect ratio at higher supersaturation which is in good agreement with microphotographs of crystal morphology shown in the Figure 8.4 and Figure 8.5.

8.3.2 Growth rate in a mixture of 99% 2-MeTHF and 1% water

A sequence of images of crystals grown in 99% 2-Methyl THF and 1% water in the in-situ crystallisation cell at $\sigma = 1.07$ and 0.87 is shown in Figure 8.7.

$\sigma = 1.07$



$\sigma = 0.87$

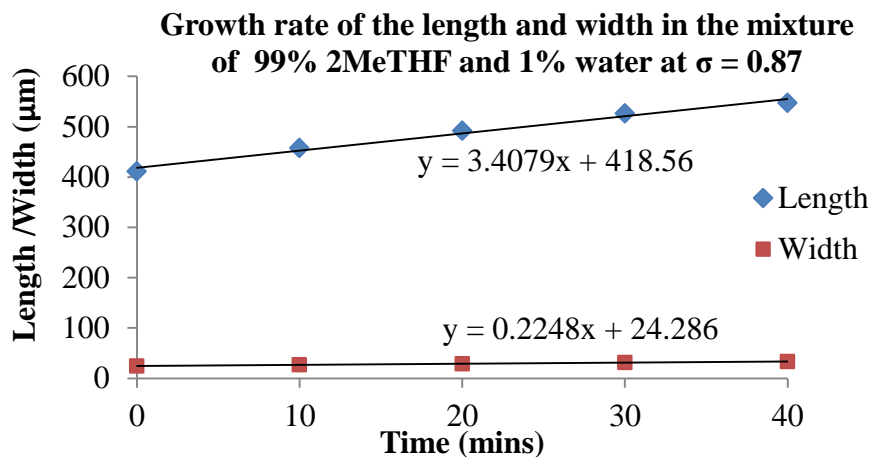


Figure 8.7 A sequence of in-situ crystal growth observations at $\sigma = 1.07$ (above) and $\sigma = 0.87$ (below) with 10 minutes interval between images together with an example of the plot of the length and width versus time of crystals grown from the mixture of 99% 2-MeTHF 1% water.

Table 8.3 Growth rate of length and width in 99% 2-MeTHF 1% water at $\sigma = 1.07$ and 0.87

Growth rate of crystals	$\sigma = 1.07$	$\sigma = 0.87$
Length	11.6	3.41
Width	0.42	0.22

8.4 Discussion

The morphology of compound A changes with the variation of the crystallising conditions. There were two morphologies: plate-like and needle-like crystals. Solvents and agitation showed a significant effect on the morphology of crystals.

Mostly plate-like hexagonal or rhomboid crystals are produced from 2-MeTHF in a stagnant solution-state whilst needle-like crystals are obtained from 2-MeTHF in a turbulent solution (with tilting and shaking of the cuvette). The morphology can be changed slowly over time due to the different growth rate of crystal habit faces. The fast growth faces disappear and the slow growth faces become dominant.

The mixture of 99% 2-MeTHF and 1% water only produced very needle-like crystals in both stagnant and turbulent solutions whilst the morphologies recrystallised from the pure 2-MeTHF were found to be plate-like in stagnant solutions and needle-like crystals in agitated solutions.

Crystal growth kinetics: The crystal growth rate, both in the length and in the width direction, increases with increasing supersaturation. It is likely that compound A crystals are more needle-like at higher supersaturation (lower crystallising temperature). At similar supersaturation level $\sigma = 1.00$ in 2-MeTHF and $\sigma = 1.07$ in 2-MeTHF 1% water, the growth rate of the length and the width (11.6 and 4.2 μm) in the mixture of 99% 2-MeTHF and 1% water is quite similar or slightly higher than that (10.17 and 0.42 μm) in 2-MeTHF. Due to the limited time, the measurements of the growth kinetics for compound A in 99% 2-MeTHF and 1% water were not able to repeat to obtain more accurate data.

The growth rate dispersion in this material was found to be higher than in ibuprofen. It is postulated that this is probably due to the variation of the shape of crystals in a population of nucleated crystals. The growth rate of the length and width in the same crystallising conditions are also different depending on the shape of crystals (shape-

dependant growth rate). The growth rate of the length is greater than the growth rate of the width, this is more apparent in more needle-like crystals. Furthermore, A has quite a low solubility in pure 2-MeTHF and 2-MeTHF 1% water thus local supersaturation levels are expected to decrease rapidly when small amounts of material are crystallised out.

The study of effect of crystallisation (solvent, agitation, supersaturation) on the morphology and growth kinetics of compound A confirmed the application of this cuvette crystallisation cell in the pharmaceutical industry. The application of this routine, easy-to use and effective cuvette cell instrumentation for crystal growth rate measurements, is an example of an achievement of this PhD work, which can be employed not only for the pharmaceutical industry but also as a research tool for crystallisation study in academic research and teaching.

9 Conclusions and suggestions for future work

Summary:

This chapter summarizes the research results and outcomes from this study together with the re-assessment of the thesis aims and objectives and provides some suggestions for future work in this area.

9.1 Introduction

This work presented the study of influence of crystallisation conditions on the nucleation and growth of single crystals of (RS)-ibuprofen. The current practice in industrial crystallisation are aimed at measuring average growth rate values at large scale based on an assessment of a crystal population. In this study, the use of developed *in-situ* crystallisation platforms at different scale-sizes for a real-time study of the morphology and growth rate of individual crystal faces as functions of their crystallising conditions showed a potential for the rapid and reliable study of the crystal growth kinetics for drugs and fine chemicals in the early stage of research and development. Such measurements are helpful in that they provide baseline crystal growth kinetics from which the impact of agitation and mixing can be assessed. Drawing together the aspects of this PhD work has yielded a number of key outcomes in terms of:

- Laboratory instrument development.
- Studies of the influence of crystallisation environment on the nucleation and growth of single crystals.
- A rationalization and correlation of the experimental data with molecular and solid state modelling including conformational analysis, morphological simulation in various solvents, and surface chemistry analysis.

The aims and objectives set out initially are then reviewed and suggestions for future work are given to further develop this study.

9.2 Conclusions for this study

Each chapter plays an important part in this work and they are interdependent. Solubility and nucleation data in chapter 6 was useful in designing the growth rate measurement experiments in both non-agitated (spontaneously nucleated crystallisation) and agitated vessels (seeding crystallisation). The modelling work enabled calculation of the predicted morphology and from that dominant faces of the model compound can be identified and indexed for the measurements of the growth rate of individual faces. In addition, intermolecular interactions and surface chemistry analysis aided the rationalisation of the experimental observation and data to enable understanding in more detail the effect of crystallising environment on morphology, growth rate, shapes and

aspect ratio at the molecular scale. The findings of this PhD can be summarised as follows:

9.2.1 Molecular modelling

A conformer search for an ibuprofen molecule was successful in showing the favoured conformational space of a free ibuprofen molecule. The molecule is located within a minimum energy space or is close to the minimum energy. The energy of a free molecule before and after geometry optimisation does not seem to change much for this material indicating it is a rigid molecule.

The conformer population were calculated using a COSMOtherm software package and showed there was no significant solvent effect on the conformer distribution in different solvents. This indicates there is no conformational polymorphism for ibuprofen, which supports the polymorphism screening results in chapter 6. This methodology showed a potential in predicting and rationalising conformational polymorphism for many chemical compound models. It can also be used for solvent screening and selection based on the relative population of conformers in solvents.

9.2.2 Solid-state and morphological simulation

Morphological predictions for the growth unit based on the monomer and dimers were obtained and compared with the *in-situ* observations of the ibuprofen crystal morphology, recrystallised from various solvents. The calculated value of the lattice energy was found to be -28.93 kcal/mol, which reveals a sensible agreement with the experimental lattice energy calculated from the heat of sublimation; 30.10 kcal/mol [136]. Morphological simulation was quite successful in predicting the ibuprofen morphology; except that the over-prediction of the importance of the {110} face and the aspect ratio of crystals. The dimer growth unit calculation seems to provide a slightly better prediction of ibuprofen morphology than the monomer growth unit calculation. The dimer showed the less important {110} face present in the crystal morphology and the morphology grows more in the b axis direction. However, full correlation was limited mindful that the ibuprofen crystal habit can vary between needles and plates,

depending on the crystallising environment and conditions such as solvent-type, supersaturation etc.

The rationalisation of the growth rate data of the {011} and {001} faces and the growth rate kinetics was shown in chapter 7. The intermolecular bonding in the bulk crystal lattice and on the dominant crystal surfaces was also analysed. Carbonyl oxygen (C=O) and hydroxyl hydrogen (O-H) atoms were found to account for the most energy in the lattice energy and the strongest intermolecular interactions are the hydrogen bond chain O---H bonds. It was found that most of the strong bonds contributes to the slice energy for the {100} face making this face one of the most morphologically important. The strongest bond (-7.47 kcal/mol) contributes to attachment energy on face {011} and to the slice energy of face {001}, which verifies the growth rate of face {011} is generally greater than the growth rate of face {001}.

The surface property analysis was carried out by the examination of the interaction between solvent molecules and the structures of specific growing faces as characterized by molecular modelling, e.g. polar protic solvents being likely to inhibit the growth rate of faces containing available binding sites and/or exposed groups for hydrogen bond formation such as carboxylic acid -COOH groups. This study revealed that:

- Molecular packing on the {001} face shows a non-polar property with methyl groups -CH₃ projecting out of the surface and -COOH groups exposed in one direction.
- The {011} face is more polar and -COOH groups on the {011} face with two different directions that are more exposed and easier accessible than the exposed -COOH group on face {001}.
- The {011} face provides good binding sites for polar solvent molecules. In this case, the use of polar protic solvents (ethanol which can act either as a hydrogen bond donors or acceptors) would inhibit the growth of the {011} face resulting in plate-like crystals. In contrast, a polar aprotic solvent such as ethyl acetate or acetonitrile or a non-polar solvent such as toluene can be expected to interact less with the {011} face compared to ethanol thus producing more elongated crystals. Moreover, bindings of less polar solvents with exposed alkyl groups on the {001} face might hinder the growth of this face.

9.2.3 Instrumentation for studying the growth kinetics

A series of novel and effective platforms for the measurement of face-specific growth rates in crystalline systems at various scale-sizes include: a 0.5ml cuvette prototype crystallisation cell, a 0.5 ml peltier cell, a platform 8-cell crystalliser unit (sample volume ca. 100 μ l) based on Morphologi G3 and a 15ml jacketed vessel were developed in this PhD. The latter has been integrated with the use of an ATR UV/Vis spectrophotometer with the overall system being based on an inverted optical polarizing microscope for *in-situ* crystallisation studies were developed and improved throughout this PhD work. The use of these instruments enables characterisation of crystal morphology and analysis of the individual crystal face (hkl) growth rates and growth mechanisms during representative crystallisation processes of ibuprofen. Although based on small-scale laboratory work under diffusion limited conditions, the work has focused and has been optimised for enabling the design of reproducible processes; they would be designed for deriving the data needed for process scale-up to manufacturing. The 0.5ml cuvette crystallisation cell, is an effective and easy-to-use apparatus for screening studies, e.g. solvent(s) and /or solid form evaluation, studying and understanding effects of processing conditions (solvents, temperature, supersaturation, impurities, seeding etc.) and processing scale-sizes on final product forms and acquiring fundamental growth kinetics data for use in process scale-up. However, there was no direct measurement of the de-supersaturation of solutions in the cuvette cell during crystal growth and this is also coupled with the slightly slow temperature exchange with the heater/chiller bath. This problem was addressed with the design and development of a peltier system for rapid change of temperature, which can be used to measure the dissolution rate of crystals.

9.2.4 Nucleation as a function of solvent

The solubility, enthalpy and entropy of dissolution and activity coefficient of ibuprofen in various solvents at different temperatures were determined using ATR UV/Vis and gravimetric method and compared to the published data showing quite similar values. The experimentally measured solubility using ATR UV/Vis spectroscopy was found to be lower than that calculated by the van't Hoff equation showing a deviation from ideal

behaviour. This can be rationalised by the consideration of the component groups and also the polarity of solute and solvent molecules. ATR UV/Vis is a rapid and efficient technique for solubility measurements of strongly absorbing materials but it has some limiting value due to the refractive index in some solvents (in the case of toluene).

Though consideration of the crystallisation temperature in polythermal crystallisation and the induction time in isothermal crystallisation which varied hugely for all solvent systems, it has been shown that the MSZW of ibuprofen is not very large ($\Delta T = 10.0$ - 13.9°C) which is not typical for many organic or pharmaceutical compounds. The nucleation order is 1.55, 3.27 and 0.94 in ethyl acetate, acetonitrile and toluene respectively. The interfacial energies were found to be in the range of $5.52 \cdot 10^{-3} \text{ J/m}^2$, $5.33 \cdot 10^{-3} \text{ J/m}^2$, $4.38 \cdot 10^{-3} \text{ J/m}^2$ and $2.56 \cdot 10^{-3} \text{ J/m}^2$ for acetonitrile, ethanol, toluene and ethyl acetate, respectively indicating that ibuprofen has the smaller MSZW in toluene and ethyl acetate compared to that in ethanol and acetonitrile.

Owing to the limited time and compromise with other core objectives of this PhD work, the MSWZ determination experiments were not able to be repeated to obtain more reproducible induction time data. However, analysis does reveal the data exemplifies the induction time increases with increasing of temperature, which implies the critical nuclei radius increases with decreasing the degree of supersaturation and increasing temperature. These results are in good agreement with classic nucleation theory.

9.2.5 Effect of crystallisation environmental conditions on the growth rate of individual crystal faces

The growth rate measurements of the {001} and {011} faces on spontaneously nucleated crystals of ibuprofen under diffusion limited conditions (stagnant solutions) have shown that the mean growth rate of the {001} and {011} faces increases with increasing relative supersaturation. $R_{\{011\}}$ has been measured to be higher than $R_{\{001\}}$ in ibuprofen crystals, in particular for crystals grown in ethyl acetate, acetonitrile and toluene (elongated and needle-like crystals) at two scale sizes: a 0.5ml cuvette crystallisation cell immersed in a water tank and a 15ml jacketed vessel. For 4 solvents at the same supersaturation solutions, $R_{\{011\}}$ in acetonitrile is the highest and $R_{\{011\}}$

in ethanol is the lowest. $R_{\{001\}}$ in ethanol and ethyl acetate are quite similar and highest whereas $R_{\{001\}}$ in toluene is the lowest. The rate of change of growth rate with changing supersaturation, $dR/d\sigma$, for the $\{001\}$ and $\{011\}$ faces in four solvents was not found to be constant. $R_{\{011\}}$ in acetonitrile increases much more with increasing supersaturation compared to that in the other solvents.

The difference of the growth rate between different surfaces and the growth rate of the same surface in different solvents was rationalized by surface chemistry and the interaction of the solvents on these crystal surfaces. Changes of the relative growth rate of the $\{001\}$ and $\{011\}$ faces with solvent-type and supersaturation level cause variation of aspect ratios of the crystals. Ibuprofen crystals become more elongated in ethyl acetate, acetonitrile and toluene in comparison to the crystals grown in ethanol. The aspect ratios at two scale-sizes; 0.5 ml and 15ml, are quite similar or slightly higher at a 15ml scale-size.

The data also revealed evidence for a degree of GRD in the crystal growth behaviour for both faces and for all supersaturations. However it is comparatively low (the average GRD typically observed is 12% of the mean growth rate) compared to the GRD in a stirred batch crystalliser measured from crystal size distribution over time from Rashid [15] and it is also lower compared to some other organic and inorganic materials [20, 21, 174, 175].

The growth rate $R_{\{001\}}$ and $R_{\{011\}}$ in the 15ml vessel were found to be slightly greater than those observed for the growth rates in the 0.5ml cuvette cell. At the 15ml scale-size, integration with an ATR UV/Vis spectrophotometer demonstrated this techniques capability to monitor supersaturation levels during crystal growth. Nonetheless, it should be noted that only the supersaturation of the bulk solution, not the boundary layer of liquid adjacent to the growing crystal faces, was monitored and measured during the experiments. This drawback can be improved by integrating an overhead stirrer to gently agitate the solutions.

The B&S growth mechanism model was found to provide the best description of the dependence of the growth rate of the $\{011\}$ face and $\{001\}$ face on the solution. For

supersaturations from 0.54 to 1.22, this mechanism was found to provide a good fit to the data with no mechanistic change found upon scale-size.

The calculated surface entropy α factor has a value smaller than 5 so the B&S mechanism on the {011} and {001} face is expected to occur in these solvents, which agrees with the measured and fitted growth mechanisms from the experimental data.

Additionally, it was noted that, for all solvents (particularly in ethanol producing plate-like crystals), re-entrant faces appear at high levels of supersaturation. Crystals showed no evidence for any substantial defects such as twinning being present. These re-entrant (concave) edges were confirmed which is not due to twinning through the polarizer microscopy technique. The critical supersaturation for this phenomenon was found to be higher than 0.66 for ethanol and ethyl acetate and 0.79 for acetonitrile and toluene. This observation was consistent with surface nucleation at the boundary between the {011} and {0-11} growth sectors probably due to kinetic roughening. Analysis of the interplanar angles for the experimental data using morphological simulation by measuring interfacial angles of the {011} face and these re-entrant faces being consistent and reproducible propose that the higher index face planes are either the {012} or {112} face.

The overall growth rate in ethanol in an agitated 7mL batch reactor of CRYSTALLINE were also measured and compared to that in a non-agitated 7ml jacketed vessel. It was shown that the growth rate in the non-agitated jacketed vessel is slightly higher than the growth rate in the agitated reactors. It is sensible in this study because the agitated reactors retain higher secondary nucleation rates. Agitation causes the breakage of particles and the image analysis analyses the growth rate based on a population of uneven particle size distribution including seed crystals and secondary nucleated and broken crystals. In addition, the growth rate measured in an agitated 7mL batch reactor in this study is slightly lower than the calculated growth using the first order growth kinetics for the growth rate measurement for ibuprofen in ethanol in a stirred seeded batch crystallisation reactor reported in literature [15].

9.3 Review aims and objectives

In accordance with the initial aims and objectives, this study has made progress in establishing methodology for investigating the influence of crystallisation environment on the crystal growth at the single crystal level and integrating this with the molecular-scale understanding. The solution behaviour and nucleation kinetics of ibuprofen in solvents were revealed as a function of solvents and temperature. The growth rate of the {001} and {011} faces of spontaneous nucleated single ibuprofen crystals under diffusion limited conditions as a function of environment conditions such as solvent type, supersaturation and reactor scale-sizes were measured demonstrating a great impact of these factors on growth rate of the crystal habit faces. This experimental data was linked to and rationalized using molecular modelling including conformation analysis and morphological prediction. Yet the work has still not completed several objectives:

- Measurement of the growth rate of the {100} faces.
- Complete development of a medium throughput screening particle characterisation system facility using the Morphologi G3 and the automated image analysis.
- Measurement crystal growth rate at 0.5L scale size.
- Using grid-search based method to predict crystal morphology in growth solutions.

9.4 Suggestions for future work

9.4.1 The measurement of the growth rate for the {100} face

Ibuprofen crystals show three important faces; {100}, {001} and {011} however in this work, growth rates of the {001} and {011} faces were measured. Growth rates of the {100} face can be measured using incident light such as an interferometry (fringes), Nomarski phase contrast, differential interfere contrast or AFM to measure the growth rates of the surfaces (described in chapter 3). There is also a motivation to investigate the growth mechanism of the {100} face because it is a dominant face of the Ibuprofen crystals which is expected to possess a slow growth rate.

9.4.2 Development of a medium throughput screening particle characterisation system facility using the Morphologi G3

From the 0.5ml cuvette crystallisation cell, a further development of a novel platform 8-cell crystalliser unit (sample volume ca. 100 μ l) (Figure 9.1a) which can be fitted on the stage of a Morphologi G3 automated particle size and shape measurement system (Figure 9.1b) for the measurement of face-specific growth rates and an integration of the image analysis code, potentially have significant value to industry notably in the pharmaceutical, agrochemical, personal products, detergents and energy materials sectors.

The current particle shape software provided by the G3 system is optimised for the analysis of static powder samples rather than for the analysis of the time-dependant growth rates of polyhedrally shaped crystals located with a crystallisation cell. Hence, new image analysis software, developed in collaboration with Professor David Hogg's group in the School of Computing, now allows for automated image analysis from the cell which can be fed directly and correlated with the predictions provided by the HABIT software.

Further work is needed to test this new multi-reactor crystalliser on the G3 instrument, to implement of the automated integration of the 8 individual growth cells within the system control software and integrate the Leeds image analysis software within the overall system. These technologies combined will enhance the value of the G3 product transforming it from e.g. being a static image off-line system used for QA purposes, into a fully automated platform for *in-situ* crystallisation and characterisation studies. Through measurement of the growth rate of individual crystal faces growing in the multi micro-reactors that will be integrated into the Morphologi G3, the new system will provide a highly effective system for the rapid and efficient development and manufacture of advanced particulate solids.



Figure 9.1 (a) Multi-micro-reactor (8-cell crystalliser) designed to be integrated with the Morphologi G3; (b) Malvern Instruments Morphologi G3; (c) Representative images of crystals captured in the in-situ cell.

9.4.3 Development of software for automated image analysis

Development of an automated image analysis software in collaboration with Dr. Ardhendu Behera and Prof. David Hogg of the Artificial Intelligence Group of the Computing School at the University of Leeds for developing image analysis software for analysis of the growth rates of individual faces of a population of crystals. Currently the automated image analysis has been able to analyse the growth rate of the surrounding faces of single crystals on the image (not a population of single crystals). The crystal detection procedure is briefly described as follows: An input image is processed with the Gaussian filter in order to remove noise and then converted into grayscale (8-bit single channel). A binary image from the resulting grayscale image is generated by thresholding. During the process, each pixel in the image is compared to a predefined threshold T . If the pixel value is greater than T then it is set to 1 else 0. Now, we obtain contours from the resulted binary image by using the algorithm described by Suzuki et al [184]. In the first stage of the detection process, the proposed algorithm approximates a contour with a hexagon, which is the actual representation of a crystal. The approximation process is done by using the Douglas-Peucker algorithm [185]. The provided contour will be considered for further processing if the approximation error is less or equal to the specified precision. The approximation error in the proposed algorithm is 0.8% of the maximum distance between the original contour and its approximated hexagon. In the following stage, the confirmation of the hexagon is carried out by computing angles between sides and the ratio of its length. A crystal hexagon consists of three pairs of parallel lines and the length of each individual line in each pair is the same length. The above-mentioned knowledge is used for re-

establishing a side of the hexagon if it is corrupted by the overlapping of other crystals. The same approach is used for a video sequence containing the growth of a crystal. Each frame in the video is considered as an input image to the algorithm.

9.4.4 Measurement of the growth rate at 0.5L scale –sizes

Crystal growth kinetics and the properties of the final product e.g. final crystal size distribution, morphology and purity etc. are profoundly affected by the hydrodynamics of the system (agitation and mixing). Hence, the scale-up for the crystallisation process is based on maintaining process similarity including geometry of reactor; flow characteristics, supersaturation profile, etc. should follow these rules [26, 186]:

- Geometrically similar vessels (identical ratios of corresponding dimensions) upon scale-up.
- Kinematic similarity and dynamic similarity: the slurry densities, contact times between the crystals and supersaturated solutions and the Reynolds numbers ($Re = \frac{\rho n d^2}{\mu}$) and the Froude number ($Fr = \frac{n^2 d}{g}$) of the fluid etc. should be identical where d is the agitator diameter, n is agitator speed, ρ is the liquid density, μ is the dynamic viscosity of the fluid and g is gravitational acceleration
- Maintaining constant specific power input to minimize excessive nucleation
- Ensuring adequate agitation and mixing associated with vessel dimensions, baffles, impeller type, and agitation speed which determines the supersaturation gradient is dispersed throughout the vessel so that there is a homogeneous mass transfer from the bulk solution to the growing crystals and thus the CSD and crystal purity are optimised.

However, it is usually impossible to achieve the exact scale-up crystalliser by satisfying all these criteria e.g. to achieve the homogeneous level of supersaturation or to replicate mixing parameters, constant Reynolds and Froude numbers together with geometric similarity at the same time. In addition, MSZW is likely to be effected during process scale-up which is worthy of consideration. Hence, a compromise has to be made and assessed when designing a scale-up of a batch crystalliser. Therefore, robust models need to be developed and improved using process analytical techniques such as ATR FTIR, FBRM and CFD modelling techniques.

A further measurement of the growth rate of ibuprofen should be carried on at larger scale-sizes e.g. use of an insertion optical probe (Perdix ISPV) at 0.5L vessel size (Figure 9.2) to compare with the data of the overall growth rate of ibuprofen in ethanol 95% to evaluate the effect of scale-size in agitated reactors.

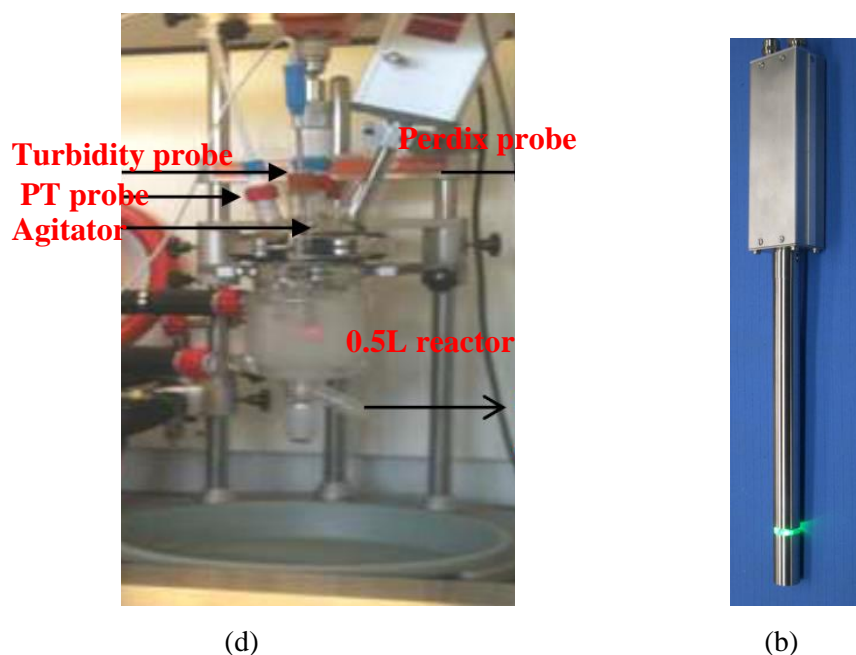


Figure 9.2 (a) Experiment set-up for 0.5L scale-size using a Perdix camera for the measurement of the size distribution of crystals versus time; (b) Perdix camera probe with 19mm diameter and 2.5 micron optical resolution.

The growth rates in this work can be used as a reference for comparing to the growth rate of ibuprofen at bigger scale-sizes e.g. use of an insertion optical probe (Perdix ISPV) at the 0.5L vessel size or 0.2L crystallisation jacketed vessel with a small flat window on the wall of the reactor for a camera.

9.4.5 Dissolution modelling using Peltier crystallisation cell

The peltier crystallisation cell developed in this work can be used for dynamic studies of dissolution kinetics as its heating and cooling performance is rapid (30°C/min) and easily controlled.

The peltier cell design utilised an annular round block with a moulded space at its centre for a peltier device to fit in and a PTFE base with a tunnel for a cuvette cell containing Ibuprofen solution to slide in. The 2 parts assemble together so the cuvette cell contacts the peliter element which was used to rapidly heat and cool solutions for crystallisation studies. The brass block is connected with a water bath, contacting with the hot side of the peltier which is working as a heat sink to remove heat from the cold side of the peltier. A hole at the centre enables observation of the crystallisation process and also allows image capture of crystals in-situ.

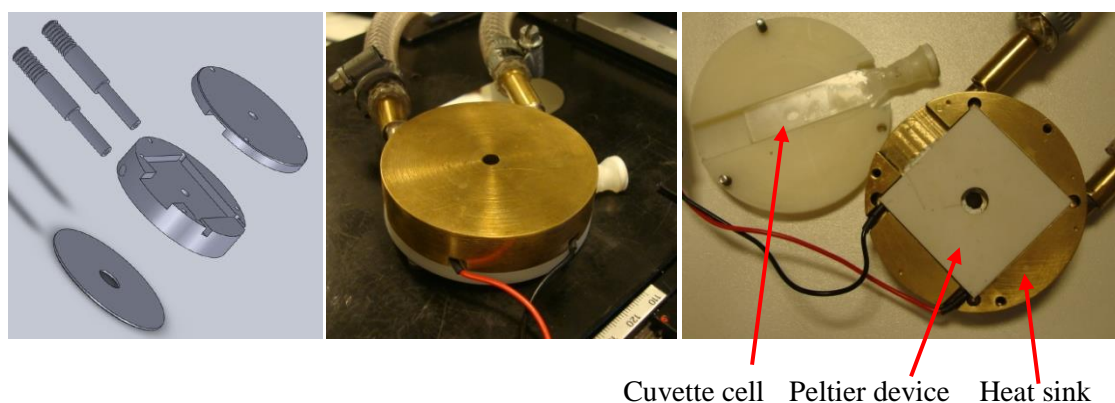


Figure 9.3 Peltier crystallisation cell based on an inverted microscope using a Labview program for controlling the temperature of the peltier.

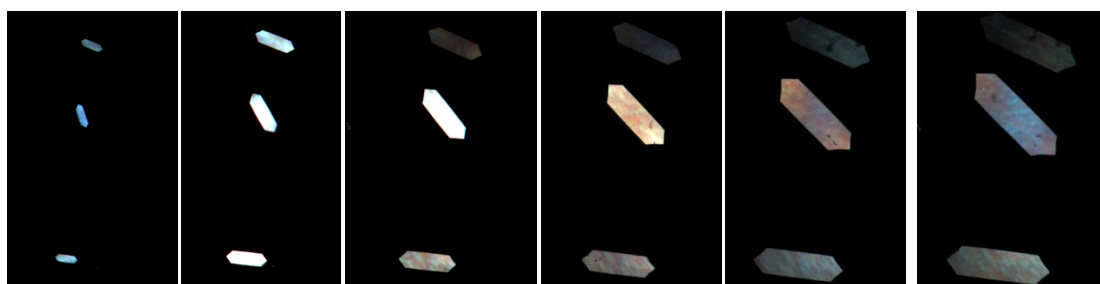


Figure 9.4 A sequence of in situ crystals grown from ethanol 95% at $\sigma = 0.79$ in the peltier crystallisation cell with 4 minute intervals between images captured

Table 9.1 Comparison of the growth rate of face {011} and {001} in ethanol in the 0.5ml cuvette crystallisation cell using a re-circulation bath and peltier heat-pump

Relative supersaturation (σ)	Cuvette cell (re-circulation bath)		Cuvette cell (Peltier heat-pump)	
	Face {001}	Face {011}	Face {001}	Face {011}
0.79	10.5 ± 1.3	4.6 ± 0.7	11.5 ± 1.2	4.3 ± 0.6

The growth rate in the cuvette cell (using the peltier heat-pump) is similar to the growth rate in the cuvette cell (using the re-circulation bath), which validates the observed crystal growth data in the cuvette cell using the re-circulation bath and demonstrates the competence of the temperature control of the peltier cell.

9.4.6 Modelling crystal growth in the {001} and {011} directions using morphological population balance

The individual growth rates of the {011} and {001} faces produced can be imputed directly into a morphological population balance model which was developed by Ma et al. [27] for prediction of the evolution of crystal population in terms of surface area of individual crystal habit faces, crystal shapes and sizes. In this method, the crystal shape information for a single crystal either through predicted morphology or experimental morphology as the initial face locations together with the kinetic parameters for the crystal growth rates of each face to predict the shape evolution of the crystal population. At specific times during the crystallisation process, the prediction uses its shape at the previous time moment, and the growth rate for the specific crystal habit plane. This methodology was successfully demonstrated through potash alum [27]. In addition, the advantages are the resultant PBM can be integrated with Computational Fluid Dynamics and used to scale up the vessel size [187-190].

9.4.7 Integration with grid search to calculate solvent binding the surface

The influence of solvent on crystal habit of ibuprofen might be predicted through the calculations of the interactions between the solvent and solute molecules at the surfaces of the crystals. These interactions can be predicted using a computer program developed by Hammond et al (2003) known as the systematic search method [191]. In this, the competitive interaction between the ibuprofen solute and various solvents on the individual crystal surfaces can be predicted and from this the solvent-mediated growth morphologies calculated. The methodology is shown in Figure 9.5.

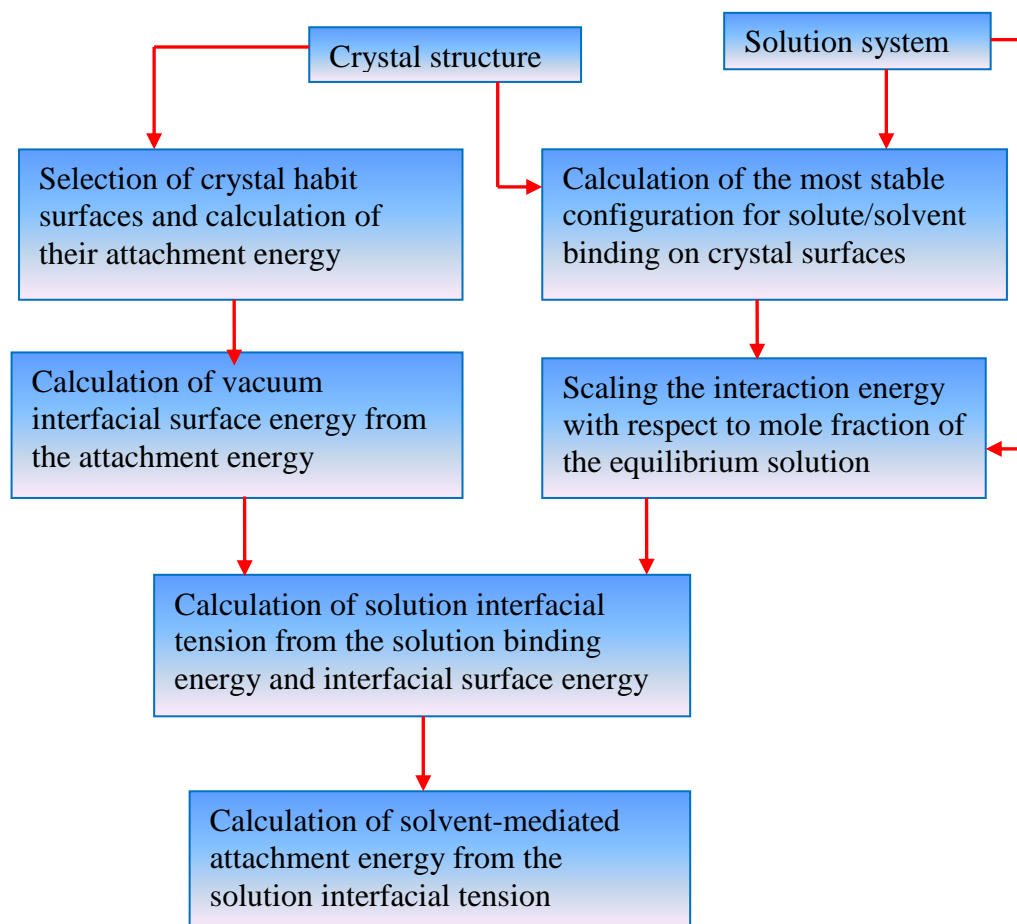


Figure 9.5 Schematic diagram for calculating specific surface energies of crystal surface in solution [192].

The calculated modified attachment energies representing for the relative growth rate of the crystal habit faces were used to predict a solvent-mediated crystal habit.

REFERENCES

1. Giulietti, M., M.M. Seckler, S. Derenzo, M.I. Ré, and E. Cekinski, *Industrial crystallization and precipitation from solutions: state of the technique*. Brazilian Journal of Chemical Engineering, 2001. **18**: p. 423-440.
2. Myerson, A., *Handbook of industrial crystallization* 2002: Butterworth-Heinemann.
3. Food, U., *Drug Administration. Challenge and opportunity on the critical path to new medical products*. US Department of Health and Human Services, 2004.
4. Beckmann, W., *Simultaneous measurement of the growth rates of the (001) and (110) faces of stearic acid growing from solution*. Journal of Physics E: Scientific Instruments, 1986. **19**(6): p. 444.
5. Cano, H., N. Gabas, and J. Canselier, *Experimental study on the ibuprofen crystal growth morphology in solution*. Journal of Crystal Growth, 2001. **224**(3): p. 335-341.
6. Davey, R., W. Fila, and J. Garside, *The influence of biuret on the growth kinetics of urea crystals from aqueous solutions*. Journal of Crystal Growth, 1986. **79**(1): p. 607-613.
7. Davey, R. and J. Mullin, *Growth of the {100} faces of ammonium dihydrogen phosphate crystals in the presence of ionic species*. Journal of Crystal Growth, 1974. **26**(1): p. 45-51.
8. Davey, R. and J. Mullin, *Growth of the {101} faces of ammonium dihydrogen phosphate crystals in the presence of ionic species*. Journal of Crystal Growth, 1974. **23**(2): p. 89-94.
9. Ristic, R., S. Finnie, D. Sheen, and J. Sherwood, *Macro-and micromorphology of monoclinic paracetamol grown from pure aqueous solution*. The Journal of Physical Chemistry B, 2001. **105**(38): p. 9057-9066.
10. Sweegers, C., H. Meekes, W. Van Enkevort, I. Hiralal, and A. Rijkeboer, *Growth rate analysis of gibbsite single crystals growing from aqueous sodium aluminate solutions*. Crystal Growth & Design, 2004. **4**(1): p. 185-198.
11. Arellano, M.a.P., J.M. Aguilera, and P. Bouchon, *Development of a digital video-microscopy technique to study lactose crystallisation kinetics in situ*. Carbohydrate Research, 2004. **339**(16): p. 2721-2730.

12. De Anda, J.C., X. Wang, X. Lai, K. Roberts, K. Jennings, M. Wilkinson, D. Watson, and D. Roberts, *Real-time product morphology monitoring in crystallization using imaging technique*. *AIChE journal*, 2005. **51**(5): p. 1406-1414.
13. Li, R., G. Thomson, G. White, X. Wang, J.C. De Anda, and K. Roberts, *Integration of crystal morphology modeling and on-line shape measurement*. *AIChE journal*, 2006. **52**(6): p. 2297-2305.
14. Ma, C.Y., X.Z. Wang, and K.J. Roberts, *Multi-dimensional population balance modeling of the growth of rod-like L-glutamic acid crystals using growth rates estimated from in-process imaging*. *Advanced Powder Technology*, 2007. **18**(6): p. 707-724.
15. Rashid, A., E. White, T. Howes, J. Litster, and I. Marziano, *Growth rates of ibuprofen crystals grown from ethanol and aqueous ethanol*. *Chemical Engineering Research and Design*, 2012. **90**(1): p. 158-161.
16. Stapley, A.G., C. Himawan, W. MacNaughtan, and T.J. Foster, *A computational method for extracting crystallization growth and nucleation rate data from hot stage microscope images*. *Crystal Growth & Design*, 2009. **9**(12): p. 5061-5068.
17. Wang, X., J. Calderon De Anda, and K. Roberts, *Real-time measurement of the growth rates of individual crystal facets using imaging and image analysis: a feasibility study on needle-shaped crystals of L-glutamic acid*. *Chemical Engineering Research and Design*, 2007. **85**(7): p. 921-927.
18. Wang, X., J. Calderon De Anda, K. Roberts, R. Li, G. Thomson, and G. White, *Advances in on-line monitoring and control of the morphological and polymorphic forms of organic crystals grown from solution*. *KONA (Powder and Particle)*, 2005. **23**: p. 69-85.
19. Ristić, R., J. Sherwood, and K. Wojciechowski, *Assessment of the strain in small sodium chlorate crystals and its relation to growth rate dispersion*. *Journal of Crystal Growth*, 1988. **91**(1): p. 163-168.
20. Garside, J. and R. Ristić, *Growth rate dispersion among ADP crystals formed by primary nucleation*. *Journal of Crystal Growth*, 1983. **61**(2): p. 215-220.
21. Judge, R.A., E.L. Forsythe, and M.L. Pusey, *Growth rate dispersion in protein crystal growth*. *Crystal Growth & Design*, 2010. **10**(7): p. 3164-3168.
22. Derdour, L., C. Sivakumar, D. Skliar, S. Pack, C. Lai, J. Vernille, and S. Kiang, *Crystallization from Solutions Containing Multiple Conformers. 2. Experimental*

- Study and Model Validation*. *Crystal Growth & Design*, 2012. **12**(11): p. 5188-5196.
23. Markande, A., A. Nezzal, J. Fitzpatrick, and L. Aerts, *Investigation of the crystallization kinetics of dextrose monohydrate using in situ particle size and supersaturation monitoring*. *Particulate Science and Technology*, 2009. **27**(4): p. 373-388.
 24. Schöll, J., C. Lindenberg, L. Vicum, J. Brozio, and M. Mazzotti, *Precipitation of α L-glutamic acid: determination of growth kinetics*. *Faraday Discussions*, 2007. **136**: p. 247-264.
 25. Garside, J., *Industrial crystallization from solution*. *Chemical Engineering Science*, 1985. **40**(1): p. 3-26.
 26. Mullin, J.W., *Crystallization*2001: Butterworth-Heinemann.
 27. Ma, C.Y., X.Z. Wang, and K.J. Roberts, *Morphological population balance for modeling crystal growth in face directions*. *AIChE journal*, 2008. **54**(1): p. 209-222.
 28. Sun, C.C., *Materials science tetrahedron—A useful tool for pharmaceutical research and development*. *Journal of Pharmaceutical Sciences*, 2009. **98**(5): p. 1671-1687.
 29. Almac. Available from: <http://www.almacgroup.com/api-services-chemical-development/solid-state-services/amorphous-materials/>.
 30. Griesser, U. and R. Hilfiker, *Polymorphism in the Pharmaceutical Industry*. ed. Rolf Hilfiker, Wiley-VCH Verlag GmbH & Co, 2006: p. 211-233.
 31. Van Hook, A. and A.P. VanHook, *Crystallization: Theory and practice*1961: Reinhold New York.
 32. Miller, W.H., *A treatise on crystallography*1839: Printed at the Pitt Press for J. & JJ Deighton.
 33. Bravais, A., *J. l'Ec. Polytech.*, 1850. **19** (**33**): p. 1-128.
 34. Guinier, A., A. Kastler, and W. Duffin, *The structure of matter: from the blue sky to liquid crystals*1984: E. Arnold.
 35. Roberts, K.J., *Characterisation and growth mechanisms of flux grown Yttrium Aluminium Garnet*. PhD thesis, 1978.
 36. Lovell, M.C., A.J. Avery, and M.W. Vernon, *Physical properties of materials*. 1976.

37. Bernstein, J., *Polymorphism in molecular crystals*. Vol. 14. 2002: Oxford University Press.
38. Ostwald, W., *Studies on formation and transformation of solid materials*. Z. Phys. Chem, 1897. **22**: p. 289-330.
39. Ostwald, W., *Grundriss der allgemeinen Chemie* 1899: W. Engelmann.
40. Ostwald, W., *On the supposed isomerism of red and yellow mercury oxide and the surface tension of solid substances*. Z. Phys. Chem, 1900. **34**: p. 495-503.
41. Giron, D., *Thermal analysis and calorimetric methods in the characterisation of polymorphs and solvates*. Thermochemica Acta, 1995. **248**: p. 1-59.
42. Brittain, H.G., *Polymorphism in pharmaceutical solids* 1999: M. Dekker New York.
43. History, S.N.M.o.N., *The Dynamic Earth*.
44. Gibbs, J.W., *Abstract of the "Equilibrium of heterogeneous substances"*. American Journal of Science, Serie, 1978. **3**: p. 16.
45. Wulff, G., *Zeitschrift fur Krystallographie und Mineralogie*, 1901. **34**,(5/6): p. 449-530.
46. Cooper, S., *Crystallisation kinetics*
47. Gavezzotti, A., *Theoretical aspects and computer modeling of the molecular solid state* 1997: J. Wiley.
48. Donnay, J. and D. Harker, *A new law of crystal morphology extending the law of Bravais*. Am. Mineral, 1937. **22**(5): p. 446-467.
49. Hartman, P. and W. Perdok, *On the relations between structure and morphology of crystals. I*. Acta Crystallographica, 1955. **8**(1): p. 49-52.
50. Momany, F., L. Carruthers, R.t. McGUIRE, and H. Scheraga, *Intermolecular potentials from crystal data. III. Determination of empirical potentials and application to the packing configurations and lattice energies in crystals of hydrocarbons, carboxylic acids, amines, and amides*. The Journal of Physical Chemistry, 1974. **78**(16): p. 1595-1620.
51. Lifson, S., A. Hagler, and P. Dauber, *Consistent force field studies of intermolecular forces in hydrogen-bonded crystals. I. Carboxylic acids, amides, and the C: O...H-hydrogen bonds*. Journal of the American Chemical Society, 1979. **101**(18): p. 5111-5121.

52. Clydesdale, G., R. Docherty, and K. Roberts, *HABIT-a program for predicting the morphology of molecular crystals*. Computer Physics Communications, 1991. **64**(2): p. 311-328.
53. Hartman, P. and P. Bennema, *The attachment energy as a habit controlling factor: I. Theoretical considerations*. Journal of Crystal Growth, 1980. **49**(1): p. 145-156.
54. Hildebrand, J. and R. Scott, *The Solubility of Non-Electrolytes, 1950*. Reinhold, New York, 1964.
55. Ostwald, W., *File history*. Zeitschrift für physikalische Chemie, 1897. **22**: p. 289-330.
56. Miers, H. and F. Isaac, *The Spontaneous Crystallisation of Binary Mixtures. Experiments on Salol and Betol*. Proceedings of the Royal Society of London. Series A, 1907. **79**(531): p. 322-351.
57. Miers, H.A. and F. Isaac, *XLVII.—The refractive indices of crystallising solutions, with especial reference to the passage from the metastable to the labile condition*. Journal of the Chemical Society, Transactions, 1906. **89**: p. 413-454.
58. Nývlt, J., *Kinetics of nucleation in solutions*. Journal of Crystal Growth, 1968. **3**: p. 377-383.
59. Freundlich, H. and H.S. Hatfield, *Colloid and capillary chemistry*. 1926.
60. Cubillas, P. and M.W. Anderson, *Synthesis mechanism: crystal growth and nucleation*. Zeolites and Catalysis: Synthesis, Reactions and Applications, 2010: p. 1-55.
61. Volmer, M., *Kinetik der Phasenbildung*. Vol. 4. 1939: T. Steinkopff Dresden.
62. Strickland-Constable, R. *The breeding of crystal nuclei-a review of the subject*. in *AIChE Symp. Ser.* 1972.
63. Kwokal, A., T.T. Nguyen, and K.J. Roberts, *Polymorph-directing seeding of entacapone crystallization in aqueous/acetone solution using a self-assembled molecular layer on Au (100)*. Crystal Growth & Design, 2009. **9**(10): p. 4324-4334.
64. Rodríguez-hornedo, N. and D. Murphy, *Significance of controlling crystallization mechanisms and kinetics in pharmaceutical systems*. Journal of Pharmaceutical Sciences, 1999. **88**(7): p. 651-660.

65. Noyes, A.A. and W.R. Whitney, *The rate of solution of solid substances in their own solutions*. Journal of the American Chemical Society, 1897. **19**(12): p. 930-934.
66. Li, L. and N. Rodriguez-Hornedo, *Growth kinetics and mechanism of glycine crystals*. Journal of Crystal Growth, 1992. **121**(1): p. 33-38.
67. Kirkpatrick, R., *Crystal growth from the melt: a review*. American Mineralogist, 1975. **60**(9-10): p. 798-814.
68. Ohara, M. and R.C. Reid, *Modeling crystal growth rates from solution*. Vol. 225. 1973: Prentice-Hall Englewood Cliffs.
69. Van der Eerden, J., P. Bennema, and T. Cherepanova, *Survey of Monte Carlo simulations of crystal surfaces and crystal growth*. Progress in Crystal Growth and Characterization, 1978. **1**(3): p. 219-254.
70. Bennema, P.a.v.d.E., J.P., *Morphology of crystals* 1987, Tokyo: Terra Scientific
71. Libbrecht, K.G., *SnowCrystals.com*.
72. Roberts, K., R. Docherty, P. Bennema, and L. Jetten, *The importance of considering growth-induced conformational change in predicting the morphology of benzophenone*. Journal of Physics D: Applied Physics, 1993. **26**(8B): p. B7.
73. Bennema, P. and J.P. van der Eerden, *Crystal growth from solution: Development in computer simulation*. Journal of Crystal Growth, 1977. **42**(0): p. 201-213.
74. Davey, R., *The role of the solvent in crystal growth from solution*. Journal of Crystal Growth, 1986. **76**(3): p. 637-644.
75. Bennema, P., G. Gilmer, and P. Hartman, *Crystal Growth: An Introduction*. North-Holland, Amsterdam, 1973: p. 263.
76. Davey, R., *The Role of Additives in Precipitation Processes, Industrial Crystallization 81, SJ Jancic and EJ de Jong, Eds*, 1982, North-Holland Publishing Co.
77. Human, H., J. Van der Eerden, L. Jetten, and J. Odekerken, *On the roughening transition of biphenyl: Transition of faceted to non-faceted growth of biphenyl for growth from different organic solvents and the melt*. Journal of Crystal Growth, 1981. **51**(3): p. 589-600.

78. Jetten, L., H. Human, P. Bennema, and J. Van der Eerden, *On the observation of the roughening transition of organic crystals, growing from solution*. Journal of Crystal Growth, 1984. **68**(2): p. 503-516.
79. Bourne, J. and R. Davey, *The role of solvent-solute interactions in determining crystal growth mechanisms from solution: I. The surface entropy factor*. Journal of Crystal Growth, 1976. **36**(2): p. 278-286.
80. Bourne, J. and R. Davey, *The role of solvent-solute interactions in determining crystal growth mechanisms from solution: II. The growth kinetics of hexamethylene tetramine*. Journal of Crystal Growth, 1976. **36**(2): p. 287-296.
81. Tomozawa, H., M. Momonaga, T. Uemura, and H. Yazawa, *Influence of powder characteristics of bulk substance with pharmaceutical processing*. Drug Development and Industrial Pharmacy, 1998. **24**(9): p. 857-861.
82. Prlic'Kardum, J., A. Sander, and M. Kirincic, *The Influence of Process Parameters on the Granulometric Properties of Pentaerythritol in Batch Crystallization*. 2009.
83. Garnier, S., S. Petit, and G. Coquerel, *Influence of supersaturation and structurally related additives on the crystal growth of α -lactose monohydrate*. Journal of Crystal Growth, 2002. **234**(1): p. 207-219.
84. Libbrecht, K.G. *SnowCrystals.com: A snowflake primer*. Available from: <http://www.its.caltech.edu/~atomic/snowcrystals/primer/primer.htm>.
85. Keraliya, R.A., T.G. Soni, V.T. Thakkar, and T.R. Gandhi, *Effect of solvent on crystal habit and dissolution behavior of tolbutamide by initial solvent screening*. Dissolution Technology, 2010. **1**: p. 16-21.
86. Bolourtchian, N., A. Nokhodchi, and R. Dinarvand, *The effect of solvent and crystallization conditions on habit modification of carbamazepine*. DARU Journal of Pharmaceutical Sciences, 2001. **9**(1-2): p. 12-22.
87. Nokhodchi, A., N. Bolourtchian, and R. Dinarvand, *Crystal modification of phenytoin using different solvents and crystallization conditions*. International Journal of Pharmaceutics, 2003. **250**(1): p. 85-97.
88. Lahav, M. and L. Leiserowitz, *The effect of solvent on crystal growth and morphology*. Chemical Engineering Science, 2001. **56**(7): p. 2245-2253.
89. Granberg, R.A., C. Ducreux, S. Gracin, and Å.C. Rasmuson, *Primary nucleation of paracetamol in acetone–water mixtures*. Chemical Engineering Science, 2001. **56**(7): p. 2305-2313.

90. Hendriksen, B.A., D.J. Grant, P. Meenan, and D.A. Green, *Crystallisation of paracetamol (acetaminophen) in the presence of structurally related substances*. Journal of Crystal Growth, 1998. **183**(4): p. 629-640.
91. Sander, A., A. Gelemanovic, and M. Hrkovac, *The influence of the crystallizer geometric characteristics on the crystal granulometric properties*. 2009.
92. Ghassempour, A., H. Rafati, L. Adlnasab, Y. Bashour, H. Ebrahimzadeh, and M. Erfan, *Investigation of the solid state properties of amoxicillin trihydrate and the effect of powder pH*. AAPS PharmSciTech, 2007. **8**(4): p. 91-96.
93. Joiris, E., P. Di Martino, C. Berneron, A.-M. Guyot-Hermann, and J.-C. Guyot, *Compression behavior of orthorhombic paracetamol*. Pharmaceutical Research, 1998. **15**(7): p. 1122-1130.
94. Tye, C.K., C.C. Sun, and G.E. Amidon, *Evaluation of the effects of tableting speed on the relationships between compaction pressure, tablet tensile strength, and tablet solid fraction*. Journal of Pharmaceutical Sciences, 2005. **94**(3): p. 465-472.
95. Howard, K.S., Z.K. Nagy, B. Saha, A. Robertson, G. Steele, and D. Martin, *A process analytical technology based investigation of the polymorphic transformations during the antisolvent crystallization of sodium benzoate from IPA/water mixture*. Crystal Growth and Design, 2009. **9**(9): p. 3964-3975.
96. Garside, J., A. Mersmann, and J. Nývlt, *Measurement of crystal growth and nucleation rates* 2002: IChemE.
97. Randolph, A., *Theory of particulate processes: analysis and techniques of continuous crystallization* 1971: Academic press.
98. Omar, W., S. Al-Sayed, A. Sultan, and J. Ulrich, *Growth rate of single acetaminophen crystals in supersaturated aqueous solution under different operating conditions*. Crystal Research and Technology, 2008. **43**(1): p. 22-27.
99. White, E. and P. Wright. *Magnitude of size dispersion effects in crystallization*. in *Chemical Engineering Progress Symposium Series No.* 1971.
100. Wang, S. and A. Mersmann, *Initial-size-dependent growth rate dispersion of attrition fragments and secondary nuclei*. Chemical Engineering Science, 1992. **47**(6): p. 1365-1371.
101. Mitrović, M., *Influence of initial crystal size on growth rate of crystals from solutions*. Journal of Crystal Growth, 1994. **139**(3): p. 332-335.

102. Garside, J. and M. Larson, *Direct observation of secondary nuclei production*. Journal of Crystal Growth, 1978. **43**(6): p. 694-704.
103. Rusli, I., M. Larson, and J. Garside, *Initial growth of secondary nuclei produced by contact nucleation*. Design, Control and Analysis of Crystallization Processes-AI Ch. E. Syrup. Ser. J, 1980. **76**(193): p. 52.
104. Sherwood, J.N. and R.I. Ristic, *The influence of mechanical stress on the growth and dissolution of crystals*. Chemical Engineering Science, 2001. **56**(7): p. 2267-2280.
105. Randolph, A. and E. White, *Modeling size dispersion in the prediction of crystal-size distribution*. Chemical Engineering Science, 1977. **32**(9): p. 1067-1076.
106. Daudey, P.J., *Crystallization of ammonium sulfate* 1987: Ph. D. diss., Delft University of Technology, the Netherlands.
107. Davey, R. and J. Mullin, *The effect of supersaturation on growth features on the {100} faces of ammonium dihydrogen phosphate crystals*. Journal of Crystal Growth, 1975. **29**(1): p. 45-48.
108. Suharso, S., *In Situ Measurement of the Growth Rate of the (111) Face of Borax Single Crystal*. Jurnal Matematika dan Sains, 2009. **10**(3): p. 101-106.
109. Ma, C.Y. and X.Z. Wang, *Model identification of crystal facet growth kinetics in morphological population balance modeling of l-glutamic acid crystallization and experimental validation*. Chemical engineering science, 2012. **70**: p. 22-30.
110. Liu, J.J., C.Y. Ma, Y.D. Hu, and X.Z. Wang, *Modelling protein crystallisation using morphological population balance models*. Chemical Engineering Research and Design, 2010. **88**(4): p. 437-446.
111. Luo, Y.-H., G.-G. Wu, and B.-W. Sun, *Antisolvent Crystallization of Biapenem: Estimation of Growth and Nucleation Kinetics*. Journal of Chemical & Engineering Data, 2013. **58**(3): p. 588-597.
112. Mettler-Toledo, *Focused Beam Reflectance Measurement*.
113. Binnig, G., C.F. Quate, and C. Gerber, *Atomic force microscope*. Physical Review Letters, 1986. **56**(9): p. 930.
114. McPherson, A., A. Malkin, Y.G. Kuznetsov, and M. Plomp, *Atomic force microscopy applications in macromolecular crystallography*. Acta Crystallographica Section D: Biological Crystallography, 2001. **57**(8): p. 1053-1060.

115. Kuznetsov, Y.G., A. Malkin, and A. McPherson, *AFM studies of the nucleation and growth mechanisms of macromolecular crystals*. Journal of Crystal Growth, 1999. **196**(2): p. 489-502.
116. Land, T., A. Malkin, Y.G. Kuznetsov, A. McPherson, and J. De Yoreo, *Mechanisms of protein crystal growth: an atomic force microscopy study of canavalin crystallization*. Physical Review Letters, 1995. **75**(14): p. 2774.
117. Maiwa, K., M. Plomp, W.J.P. van Enckevort, and P. Bennema, *AFM observation of barium nitrate {100} and {000} faces: spiral growth and two-dimensional nucleation growth*. Journal of Crystal Growth, 1998. **186**(1-2): p. 214-223.
118. Dobson, P.S., L.A. Bindley, J.V. Macpherson, and P.R. Unwin, *Atomic force microscopy investigation of the mechanism of calcite microcrystal growth under Kitano conditions*. Langmuir, 2005. **21**(4): p. 1255-1260.
119. Malkin, A.J., T.A. Land, Y.G. Kuznetsov, A. McPherson, and J.J. DeYoreo, *Investigation of Virus Crystal Growth Mechanisms by In Situ Atomic Force Microscopy*. Physical Review Letters, 1995. **75**(14): p. 2778-2781.
120. *Schematic diagram of AFM*. Available from: http://en.wikipedia.org/wiki/Atomic_force_microscopy.
121. Zikic, A., R. Ristic, and J. Sherwood, *An instrument for in situ growth rate characterization of mechanically strained crystals*. Review of Scientific Instruments, 1998. **69**(7): p. 2713-2719.
122. Vekilov, P.G., M. Ataka, and T. Katsura, *Laser Michelson interferometry investigation of protein crystal growth*. Journal of Crystal Growth, 1993. **130**(1-2): p. 317-320.
123. Shekunov, B.Y. and D.J. Grant, *In situ optical interferometric studies of the growth and dissolution behavior of paracetamol (acetaminophen). 1. Growth kinetics*. The Journal of Physical Chemistry B, 1997. **101**(20): p. 3973-3979.
124. Shekunov, B.Y., D.J. Grant, R.J. Latham, and J.N. Sherwood, *In situ optical interferometric studies of the growth and dissolution behavior of paracetamol (acetaminophen) crystals. 3. Influence of growth in the presence of p-acetoxyacetanilide*. The Journal of Physical Chemistry B, 1997. **101**(44): p. 9107-9112.
125. Thompson, C., M.C. Davies, C.J. Roberts, S.J.B. Tendler, and M.J. Wilkinson, *The effects of additives on the growth and morphology of paracetamol*

- (*acetaminophen*) crystals. *International Journal of Pharmaceutics*, 2004. **280**(1–2): p. 137-150.
126. Liu, B., C.S. Fang, S.L. Wang, and X.M. Mou, *In situ measurement of growth kinetics of {100} KDP crystal faces in the presence of polyphosphate impurities*. *Crystal Research and Technology*, 2008. **43**(7): p. 700-708.
 127. Van Driessche, A.E.S., F. Otalora, G. Sazaki, M. Sleutel, K. Tsukamoto, and J.A. Gavira, *Comparison of Different Experimental Techniques for the Measurement of Crystal Growth Kinetics*. *Crystal Growth & Design*, 2008. **8**(12): p. 4316-4323.
 128. Bower, J. *Ibuprofen*. 2001 [10/04/2010]; Available from: <http://www.chm.bris.ac.uk/motm/ibuprofen/homepage.htm>.
 129. Leising, G., R. Resel, F. Stelzer, S. Tasch, A. Lanziner, and G. Hantich, *Physical aspects of dexibuprofen and racemic ibuprofen*. *The Journal of Clinical Pharmacology*, 1996. **36**(12 suppl): p. 3S-6S.
 130. Shankland, N., A.J. Florence, P.J. Cox, D.B. Sheen, S.W. Love, N.S. Stewart, and C.C. Wilson, *Crystal morphology of ibuprofen predicted from single-crystal pulsed neutron diffraction data*. *Chemical Communications*, 1996(7): p. 855-856.
 131. Dudognon, E., F. Danède, M. Descamps, and N.T. Correia, *Evidence for a new crystalline phase of racemic ibuprofen*. *Pharmaceutical Research*, 2008. **25**(12): p. 2853-2858.
 132. Freer, A.A., J.M. Bunyan, N. Shankland, and D.B. Sheen, *Structure of (S)-(+)-ibuprofen*. *Acta Crystallographica Section C: Crystal Structure Communications*, 1993. **49**(7): p. 1378-1380.
 133. Dwivedi, S., S. Sattari, F. Jamali, and A. Mitchell, *Ibuprofen racemate and enantiomers: phase diagram, solubility and thermodynamic studies*. *International Journal of Pharmaceutics*, 1992. **87**(1): p. 95-104.
 134. Romero, A. and C. Rhodes, *Approaches to stereospecific preformulation of ibuprofen*. *Drug Development and Industrial Pharmacy*, 1991. **17**(5): p. 777-792.
 135. Gordon, R.E. and S.I. Amin, *Crystallization of ibuprofen*, 1984, Google Patents.
 136. Bunyan, J., N. Shankland, and D. Sheen. *Solvent effects on the morphology of ibuprofen*. in *AIChE Symposium Series*. 1991.
 137. Garekani, H., F. Sadeghi, A. Badiiee, S. Mostafa, A.R. Rajabi-Siahboomi, and A. Rajabi-Siahboomi, *Crystal habit modifications of ibuprofen and their*

- physicomechanical characteristics*. Drug Development and Industrial Pharmacy, 2001. **27**(8): p. 803-809.
138. Labhasetwar, V., S. Deshmukh, and A. Dorle, *Studies on some crystalline forms of ibuprofen*. Drug Development and Industrial Pharmacy, 1993. **19**(6): p. 631-641.
139. Nikolakakis, I., K. Kachrimanis, and S. Malamataris, *Relations between crystallisation conditions and micromeritic properties of ibuprofen*. International Journal of Pharmaceutics, 2000. **201**(1): p. 79-88.
140. Rasenack, N. and B. Müller, *Properties of ibuprofen crystallized under various conditions: A comparative study*. Drug Development and Industrial Pharmacy, 2002. **28**(9): p. 1077-1089.
141. Rasenack, N. and B.W. Muller, *Crystal habit and tableting behavior*. International Journal of Pharmaceutics, 2002. **244**(1-2): p. 45-57.
142. Accelrys, *Material Studio*
143. Mayo, S.L., B.D. Olafson, and W.A. Goddard, *DREIDING: a generic force field for molecular simulations*. Journal of Physical Chemistry, 1990. **94**(26): p. 8897-8909.
144. Delley, B., *From molecules to solids with the DMol approach*. The Journal of Chemical Physics, 2000. **113**: p. 7756.
145. Perdew, J.P., K. Burke, and M. Ernzerhof, *Generalized gradient approximation made simple*. Physical Review Letters, 1996. **77**(18): p. 3865.
146. RevPBE Expt, M.L.P., *Perdew, Burke, and Ernzerhof Reply: Our goal in*. J. Chem. Phys, 1997. **106**(10): p. 184.
147. Klamt, A. and G. Schüürmann, *COSMO: a new approach to dielectric screening in solvents with explicit expressions for the screening energy and its gradient*. J. Chem. Soc., Perkin Trans. 2, 1993(5): p. 799-805.
148. Eckert, F. and A. Klamt, *COSMOtherm, Version C2. 1, Release 01.05; COSMOlogic GmbH &Co. KG: Leverkusen, Germany, 2005*.
149. Stewart, J., *MOPAC 6.0,(CQCPE program# 455). Quantum Chemistry Program Exchange, Creative Arts Building 181, Indiana University, Bloomington, IN 47405 USA*.
150. Bravais, A., *Etudes Crystallographiques; Academie des Sciences: Paris, 1913*.
151. Friedel, G., Bull. Soc. Fr. Mineral., 1907. **30**: p. 326.

152. Dowty, E., *Computing and drawing crystal shapes*. American Mineralogist, 1980. **65**(5-6): p. 465-471.
153. Billot, P., M. Couty, and P. Hosek, *Application of ATR-UV spectroscopy for monitoring the crystallisation of UV absorbing and nonabsorbing molecules*. Organic Process Research & Development, 2010. **14**(3): p. 511-523.
154. Website, A., *Crystalline*. <http://www.crystallizationsystems.com/en/crystalline/>.
155. Docherty, R., K. Roberts, and E. Dowty, *MORANG—A computer program designed to aid in the determinations of crystal morphology*. Computer Physics Communications, 1988. **51**(3): p. 423-430.
156. Pro, O., 8 (2007). *About Origin Pro 8 SRO, V8. 0724 software, Copyright 1991-2007, Origin Lab Corporation*.
157. Wang, X.Z.r.g., *Process Image Analysis Expert software developed at University of Leeds*. 2010.
158. Rashid, M.A., *Crystallization engineering of ibuprofen for pharmaceutical formulation*. 2011.
159. Winn, D. and M.F. Doherty, *Modeling crystal shapes of organic materials grown from solution*. AIChE journal, 2000. **46**(7): p. 1348-1367.
160. Abramov, Y.A., M. Zell, and J.F. Krzyzaniak, *Toward a rational solvent selection for conformational polymorph screening*. Chemical Engineering in the Pharmaceutical Industry: R&D to Manufacturing, 2010: p. 491-504.
161. Xu, F., L.-X. Sun, Z.-C. Tan, J.-G. Liang, and R.-L. Li, *Thermodynamic study of ibuprofen by adiabatic calorimetry and thermal analysis*. Thermochemica Acta, 2004. **412**(1): p. 33-57.
162. Gracin, S. and Å.C. Rasmuson, *Solubility of phenylacetic acid, p-hydroxyphenylacetic acid, p-aminophenylacetic acid, p-hydroxybenzoic acid, and ibuprofen in pure solvents*. Journal of Chemical & Engineering Data, 2002. **47**(6): p. 1379-1383.
163. Romero, A., L. Savastano, and C. Rhodes, *Monitoring crystal modifications in systems containing ibuprofen*. International Journal of Pharmaceutics, 1993. **99**(2): p. 125-134.
164. Herzfeldt, C. D. and R. Kummel, *Dissociation constants, solubilities and dissolution rates of some selected nonsteroidal antiinflammatories*. Drug Development and Industrial Pharmacy, 1983. **9**(5): p. 767-793.

165. Rashid, A., T. White, T. Howes, J. Litster, and I. Marziano, *Racemic ibuprofen solubility in ethanol and aqueous ethanolic mixtures*. Chemeca 2008: Towards a Sustainable Australasia, 2008: p. 1393.
166. Manrique, J. and F. Martinez, *Solubility of ibuprofen in some ethanol+ water cosolvent mixtures at several temperatures*. Latin American Journal of Pharmacy, 2007. **26**(3): p. 344.
167. Nývlt, J., *Induction period of nucleation and metastable zone width*. Collection of Czechoslovak chemical communications, 1983. **48**(7): p. 1977-1983.
168. Jiang, S. and J.H. ter Horst, *Crystal nucleation rates from probability distributions of induction times*. Crystal Growth & Design, 2010. **11**(1): p. 256-261.
169. Sear, R.P., *Estimation of the scaling of the nucleation time with volume when the nucleation rate does not exist*. Crystal Growth & Design, 2013. **13**(3): p. 1329-1333.
170. Myerson, A.S. and P.Y. Lo, *Diffusion and cluster formation in supersaturated solutions*. Journal of Crystal Growth, 1990. **99**(1): p. 1048-1052.
171. Sorell, L. and A. Myerson, *Diffusivity of urea in concentrated, saturated and supersaturated solutions*. AIChE journal, 1982. **28**(5): p. 772-779.
172. Klug, D.L. and R.L. Pigford, *The probability distribution of growth rates of anhydrous sodium sulfate crystals*. Industrial & Engineering Chemistry Research, 1989. **28**(11): p. 1718-1725.
173. Finnie, S.D., R.I. Ristic, J.N. Sherwood, and A.M. Zikic, *Morphological and growth rate distributions of small self-nucleated paracetamol crystals grown from pure aqueous solutions*. Journal of Crystal Growth, 1999. **207**(4): p. 308-318.
174. Berglund, K.A. and V.G. Murphy, *Modeling growth rate dispersion in a batch sucrose crystallizer*. Industrial & Engineering Chemistry Fundamentals, 1986. **25**(1): p. 174-176.
175. Berglund, K. and M. Larson, *Modeling of growth rate dispersion of citric acid monohydrate in continuous crystallizers*. AIChE journal, 1984. **30**(2): p. 280-287.
176. Ó'Ciardhá, C., N. Mitchell, K. Hutton, and P. Frawley, *Determination of the Crystal Growth Rate of Paracetamol As a function of solvent composition*. Industrial & Engineering Chemistry Research, 2012. **51**(12): p. 4731-4740.

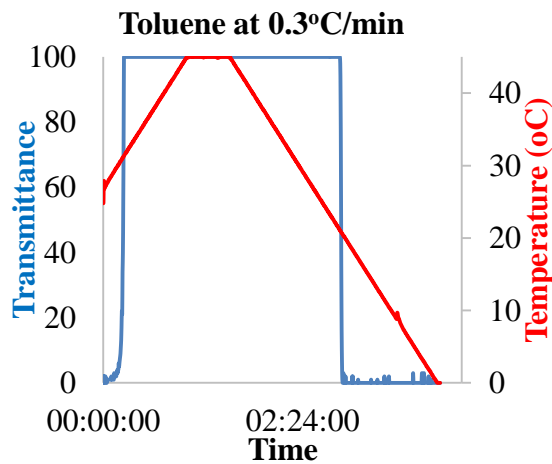
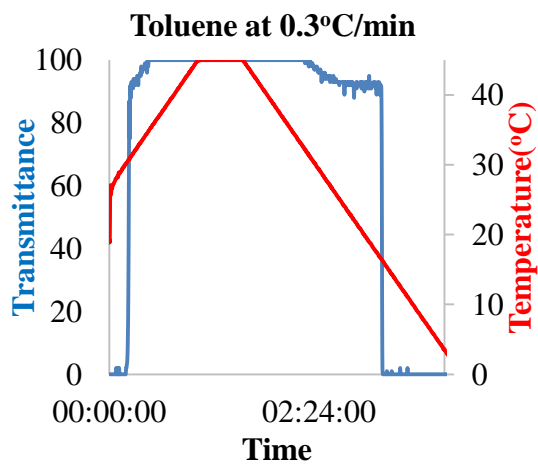
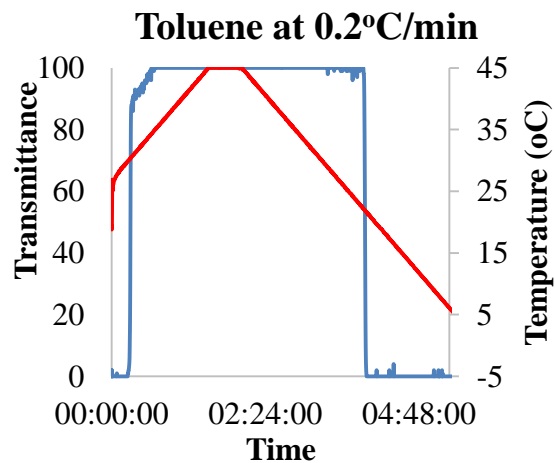
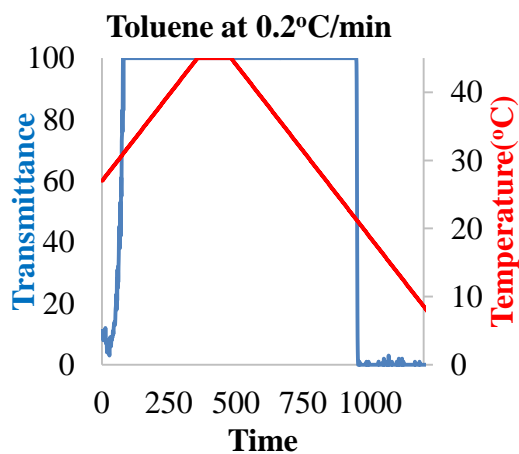
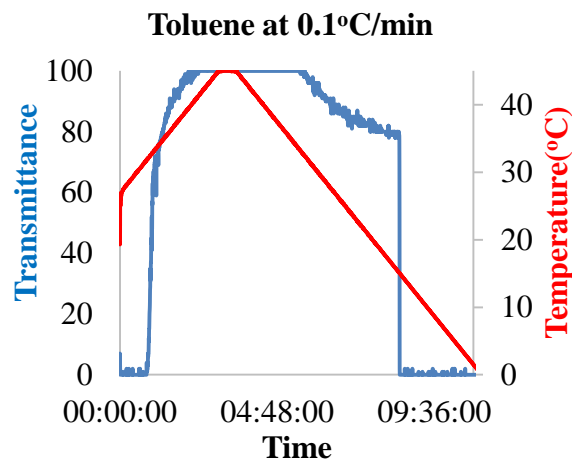
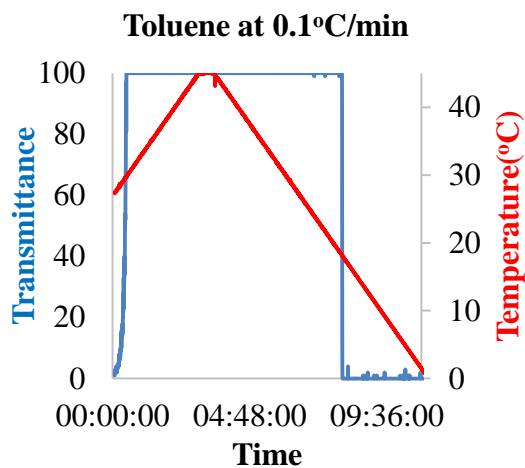
177. Wardani, A.M., *Versetzungen und mechanische Eigenschaften von Hydrazinium-Lithium-Sulfat und verwandten Verbindungen*. Diploma Thesis, 1978. RWTH Aachen University.
178. Jaffe, H. and B.R. Kjellgren, *Controlled growth inhibition in large-scale crystal growth*. Discussions of the Faraday Society, 1949. **5**: p. 319-322.
179. Lai, X., K.J. Roberts, M.J. Bedzyk, P.F. Lyman, L.P. Cardoso, and J.M. Sasaki, *Structure of habit-modifying trivalent transition metal cations (Mn^{3+} , Cr^{3+}) in nearly perfect single crystals of potassium dihydrogen phosphate as examined by X-ray standing waves, X-ray absorption spectroscopy, and molecular modeling*. Chemistry of materials, 2005. **17**(16): p. 4053-4061.
180. Remédios, C., A. dos Santos, X. Lai, K. Roberts, S. Moreira, M. Miranda, A. de Menezes, F. Rouxinol, and L. Cardoso, *Experimental Evidence for the Influence of Mn^{3+} Concentration on the Impurity Incorporation and Habit Modification Mechanism of Potassium Dihydrogen Phosphate*. Crystal Growth & Design, 2010. **10**(3): p. 1053-1058.
181. Tulke, A.O., H. , *The problem of growth rate dispersion*. Proceedings of the 11th symposium on industrial crystallisation, 1990: p. 441-446.
182. Berglund, K.A., *Summary of recent research on growth rate dispersion of contact nuclei*. Chemical Engineering Communications, 1986. **41**(1-6): p. 357-360.
183. Mahajan, A.J., C.J. Orella, and D. Kirwan. *Analysis of size distribution and growth kinetics during the batch crystallization of L-asparagine*. in *AIChE Symp. Ser.* 1991.
184. Suzuki, S., *Topological structural analysis of digitized binary images by border following*. Computer Vision, Graphics, and Image Processing, 1985. **30**(1): p. 32-46.
185. Douglas, D., *Algorithms for the reduction of the number of points required to represent a line or its a caricature*. The Canadian Cartographer, 1973. **10**(2): p. 112-122.
186. Genck, W.J., *Optimizing crystallizer scale up*. Chem. Eng. Prog, 2003. **99**(6): p. 36-44.
187. Haque, J.N., T. Mahmud, K.J. Roberts, and D. Rhodes, *Modeling turbulent flows with free-surface in unbaffled agitated vessels*. Industrial & Engineering Chemistry Research, 2006. **45**(8): p. 2881-2891.

188. Haquea, J., T. Mahmuda, K. Roberts, K. Liang, G. White, D. Wilkinson, and D. Rhodesc, *Simulation of free-surface flow in an unbaffled stirred tank reactor. The Canadian journal of chemical engineering.* **89**(4): p.745-753.
189. Li, M., G. White, D. Wilkinson, and K.J. Roberts, *LDA measurements and CFD modeling of a stirred vessel with a retreat curve impeller.* Industrial & engineering chemistry research, 2004. **43**(20): p. 6534-6547.
190. Li, M., G. White, D. Wilkinson, and K.J. Roberts, *Scale up study of retreat curve impeller stirred tanks using LDA measurements and CFD simulation.* Chemical Engineering Journal, 2005. **108**(1-2): p. 81-90.
191. Hammond, R.B., C. Ma, K.J. Roberts, P.Y. Ghi, and R.K. Harris, *Application of systematic search methods to studies of the structures of urea-dihydroxy benzene cocrystals.* The Journal of Physical Chemistry B, 2003. **107**(42): p. 11820-11826.
192. Hammond, R.B., K. Pencheva, V. Ramachadran, K.J.Roberts. *Application of grid-based molecular methods for modeling solvent-dependent crystal growth morphology: aspirin crystallized from aqueous ethanolic solution.* Crystal Growth & Design, 2007. **7**(9): p. 1571-1574.

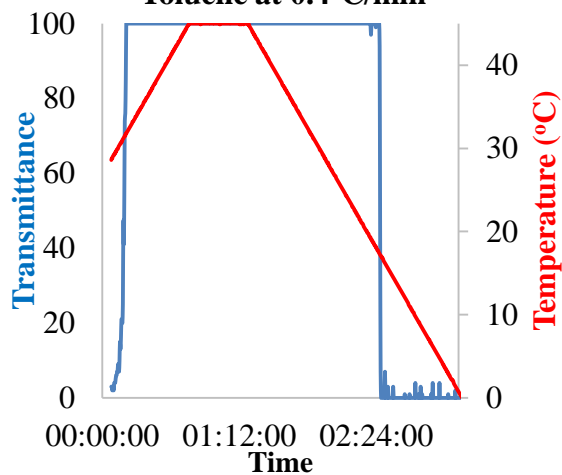
**APPENDIX A: MSZW AND INDUCTION TIMES
DETERMINATIONS**

A1. MSZW

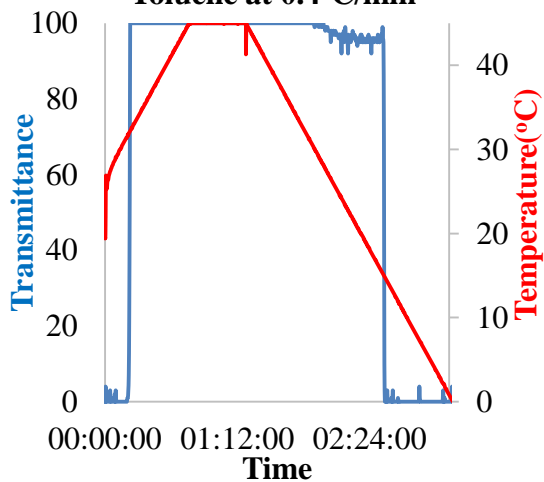
A1.1 Toluene Solutions



Toluene at 0.4°C/min

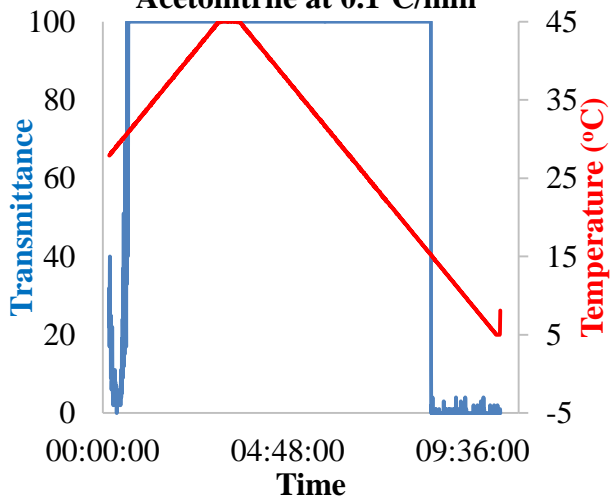


Toluene at 0.4°C/min

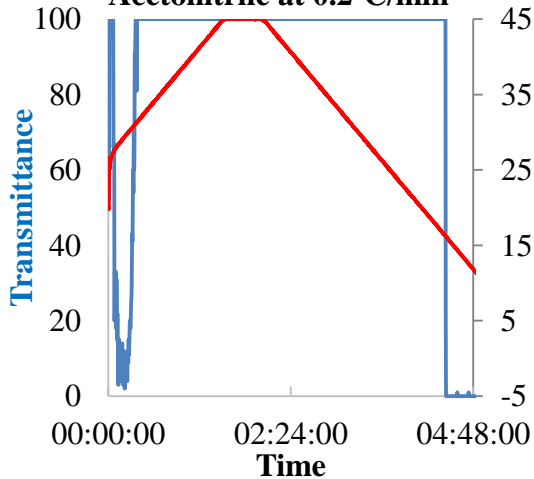


A1.2 Acetonitrile Solutions

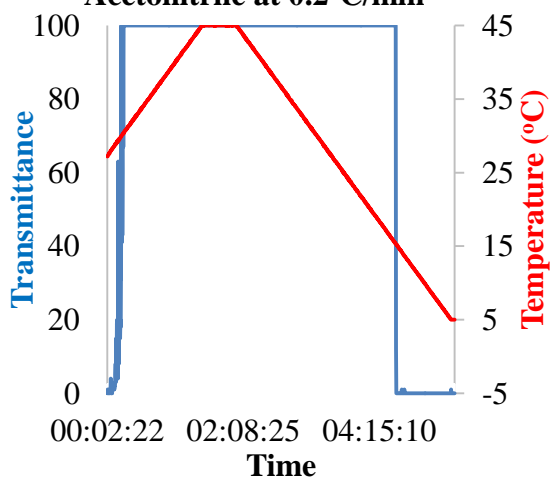
Acetonitrile at 0.1°C/min

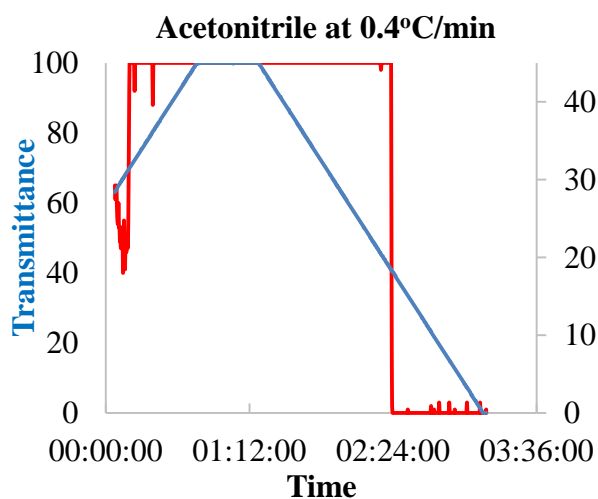
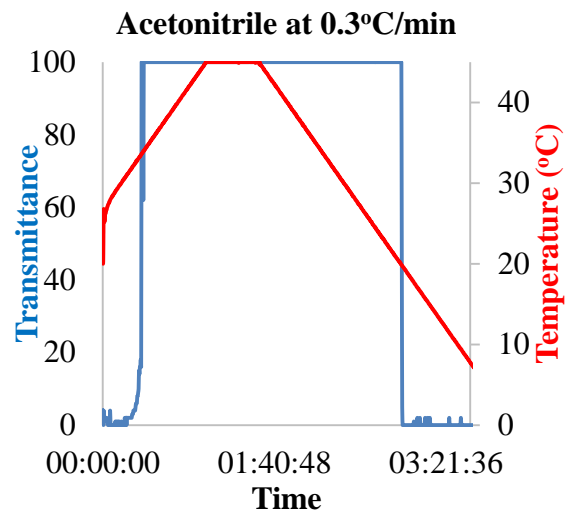
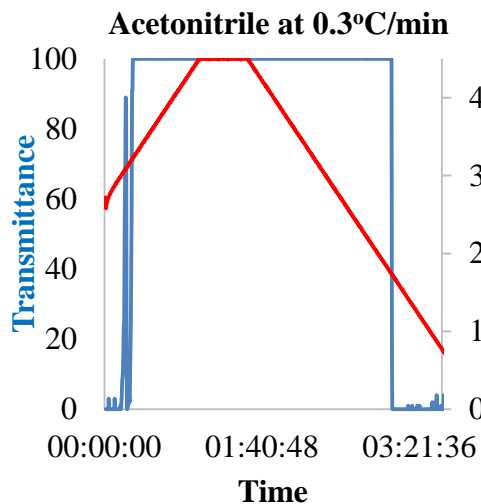


Acetonitrile at 0.2°C/min

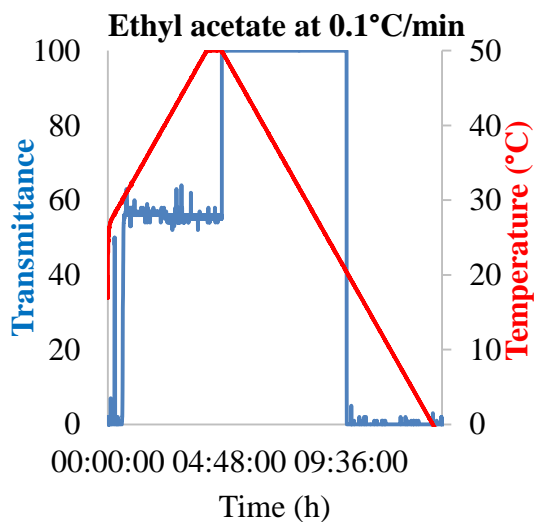
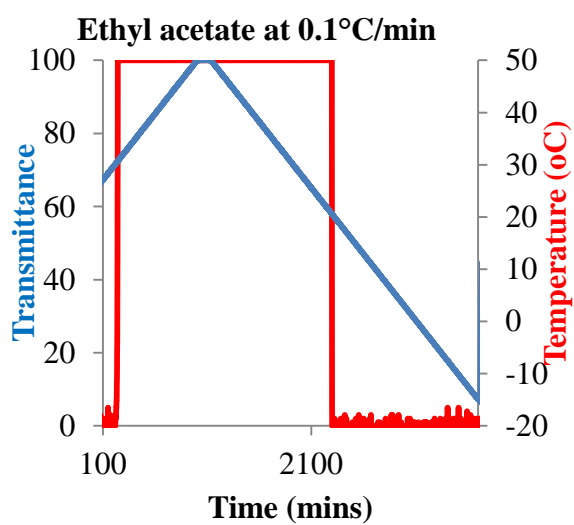


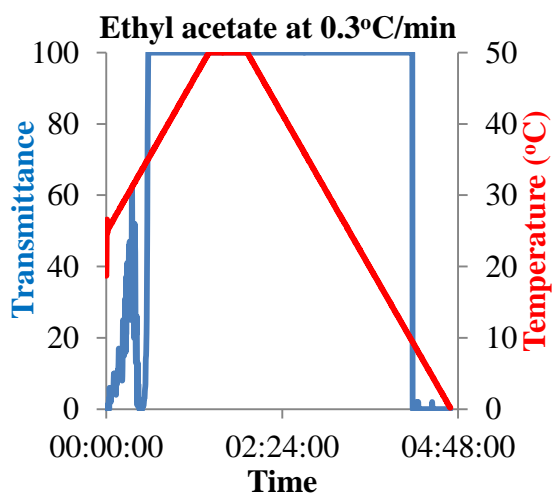
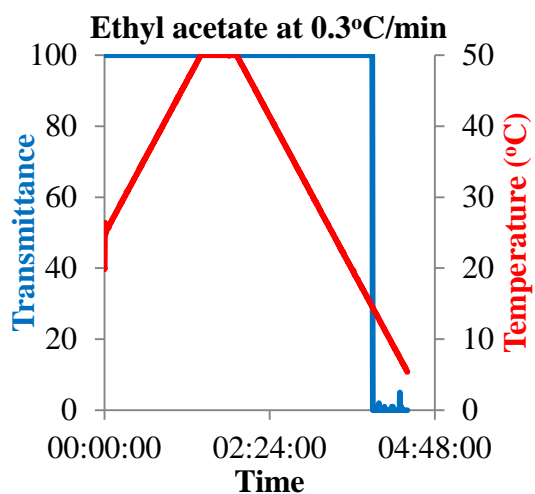
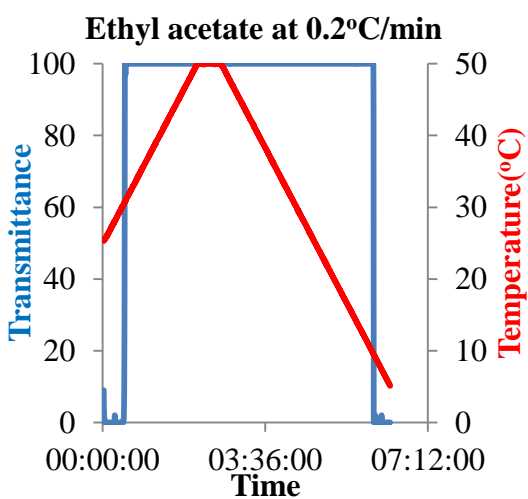
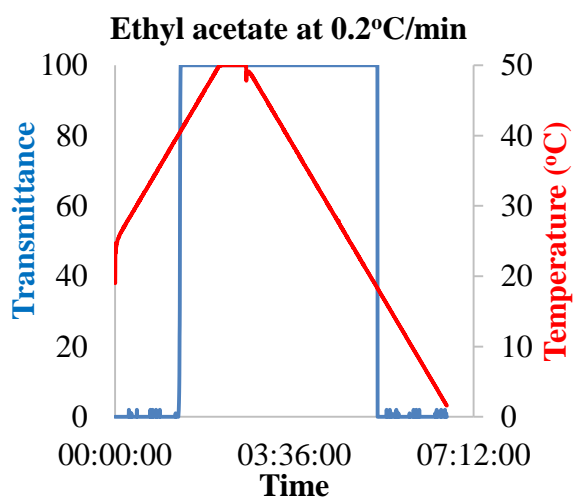
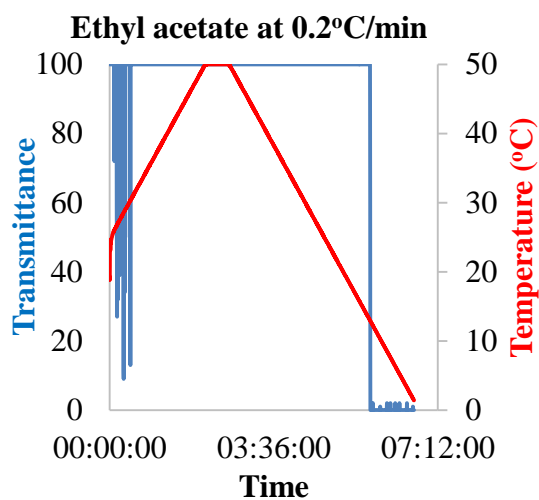
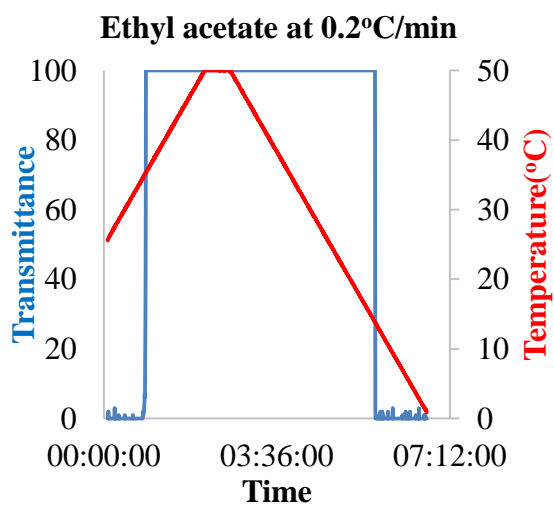
Acetonitrile at 0.2°C/min

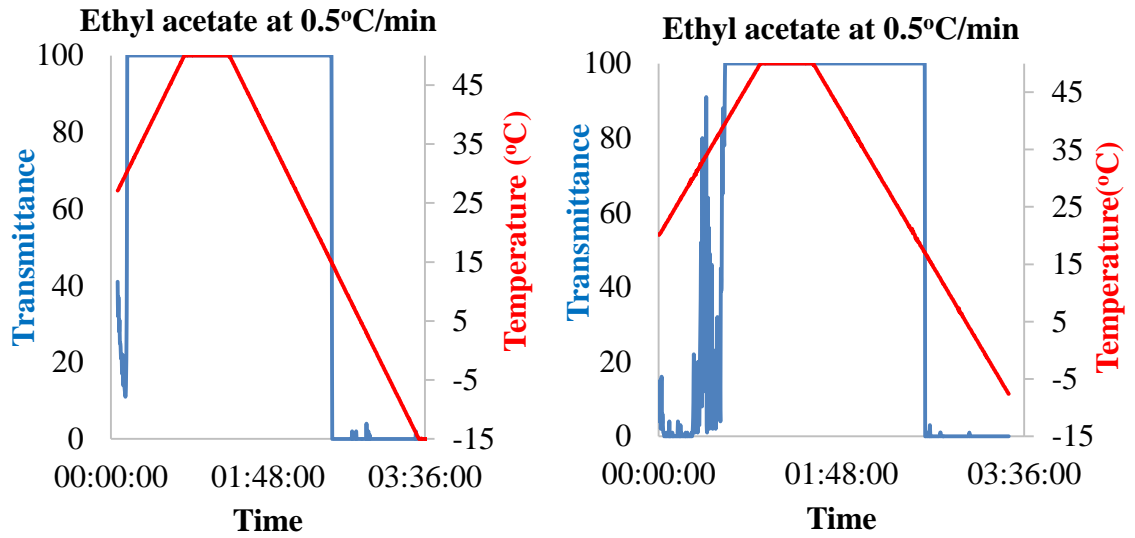




A1.3 Ethyl Acetate Solutions

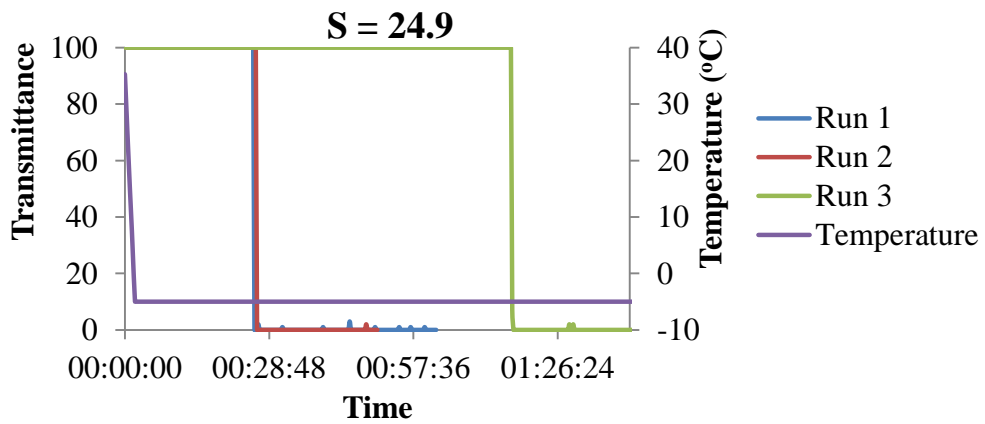




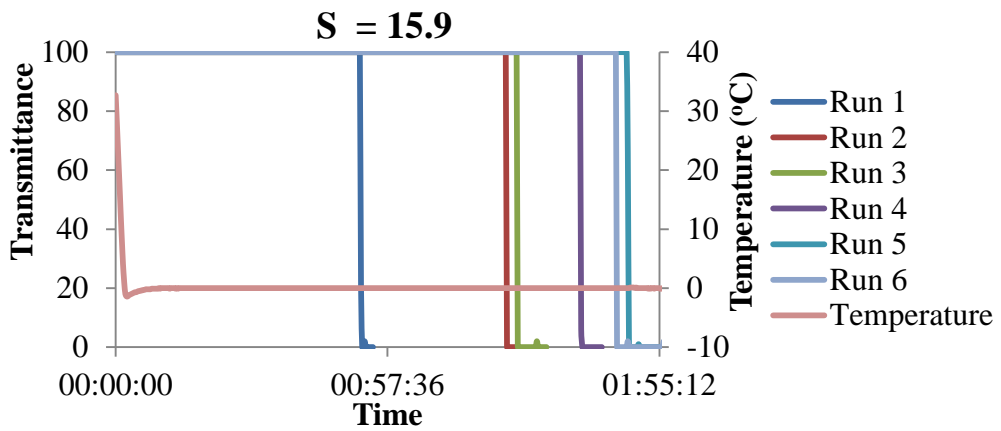


A2. Induction times

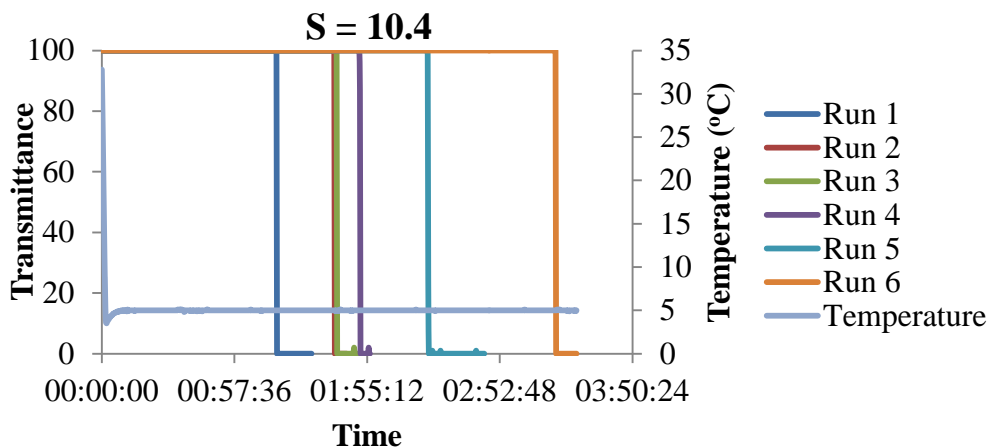
A2.1 Acetonitrile Solutions



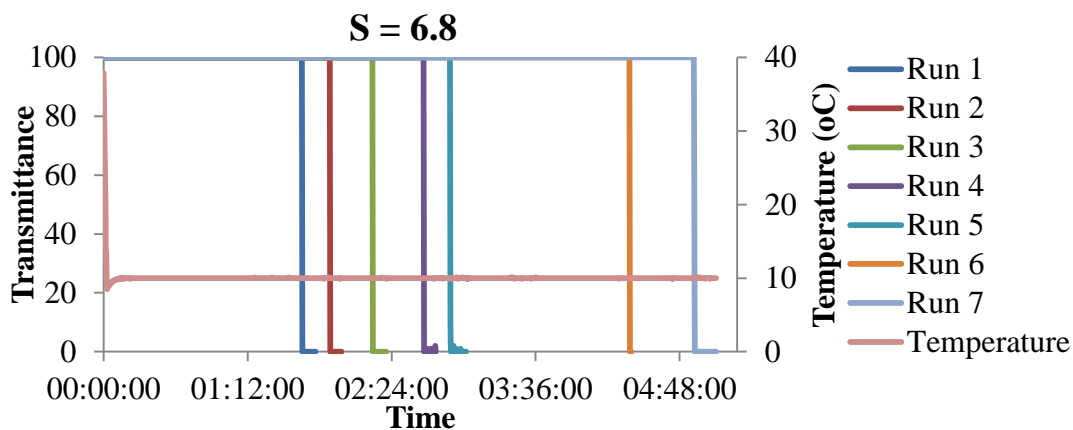
(a)



(b)

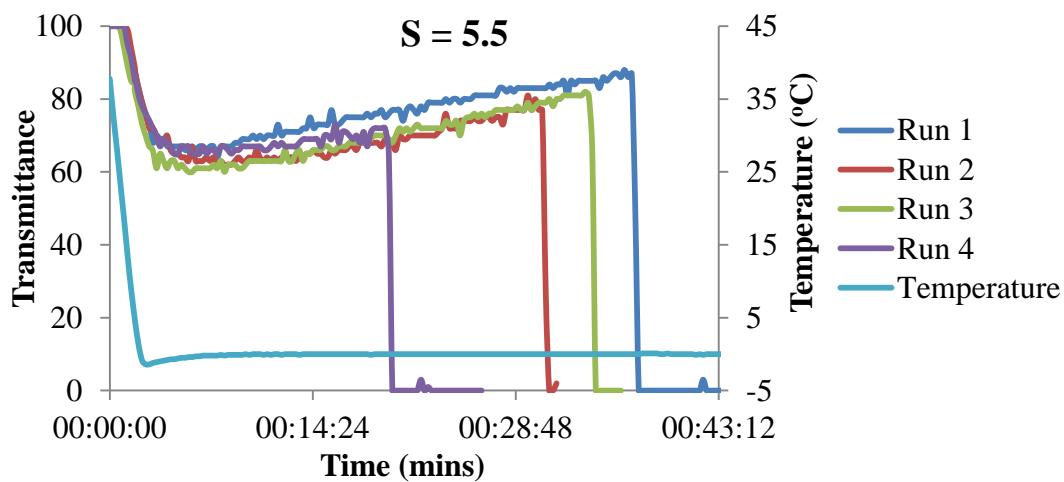


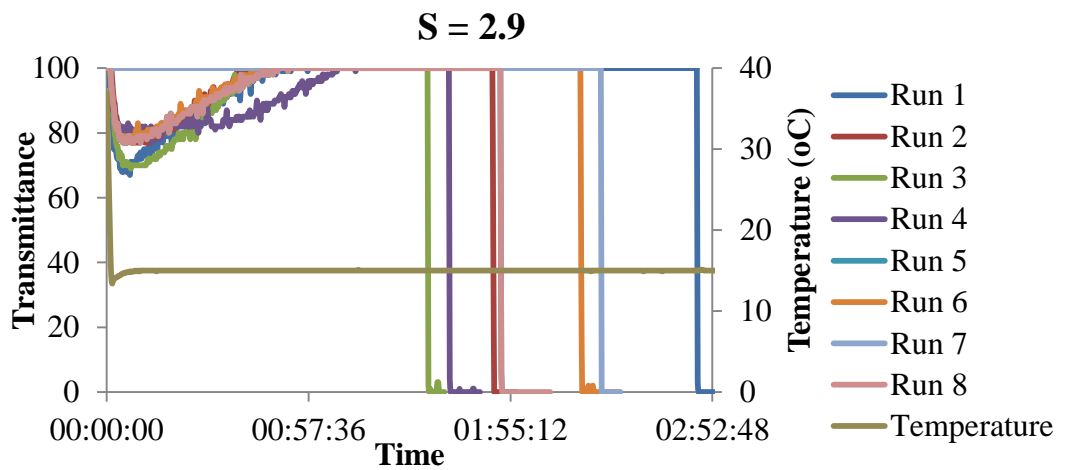
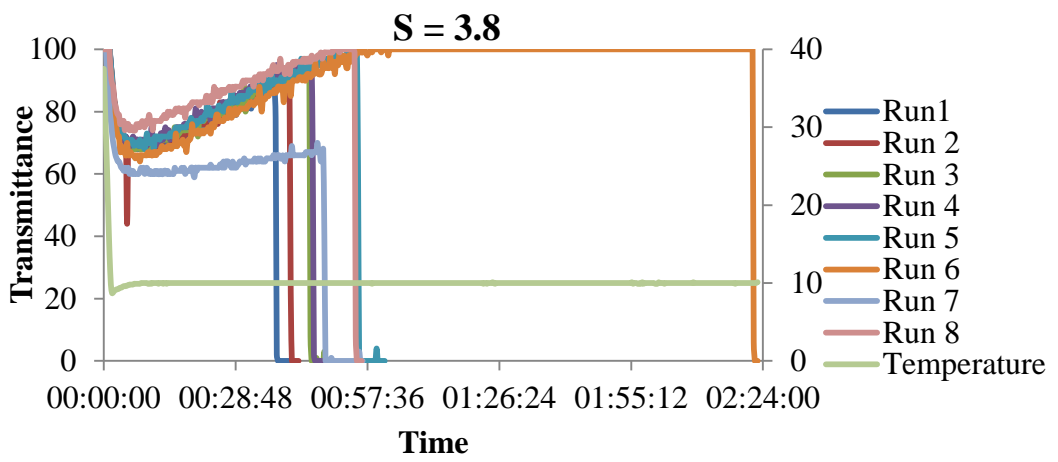
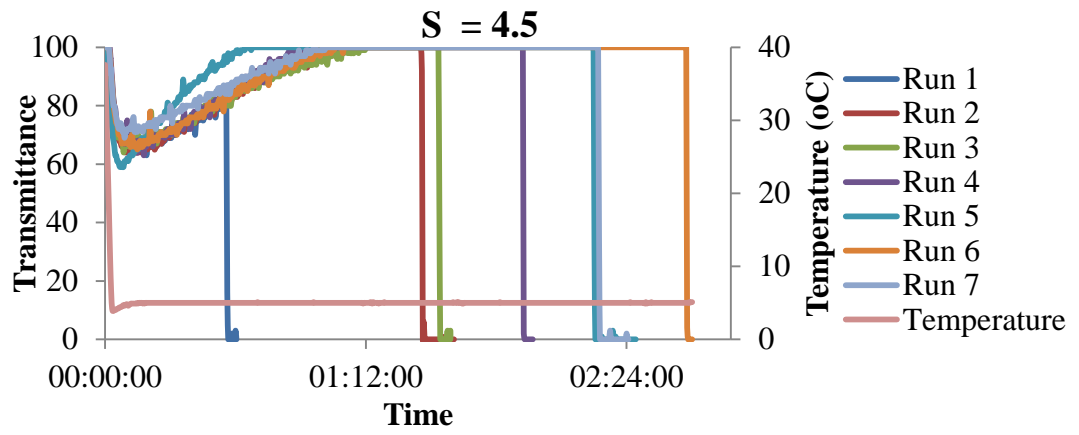
(c)



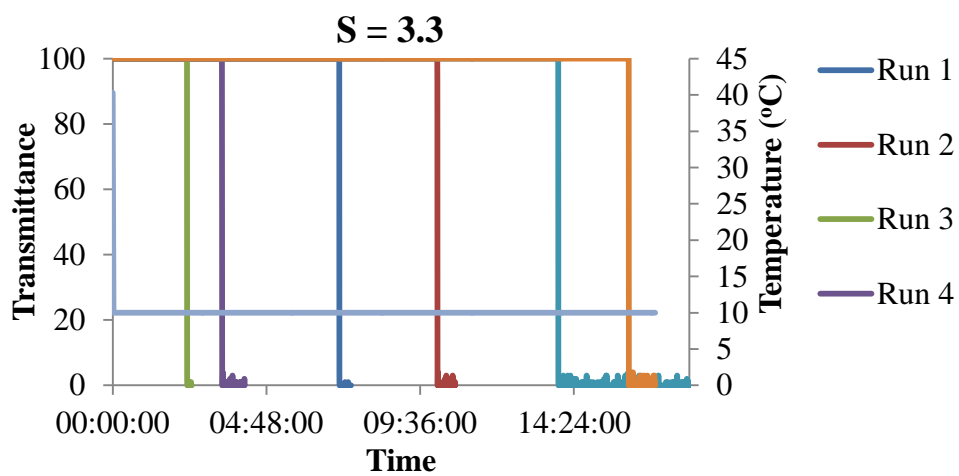
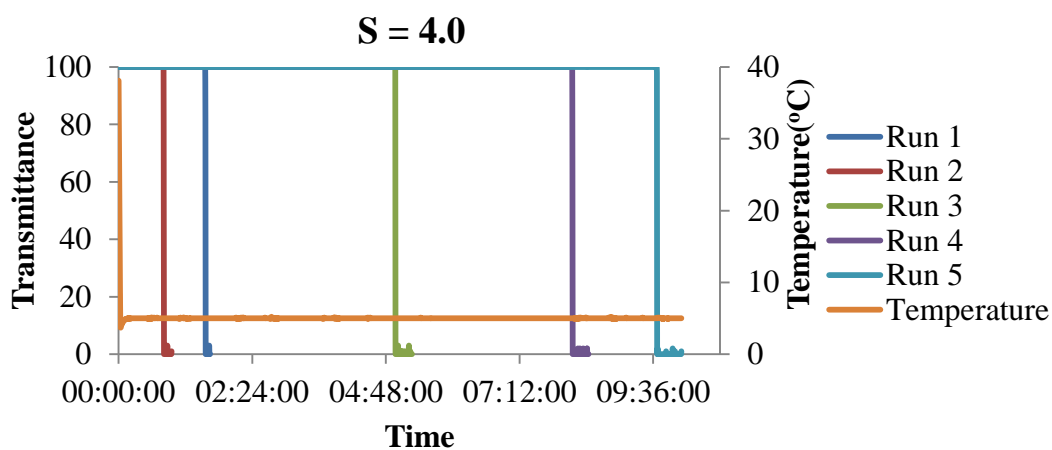
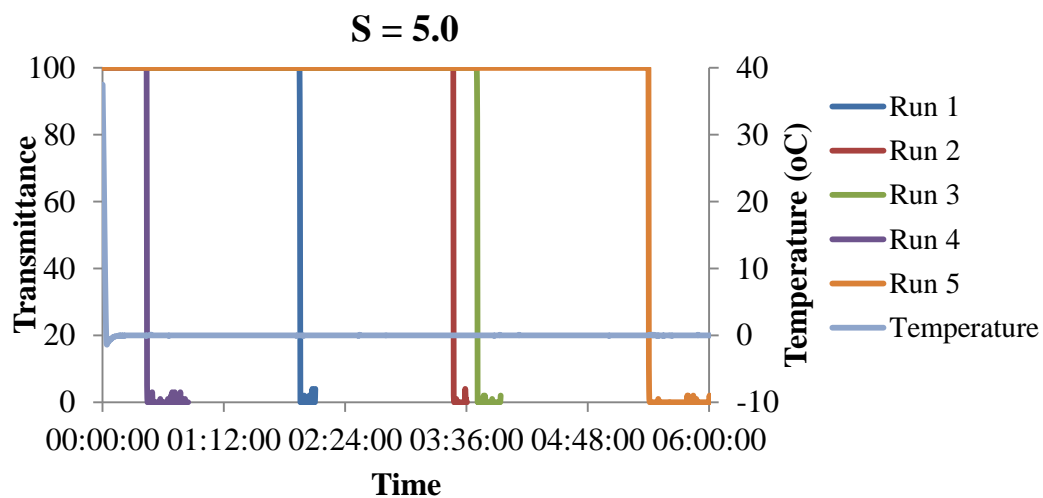
(d)

A2.2. Toluene Solutions

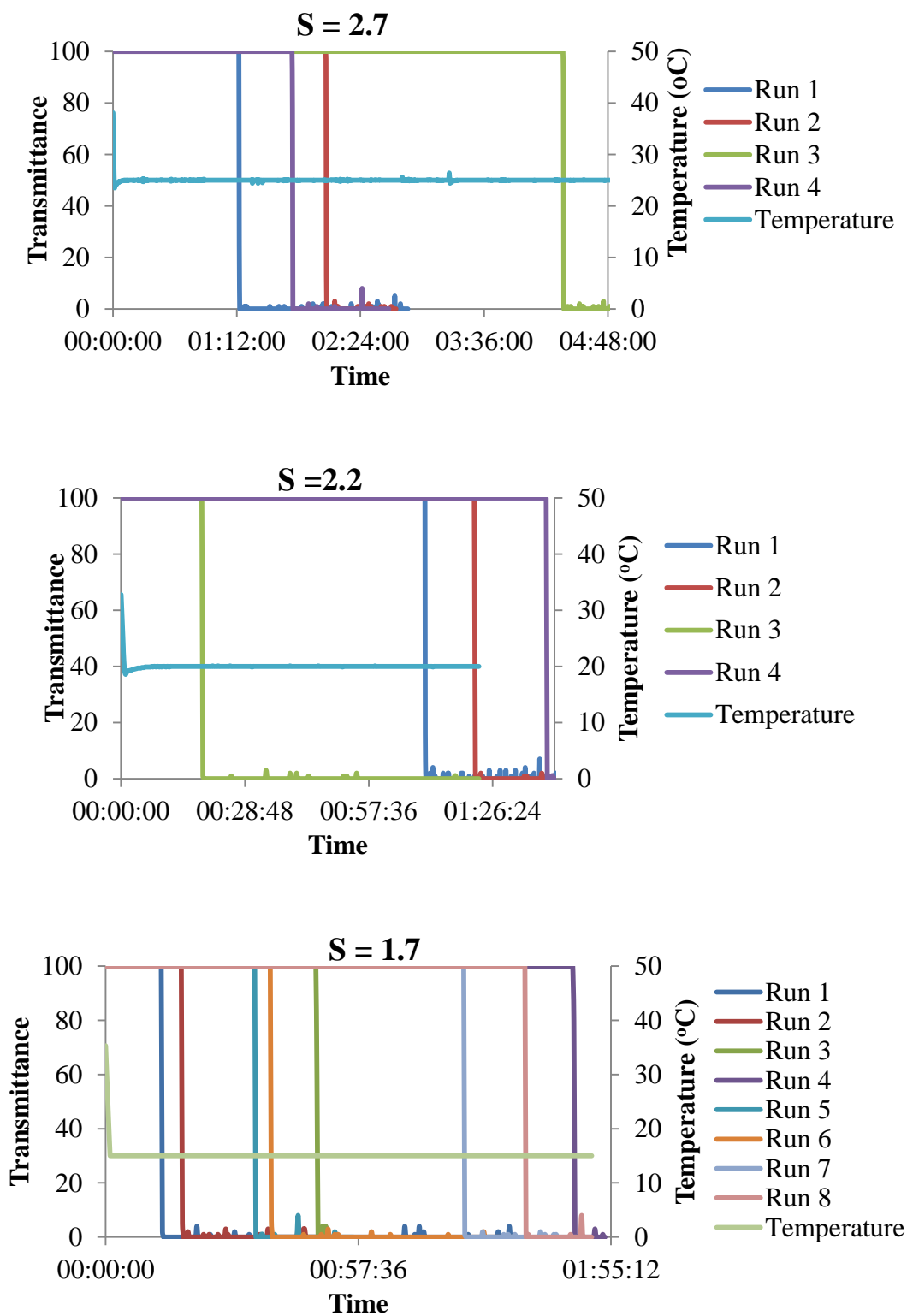




A2.3. Ethanol 95% Solutions



A2.4. Ethyl Acetate Solutions



APPENDIX B:

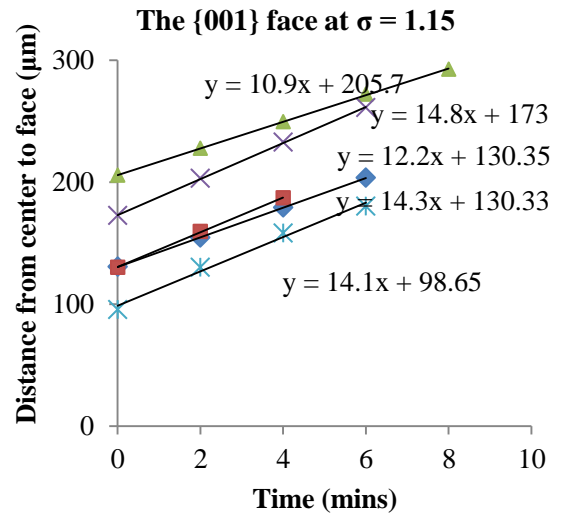
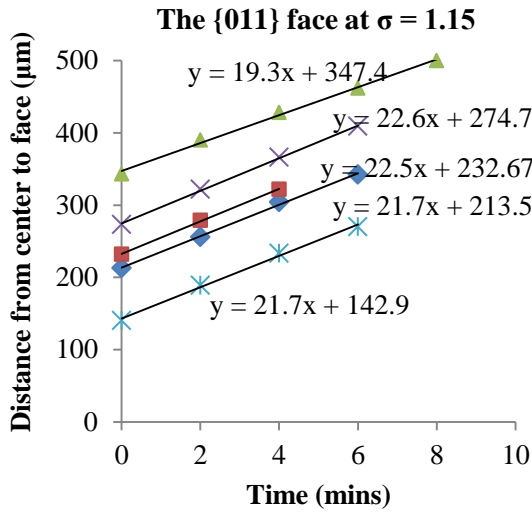
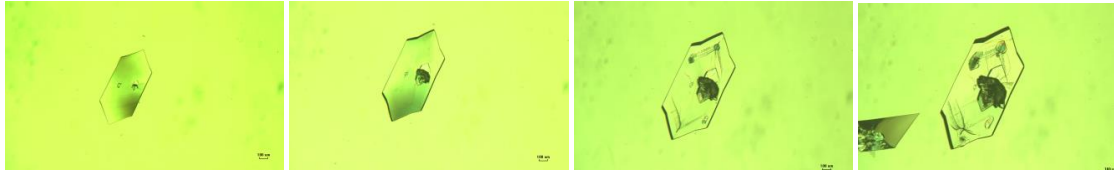
CRYSTAL GROWTH RATE MEASUREMENT IN THE 0.5ML CUVETTE CELL AND THE 15ML JACKETED VESSEL

The data presented comprises plots of growth rate versus time for the {011} and {001} faces for all the crystals measured together with a representative image set for one of these crystals.

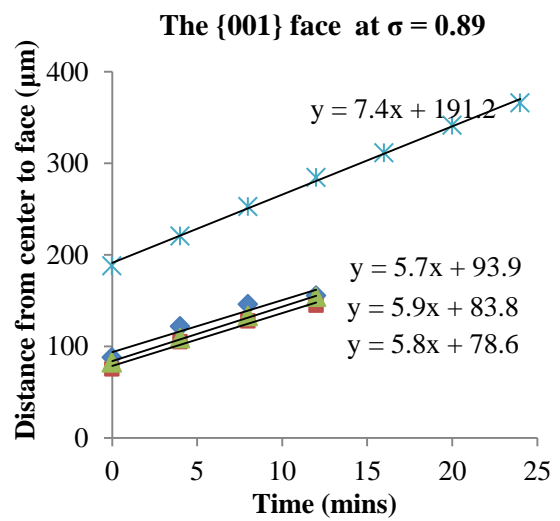
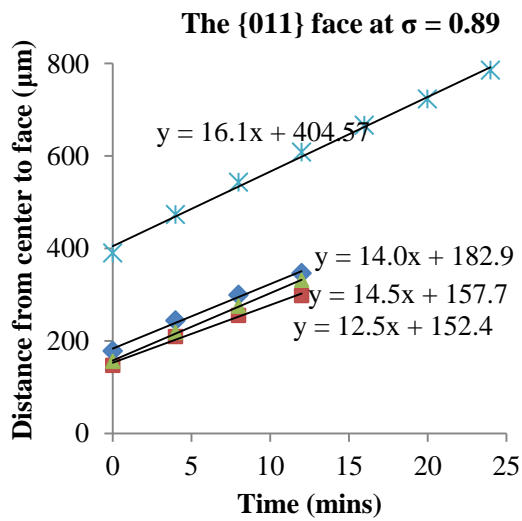
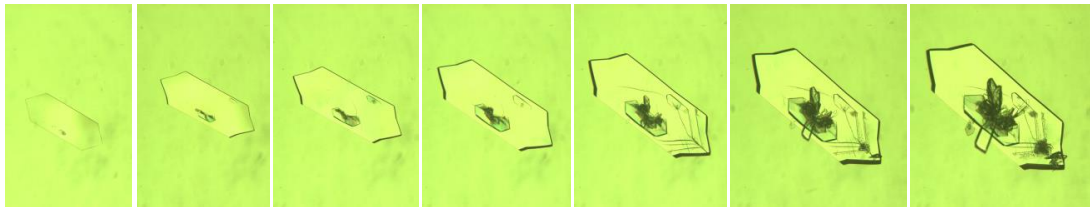
B1. Data from the 0.5ml cuvette cell

B1.1 Ethanol 95% Solutions

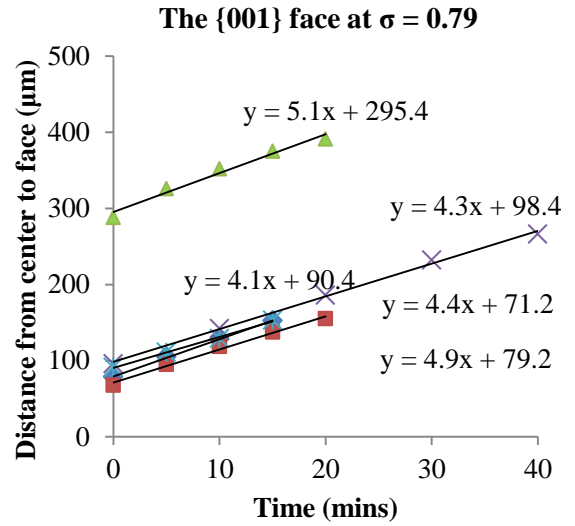
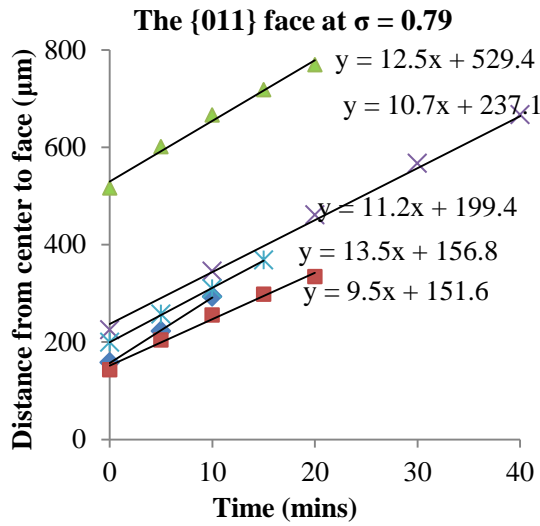
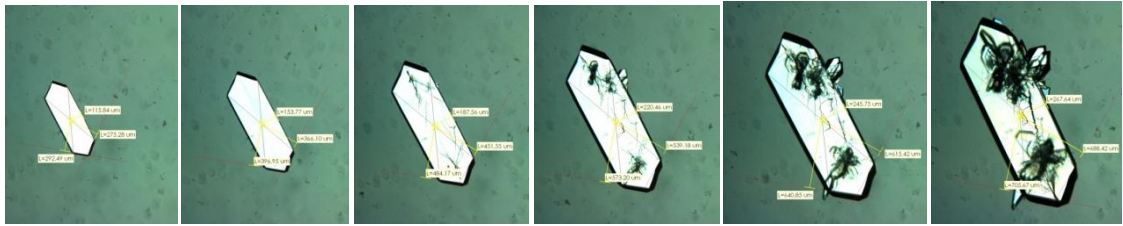
$\sigma = 1.15$



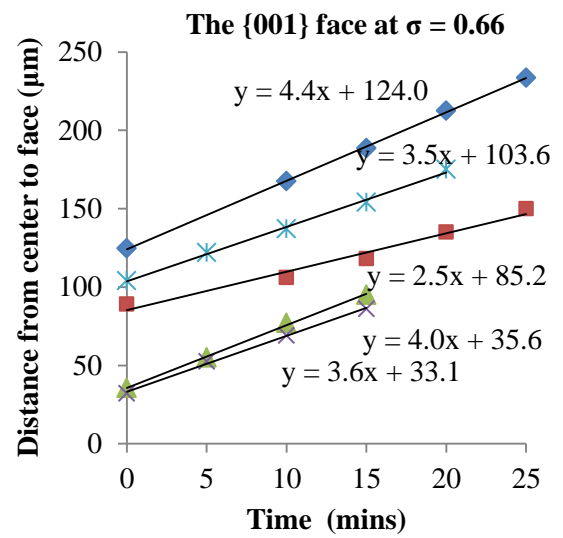
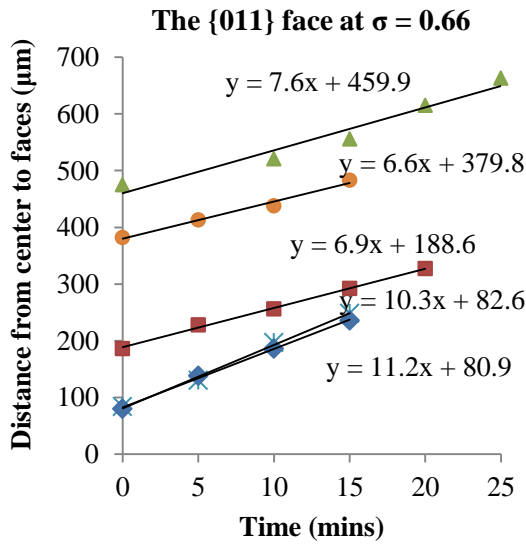
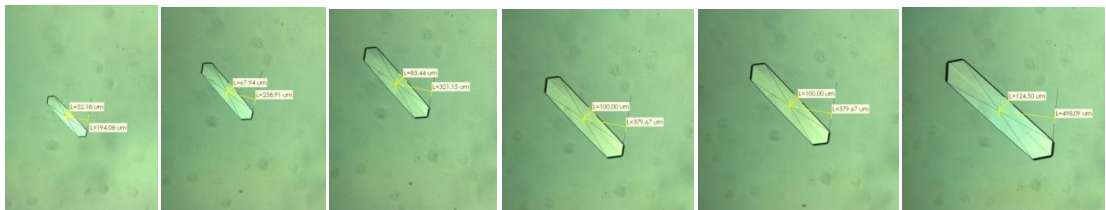
$\sigma = 0.89$



$\sigma = 0.79$

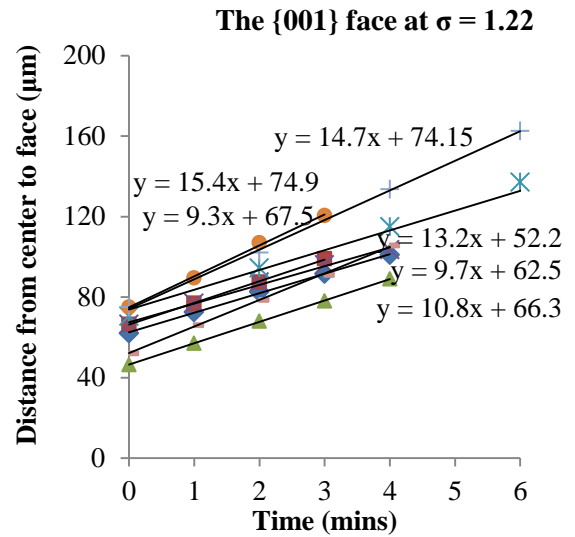
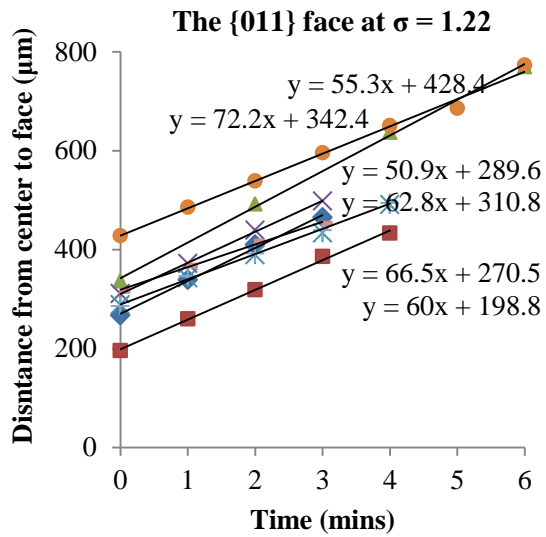
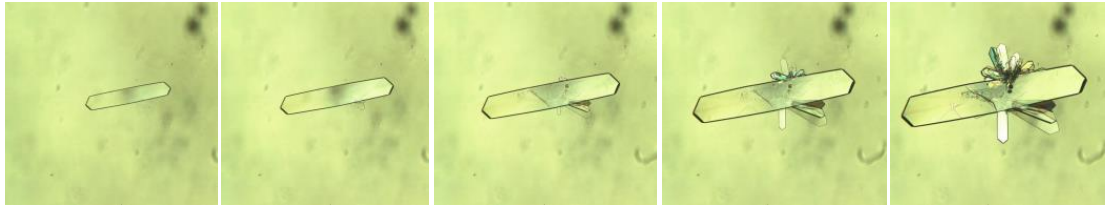


$\sigma = 0.66$

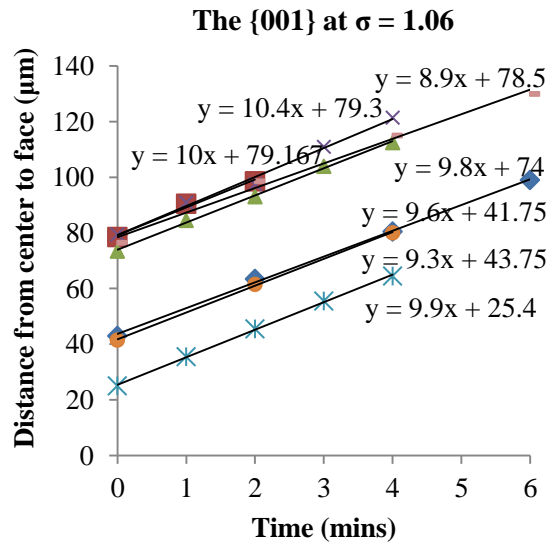
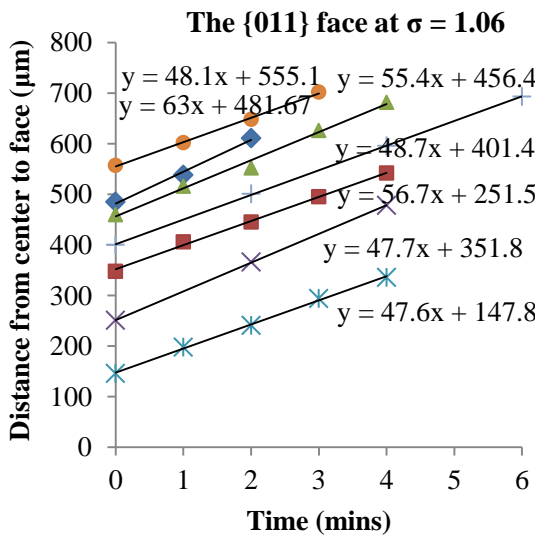
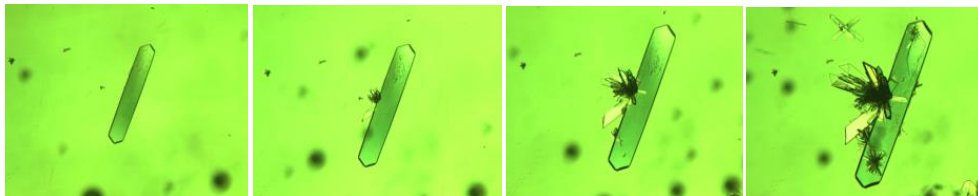


B1.2 Ethyl Acetate Solutions

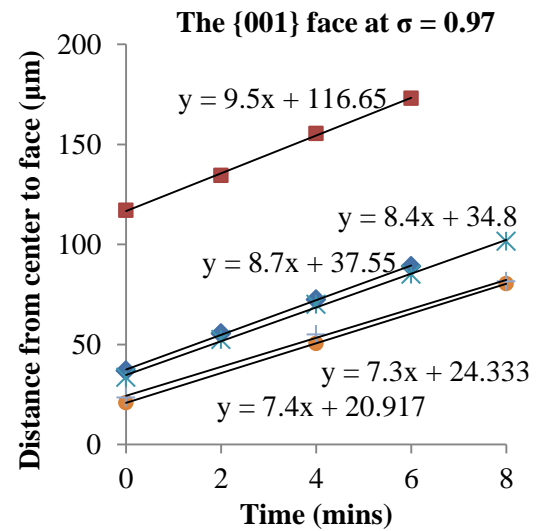
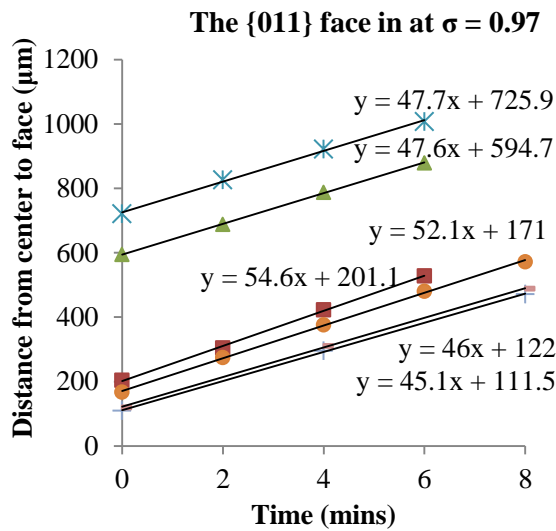
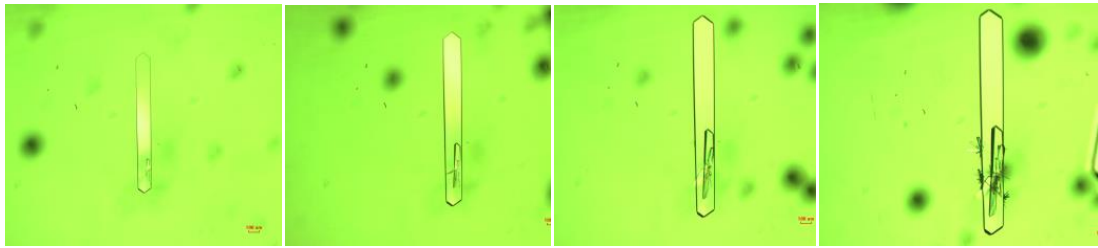
$\sigma = 1.12$



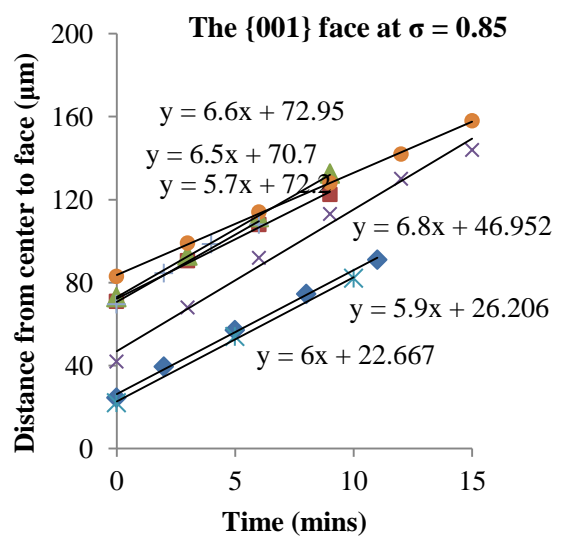
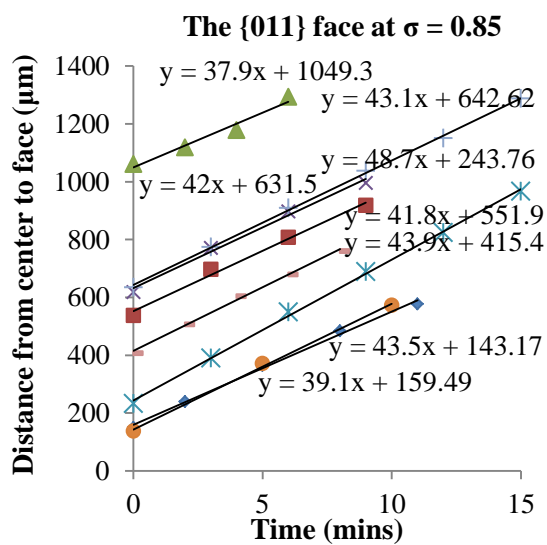
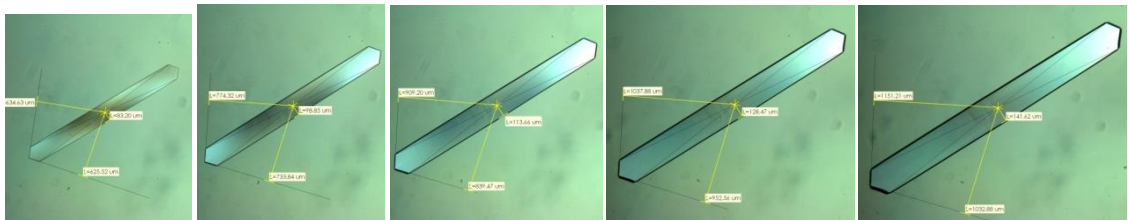
$\sigma = 1.06$



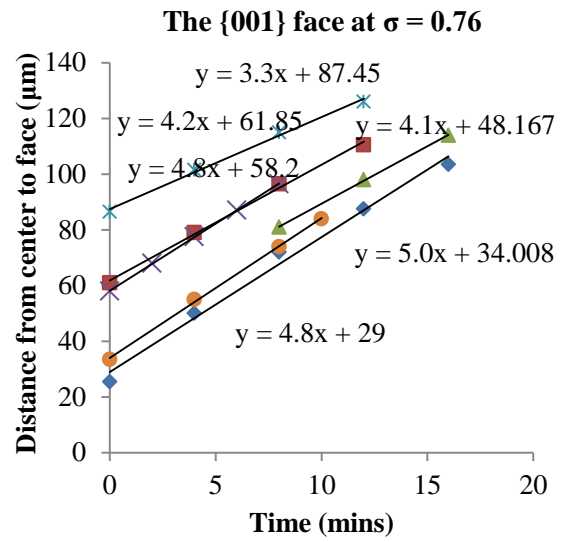
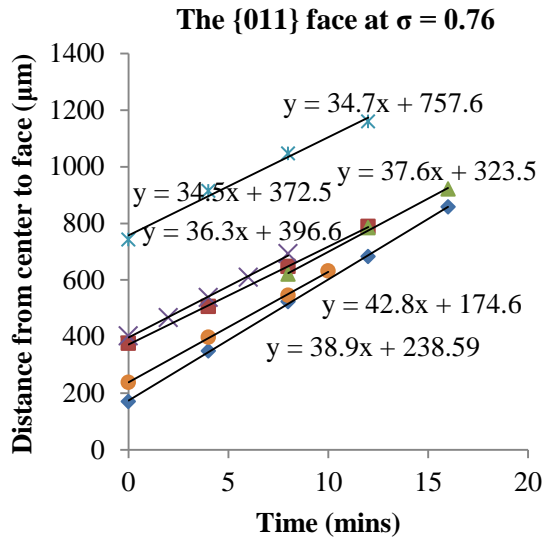
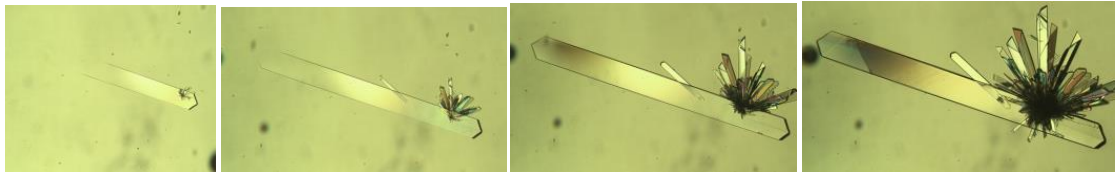
$\sigma = 0.97$



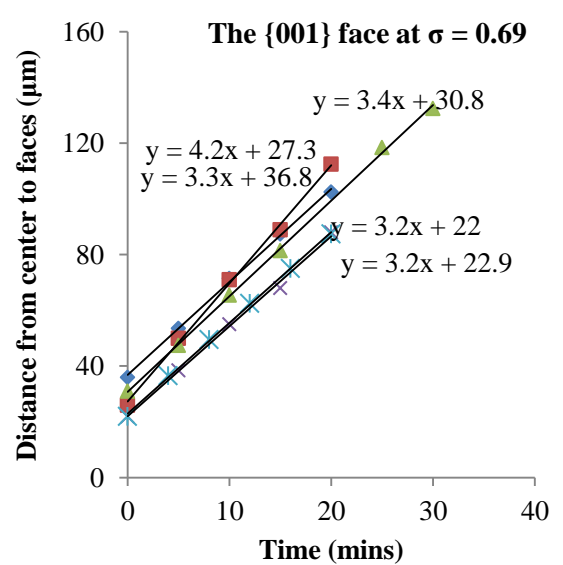
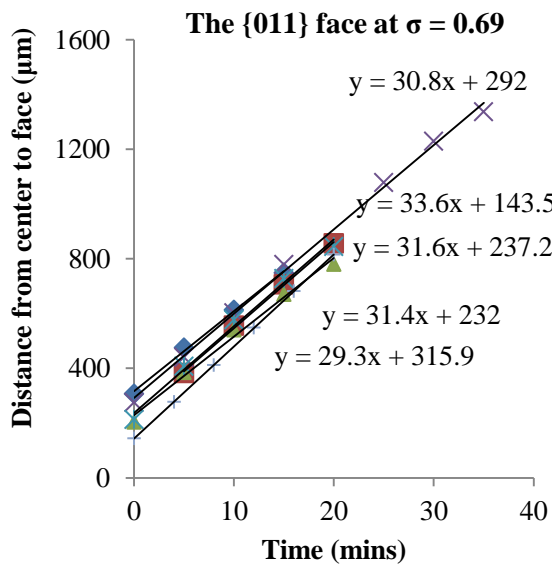
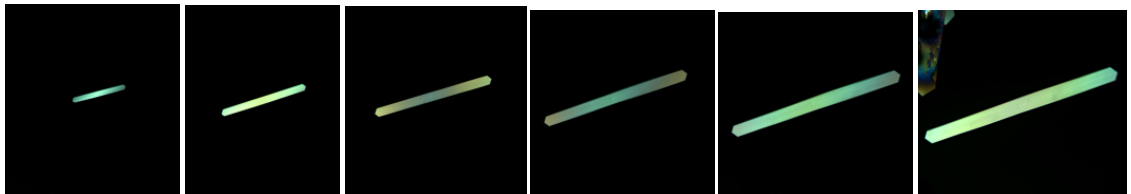
$\sigma = 0.85$



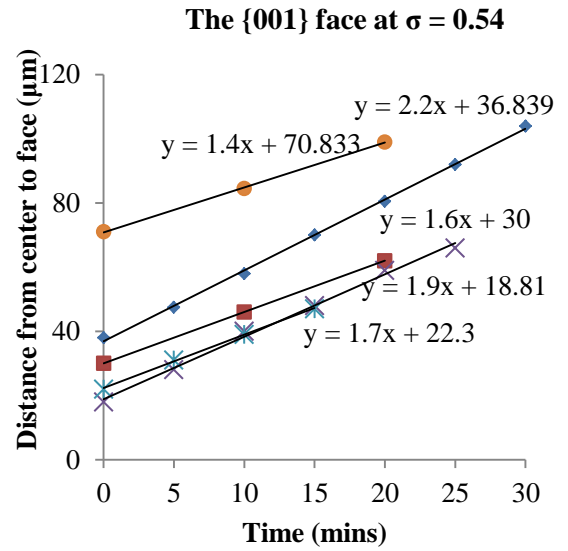
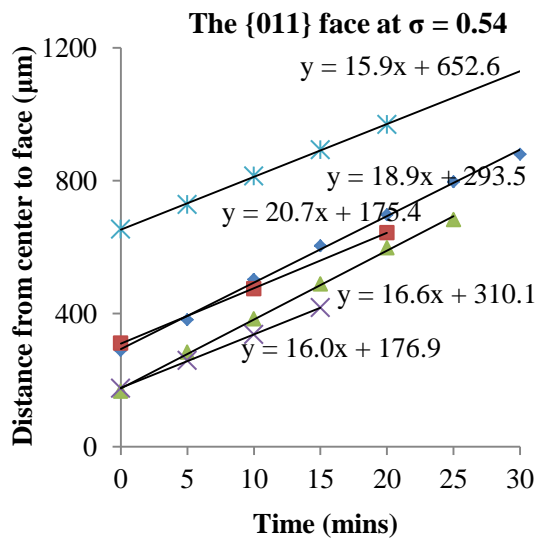
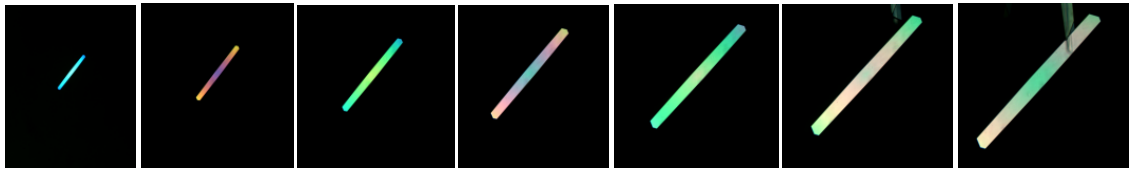
$\sigma = 0.76$



$\sigma = 0.69$

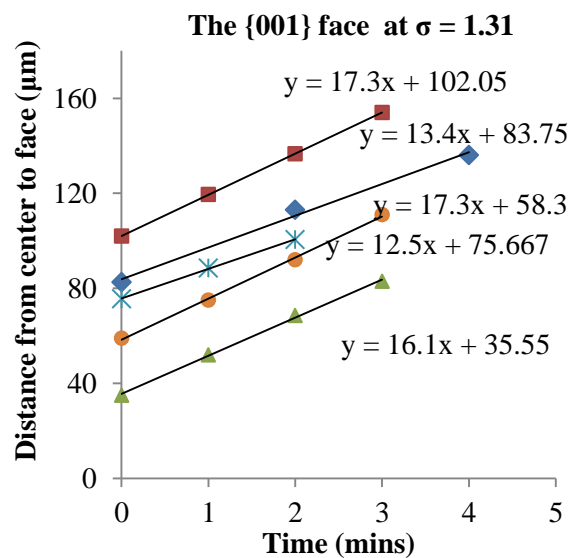
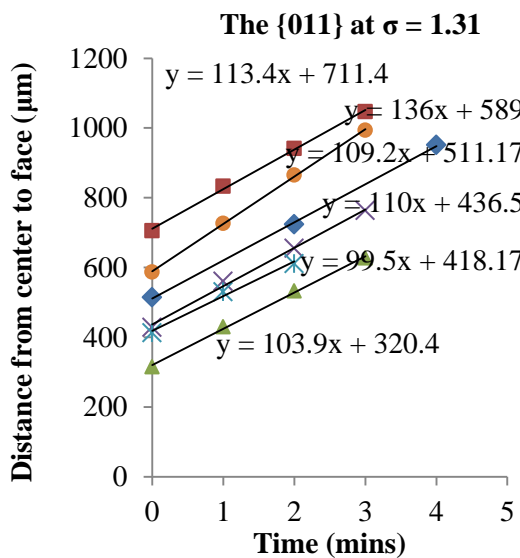
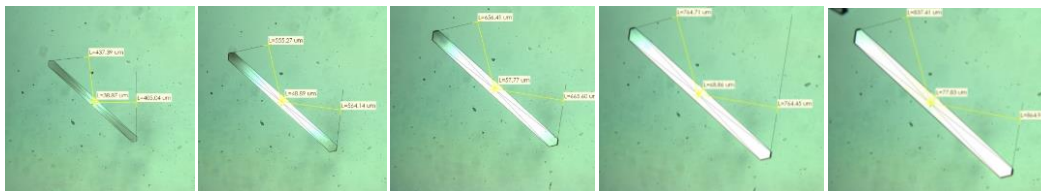


$\sigma = 0.54$

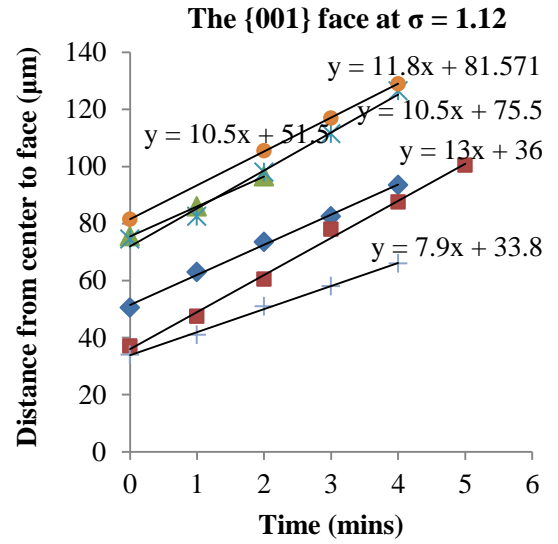
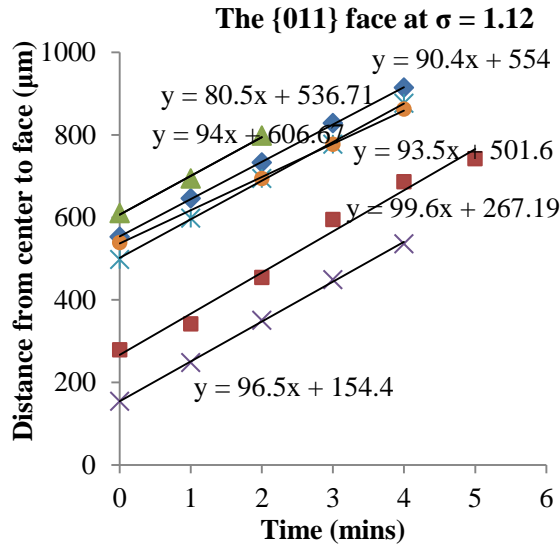


B1.3 Acetonitrile Solutions

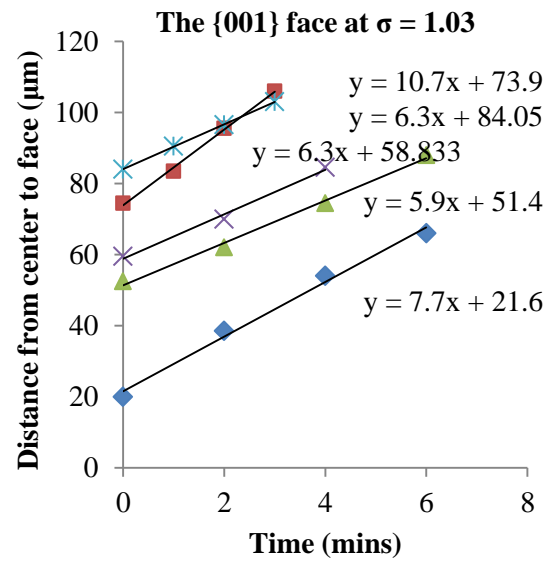
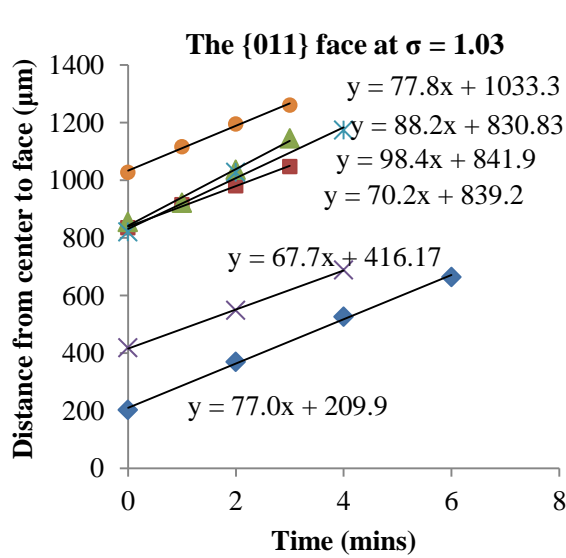
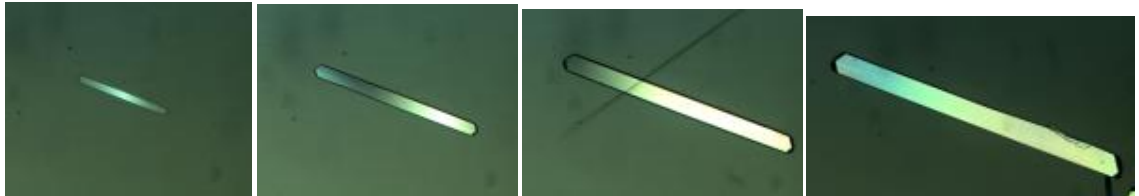
$\sigma = 1.31$



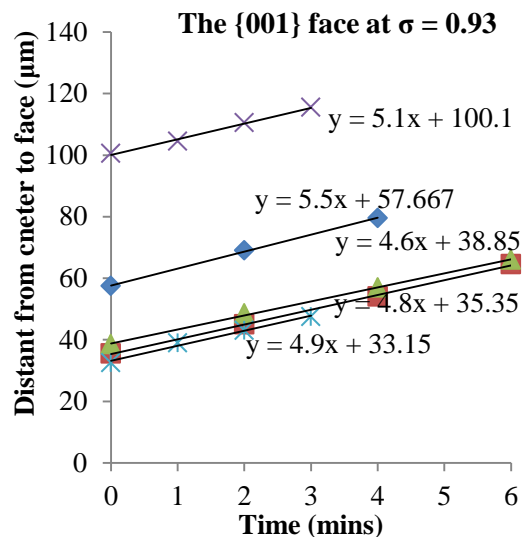
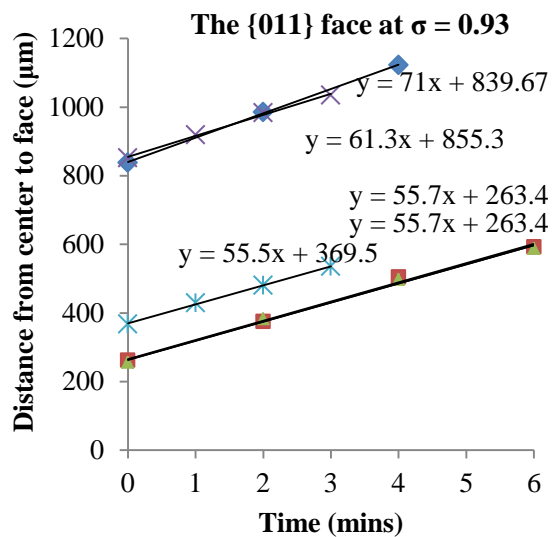
$\sigma = 1.12$



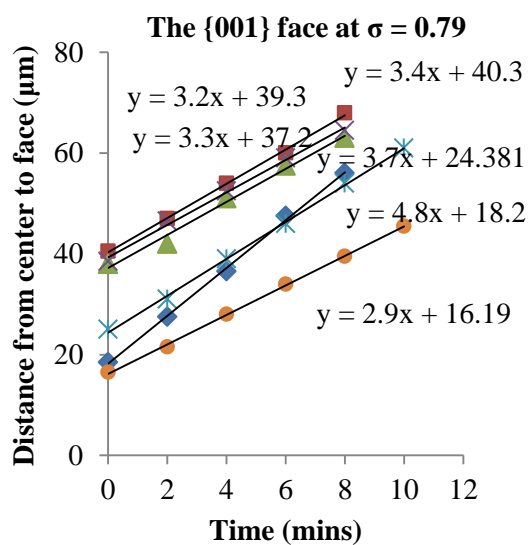
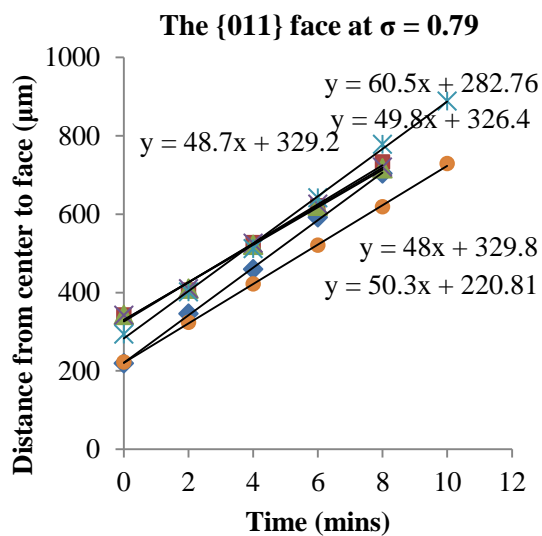
$\sigma = 1.03$



$\sigma = 0.93$

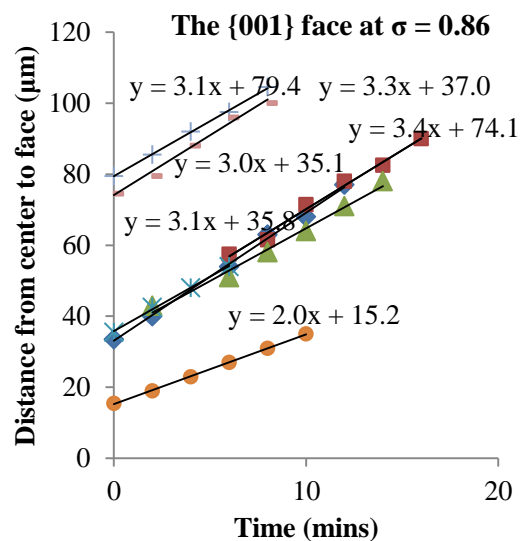
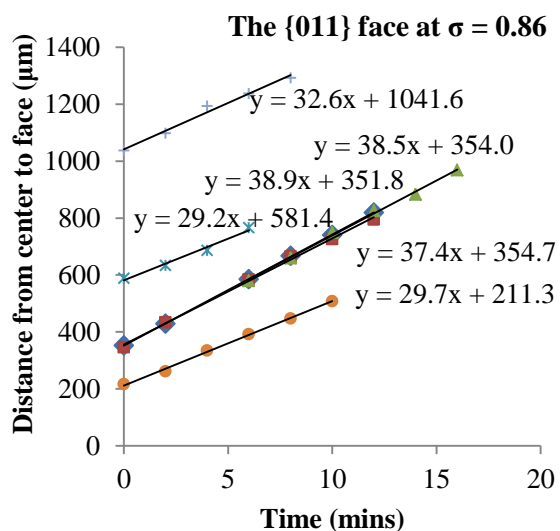
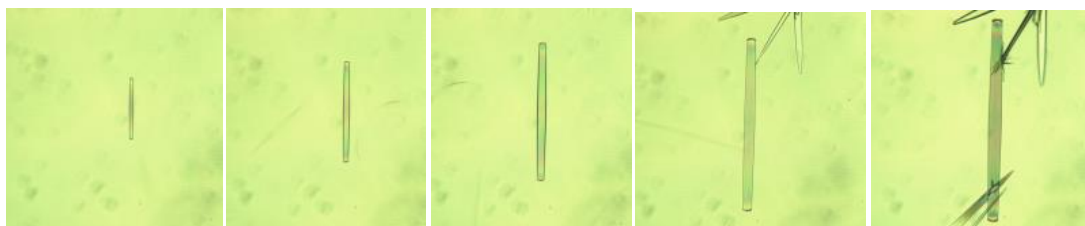


$\sigma = 0.79$

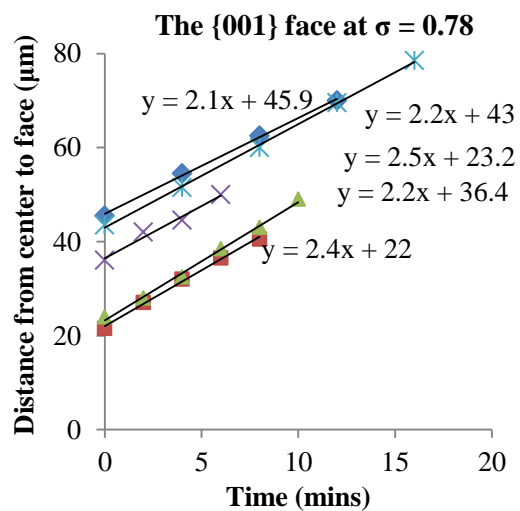
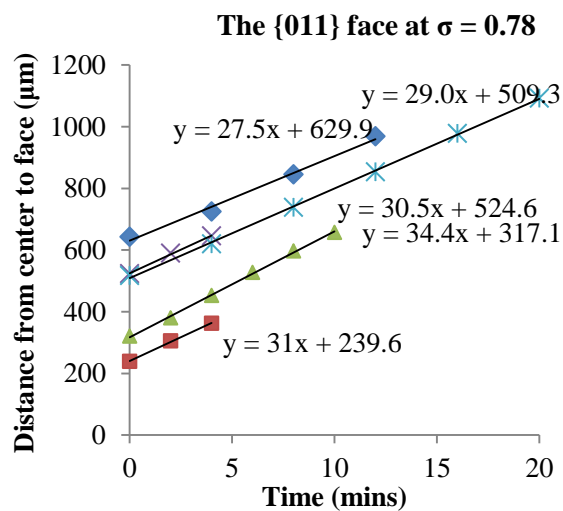
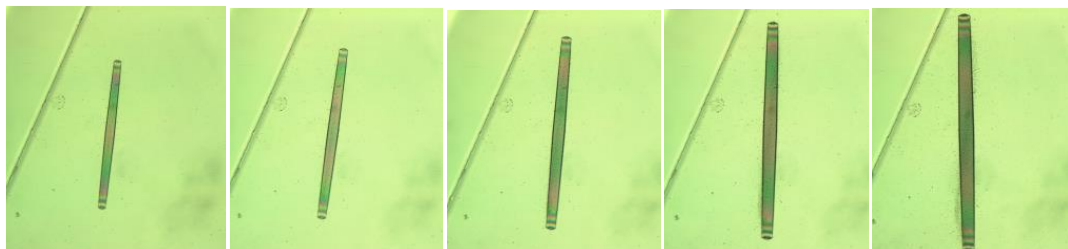


B1.4 Toluene Solutions

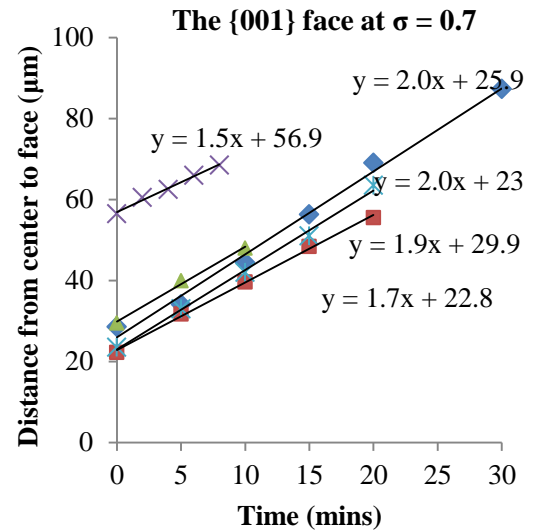
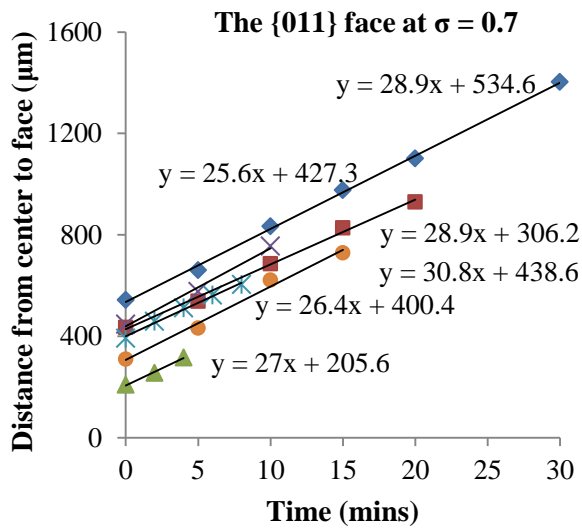
$\sigma = 0.86$



$\sigma = 0.78$



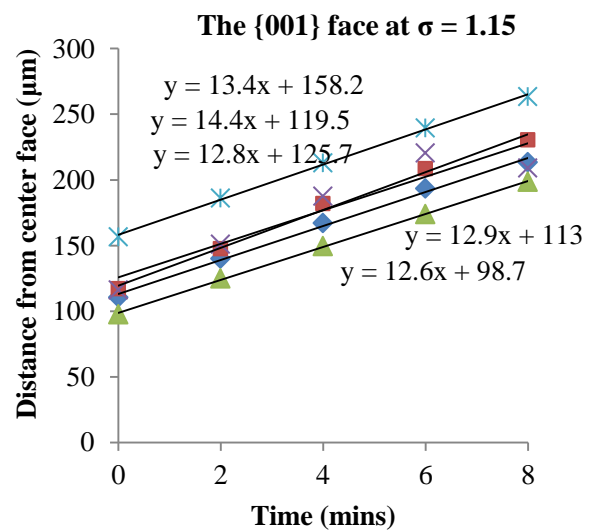
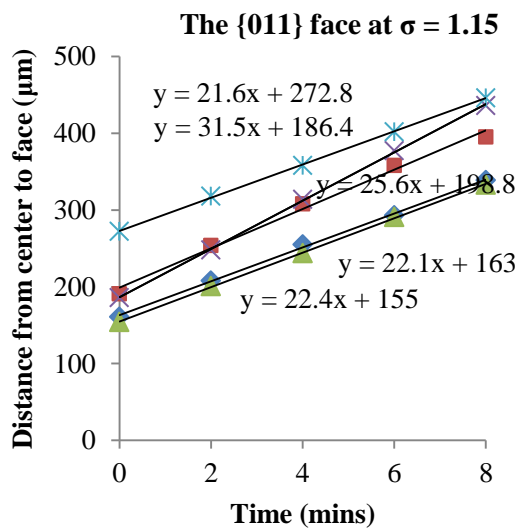
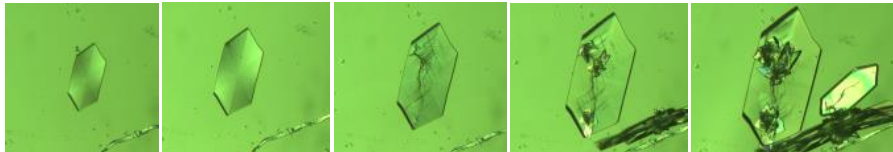
$\sigma = 0.70$



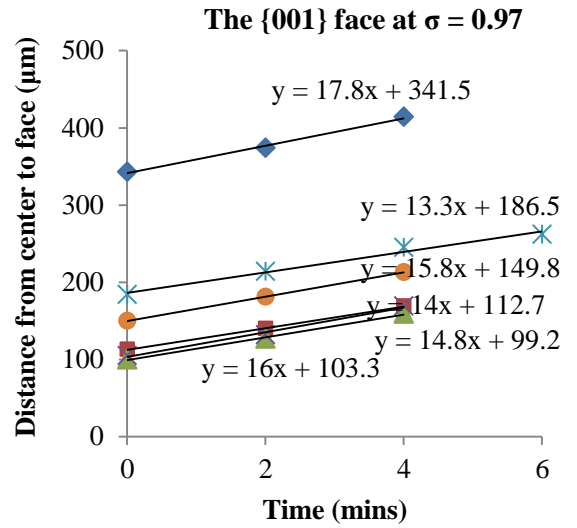
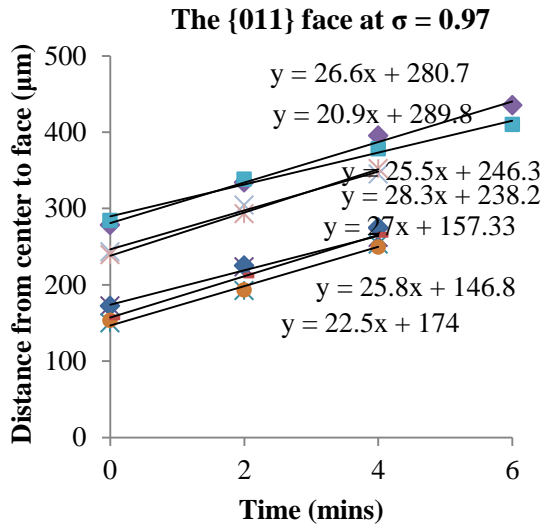
B2 Data from the 15ml jacketed vessel

B2.1 Ethanol 95% Solutions

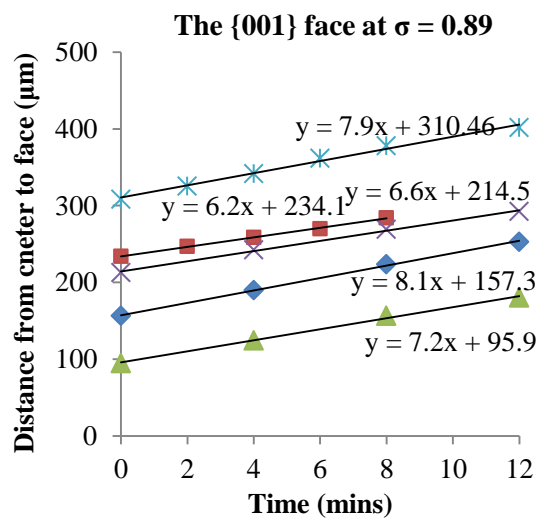
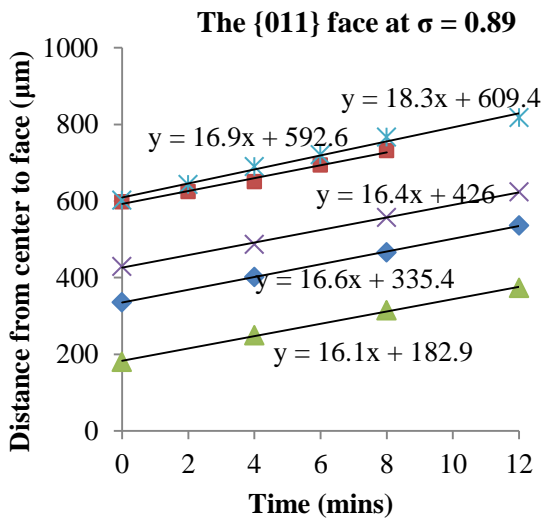
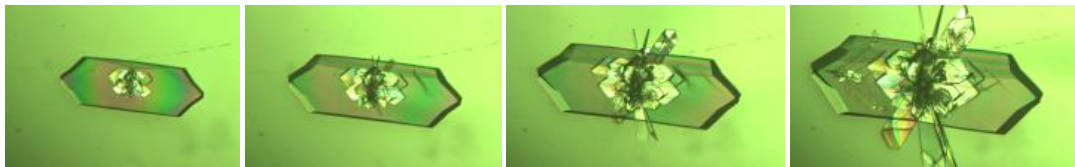
$\sigma = 1.15$



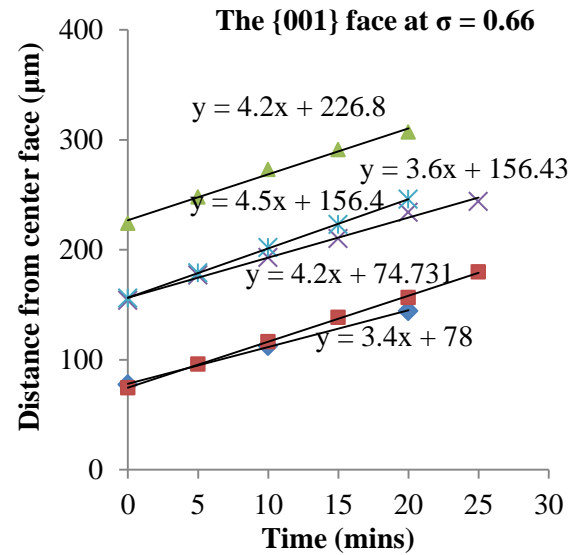
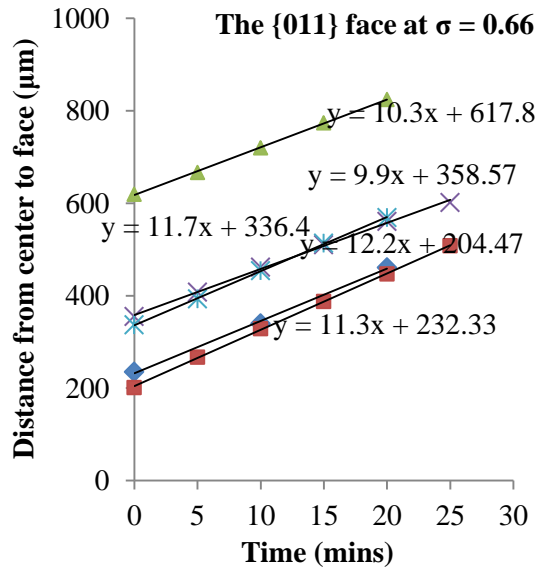
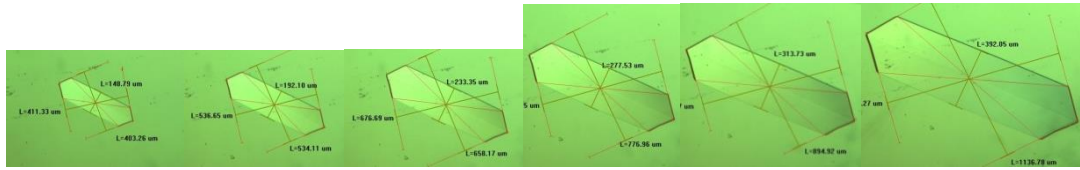
$\sigma = 0.97$



$\sigma = 0.89$

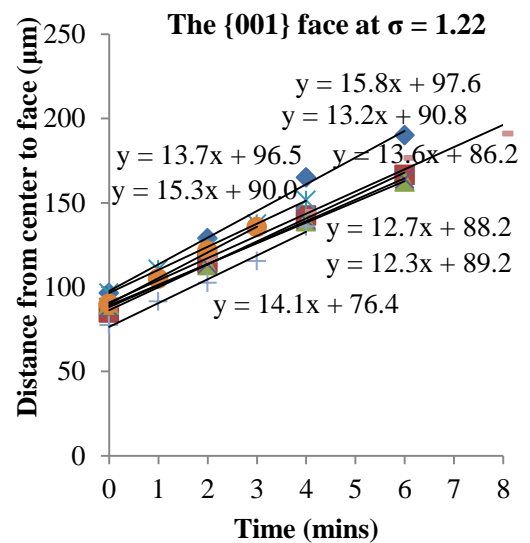
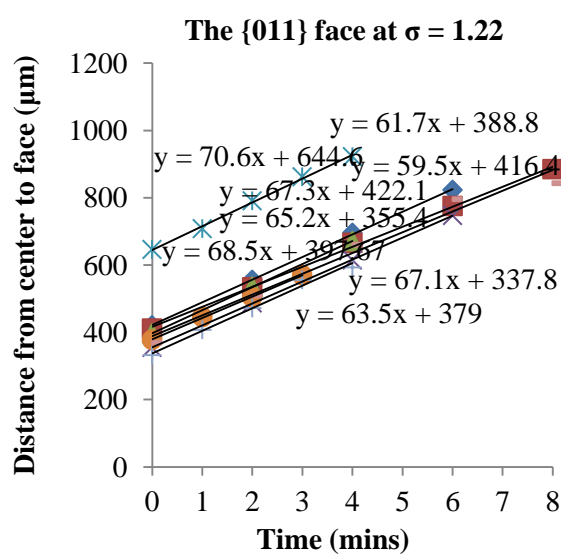
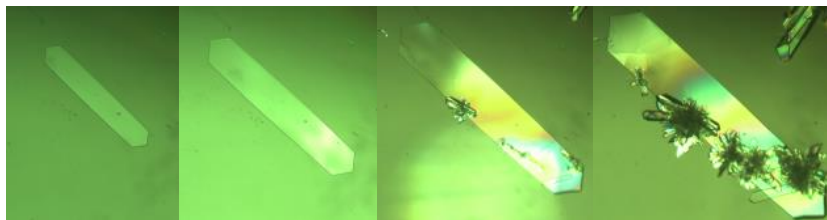


$\sigma = 0.66$

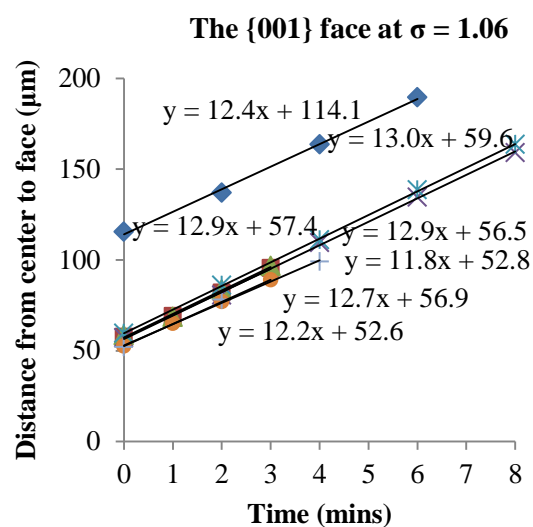
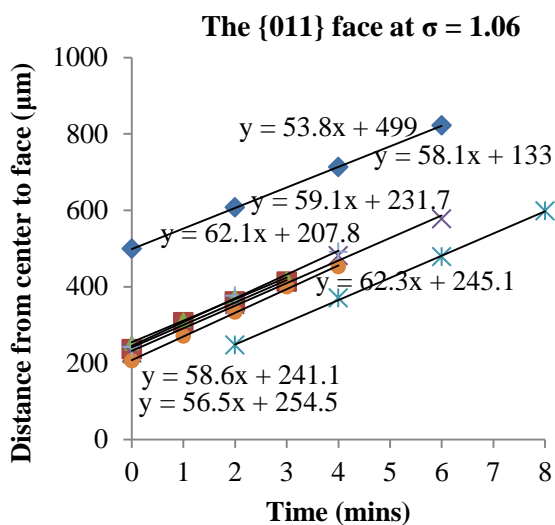
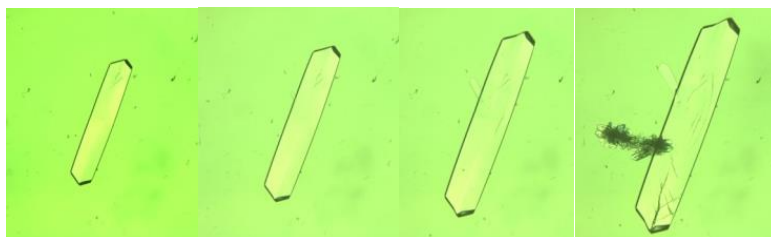


B2.2 Ethyl Acetate Solutions

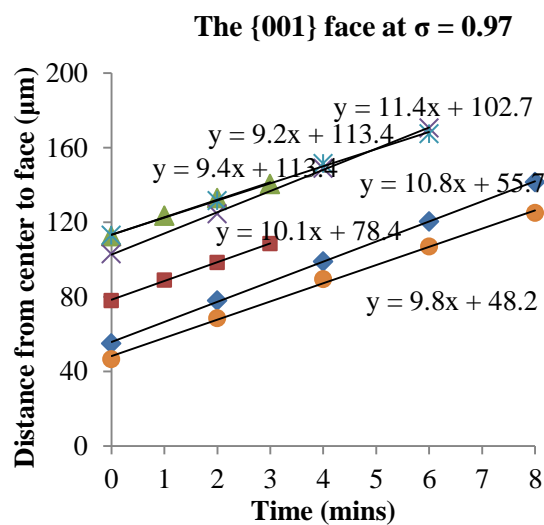
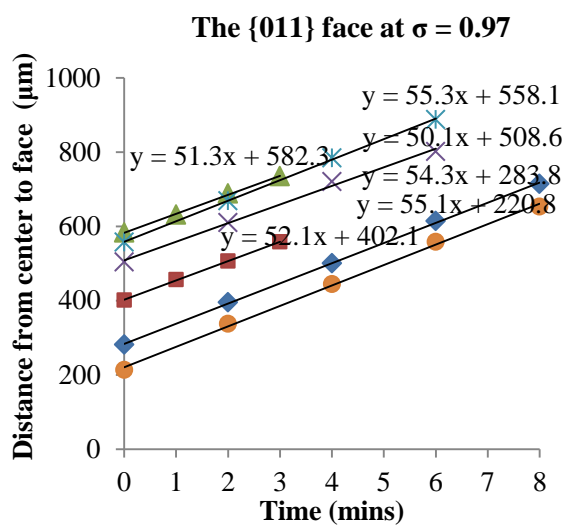
$\sigma = 1.22$



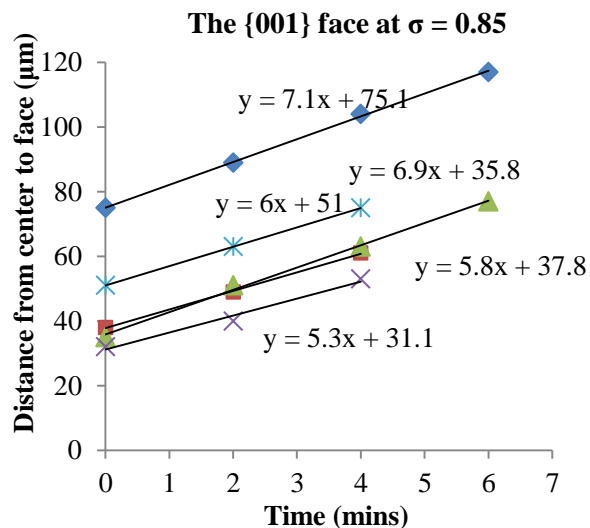
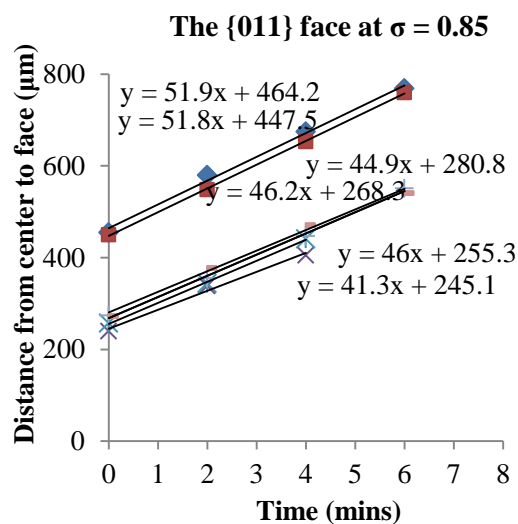
$\sigma = 1.06$



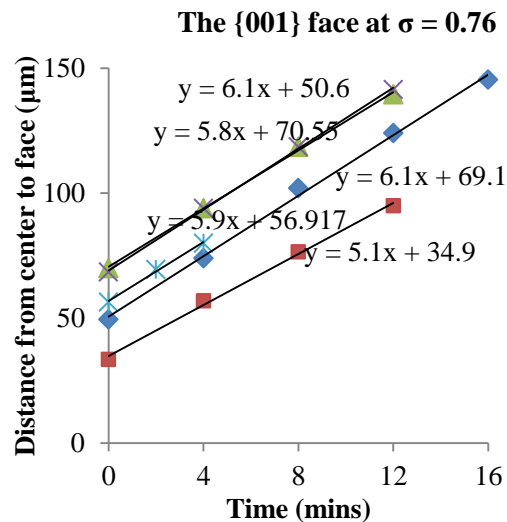
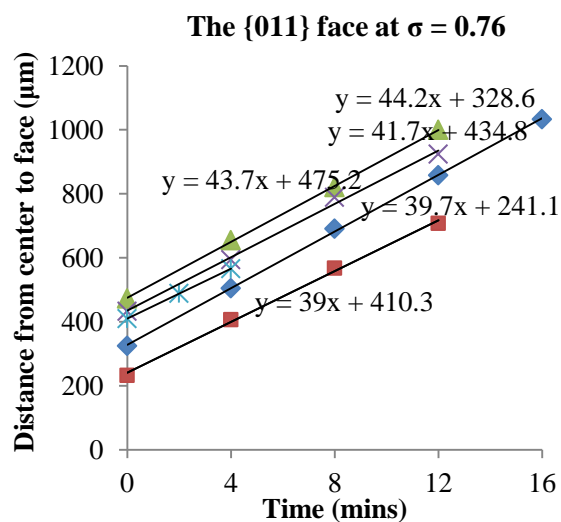
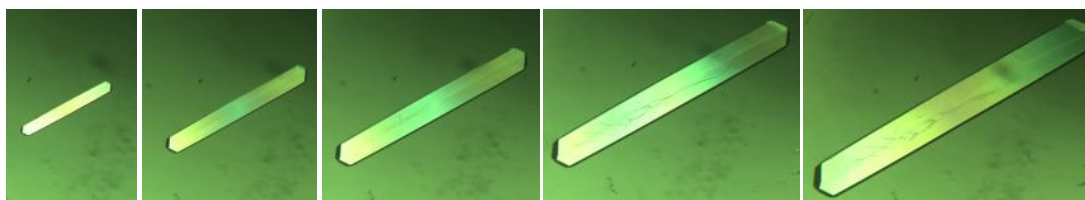
$\sigma = 0.97$



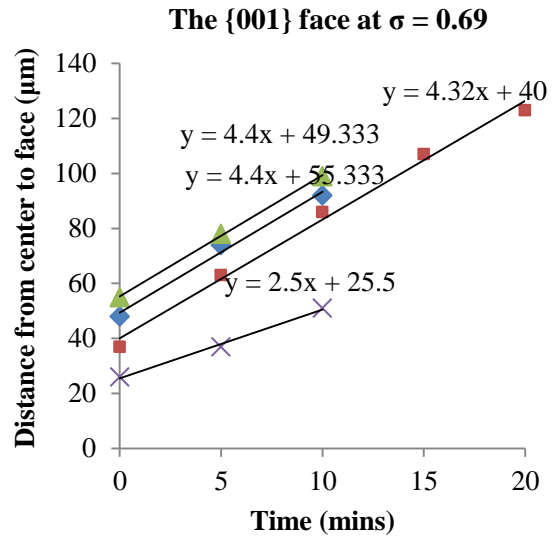
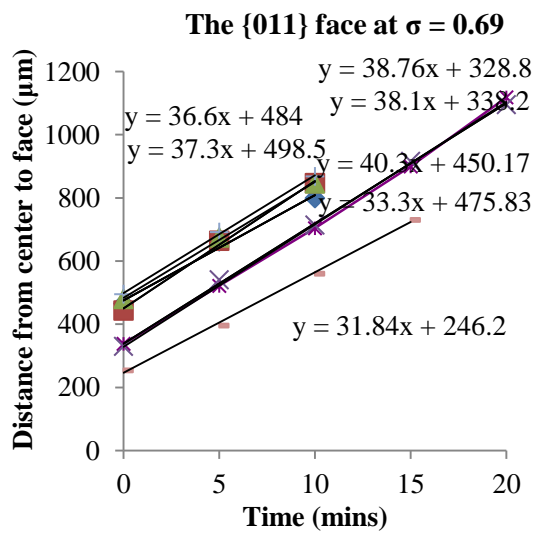
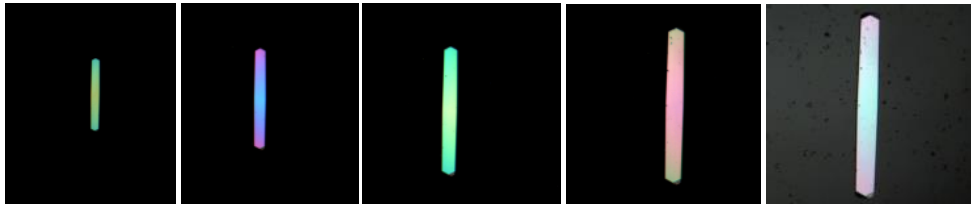
$\sigma = 0.85$



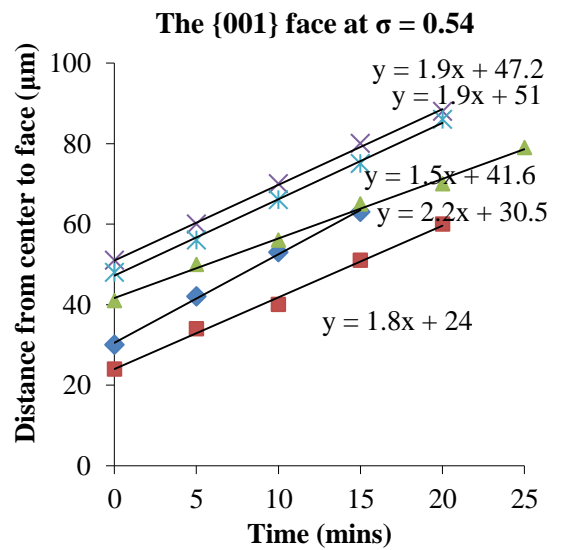
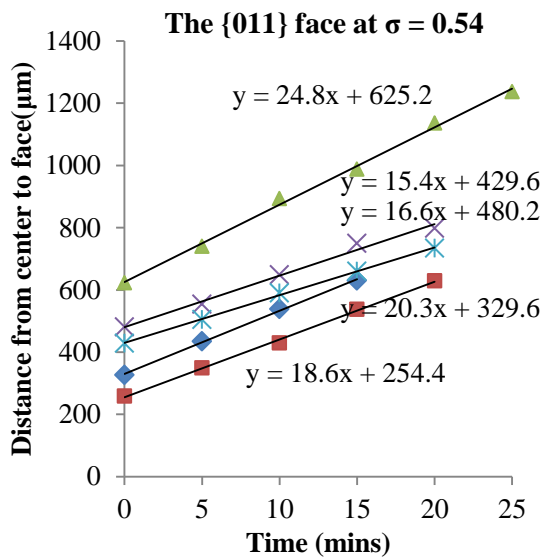
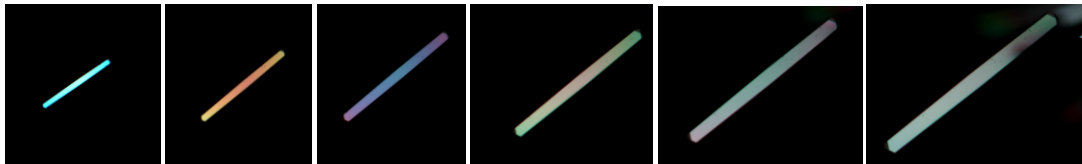
$\sigma = 0.76$



$\sigma = 0.69$

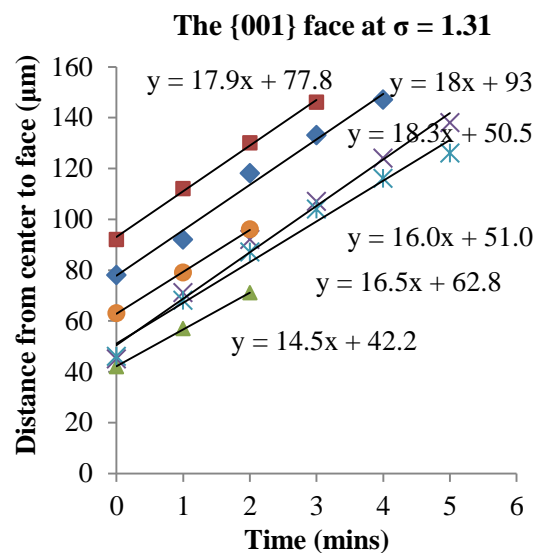
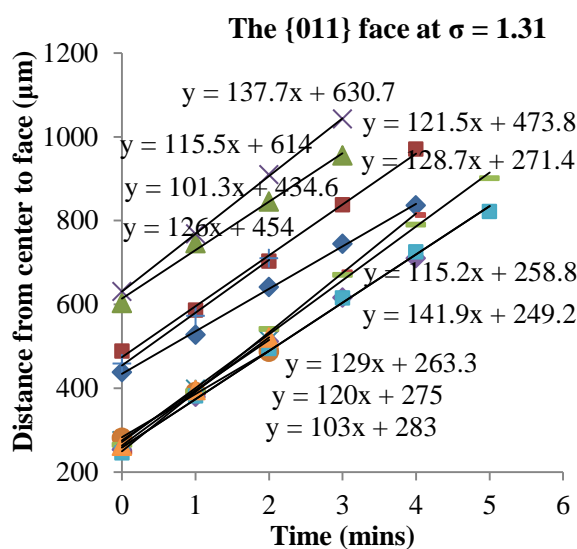


$\sigma = 0.54$

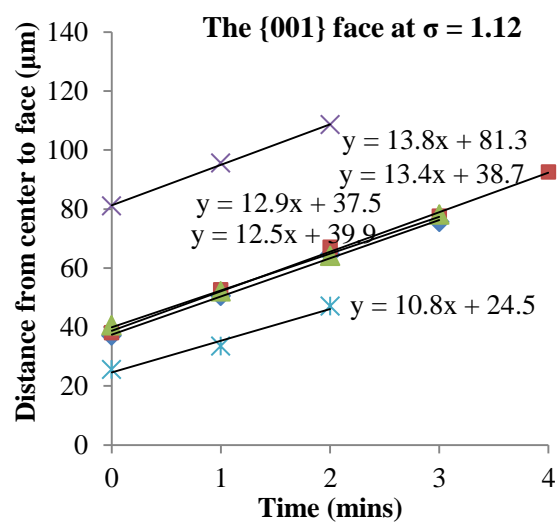
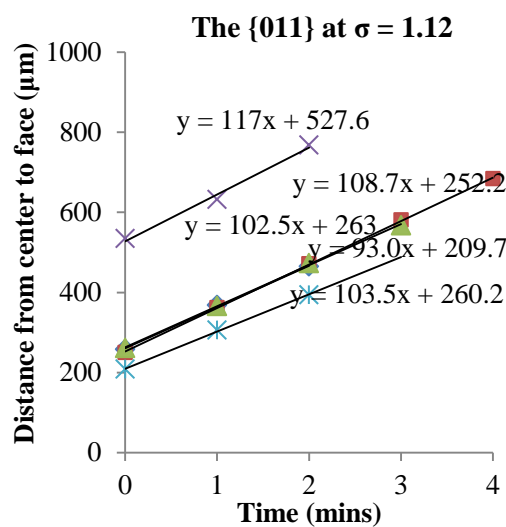
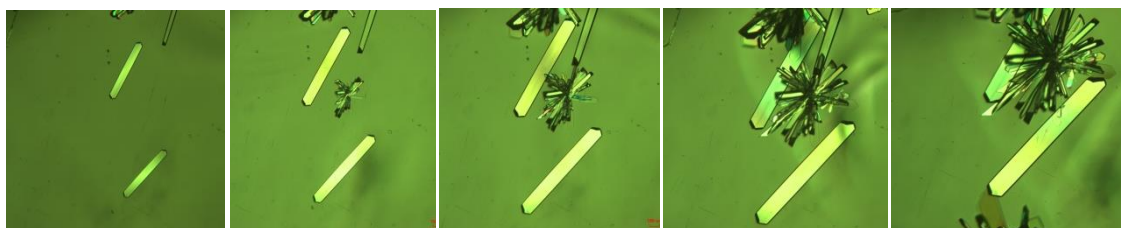


B2.3 Acetonitrile Solutions

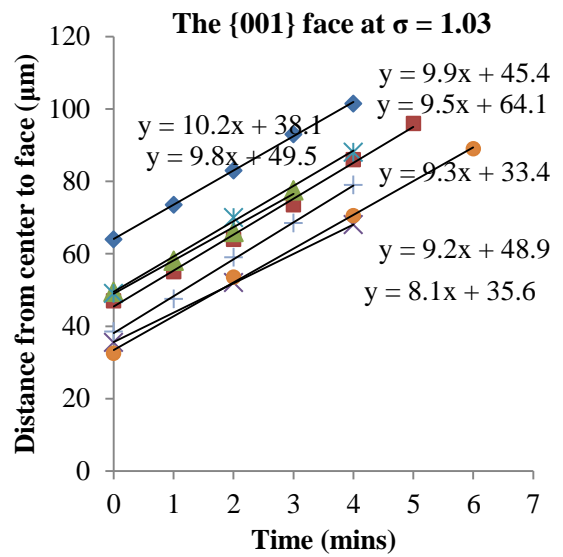
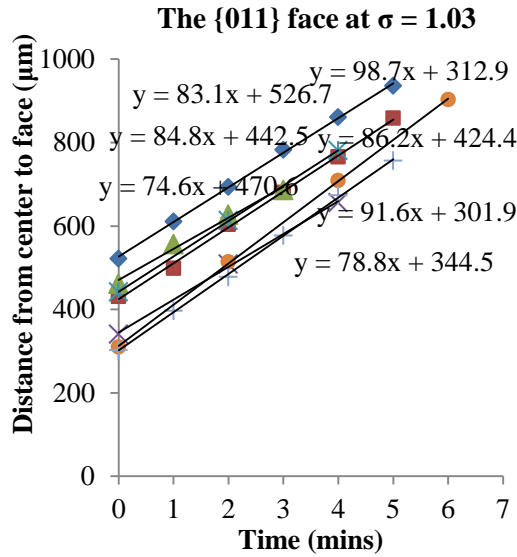
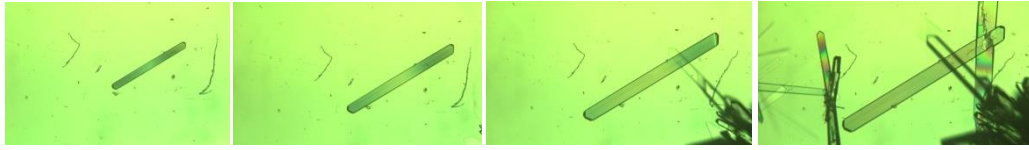
$\sigma = 1.31$



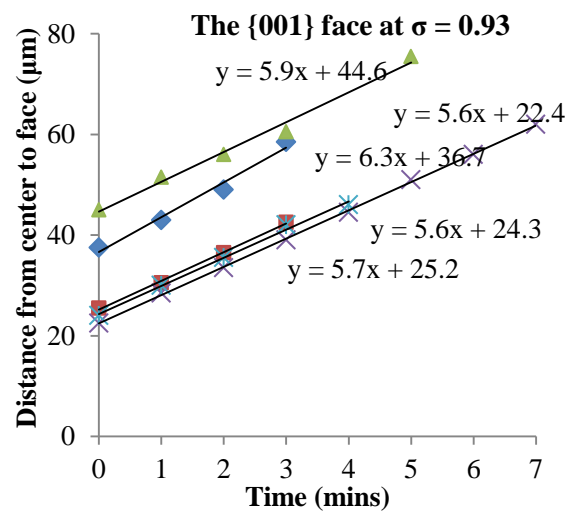
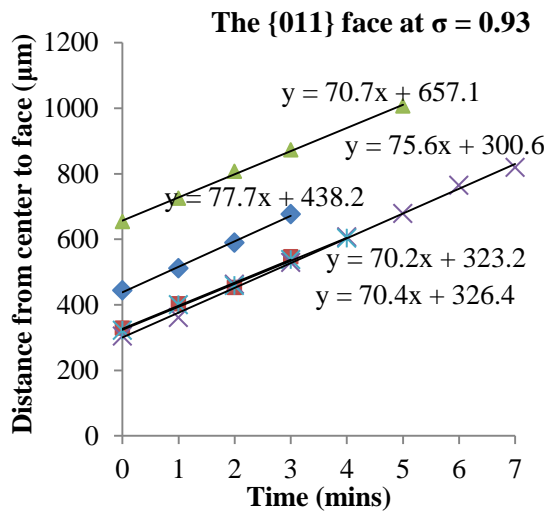
$\sigma = 1.12$



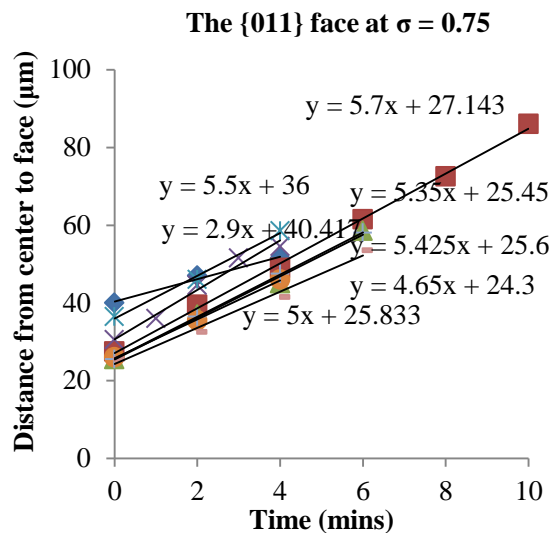
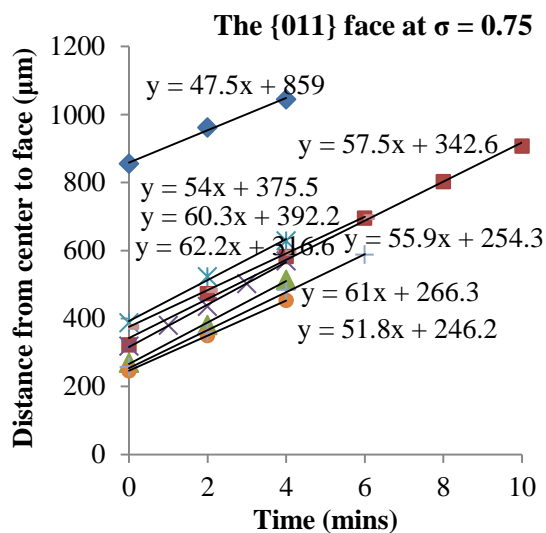
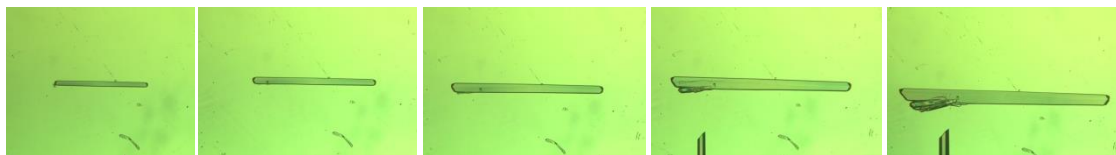
$\sigma = 1.03$



$\sigma = 0.93$

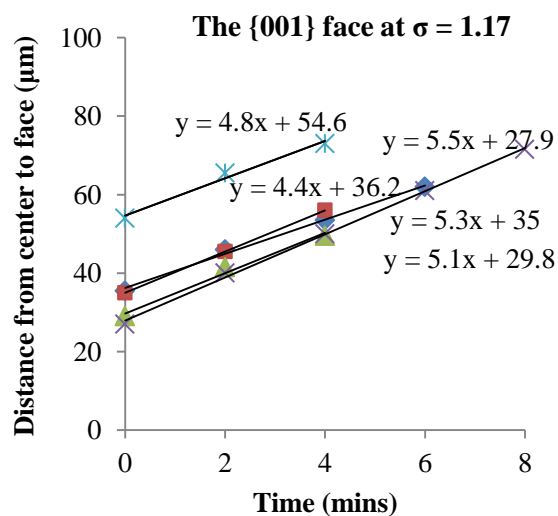
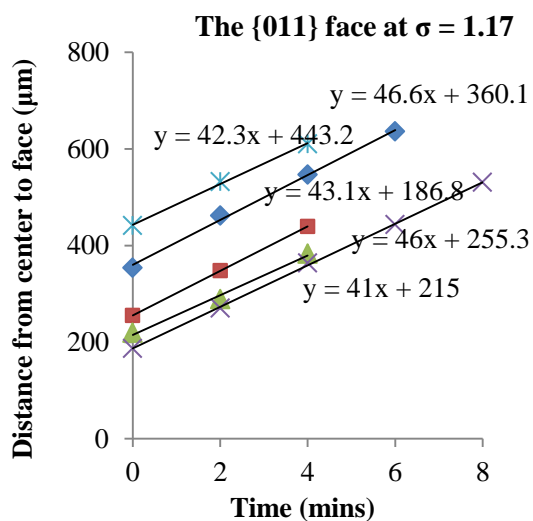
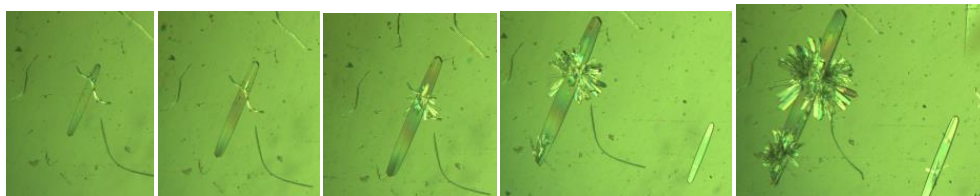


$\sigma = 0.75$

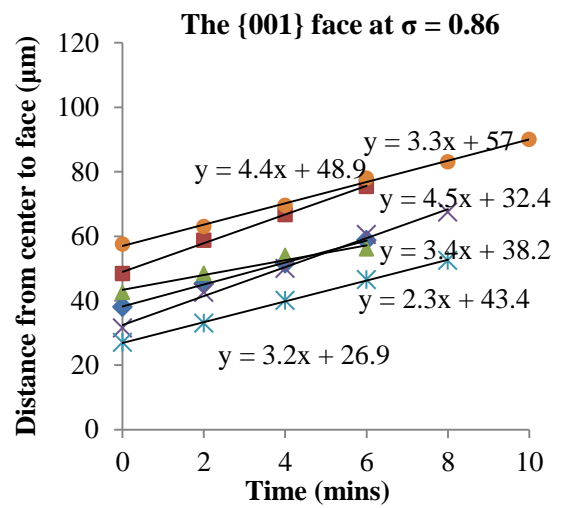
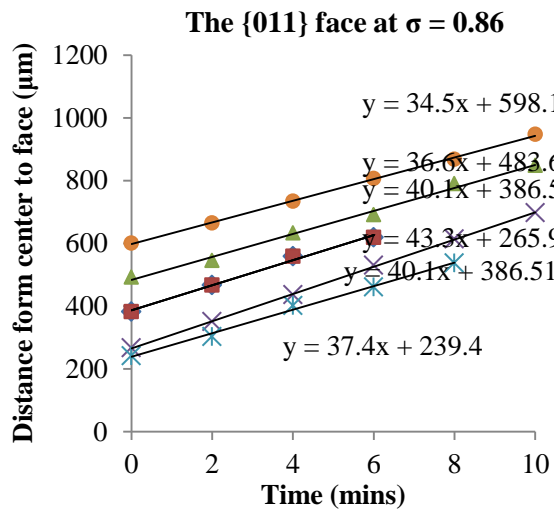
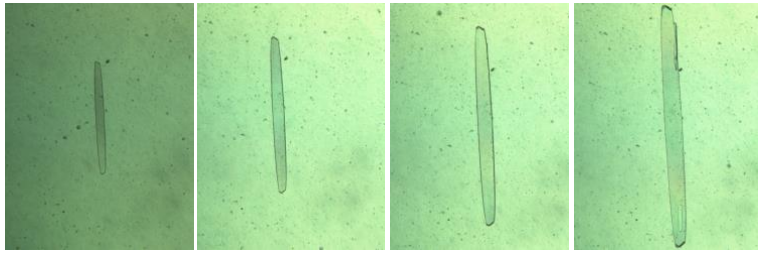


B2.4 Toluene Solutions

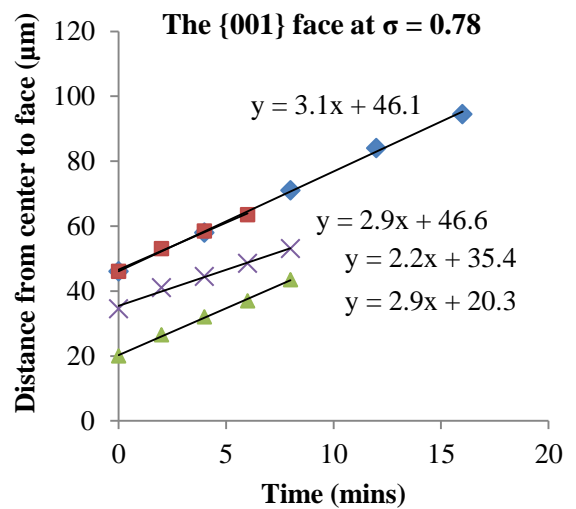
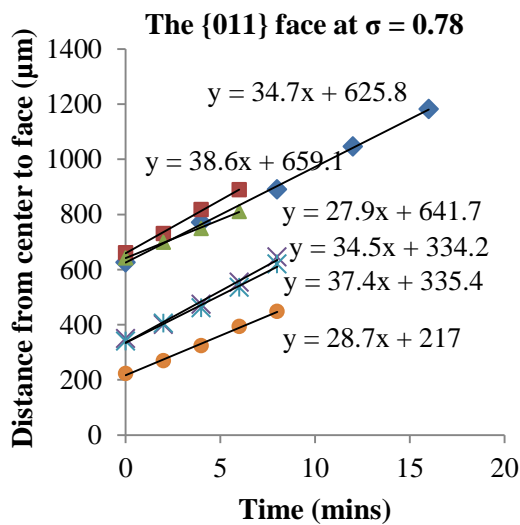
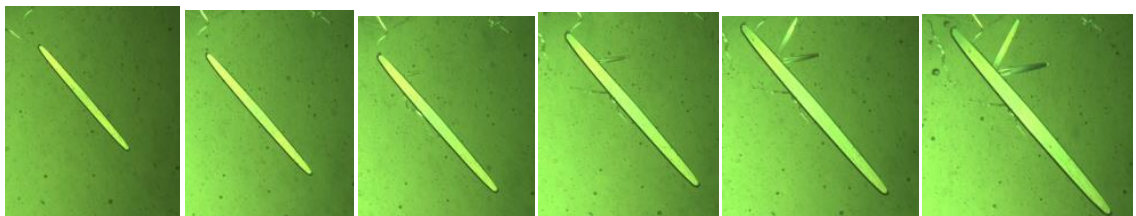
$\sigma = 1.17$



$\sigma = 0.86$



$\sigma = 0.78$



$\sigma = 0.70$

